CHARLES PANKOW FOUNDATION

Building Innovation through Research

DESIGN REQUIREMENTS FOR MECHANICALLY SPLICED HIGH-STRENGTH REINFORCING BARS IN HINGE REGIONS

The University of Texas at San Antonio

Principle Investigator

Wassim M. Ghannoum

Graduate Students and Researchers

Latip Kumar Sharma

Narayan Budhathoki

Wrya Abdullah

Sudhir Niroula

Seyed Sasan Khedmatgozar Dolati

Arjun Basnet

Sponsored by

The Charles Pankow Foundation

The Concrete Reinforcing Steel Institute

The American Concrete Institute's Foundation Concrete Research Council

October 2025

Table of Contents

List of Tables

List of Figures

1 Introduction

The demand for higher strength steel reinforcing bars is steadily increasing in both seismic and non-seismic applications, driven by the need to mitigate reinforcement congestion, reduce material usage, and enhance the economic and environmental efficiency of concrete construction. Reinforcement congestion poses a significant challenge in regions requiring ductile seismic detailing, where traditional lap splicing of bars can exacerbate the problem. Lap splices not only contribute to congestion but may also lead to over-reinforcement, increasing the risk of non-ductile behavior due to stress concentrations at lap ends, thereby compromising the deformation capacity of critical regions of a structure (Almeida et al., 2017; Villalobos et al., 2017). Furthermore, lap splices are not permitted in plastic hinge regions of special moment-resisting frames and wall systems, often resulting in impractically long dowel bars, particularly in shear wall construction. Mechanical couplers offer a practical alternative, allowing for reduced dowel lengths and improved constructability when permitted in hinge regions.

The 2019 revision of ACI 318 marks a significant shift in support of higher-Grade reinforcing bars, explicitly permitting the use of Grades 80 and 100 (550 and 690 MPa) in reinforced concrete construction(ACI Committee 318, 2019). While mechanical splices for Grade 60 (420 MPa) bars have long been accepted for use in regions expected to experience inelastic strains during seismic events, the 2019 update still introduces restrictions on the use of mechanical splices for Grade 80 and 100 bars in critical regions where yielding is likely to occur. Similarly, Caltrans and AASHTO prohibit splices in hinge zones and further restrict their use for higher Grade bars anywhere in a structure(AASHTO., 2011; Caltrans CT670, 2022). These limitations reflect concerns about mechanical coupler capacity to develop the tensile strength of higher-Grade bars and the risk of premature failure due to low-cycle fatigue under seismic strain demands.

During seismic events, longitudinal reinforcement in hinge regions is subjected to large inelastic strain reversals, which can lead to low-cycle fatigue damage and, in some cases, bar fracture (Rautenberg et al., 2012; Sokoli et al., 2019; To et al., 2021). In fact, when concrete members are designed in accordance with the latest seismic provisions of ACI 318, the provided confinement typically delays concrete damage to the extent that significant loss of strength is primarily attributed to reinforcing bar fracture caused by low-cycle fatigue. (D. Sokoli & W. M. Ghannoum,

2016; Sokoli et al., 2019; D. Sokoli et al., 2020; D. Sokoli et al., 2025; Zhong et al., 2021). Low-cycle fatigue is defined as the premature failure of materials subjected to a relatively small number of high-amplitude deformation cycles that extend beyond the elastic range of behavior(Brown & Kunnath, 2004; Ghannoum & Slavin, 2016; J. B. Mander et al., 1994). Although relatively few experiments have evaluated the performance of mechanical couplers with Grade 60 (420 MPa) bars under hinge-region demands (Bompa & Elghazouli, 2019; Brueggen et al., 2007; Haber et al., 2014), and one recent study has assessed their behavior with Grade 100 (690 MPa) bars(Neupane et al., 2025), there is still limited test data to support the use of coupled Grade 80 (550 MPa) and 100 (690 MPa) reinforcing bars under harsh seismic demands. Furthermore, given the large diversity of coupler types available in the U.S. market, results from a limited set of tests cannot be generalized to all coupler types. And while testing all coupler types in concrete members subjected to realistic loading protocols is one way to qualify use of couplers in hinge regions, cost implications make such an approach impractical. One solution is to offer cost-effective pre-qualification testing. This testing should impose realistic demands on couplers that are reflective of those occurring in hinge regions of concrete members. At the same time, the pre-qualification testing procedures should include acceptance criteria that ensure adequate seismic performance in concrete members.

Unfortunately, none of the currently available specifications for qualifying mechanical splices include a loading protocol that is representative of the reversed inelastic strain demands applied to bars and couplers in seismic hinge regions. ACI 318-19 only requires strength-based pre-qualification requirements and classifies splices as Type 1 or Type 2 through only tension and compression strength requirements. Other specifications such as the TxDOT (TEX-744-I/DMS-4510) (DMS 4510, 2023; Tex-744-I, 2019) , Caltrans' CT670 (Caltrans CT670, 2022), and AASHTO LRFD (AASHTO., 2011) only consider loading protocols that do not exceed the yield strength of reinforcing bars. AC 133 (2020)(AC133, 2020) and ISO 15835 (2018) have one protocol that exceeds yield strength but does not reverse strains inelastically and therefore do not capture the demands on mechanical splices in higher regions.

In this report, the mechanical coupler refers to the coupling device used, while mechanical splice refers to the coupler and the adjacent bars it connects.

1.1 Objective and Scope

The overarching objective of this study is to provide experimental evidence supporting the safe use of mechanical couplers in hinge regions of reinforced concrete members. Of particular interest is the performance of coupler with Grade 80 (550 MPa) reinforcing bars that are seeing increasing use and are overtaking Grade 60 (420 MPa) in critical seismic members in regions of high seismicity in the U.S.

To achieve this aim, the study is divided into two core tasks as follows.

Task 1: In-Air Inelastic Cyclic Testing

Within this task, mechanical splices were subjected to reversed inelastic cyclic strain demands in a uniaxial testing machine. These tests allowed the quantification of the low-cycle fatigue performance of various couplers and provided relative performance comparisons between them and the fatigue life of the bare bars they couple. As these tests were being conducted, the protocols and test setup were adjusted to arrive at a reliable protocol that could be used for pre-qualifying devices under realistic seismic demands. Eleven different coupler types from five manufacturers were tested. Grade 80 ASTM A706 bars produced using the two main processes used in the United States were included, namely the Micro-Alloying (MA) and Quenching and Self-Tempering (QST) bar production processes(Ghannoum & Slavin, 2016; Gonzalez et al., 2025). Only one batch of Grade 80 MA bars and one batch of Grade 80 QST bars were used for all samples in Task 1 and in all walls tested in Task 2. This was done to focus on the influence of the couplers on the low-cycle fatigue life of mechanical splices, without introducing additional variability from the fatigue performance of the bare bars themselves. In-air test results were used to screen potentially viable mechanical couplers for use in the full-scale reinforced concrete wall tests conducted in Task 2. Additionally, monotonic tension tests were conducted for each splice type to evaluate their strength and ductility performance and to explore potential correlations with their inelastic cyclic performance.

Task 2: Full-Scale Reinforced Concrete Wall Tests

Four full-scale reinforced concrete wall specimens, including one control wall specimen without splices, were constructed and tested under reversed cyclic loading until significant strength

degradation occurred. The hinge regions of lateral load-resisting elements with relatively long cross-section, such as walls, experience the most severe inelastic strain demands during seismic events(D. Sokoli et al., 2025; Zhong et al., 2021), making them critical locations for assessing mechanical splice performance.

Results from wall tests served to identify correlation between the fatigue lives of mechanical splices in the walls and in the in-air tests conducted in Task 1. Wall tests therefore served to determine the minimum acceptance criteria in terms of half-cycles to fracture under the testing protocol developed in Task 1, for mechanical splices to be safely used in hinge regions.

1.2 Report Organization

The report is organized in two introductory chapters followed by two parts (one for each task) and a final conclusions chapter.

Chapter 1: Introduction

Chapter 2: Background

This chapter provides background information on existing mechanical-splice qualification procedures and specifications. The chapter also presents relevant past work from literature on in-air testing and in-concrete testing of mechanical splices.

Part I: In-Air Testing

Chapter 3: Low-cycle fatigue experimental program

This chapter describes the in-air low-cycle fatigue testing program carried out in this study. It begins with the test matrix, summarizing the mechanical coupler types, reinforcing bar batches, and bar sizes included in the program. The next section outlines the test parameters, highlighting the use of braced and unbraced configurations and the clear gripping span. The chapter then presents the loading protocol adopted, followed by a detailed description of the test procedures.

Chapter 4: Test Results and Observations

This chapter presents the results from low-cycle fatigue and monotonic tests of mechanical splice samples, organized in two phases.

- *Phase 1* includes unbraced tests on #8 (25 mm) bar specimens, covering both bare bars and mechanical splices.
- *Phase 2* includes the performance of mechanical splices under braced conditions for two bar sizes: # 8 (25 mm) and # 11 (36 mm).

The primary performance metric used to compare fatigue performance was the mean half-cycles to fracture, with the bare bar values serving as the baseline for comparison. Monotonic tension test results for both bare bar and mechanical splice specimens are also included to examine correlations between monotonic and reversed inelastic cyclic performance.

Part II: Wall Testing

Chapter 5: Wall experimental program

This chapter describes the wall testing program carried out in this study. It details the wall designs, layouts and testing protocol. The chapter also contains information about instrumentation.

Chapter 6: Wall experimental test results

This chapter presents detailed experimental results from the four wall tests conducted. The chapter presents the lateral force versus deformation response of the walls, including information about key behavioral milestones as they occurred in each test. Test results include strain demands obtained for strain gauges placed on reinforcing bars adjacent to mechanical couplers, and surface strain readings from a digital image correlation system.

Chapter 7: Discussion and Comparison between Wall Specimens

This chapter compares the behavior and performance of the walls and the mechanical couplers in the walls. The Chapter also compares the performance of coupler in the walls with their performance under the inelastic cyclic testing protocol proposed in Part I.

Chapter 8: Conclusions

Salient conclusions for both parts of this report are presented in this chapter.

2 Background

2.1 Literature review on existing qualification testing protocols for mechanical splices

Existing in-air qualification protocols and acceptance criteria used to evaluate mechanical splices for reinforced concrete structures are presented in this section. Specifications from ACI 318-19, ICC-ES AC133 (2020)(AC133, 2020), ISO 15835 Part I and II (2018)(ISO 15835, 2018), NF A35-020-2-1 (France)(Normalisation, 2017), ASTM A1034 (2023)(ASTM A1034/A1034M-23 2023), TEX-744-I/DMS-4510 (TxDOT)(Tex-744-I, 2019), CT 670 (CALTRANS), AASHTO (2011) (AASHTO, 2011)and NZS 3101(N.Z.S., 2006) are reviewed with a focus on their applicability to high-strength reinforcement and cyclic performance evaluation. Most existing testing protocols for mechanical splices are based on test results using Grade 60 reinforcement and may not scale appropriately for Grade 80 and higher-strength bars. These protocols can generally be classified into four broad categories: slip tests, monotonic tension/compression tests, low-cycle fatigue tests, and high-cycle fatigue tests.

2.1.1 Slip Tests

Slip is a key serviceability criterion defined in most specifications. Slip is measured between a coupling device and adjacent bars and can be influenced by coupler type, interlock effectiveness, stress level, and cycling load. Slip is typically required to be measured across the entire mechanical splice and therefore combines potential slip at both ends of a coupler. Existing protocols require slip to be measured as either residual slip after unloading from a tensile load or slip at peak load measured at a service load level. In the case of peak-load slip measurement (ISO 15835 (2018)(ISO 15835, 2018)), elastic elongation of a bare bar of equivalent length to the measurement gage length is subtracted from the reading to arrive at a differential elongation measurement compared to what a bare bar would experience. Table 2.1 summarizes various slip criteria in the literature. In the table, positive stress indicated tension and negative stress indicates compression.

Table 2.1-Slip loading protocol and acceptance criteria across different standards (1ksi=6.89 MPa, 1 in.=25.4 mm)

Standard	***Slip type***	***Gage length***	***Loading protocol / Number of cycles***	***Maximum allowable slip***
CT670 (2022)	*Residual*	*L_c + $2d_b$ on each side*	5% f_y to 50% f_y / 1 cycle	*#4 (12 mm) to #6 (19 mm)= 0.020 in. (0.508 mm)* *#7 (22 mm) to #9 (29 mm) = 0.028 in. (0.711 mm)* *#10 (32 mm) to #11(36 mm) = 0.036 in. (0.914 mm)* *#14 (43 mm) = 0.048 in. (1.219 mm)* *#18 (57 mm) = 0.048 in. (1.219 mm)*
AASHTO	*Residual*	*Clear of coupler device*	*Load up to 30 ksi (206.84MPa) and unload to 3 ksi (20.68 MPa) /1 cycle*	*#14 (43 mm) and smaller = 0.010 in. (0.254 mm)* *#18 (57 mm) = 0.030 in. (0.762 mm)*
TEX-744-I / DMS 4510	*Residual*	*L_c + (1±0.5 in.) on each side*	*5% f_y to 50% f_y / 1 cycle*	*# 14 (43mm) and smaller =0.010 in. (0.254 mm)* *#18 (57 mm)= 0.030 in. (0.762 mm)*
AC 133-2020	*Residual*	*L_c + d_b from affected zone on each side*	*0 to 95% f_y, then 95% f_y to -50% f_y / 20 cycles*	*0.012 in. (0.3 mm)*
ISO 15835-1 & 2 (2018)	*Residual or Peak Slip*	*L_c + (2 to 6) d_b*	*0 to 2% $R_{eH,spec}$, 2% to 60% of $R_{eH,spec}$, back to 2% of $R_{eH,spec}$ / 1 cycle*	*Median ≤ 0.004 in.(0.1mm)* *Outlier ≤ Median + 0.002in. (0.05 mm)*
NF A 35-020-1 / -2-1	*Residual*	*As close as possible to L_c*	*0 to 5% of R_{e_nom}, 5% to 60% of R_{e_nom}, back to 5% of R_{e_nom} , then unload / 3 cycles*	*Median ≤ 0.004 in. (0.1 mm)* *Individual ≤ 0.008 in. (0.20 mm)*
ASTM A1034-23	*Residual*	*L_c + (1 to 3) d_b on each side*	*Load not explicitly mentioned / 1 cycle*	*Not mentioned*

where,

L_c is the length of the coupler device.

f_y is the specified yield strength of the reinforcing bars.

d_b is nominal bar diameter of reinforcing bar being spliced.

$R_{eH,spec}$ is specified characteristic yield strength of reinforcing bar being spliced.

$R_{e,nom}$ is nominal yield strength of reinforcing bar being spliced.

Except for AC133 (2020), the documents listed in Table 2.1 specify that slip testing should involve applying a tensile load equal to 50% or 60% of the specified yield strength of the spliced reinforcing bars. These documents generally do not incorporate compressive loading or reverse cyclic loading during slip tests. In contrast, AC 133 includes reverse tension-compression loading, with tension levels reaching up to 95% of the yield strength and compression down to -50% of the same. Some standards, including AC133 (2020), NZS3103, and NF A35-020-2-1 (E), also account for slip accumulation due to repeated load cycles at service-level loads, requiring multiple loading cycles before slip is measured.

2.1.2 Monotonic Tension/Compression Tests

All specifications summarized in Table 2.2 require mechanical splices to achieve a minimum tensile strength typically taken as 1.25 times the bar specified yield strength (f_y) or equal to the bar specified tensile strength (f_u) depending on splice classification (Table 2.2). Most specifications also provide a minimum strength requirement in compression. Furthermore, some specifications require minimum elongation under tension that are measured on the bars adjacent to the couplers.

Table 2.2-Provisions for monotonic tension tests (Note 1ksi=6.89 MPa, 1 in.=25.4 mm)

Standard Testing Method	***Stress Criteria***	***Strain / Ductility Criteria***
AC 133	• *Type 1 splice: Minimum of 1.25 x f_y.* • *Type 2 splice: Minimum of 1.25 × f_y and 1.0 × f_u.* • *Type 2HS (high strain): After the 4th stage of cyclic loading, must achieve at least 1.25 × f_y and 1.0 × f_u.*	• *For Type 2HS splices, ductility is assessed based on uniform elongation requirements for deformed reinforcement as outlined in ACI 318-19 Table 20.2.1.3(c) as reproduced in Table 2.3 below*
Caltrans CT670	• *Minimum tensile strength of 80 ksi for Grade 60 bars and 100 ksi for Grade 80 bars.*	*For Grade 60 bars* • *9% for #10 bars and smaller.* • *6% for #11 bars and larger* *For Grade 80 bars: 6%*

ISO 15835-1 & 2	• *Minimum strength = $R_{eH,spec}$ × $(R_m / R_{eH})_{spec}$* • *Where, $(R_m / R_{eH})_{spec}$ is the specific tensile/yield strength ratio for reinforcing bar. $R_{m,spec}$ is the specified (or nominal) tensile strength value of reinforcing bar. $R_{eH,spec}$ is the specified characteristic yield strength value of reinforcing bar.*	*The total elongation after fracture (A_{gt}), measured on the bar outside the coupler in accordance with ISO 15630-1, must be at least 70% of the A_{gt} specified for the parent bar*
NF A 35-020-2-1 (E) *(French Standard)*	• *The maximum force resisted by the splice must be at least 95% of the actual maximum force capacity of the bar*	*The total elongation at peak load (A_{gt}), measured in the unaffected bar region on the failure side, must meet the minimum value specified for the bar grade*
DMS-4510 / TEX-744-I	• *The mechanical splice must develop at least 125% of the minimum yield strength required for the lowest grade bar in the splice*	
AASHTO	• *The required strength shall not be less than 125 percent of specified yield strength of the bar in tension or compression, as required.*	

ACI 318-2019 and AC133-2020 define Type 1 mechanical splices as those able to withstand 1.25 f_y in tension, and Type 2 splices as those able to withstand f_u in tension. AC133 further introducing Type 2HS splices that must satisfy both strength (1.25 f_y and 1.0 f_u) and uniform elongation requirements as shown in Table 2.3 (uniform elongation is determined as elongation at maximum force). AC133 also requires splices to develop at least 125% f_y in compression for type 1 splice, type 2 and for type 2HS (need not to exceed fu of the reinforcing bar) splice.

Table 2.3-Uniform elongation requirements for ASTM A706 reinforcement

Bar Designation No.	***Grade 60***	***Grade 80***	***Grade 100***
3, 4, 5, 6, 7, 8, 9, 10	*9%*	*7%*	*6%*
11, 14, 18	*6%*	*6%*	*6%*

CT670 imposes strain requirements for ultimate butt splices, mandating either visible necking outside the affected zone (≥2d_b from the coupler) or minimum uniform elongation per ASTM

A706/A706M-22(ASTM Standard A706/A706M-22a, 2022). It specifies minimum tensile strengths of 80 ksi (550 MPa) for Grade 60 (550 MPa) and 100 ksi (690 MPa) for Grade 80 (550 MPa) with strain thresholds of 9% for smaller bars and 6% for larger ones as shown in Table 2.3-Uniform elongation requirements for ASTM A706 reinforcement. ISO 15835 (2018) also specifies elongation requirements, mandating that the measured elongation outside the splice must be at least 70% of the characteristic elongation value of the parent reinforcing bar. Similarly, NF A35-020-2-1 requires the mechanical splice to develop no less than 95% of the actual maximum force of the bar, while also ensuring that the total elongation of adjacent bars at maximum force meets the minimum values specified for the bar grade. DMS-4510/TEX-744-I focuses solely on strength, requiring splices to reach 125% f_y with no ductility criteria.

2.1.3 Low-cycle Fatigue Tests

The primary objective of low-cycle fatigue (LCF) testing is to simulate the effects of seismic loading or overloads. Standards such as AC133, NF A 35-020-2-1, and ISO 15835 specify reversed tension-compression loading sequences to evaluate mechanical splice performance under seismic demands. These protocols typically involve staged cyclic loading (as shown Table 2.4) with progressively increasing strain amplitudes. Residual slip is also measured at the end of each stage. For Type 2 and Type 2HS splices in AC133, the allowable maximum residual slip is 0.012 in. (0.3 mm) after Stage 1 and 2, and 0.024 in. (0.6 mm) after Stage 3. Specimen are required to complete all loading stages without failure. In ISO 15835, splices qualified under Category S must similarly withstand all specified loading stages.

Table 2.4-Elastic and inelastic test sequence

STAGE	TENSION	COMPRESSION	NUMBER OF CYCLES
1	$0.95f_y$	$0.5f_y$	20
2	$2\varepsilon_{ya}$	$0.5f_y$	4
3	$5\varepsilon_{ya}$	$0.5f_y$	4

The French standard (NF A 35-020-2-1) proposes similar test as Oligocyclic test that includes both elastic and inelastic reversed cyclic loading. The specimen is first subjected to 10 elastic load cycles with the same loading magnitude as stage 1 of Table 2.4, followed by 10 inelastic load cycles with the same loading magnitude stage 3 of Table 2.4, before being pulled in tension to failure. However, Caltrans CT 670 requires only cyclic loading in the elastic range from 5%f_y and 90%f_y for 100 cycles and therefore does not require testing under inelastic strain demands. If no fracture occurs at the loading protocol, the axial tensile load is increased until the fracture. It should be noted that Caltrans does not allow couplers in hinge regions where large inelastic strain demands may occur(Transportation, 2013).

As presented above, none of the well-established mechanical splice testing protocol explicitly include reversed inelastic strain cycles, which are critical for evaluating performance in seismic hinge regions. The protocol in Table 2.4 includes inelastic cyclic excursions for Type 2 and Type 2HS splices, involving strain amplitudes up to 5ε_y in tension and –0.5 f_y in compression. Therefore, the compressive loading does not apply reversed inelastic demands. As such, it does not fully replicate the strain reversals observed in hinge regions, where bars undergo inelastic deformation in both tension and compression.

2.1.4 High-cycle Fatigue Tests

High-cycle testing is commonly used to evaluate the fatigue performance of mechanical splices (MS) under a large number of load cycles (common on bridge structures) within the elastic stress range. High-cycle fatigue testing protocols vary across standards in terms of stress range, frequency, and required cycle counts. CT670 specifies cycling between ±25 ksi (172.37 MPa) for 10,000 cycles for Grade 60 Mechanical splice, ±33 ksi (227.53 MPa) for Grade 80 Mechanical splice, while DMS 4510/TEX-744-I applies +5 ksi (34.47 MPa) to +30 ksi (206.84 MPa) in tension at 5 Hz for 80,000 cycles. In contrast, ISO 15835-1 & 2 and NF A 35-020-1 require a stress range up to 60% of yield strength, sustained for 2 million cycles, reflecting the most demanding fatigue endurance criteria among the listed standards. The test concludes either upon fracture within the mechanical splice zone or after a specified number of cycles without fracture.

2.2 Literature review on performance of mechanical splices in plastic hinge regions

The use of mechanical splices in reinforced concrete (RC) structures, particularly within plastic hinge regions, has gained increasing attention in recent years with the advancement of accelerated construction practices and the growing adoption of high strength reinforcing bars (HSRBs). Traditionally, most experimental studies and design provisions have been developed around Grade 60 (420 MPa) reinforcement. However, as design trends shift toward higher grades such as Grade 80 (550 MPa) and 100 (690 MPa), there is a pressing need to reassess the performance of mechanical couplers with HSRB under the inelastic strain demands representative of hinge regions. The current body of literature predominantly evaluates the behavior of mechanical splices using Grade 60 (420 MPa) bars under reversed cyclic loading, focusing on parameters such as lateral load–displacement behavior, bar fracture strains, crack initiation and propagation, energy dissipation, deformation components, and failure modes. These studies generally highlight the critical influence of coupler type, geometry, and placement on the plastic hinge behavior and global response of structural members. Among the limited number of studies incorporating high-strength bars, Neupane et al. (2025) provides one of the closest parallels to the present research by investigating splice performance using Grade 100 (690 MPa) reinforcement in structural walls subjected to reversed inelastic cyclic loading.

2.2.1 Neupane et al. (2025)

(Neupane et al., 2025) investigate the seismic performance of reinforced concrete structural walls with mechanically spliced Grade 100 (690 MPa) steel reinforcement, aiming to determine the viability of mechanical couplers in regions where bar yielding is expected. The study focuses on the behavior of three full-scale slender walls designed for earthquake resistance, each incorporating a different Type 2 mechanical splice per ACI 318-19: taper-threaded (Wall 1), swaged-threaded (Wall 2), and shear-screwed (Wall 3). All splices were located 2 in. (51 mm) above the base block, where strain demands are typically highest during seismic events.

The walls were 100 in. (2540 mm) long, 10 in. (254 mm) thick, and subjected to cyclic lateral displacements up to 4% drift. Wall satisfied special wall provision of ACI 318-19(318-19, 2019) except for the clear cover within the length of splice for Wall 2 and 3. Reinforcement consisted of Grade 100 bars with measured properties closely aligning with ASTM A706/ASTM-2022a(ASTM

Standard A706/A706M-22a, 2022), except for a slight deviation in yield stress observed for the #10 (32 mm) bar, which measured 99 ksi (682 MPa). Specimens were subjected to reversed cyclic loading with displacement-controlled drift ratios ranging from ±0.2% to ±4.0%.

Lateral Load-Displacement Response

- All three walls achieved lateral strengths exceeding calculated nominal flexural strength, indicating flexure-governed behavior.
- Wall 1 exhibited bar fractures at the mechanical splice (#4 [13 mm] web bars) beginning at drift ratio of 2.7%, resulting in significant strength degradation by the second cycle to the drift ratio of 3%.
- Walls 2 and 3 sustained lateral loads through drift cycles of 3% with no bar fracture; Wall 2 failed in boundary compression, while Wall 3 failed in shear/compression in the web.

Cracking pattern

- Wall 1 displayed uniform cracking along its lower height, but experienced concentrated damage near the bar splice zone.
- Walls 2 and 3 exhibited reduced cracking within the splice length but increased strain and crack width just above the splice region, likely due to increased local stiffness from longer or bulkier couplers.
- Notably, Wall 1 had a clear weak zone in the mechanical splices where bar threads extended beyond the coupler, leading to premature bar fracture.

Bar strains

- Longitudinal web and boundary bars yielded in all specimens by the drift ratio of 1.5%.
- Peak boundary bar strains reached over 6% in Wall 1 and over 9% in Wall 2, exceeding the bars' measured uniform elongation capacity, while Wall 3 strain demands were similar to the fracture strain observed in direct tensile tests.
- The fracture of web bars in Wall 1 led to strain localization and elevated boundary bar strains, supporting the notion that splice failure accelerates damage accumulation.

Energy Dissipation

- All walls maintained 80% of peak lateral strength through at least one to a drift ratio of 3%.
- Wall 1's energy dissipation declined rapidly after bar fractures initiated.
- Walls 2 and 3 sustained ductile behavior through larger drifts, demonstrating better hysteretic energy dissipation and cyclic stability.

Ultimate Drift

Ultimate drift was defined when strength loss reached 20% of peak strength.

- Wall 1: Ultimate drift occurred at a drift ratio of 3% due to bar fracture at the taper-threaded splice region.
- Wall 2: Boundary compression failure resulted in ultimate drift being reached at a drift ratio of 3%, without any bar fracture.
- Wall 3: Strength loss due to shear-induced web deformation resulted in an ultimate drift at a drift ratio of 4%, though no bar fracture occurred.

The findings of the study demonstrate that mechanical splices which force bar fracture to occur away from the splice (i.e., develop the full uniform elongation of the bars) can produce deformation capacity and failure modes equivalent to continuous reinforcement. By contrast, compliance with ACI Type 2 mechanical splice strength alone was insufficient to ensure ductile wall behavior. As seen in Wall 1, premature bar fracture occurred at the Type 2 splices and led to early strength degradation. The authors recommend against relying solely on ACI 318-19 Type 2 classification for seismic design and call for updated criteria that consider the bar failure location and strain capacity within a mechanical splice.

2.2.2 Aaleti et al. (2013)

Aaleti et al. (2013) (Aaleti et al., 2013) investigated the cyclic lateral response of reinforced concrete walls with three types of anchorage details at the wall-foundation interface: continuous reinforcement (RWN), conventional lap splices (RWS), and mechanical couplers (RWC). The test matrix comprised three large-scale rectangular walls, each 6 in. (150 mm) thick, 90 in. (2280mm)

wide, and 252 in. (6400 mm) tall. In terms of structural detailing, all specimens adhered to ACI 318-02(ACI Committee 318, 2002a) requirements for Special Walls, and reinforcement included asymmetric longitudinal steel layouts as shown in Figure 2.1 to simulate T-shaped wall behavior under varying moment gradients. RWS incorporated lap splices just above the foundation, while RWC had friction-welded mechanical couplers (length of couplers ranges from 2.75 in. (70mm) for #4 (13 mm) bars to 5 in. (127mm) for #9 bars, which were placed just above the top of the foundation block. The measured concrete strength for wall specimens were 8980 psi (61.9 MPa) for RWN and 8330 psi (57.4 MPa) for walls RWC and RWS. Measured properties for reinforcements satisfies Grade 60 reinforcing steel satisfying ASTM A706/A706-09b (2011)(ASTM Standard A706/A706M-24, 2024) .

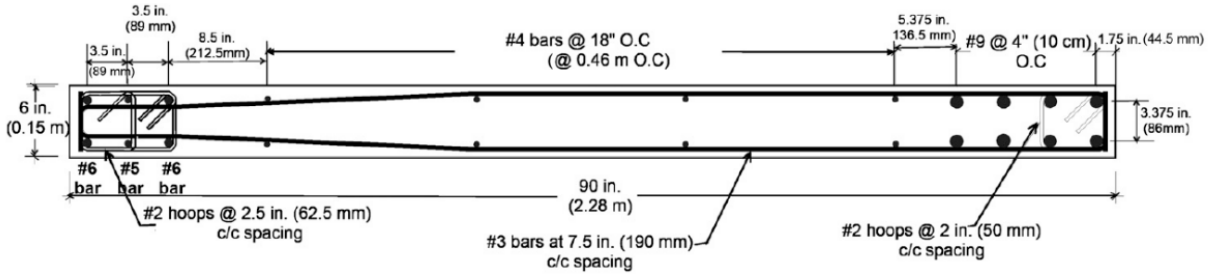

Figure 2-1-Cross-sectional details of all three rectangular concrete walls (RWN, RWC and RWS) (ACI)

The specimens were subjected to displacement-controlled reversed cyclic lateral loading up to drift ratio of 4%. Loading in the # 5 (16 mm) and #6 (19 mm) bars was defined as the positive direction, while tension in the No. 9 (29 mm) bars was the negative direction. Each displacement level was repeated three times. Up to drift ratio of 1%, cycles were symmetric; beyond that, negative direction loading was limited to prevent premature shear failure.

Walls RWN and RWC maintained stable behavior up to drift ratios of approximately +2.5% and −2.0%, without significant strength degradation. By contrast, Wall RWS remained stable only up to drift ratios of +2.0% and −1.0%, with noticeable strength degradation at −1.0%, likely due to slip in the lap splice region.

Initial yielding of the longitudinal reinforcement occurred at around drift ratio of 0.4% in both loading directions for all specimens. Similar responses and crack patterns for all walls were observed up to drift ratio of 1%, beyond which the behaviors began to diverge.

Lateral Load-Displacement Response

- RWS (with lap splice) showed the highest initial stiffness due to increased steel area in the splice region, resulting in higher load resistance at early drift levels.
- RWN (continuous reinforcement) and RWC (with mechanical couplers) demonstrated similar load-displacement behavior and backbone curves up to a drift ratio of 2.5%.
- RWC sustaining three full cycles up to a drift ratio of 4% in positive direction. Testing of RWN was limited to a drift ratio of 2.5% due to physical constraints.
- RWS experienced fracture of multiple bars (#5 [16 mm], #6 [19 mm], and # 4 [13 mm]) between drift ratios of 2.0% and 2.5%, accompanied by significant crack widening and bond slip in the lap region. Lateral resistance dropped sharply afterbar fracture.

Cracking and Deformation components

- Flexural cracks developed over the bottom 50 in. (1270 mm), around 0.55 of the length of the walls. RWS exhibited narrower cracks within the lap splice zone but larger cracks above the splice due to strain concentrations.
- RWS showed a significantly higher contribution of strain penetration and bar slip at large drift ratios up to 38% of total lateral deformation at a drift ratio of 1.5%, compared to around 14% for RWN/RWC. This bar slippage manifested as a 0.748 in. (19 mm) slip between lap-spliced bars at a drift ratio of 2% .
- Shear sliding cracks in RWN and RWC occurred at around 15 to 35 in. (380 to 890 mm) height at a drift ratio of 0.75%; in RWS, sliding shear crack occurred at a higher location, around 40 in. (1,020 mm) outside the lap splice region at a drift ratio of 0.5%.
- Strain penetration and sliding shear deformation were higher in RWS, contributing to greater non-flexural deformation as drift increased.

Energy Dissipation

- All specimens dissipated comparable energy up to drift ratio of 2% .
- RWN and RWC maintained their energy dissipation capacity up to the end of testing, with equivalent viscous damping around 20% at a drift ratio of 2.5% .

- Beyond drift ratio of 2%, RWS experienced a sharp decline in energy dissipation due to bar fracture and loss of load-carrying capacity attributed to bond degradation and bar slip within the lap splice region. Energy dissipation decreased substantially in subsequent cycles.

Findings of the study emphasize the significant influence of reinforcement anchorage details on the seismic performance of reinforced concrete structural walls. Specimens with continuous reinforcement (RWN) and those incorporating mechanical couplers (RWC) demonstrated stable hysteretic behavior, maintaining ductility, energy dissipation capacity, and structural integrity up to drift levels of 2.5% (test stopped due to equipment limitation) and 4%, respectively. The performance of the mechanically coupled wall was comparable to that of the continuously reinforced specimen, despite some localized bar damage near the couplers. By contrast, the wall with lap splices (RWS) exhibited premature strength degradation, bar slip, and fracture beginning at 2.0% drift, accompanied by a marked reduction in energy dissipation and concentrated damage at and above the splice region. These results reinforce current design recommendations that discourage the use of lap splices in plastic hinge regions and demonstrate that high performing mechanical couplers offer a viable and reliable alternative for use in seismically critical regions of reinforced concrete walls.

2.2.3 Haber et al. (2014)

Haber et al. (2014)(Haber et al., 2014) examined the seismic performance of precast bridge columns incorporating mechanical splices , aiming to evaluate their viability for use in plastic hinge regions, especially in accelerated bridge construction (ABC) scenarios in seismic zones.

The test matrix included:

- CIP (Cast-in-Place) benchmark column designed using Caltrans Seismic Design Criteria for a target displacement ductility $\mu_D = 7.0$.
- HCNP and HCPP used upset-headed couplers, with HCNP having no pedestal and HCPP placed atop a precast pedestal.
- GCNP and GCPP used grout-filled sleeve couplers, also with and without precast pedestals.

All specimens used # 8 (25 mm) longitudinal bars and were tested under constant axial load of 220 kips (978 kN). Precast models varied in splice type and location (within the plastic hinge or offset by the pedestal) and were designed to emulate CIP behavior with ABC-compatible connection details.

Lateral Load–Displacement Response

- **CIP column** exhibited wide, stable hysteresis loops with minimal strength degradation up to a drift ratio of 10%, meeting the target displacement ductility of μ_D = 7.0. Failure occurred due to longitudinal bar fracture approximately 3 to 10 inches (75 mm to 250 mm) above the footing, following conventional plastic hinge development.
- **HCNP (Upset headed coupler, no pedestal)** closely matched CIP performance, showing similar peak strength and post-yield plateau, but with slight pinching during unloading attributed to slack in the threaded collars. It sustained drift ratios up to 10% with bar fracture occurring at comparable locations as CIP and achieved a displacement ductility slightly below μ_D = 7.0 but above the Caltrans minimum of μ_D = 5.0.
- **HCPP (Upset headed coupler with pedestal)** showed similar load-displacement behavior as HCNP and CIP up to drift ratio of 10%. Due to the presence of the pedestal, plastic hinge formation shifted upward, concentrating strains near the pedestal-footing joint. Bar fracture initiated in this region, but the model achieved the design ductility target μ_D = 7.0.
- **GCNP (grout-filled sleeve, no pedestal)** exhibited noticeable pinching and reduced strength retention beyond a drift ratio of 4%. Bar rupture occurred during the drift ratio of 6%, below the footing surface due to strain concentration near the stiff grout sleeves. The column achieved a displacement ductility of μ = 4.5, just above the Caltrans SDC minimum of μ_c = 3.0.
- **GCPP (grout-filled sleeve with pedestal)** followed a similar response to GCNP, with early signs of softening and failure at drift ratio of 6%. Wide gaps formed at pedestal joints and spalling initiated early. Bar fracture occurred below the pedestal-footing interface. Drift and ductility capacities were limited *(*μ_D = 4.5), attributed to increased stiffness from the combined effect of grouted sleeves and ducts.

Strain Distribution and Plastic Hinge Formation

- CIP and HCNP columns displayed well-distributed strains with maximum strains approximately half a column diameter (conventional plastic hinge mechanism) above the footing, corresponding with bar fracture locations.
- GCNP and GCPP models showed non-uniform strain distribution due to rigid grout sleeves and ducts, leading to strain concentration above couplers and within the footing.
- HCPP and GCPP, with pedestals, shifted plastic hinge formation upward. Peak strain occurred near the pedestal-footing interface, with bar buckling and rupture initiated in the footing region.
- Curvature and rotation data showed higher curvature in Up-set Head Coupler (HC) collars due to bar slip, and reduced curvature in Grouted Sleeve Coupler (GC) regions due to rigidity, leading to plastic rotation outside the plastic zone.

Energy Dissipation

- Up to a drift ratio of 2%, all precast specimens dissipated energy comparable to CIP, with HC models exceeding CIP by up to 23%.
- Beyond drift ratio of 2%:
    - HCNP and HCPP dissipated 7 to14% less energy due to pinching caused by collar slack.
    - GCNP and GCPP remained within ±5% of CIP, but energy dissipation plateaued earlier due to earlier bar fracture and reduced ductility.
- Despite small differences, the cumulative energy dissipation of all precast columns was within acceptable bounds of experimental variability.

The findings highlight the critical influence of coupler detailing and placement on seismic performance, particularly in plastic hinge regions. While the cast-in-place (CIP) column exhibited conventional and well-distributed plastic hinge behavior, the introduction of mechanical splices in precast columns modified the plastic hinge mechanism depending on the coupler type, stiffness, and location. Certain configurations led to strain concentrations, reduced ductility, or shifts in

hinge location especially when combined with precast pedestals. Overall, the results highlight the need for careful design and detailing of mechanical splices to ensure ductile performance and reliable energy dissipation in precast concrete systems.

2.2.4 Aragon et al. (2017)

Aragon et al. (2017)(Aragon et al., 2017) investigated a proposed Type III grouted seismic connector designed to improve the constructability and performance of hybrid precast concrete structures. The study was motivated by the limitations of Type II grouted mechanical splices, which exhibited premature bond failure under high cyclic strain demands and the impracticality of using full ACI 318-14(ACI Committee 318, 2014) development lengths for energy-dissipating bars in precast construction(Smith & Kurama, 2014). The Type III system aims to overcome these deficiencies by enabling ASTM A706 energy-dissipating bars to reach near full tensile capacity over a short embedment length of 10 to 15 bar diameters (d_b). This is achieved using a tapered cylindrical sleeve, filled with high-strength flowable grout, and a partially unbonded (wrapped) bar segment that localizes yielding and promotes ductile behavior. This configuration significantly reduces bar protrusion and simplify precast assembly, offering a more practical solution.

The study included six full-scale test specimens, each representing a segment of a hybrid precast wall-to-foundation connection. The test setup consisted of a wall-panel block connected to a foundation block via a single energy-dissipating bar inserted into a grouted sleeve. The bar was subjected to a quasi-static cyclic axial loading protocol using a servo-controlled actuator. Instrumentation included strain gauges, displacement transducers, and load cells to monitor bar behavior and connector performance.

The parameters varied across the six specimens included:

- Connector sleeve taper angle (0°, 4.5°, 9°)
- Sleeve surface condition (smooth vs. corrugated)
- Bond length ($10d_b$ and $15d_b$)
- Grout compressive strength (ranging from ~8600 psi [59.30 MPa] to ~10,300 psi [71.01 MPa]
- Inclusion of a threaded bar coupler (Specimen 6)

Test Findings

Ductile performance

- Five out of six specimens failed by ductile low-cycle fatigue fracture of the bar, demonstrating desirable seismic performance, reaching up to 86% of the measured uniform elongation strain of the bar.
- One specimen experienced bond pullout, attributed to lower grout strength.

Short bond length effectiveness

- A bond length in the coupler of $10d_b$ was sufficient to achieve high bar strains without pullout, provided the grout had adequate strength and confinement.

Wrapped (Unbonded) Region Controlled Strain

- A debonded length of 12 bar diameter effectively distributed bar elongations, preventing concentrated plasticity and early failure.

Taper Effectiveness

- Sleeve taper angle influenced grout confinement, a 9° taper reduced bulging but may require more spacing between connectors. Surface corrugation showed limited benefit.

Grout Strength Performance

- Higher grout compressive strengths correlated with bar fracture rather than pullout. Specimen 5 with 10,324 psi [71.18 MPa] grout showed optimal performance.

Threaded Coupler Feasibility

- Specimen 6 showed that using a threaded bar coupler might help to eliminate protruding length without degrading performance and fracture of the bar away from the coupler.

The findings highlight the potential for grouted connectors to replace conventional long development lengths and Type II mechanical splices in seismic precast construction. Recommended $0.85\varepsilon_{uel}$ (uniform elongation strain of energy dissipating bar at measured ultimate strength under monotonic tests) strain limit for energy-dissipating bars in ACI ITG-5.9(ACI

Innovation Task Group 5 (ACI ITG-5), 2009) may be unconservative, as experimental evidence showed two specimens fractured before reaching this limit.

2.2.5 Bompa & Elghazouli (2019)

Bompa & Elghazouli (2019)**(Bompa & Elghazouli, 2019)** conducted an experimental study on the inelastic performance of reinforced concrete members with mechanical splices, incorporating both monotonic and cyclic tests (in-air and in-concrete) as well as four large-scale concrete beam–column tests. The primary aim was to assess the suitability of different splice systems in plastic hinge regions by examining stiffness, strength, ductility, energy dissipation, and curvature distribution. Two types of threaded couplers were tested, parallel threaded couplers (PTC) and parallel threaded sleeve couplers (PTSC). The selected couplers were part of a broader testing program conducted by the authors(Bompa & Elghazouli, 2018) and in-air tests for #5 (16mm) non-spliced and spliced specimens were also reproduced in this study to correlate in-air performance with in-concrete and in-member performance. The couplers were selected for their contrasting geometries and connection mechanisms. PTCs consisted of female-threaded couplers joined to male-threaded reinforcing bars, while PTSC couplers used steel sleeves swaged onto unmodified bars, forming male-female threaded connections. PTC is a compact coupler with a diameter of 1 in. and length of 1.77 in. (25 mm and 45 mm). PTC couplers were applied to 72 ksi (500 MPa) #5 (16mm) bars. PTSC is a slender coupler with a diameter of 1in. and length of 8.11 in. (25 and 206 mm). PTSC couplers were also applied to #5 (16mm) bars. In-air specimens for monotonic loading had a minimum clear length l_s= 13.78 in. (350 mm) between machine grips. Concrete specimens tested in the uniaxial machine consisted of an 800mm long splice between machine grips of which 23.62 in. (600 mm) was embedded in a concrete cylinder.

Four RC beam-column specimens with 11.8 in.× 11.8 in. (300 mm × 300 mm) cross-sections and a cantilever length of 53.1 in. (1350 mm) were tested:

- One specimen with continuous reinforcement and no couplers
- two specimens with PTC couplers, one without axial load and one with axial load equal to 15% of the section capacity
- one with PTSC couplers without axial load.

All four specimens were reinforced with eight #5 (0.63 in. or 16 mm diameter) longitudinal bars. In the three spliced specimens, mechanical couplers were placed within the expected plastic hinge region, centered 5.9 in. (150 mm) above the footing interface.

The in-air experimental program included uniaxial monotonic testing and one or both of the S1 and S2 reversed cyclic loading pattern defined by ISO 15835-2009, as shown in Figure 2.2. Monotonic testing of specimens without concrete swaging applied three cycles of tension between zero and 60% of the specified yield strength of the bars to assess elastic slip before pulling monotonically to fracture. Cyclic tests of mechanical splices without concrete swaging applied the S2 protocol, whereas concrete swaged specimens were subjected to the combined S1 and S2 cyclic loading.

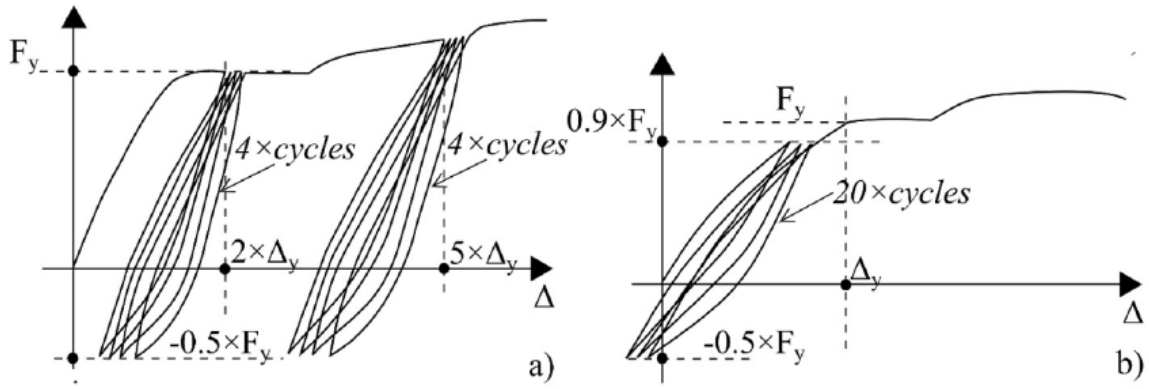

Figure 2-2-Loading procedure ISO 15835-2:2009 a) S2 inelastic cyclic b) S1 elastic cyclic (Source: Bompa and Elghazouli (2018))

In-Air Mechanical Coupler Performance

- Uniaxial monotonic and cyclic tests on #5 (16 mm) bars demonstrated that both spliced and non-spliced specimens satisfied the Eurocode 8 ductility requirement (*uniform elongation of bars* > 7.5%).
- Fracture strain (ε_f) ranged from over 15% in non-spliced bars to as low as 10.1% in specimens with slender couplers.
- In all in-air tests, fracture occurred in the bar outside the coupler region, and the residual slip at the coupler was minimal (< (0.0008 in. [0.02 mm]), confirming reliable load transfer.

Specimens swaged with concrete showed slightly lower fracture strain than in-air tests, especially for slender couplers.

- Crack patterns in-concrete specimens showed that slender couplers shifted the cracking away from the coupler, concentrating strain in adjacent unconfined rebar zones where failure eventually occurred.

In-Member Lateral Cyclic Performance

Control specimen – continuous reinforcement (C300-C0-N0)

- The control specimen exhibited well-distributed curvature along the plastic hinge region, with a hinge length (L_{pr}, distance from the section interface to the point where curvature drops to the yield curvature) of approximately 9.8 in. (250 mm).
- The yield rotation (θ_y, from a bilinear idealization of the moment–rotation envelope) was 0.60° (10.5 mrad), and the ultimate rotation (θ_u, rotation at a 20% drop from the peak moment) reached 4.01° (69.9 mrad).
- The peak lateral load (V_{max}, maximum measured horizontal load corrected for axial load effects) was 20.7 kip (92.3 kN) at a displacement of 3.54 in. (90 mm).
- The specimen maintained stable hysteresis loops with minimal inter-cycle degradation until fracture of the longitudinal reinforcement. Energy dissipation remained high throughout large inelastic cycles, confirming a ductile flexural response.

Compact threaded (PTC) couplers – no axial load (C300-CC-N0)

- The PTC specimen without axial load displayed a hinge length of about 13.0 in. (330 mm), which is significantly longer to that of the control. However, because the coupler was short (1.77 in. / 45 mm), curvature profiles were still close to the control's distribution, and the extended hinge length did not reduce ductility or shift the curvature peak significantly.
- Yield rotation was 0.52° (9.10 mrad) and ultimate rotation was 4.02° (70.2 mrad), essentially identical to the control.
- The peak lateral load reached 19.9 kip (88.4 kN). Strength, stiffness, and post-yield degradation trends closely matched those of the control specimen.

- Failure occurred by bar fracture outside the coupler zone, with only minor concrete crushing near peak displacements.
- Energy dissipation performance was also comparable, confirming that compact threaded couplers, when placed properly within the plastic hinge region, do not significantly affect member ductility or strength.

Slender threaded (PTSC) couplers – no axial load (C300-CS-N0)

- The PTSC specimen without axial load developed a longer hinge length of about 13.0 in. (330 mm) due to curvature localization below the coupler.
- Yield rotation was reduced to 0.33° (5.82 mrad) and ultimate rotation dropped to 3.09° (53.9 mrad), approximately 23% lower than the control.
- The peak lateral load was 20.9 kip (92.9 kN), comparable to the control, but the curvature concentration shifted the neutral axis toward the tension face and led to a rocking-type base response.
- Coupler–concrete debonding contributed to faster inter-cycle degradation at larger displacements (>2.36 in. [60 mm]), and energy dissipation declined more sharply than in the control or compact-coupler (PTC) specimens.
- Failure occurred by bar fracture in the rebar segment adjacent to the coupler.

Compact threaded (PTC) couplers – with 15% axial load (C300-CC-N1)

- The PTC specimen with axial load had a slightly longer hinge length than the control. Yield rotation was 0.65° (11.3 mrad) and ultimate rotation was limited to 1.94° (33.9 mrad), about 51% lower than the control.
- The peak lateral load reached 31.0 kip (138 kN), the highest among all specimens, reflecting the strengthening effect of axial compression. However, the axial load accelerated concrete crushing and bar buckling near the coupler, causing a rapid drop in lateral capacity after peak load. Energy dissipation declined steeply once crushing initiated, and the failure mode was governed by compression-zone damage followed by fracture at the coupler–bar interface.

The findings of this study emphasize the influence of coupler geometry, stiffness, and location on plastic hinge formation and ductility capacity. While compact threaded couplers can match the performance of continuous reinforcement in seismic regions, bulkier or slender threaded systems are recommended to be evaluated more carefully due to their tendency to disrupt curvature distribution and reduce rotation capacity. This study provides design-relevant insights for engineers considering mechanical splices in ductile regions, highlighting the importance of proper detailing, stirrup confinement, and spacing from critical interfaces such as footings.

2.2.6 Mohamed et al. (2025)

Mohamed et al. (2025)(Mohamed et al., 2025) investigated six reinforced concrete column specimens were tested to investigate different splicing methods and configurations at the column-to-foundation interface. Three splicing methods were considered: continuous bars, overlapping splices, and threaded mechanical couplers. The continuous bar specimen (BCR) served as the control, with continuous reinforcement running from the foundation to the column top. The overlapping splice specimen (OLR) followed Eurocode(Institution, 2004), with the entire lap length placed at the bottom of the column. The remaining four specimens incorporated threaded mechanical couplers, classified into two coupler types (C1 and C2) and two configurations (same level and different level) as shown in Figure 2.3. The C1 configuration used a single coupler per bar, while C2 used two couplers spaced 12.6 in (320 mm) apart to reflect site-based constraints.

All longitudinal reinforcement consisted of eight 0.79 in (20 mm) (72.52 ksi) B500B ribbed threaded bars, threaded using a Linxion (Bartec) machine and normalized to relieve internal manufacturing stresses. Couplers featured an optimized olive-shaped geometry—thinner than conventional cylindrical types, with an external diameter of 0.94 in (24 mm) and length of 1.81 in (46 mm). In C1SL, all couplers were positioned 5.9 to 7.9 in. (150 to 200 mm) above the footing, while C1DL placed half at that level and the other half 39.4 in. (1000 mm) higher. In C2SL, two

couplers per bar were installed in the lower column region, while C2DL staggered additional couplers further up the bar length. All specimens included 0.39 in. (10 mm) diameter stirru

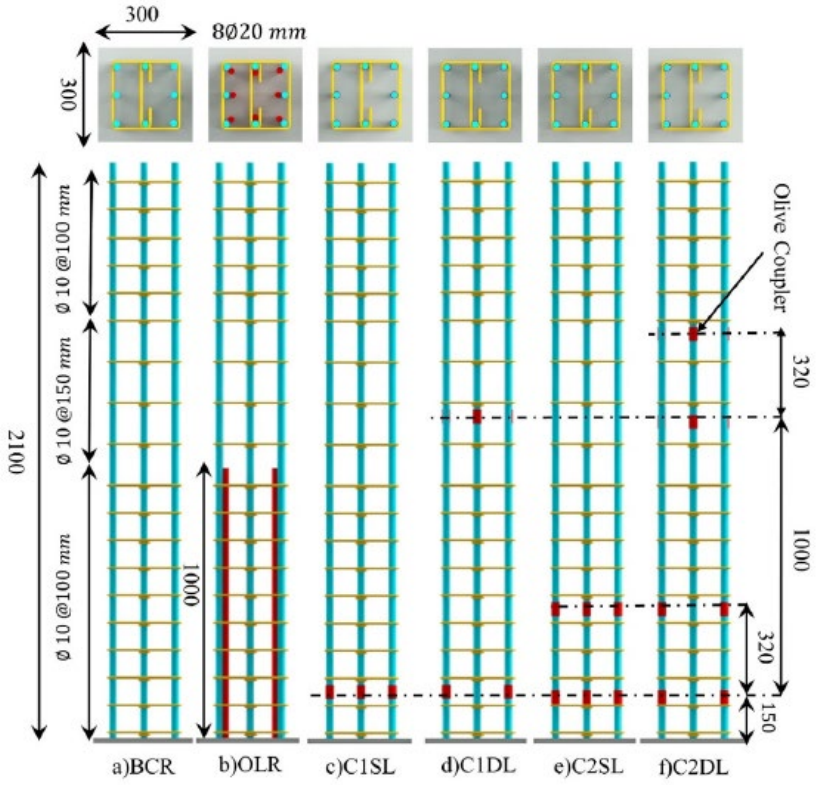

Figure 2-3-Six reinforced concrete specimen showing lap splice and mechanical coupler (red) position(Mohamed et al., 2025))

Lateral cyclic performance

Quasi-static cyclic lateral loading was applied at the top of each column using a displacement-controlled actuator until a 15% post-peak strength drop. All mechanically spliced columns (C1SL, C1DL, C2SL, C2DL) showed peak lateral strengths within ±3% of the continuous bar control specimen (BCR). Specimens with staggered couplers (C1DL and C2DL) sustained higher drift demands with stable post-yield behavior, indicating enhanced ductility and deformation capacity. By contrast, OLR (overlapping splice) peaked at a lower drift and exhibited early strength degradation.

Crack Development, Damage, and Edge Uplift

Crack initiation was detected using Digital Image Correlation (DIC) and verified visually.

- In BCR and mechanically spliced specimens, cracks initiated between 6.3 to8.3 kips (28 to 37 kN) and were well distributed across the plastic hinge.
- OLR initiated cracking earlier at 3.8 kips (17 kN), with limited flexural cracks and localized damage.
- Total flexural crack openings in the plastic hinge region were comparable between mechanical splice specimens and BCR while OLR had the smallest opening but showed significant edge uplifting (vertical displacement of the column edge from the foundation). Edge uplift was lowest in C1DL and C2DL.

Ductility, Drift, and Energy Dissipation

- Displacement ductility (μ) was calculated by dividing the ultimate drift taken at a strength drop of 15% by the yield drift obtained using a secant stiffness to 0.75 of the peak load .
  - BCR: $\mu = 3.6$
  - C1DL: $\mu = 4.2$ (increase of 17%)
  - C2DL: $\mu = 4.11$ (increase of 14%)
  - OLR: $\mu = 3.14$ (increase of 13%), with a 15% lower ultimate displacement
- All mechanical splice specimens exceeded Eurocode 8(Standardization, 2004) drift capacity thresholds.
- Cumulative Dissipated Energy (CDE), calculated as the area under each hysteresis loop, confirmed enhanced performance in mechanical splice specimens. C2DL had the highest CDE, especially after drift ratio of 3.5% , followed by C1DL and C2SL. OLR showed the lowest CDE.

Stiffness, Strength Degradation, and Self-Centering

Secant stiffness was measured at each drift level using the ratio of peak load to displacement in push and pull directions.

- All specimens showed typical stiffness degradation with increasing drift. C1DL exhibited improved stiffness retention beyond 2% drift. The strength degradation coefficient (λ) defined as the load drop from the first to the third cycle at each drift was comparable between BCR and mechanical splice specimens.
- The self-centering coefficient (γ) was calculated as a quantitative measure of a structure's ability to return to its original position after being subjected to cyclic or seismic lateral loading. It reflects how well a column or structural member can recover from deformations without residual drift or permanent displacement. Self-centering capacity was measured using coefficient, $\gamma = 1 - \Delta_r / \Delta_m$, where Δ_r is the residual displacement at zero load and Δ_m is the peak displacement per cycle. A coefficient of 1 denotes ideal self-centering, meaning the structure responds entirely elastically.
    - BCR: $\gamma = 0.89$
    - C1DL/C2DL: $\gamma = 0.87$ to 0.91 (similar)
    - OLR: $\gamma = 0.82$ (decrease of 8%), indicating greater plastic residuals

All specimens except OLR failed in a flexural mode, with yielding of longitudinal bars and concrete crushing above the coupler zone. OLR exhibited a combined flexure-shear failure due to poor stress transfer. No visible failure occurred in any of the mechanical couplers, confirming integrity of mechanical connection under reversed cyclic inelastic strain demands. It is important to note that all couplers were placed at least 6 in. (150 mm) above the critical moment section, avoiding the highest stress and strain concentrations.

2.2.7 Kheyroddin et al. (2020)

Kheyroddin et al. (2020)(Kheyroddin et al., 2020) investigated the seismic performance of reinforced concrete columns using different splicing techniques under combined axial and cyclic lateral loading. Six full-scale specimens were tested:

- RSP – No splices with continuous bars.
- OS-M – Overlap splice at mid-height (about 21.7 in. / 550 mm above footing).
- TC-A5 – Threaded couplers, all at Location 1 (about 2.0 in. / 50 mm above footing).

- TC-H5-H60 – Threaded couplers, half at Location 1 (about 2.0 in. / 50 mm above footing) and half at Location 2 (23.6 in. / 600 mm above lower couplers).
- STC-A5 – Shear screw-threaded couplers, all at Location 1 (2.0 in. / 50 mm above footing).
- STC-H5-H60 – Shear screw-threaded couplers, half at Location 1 (2.0 in. / 50 mm above footing) and half at Location 2 (23.6 in. / 600 mm above lower couplers).

All specimens had square cross-sections of 12 in. × 14 in. (300 mm × 350 mm), a height of 43.3 in. (1100 mm), and uniform transverse reinforcement of diameter 0.31 in. (8 mm) at 2 in. (50 mm) spacing. All columns were tested under a constant axial load equal to 10% of their gross axial capacity ($0.1f'_cA_g$) and displacement-controlled lateral loading. Performance was assessed using hysteresis response, ductility, energy dissipation, stiffness degradation, cracking, and failure behavior.

Lateral Load Capacity

- The reference specimen (RSP) reached a peak lateral load of 17.47 kip (77.76 kN).
- All mechanical splice specimens exceeded this value:
    - C-H5-H60: 22.20 kip (98.75 kN), representing an increase of 26.99 percent over the reference specimen.
    - STC-H5-H60: 19.34 kip (86.01 kN), representing an increase of 10.68 percent over the reference specimen.
    - OS-M: 18.78 kip (83.57 kN), representing an increase of 7.47 percent over the reference specimen, but without notable ductility or energy dissipation benefits.
    - STC-A5: 18.89 kip (84.01 kN), representing an increase of 8.04 percent over the reference specimen.
    - TC-A5: 18.37 kip (81.74 kN), representing an increase of 5.11 percent over the reference specimen.

Staggered splice placement significantly enhanced ultimate lateral load capacity by improving load distribution and reducing localized failure.

Cracking Behavior

- All specimens developed initial flexural cracks near the base.
- In mechanical splice specimens, flexural and shear cracks propagated throughout the height; TC-H5-H60 showed crack development at both splice levels.
- STC-A5 initiated cracks from mid-height, reflecting the influence of splice type and local stiffness.
- OS-M exhibited highly localized damage, lacked vertical cracks throughout, and showed early cover spalling—suggesting poor bond performance and stress concentration.

Ductility Analysis

Ductility (μ) was calculated using an energy balance method, where equivalent yield displacement was derived from the hysteresis envelope such that the pre- and post-yield areas were equal.

- TC-A5 (all couplers at base) showed the highest ductility: $\mu = 6.34$, an increase of 112% compared to RSP ($\mu = 3.00$).
- STC-A5 and STC-H5-H60 also improved ductility: $\mu = 3.85$ and $\mu = 4.05$.
- TC-H5-H60 (staggered threaded couplers) had lower ductility ($\mu = 2.88$), indicating that dual-level placement may reduce curvature concentration but limit plastic rotation.
- OS-M showed the lowest ductility ($\mu = 2.95$), validating concerns with lap splices in hinge zones.

Energy Dissipation

- Cumulative energy absorption (CAE) was determined by integrating the area enclosed within the hysteresis loops and summing it over successive load cycles.STC-A5 dissipated the most energy up to the 35th cycle, indicating strong early-cycle performance.
- Beyond cycle 35, TC-H5-H60 and RSP exhibited highest CAE, suggesting superior post-yield behavior and residual capacity.
- TC-A5, despite high ductility, showed lower total CAE, likely due to early concentrated damage.

- OS-M demonstrated limited energy dissipation, failing to maintain post-yield capacity.

Stiffness Characteristics

Secant stiffness was calculated as the ratio of peak force to total drift at each cycle.

- All specimens experienced rapid stiffness loss during initial cycles (up to 0.4 to 1.0 in. or 10 to 25 mm drift).
- TC-H5-H60 retained the highest post-yield stiffness, aided by distributed splices and distributed deformations along column height.
- STC-A5 had the lowest stiffness in mid-to-late cycles due to earlier cracking at mid-height.
- Threaded coupler specimens with dual-level placement generally exhibited more stable stiffness than lap-spliced or single-level configurations.

Failure Modes

- In monotonic tensile bar tests, all mechanical splices met ACI 318-19 Type 2 splice criteria and sustained bar fracture occurring outside the coupler zones.
- Failure typically involved concrete spalling, orthogonal cracking, and bar yielding at or above the lower splice zone.
- Nocoupler fracture or slippage was observed in any mechanically spliced column.
- The lap-spliced column (OS-M)failed through early spalling and bond slip, highlighting limitations of lap splices under cyclic loading.

Overall, the findings by Kheyroddin et al. (2020) suggest that mechanical splices, both threaded and shear screw-threaded types, can deliver seismic performance comparable to continuous reinforcement when properly detailed. While splice type and placement influenced the response characteristics, all mechanically spliced specimens demonstrated stable cyclic behavior and satisfied code requirements. Lap splices, by comparison, showed relatively lower deformation capacity and energy dissipation under similar loading conditions.

2.2.8 Reetz and Matamoros (2004)

Reetz et al. (2004)(Reetz et al., 2004) investigated the performance of mechanical splices located within the plastic hinge region of reinforced concrete beams subjected to reversed cyclic loading. The study aimed to determine whether mechanical splices could sustain the large strain demands associated with seismic plastic hinge behavior and to propose a strain-based recommendations for minimum performance criteria of couplers in seismic regions.

Two full-scale concrete beam specimens were tested under displacement-controlled cyclic loading. Specimen A1 had a 12 × 24 in. (305 × 610 mm) cross-section and a longitudinal reinforcement ratio of 0.47%, corresponding to the minimum required by ACI 318-02(ACI Committee 318, 2002b). Specimen B1 had a smaller 10 × 16 in. (254 × 406 mm) cross-section but a higher reinforcement ratio of 0.92%. Both specimens were spliced at the plastic hinge region using Lenton® A2 Standard Couplers, which are Type 1 splices per ACI 318-02, and not recommended in plastic hinge regions. Each specimen had four #7 (22 mm) Grade 65 ksi (450 MPa) bars spliced using mechanical couplers positioned approximately 3 inches (75 mm) above the beam-to-base interface. The columns were cast vertically on large base blocks and loaded horizontally using actuators. Transducers and strain gauges were positioned along the plastic hinge to monitor curvature, rotation, slip, and reinforcement strain. Tests were conducted using increasing drift ratios with load reversals to simulate seismic displacement histories.

Lateral Load and Hysteretic Behavior

- Both specimens exceeded drift ratios of 4% without substantial lateral strength degradation.
- Specimen A1 failed at drift ratio of 5.5% due to tensile fracture of a reinforcing bar at the bar-coupler interface, highlighting strain concentration effects.
- Specimen B1 achieved a drift ratio of 6% before showing significant strength degradation caused by bar buckling but did not exhibit splice failure.
- Both specimens maintained a stable moment-rotation response up to their respective failure points, with rotation concentrated within the plastic hinge length.

Strain and Curvature Distribution

- A mechanics-based model was developed to relate drift ratio to average tensile strain in bars across the plastic hinge length taken equal to beam depth. This relationship provides a basis to recommend the minimum strain capacity a coupler should resist before fracture. The derived equation utilizes the product of curvature and the distance from the reinforcing steel to the neutral axis.
- The model, grounded in flexural theory and bond-slip mechanics, was validated using data from both spliced specimens and previously tested non-spliced specimens(Matamoros, 1999).
- Predicted strains were within 30% of measured values, supporting the model as a conservative tool for splice qualification.

Recommendations

- This study recommends mechanical splices in potential plastic hinge regions should demonstrate a minimum tensile strain capacity of 4.0% under monotonic loading to avoid brittle fracture before the structure reaches its limiting drift ratio.
- The proposed strain-based requirement is more stringent than the strength-only criteria previously specified for Type 2 splices in ACI 318.

This research was one of the earliest efforts to link strain demands from seismic drifts to mechanical splice qualification, moving beyond strength-based criteria. Although the tested couplers were Type 1 and thus not allowed for hinge zones, their observed behavior, particularly the ability to reach relatively large drifts without splice failure underscored the need for detailing and bar property considerations.

2.2.9 Ameli et al. (2016)

Ameli et al. (2016)(Ameli & Pantelides, 2017) investigated the seismic performance of precast concrete column-to-footing connections incorporating grouted splice sleeve (GGSS) connectors through reversed cyclic testing of four half-scale specimens. The study examined the influence of connector placement and intentional debonding of dowel bars on overall seismic behavior which

are key considerations for ensuring monolithic-like performance in accelerated bridge construction (ABC) systems.

The test matrix was as follows

- CIP: A monolithic cast-in-place control column.
- GGSS-1: Grouted splice sleeves embedded at the base of the precast column with no bar debonding.
- GGSS-2: Sleeves embedded in the footing with pre-grouted dowel bars projecting from the column.
- GGSS-3: Same as GGSS-1 but with debonded dowel bars over a length of $8d_b$ (diameter of bar) at the footing interface.

Each column had an octagonal 21 in. (533.4 mm) diameter cross-section, 8.5 ft (2590.8 mm) in height, and was reinforced with six #8 (25 mm) longitudinal bars and #4 (13 mm spiral reinforcement. All were subjected to a constant axial load equivalent to 6% of gross axial capacity and tested to lateral drift ratios up to 9%.

Lateral Load–Displacement Response

- CIP specimen exhibited stable, wide hysteresis loops with minimal degradation up to a drift ratio of 8.9%, achieving the highest displacement ductility (μ = 8.9). Fracture of longitudinal reinforcement due to low-cycle fatigue was the primary failure mode, occurring near the column base.
- GGSS-1, without debonding, achieved the lowest displacement capacity (μ = 5.4), with early onset of stiffness degradation and bar fracture. Failure in all precast specimens occurred via low-cycle fatigue fracture of reinforcement outside the sleeve, indicating sufficient bond integrity of the GGSS connectors.
- GGSS-3, with dowel debonding, demonstrated improved displacement capacity (μ = 6.8), and delayed bar fracture compared to GGSS-1. Stable hysteretic behavior was observed up to a drift ratio of 8%.

- GGSS-2 reached a displacement ductility of μ = 6.1 and showed a hysteretic response closely resembling that of CIP, attributed to more favorable hinge formation due to connector placement in the footing.
- All specimens ultimately failed by bar fracture due to cyclic strain accumulation, but damage localization varied significantly with connector placement and detailing.

Crack Patterns and Damage Progression

- GGSS-1 and GGSS-3 showed localized damage above the connector zone. Cracks were concentrated at the interface, and spiral reinforcement became exposed at a drift ratio of 7 to 8%.
- GGSS-2 and CIP developed well-distributed flexural cracking along the column length, with gradual damage progression. Spiral reinforcement remained intact longer, indicating better energy dissipation characteristics.

Energy Dissipation

- All specimens demonstrated comparable energy dissipation up to a drift ratio of 3%.
- Beyond a drift ratio of 3%:
    - GGSS-3 and CIP exhibited higher energy dissipation due to distributed damage and delayed fracture, aided by either monolithic construction (CIP) or bar debonding (GGSS-3).
    - GGSS-1 dissipated less energy due to early stiffness loss and crack localization; equivalent viscous damping (ξ_{eq}) peaked at about 17%.
    - GGSS-2 maintained moderate energy performance with (ξ_{eq}) values of 24 to 26%, while CIP peaked at 31%.

Strain and Curvature Distribution

- CIP and GGSS-2 developed well-distributed inelastic curvature across the plastic hinge region. Inelastic strains extended 20 to 34 in. (508 mm to 863.6 mm) above the footing and into the footing itself.
- GGSS-1 and GGSS-3 exhibited reduced curvature over the connector region. Inelasticity was concentrated just above the sleeve, a result of stiffness discontinuity introduced by the embedded sleeves.

- Debonding in GGSS-3 effectively shifted peak curvature away from the sleeve region, reducing strain concentrations and improving displacement tolerance.

PART I

In-Air Testing

3 Low-cycle fatigue experimental program

A primary objective of this experimental program is to investigate the low-cycle fatigue performance of various mechanical couplers on the U.S. market when connecting Grade 80 (550 MPa) high-strength steel (HSS) reinforcing bars. The test data obtained from this experimental program were also used to support the development of qualification test procedures for mechanical splices intended for plastic hinge regions of special seismic structural systems. Test results also served to determine which mechanical couplers to use in the wall tests of *Part II-Wall tests* of this study.

To achieve these objectives, in-air uniaxial tests were conducted on mechanical splice sub-assemblies under fully reversed inelastic strain cycles until bar fracture. This type of testing builds on the methodology used by Sokoli et al. (2019)(Sokoli et al., 2019), Slavin and Ghannoum (2015)(Slavin & Ghannoum, 2015), and Ghannoum and Slavin (2016)(Ghannoum & Slavin, 2016) to evaluate the low-cycle fatigue performance of reinforcing bars of various steel grades and manufacturing processes, including higher grade bars (Grade 80 [550 MPa] and Grade 100 [690 MPa]). Additional monotonic tension tests were performed to determine the tensile strength and ductility properties of the mechanical splice specimens.

3.1 Test matrix

Eleven distinct types of mechanical couplers, employing different coupling mechanisms as summarized in

Table 3.1 were evaluated for use with Grade 80 (550 MPa) reinforcing bars conforming to ASTM A706, including Supplement 1(ASTM Standard A706/A706M-22a, 2022). The high-strength bars were produced using the two common manufacturing methods currently used in the U.S. for this grade: micro-alloying (MA) and quenching and self-tempering (QST). To reduce variability in bar properties, all reinforcing bars used in the splice specimens were sourced from a single production batch for each process type (MA and QST) in Phase 1 and in *Part II-Wall tests.* In addition, only factory-installed couplers were used to eliminate the influence of potential field installation errors.

Phase 1 of the study focused on #8 (25mm) bars with a nominal diameter of 1 in. (25.4 mm) and unbraced splice tests. Incidentally, the #8 (25mm) bars from the same MA and QST batches used

in Phase 1 were also used in the boundary elements of wall specimens tested in *Part II-Wall tests* of this research program. To simplify the test program, test parameters were selected to preclude the need for specimen lateral bracing. Unbraced in-air tests were performed on ten mechanical coupler types connecting two different manufacturing types of reinforcing bars (MA and QST). The eleventh coupler type (*Gouted-1*) could not be tested unbraced due to grout damage leading to premature specimen buckling. The eleventh type was tested braced in Phase 2.

Table 3.1-Mechanical coupler types selected for the study

Manufacturer-Coupler Type (Name)	Coupling Mechanism	Photograph
M1-Cold Swaged Coupler (*Swaged*)	Swaged bars with taper-threaded device; butt splice	
M1-Standard Threaded Coupler-1 (*Threaded-1*)	Threaded bars; butt splice	
M2-Taper Threaded Coupler-1 (*Taper Threaded-1*)	Taper-threaded bars	
M3-Upset Head Butt Splice Coupler (*End Grip*)	Mechanical butt splice with upset bar ends	
M3-Friction Forged Tapered Threaded Coupler-2 (*Friction Welded-2*)	Friction-forged bars with tapered-threaded device; butt splice	
M3-Standard Threaded Coupler-2 (*Threaded-2*)	Threaded bars; butt splice	
M4-Friction Forged Taper Threaded Coupler-1 (*Friction Welded-1*)	Friction-forged bars with tapered-threaded device	

Manufacturer-Coupler Type (Name)	Coupling Mechanism	Photograph
M4-Taper Threaded Coupler-2 (*Taper Threaded-2*)	Taper-threaded bars	
M4-Grouted/Threaded Coupler-1 (*Grouted/Threaded-1*)	Grouted connection at one end and tapered-threaded bar at the other	
M5-Grouted Splice Coupler (*Grouted-1*)	Grouted splice coupler	
M5-Slim Grouted Splice Coupler (*Grouted-2*)	Slim-profile grouted splice coupler	

In ***Phase 2***, the test matrix was extended to include braced in-air inelastic cyclic tests for both #8 (25 mm) and #11 (36 mm) bars using the mechanical splice specimens received from the manufacturers at the time of writing of this report. Braced tests were performed on two mechanical splice types with grouted mechanical couplers (*Grouted-1* and *Grouted-2*) and with #8 bars. Grouted-1 splices could not be tested in an unbraced configuration due to excessive buckling caused by grout spalling during testing. Grouted-2 splices were tested braced in Phase 2 and unbraced in Phase 1 so that comparison between their performance under the differing boundary conditions could be evaluated. Braced tests were also conducted in Phase 2 on #11 (36mm) *End Grip* and #11 *Grouted-1* and *Grouted-2* splice specimens. The #11(36mm) reinforcing bars used in Phase 2 were sourced from different batches than those in Phase 1, as this bar size was introduced at a later stage of the program. Control tests on bare bars were conducted for each steel

batch to provide a baseline for comparison with the performance of mechanically spliced specimens.

The test matrices for both phases, along with the corresponding bar batches, are presented in Table 3.2.

Table 3.2-Inelastic Cyclic Test Matrix for Mechanical Splices and Bare Bars

Phase	Bar Size	Specimen	Bar Type	Bar Batches*	Cyclic Test Frequency (Hz)	Bracing Condition	Clear bar gripping span	Strain Range
1	#8 (25 mm)	Bare Bar	MA	MAB1	0.012	Unbraced	$1.5d_b$	(+2.0%, -0.5%)
			QST	QTB1				
		All mechanical splices except Gouted-1	MA	MAB1				
			QST	QTB1				
2	#8 (25 mm)	Grouted-1	MA	MAB1		Braced		
			QST	QTB1				
		Grouted-2	MA	MAB1				
			QST	QTB1				
	#11 (36 mm)	Bare Bar	MA	MAB2	0.012			
			QST	QTB2	0.008			
				QTB3	0.012			
		End Grip	QST	QTB3	0.008			
		Grouted-1	MA	MAB2	0.012			
			QST	QTB2				
		Grouted-2	MA	MAB2				
			QST	QTB2				

* Mill certificates for all the bar batches are presented in Appendix A

3.2 Test parameters

3.2.1 Fixed variables

To enable a direct comparison between the performance of mechanical splice specimens, the following parameters were kept constant.

3.2.1.1 Bar grade

A primary objective of the testing program was to evaluate the performance of mechanical splices used with higher grade reinforcement. In this study, the focus was on the recently introduced Grade 80 reinforcing ASTM A 706 bars in ACI 318-19, as this grade is rapidly increasing in popularity in seismic designs. Grade 80 (550 MPa) bars confirming to ASTM A706 Supplement S1 additional

requirements were used exclusively in this study. Grade 100 (690MPa) bars were not considered in this study to limit scope.

3.2.1.2 Clear bar gripping span

The clear bar gripping span in mechanical splice specimens is defined as the distance from the end of a mechanical coupler to the edge of the machine grips (

Figure 3.1). Identical gripping spans were applied at both ends of each specimen to maintain symmetry. For bare bar specimens, the gripping span was taken as the sum of the clear bar lengths in the mechanical splice specimens, which resulted in a clear span between machine grips that is twice the gripping span defined for the mechanical splices. Various splice gripping spans, ranging from $1.5d_b$ to $3d_b$, where d_b denotes the nominal bar diameter, were evaluated to assess their effect on bar stability during testing.

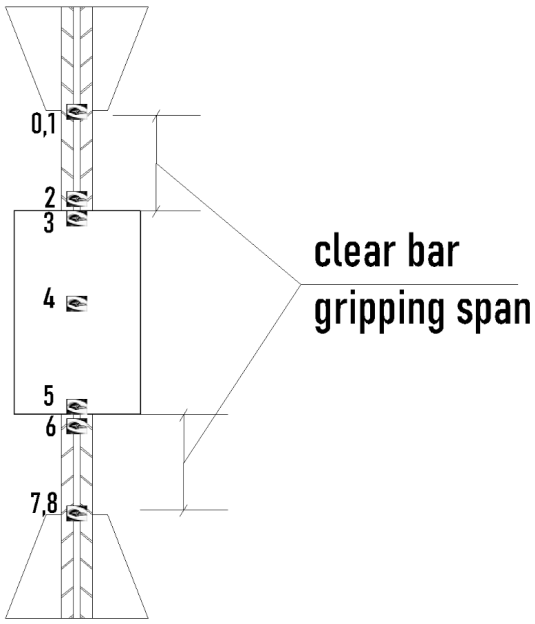

Figure 3-1-Clear bar gripping span for a mechanical splice

Preliminary test results indicated that shorter gripping spans could effectively reduce bar buckling so that lateral bracing of specimens would not be necessary. A clear gripping span of $1.5d_b$ was therefore selected for all reported tests to simplify the test setup. This decision to simplify the test

setup was also made to support the use of the test setup and protocols for pre-qualification testing of mechanical splices for seismic applications.

The short gripping span configuration mostly mitigated buckling in all specimens except one, the *Grouted-1* splices, where grout spalling at the coupler ends increased the effective gripping span, leading to excessive buckling (Figure 3.2).

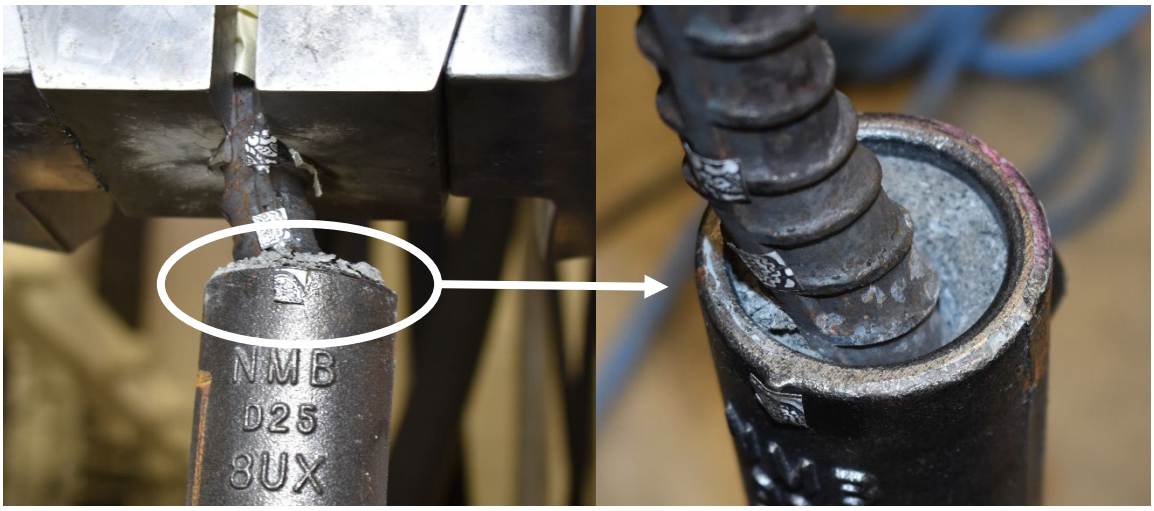

Figure 3-2-Grout spalling on Grouted-1 coupler during test causing increased clear bar gripping span

3.2.1.3 Strain loading protocol

For all low-cycle fatigue tests, a strain-controlled loading protocol cycling specimens between +2% in tension and –0.5% in compression was adopted to evaluate the low-cycle fatigue performance of bare bars and mechanically spliced specimens. This strain range was selected to be representative of strain demands in longitudinal bars in hinge regions of concrete members subjected to seismic loading (Sajedul Huq et al., 2017; D. Sokoli et al., 2025). While longitudinal bars in hinge regions can experience strain demand amplitudes reaching 6% or more (see Part II results), they typically will experience inelastic strain cycles of varying amplitudes below such an extreme (Zhong et al., 2021). Keeping strain demands within that range during testing also avoided premature buckling of specimens.

A larger strain amplitude ranging from +3% in tension to –1% in compression was initially considered to represent the inelastic strains experienced by longitudinal bars in seismically detailed concrete members. That strain range was used in low-cycle fatigue testing of high-strength

reinforcing bars in production in the U.S.(Ghannoum & Slavin, 2016; Sokoli et al., 2019). However, these higher strain reversals caused rapid low-cycle fatigue failure and excessive bar buckling, as also reported by previous studies on low -fatigue tests of reinforcing bars (Brown & Kunnath, 2004; Ghannoum & Slavin, 2016; J. Mander et al., 1994; Slavin & Ghannoum, 2015). In addition, the presence of couplers with lengths of 3 in. to 16 in. (75mm to 400 mm) increased the unbraced specimen length, amplifying buckling and reducing fatigue life (Ghannoum & Slavin, 2016; Venture & Venture, 2017).

Moreover, higher tensile strains increased vulnerability to buckling upon reversal into compression, as shown by Moyer and Kowalsky (2003). On the compression side, large compressive strains also accelerated bending demands in buckled segments, often reaching the critical bending strain that triggers bar fracture in subsequent cycle as shown BBT test by Barclay and Kowalsky (2019)(Barcley & Kowalsky, 2019).

After some preliminary testing under various strain protocols, a strain amplitude of 2.5% was finally adopted as is representative of seismic demands in hinge regions and results in more stable behavior with limited specimen buckling during testing.

3.2.2 Variable parameters

The following parameters were varied to assess their influence on the low-cycle fatigue performance of mechanical splices.

3.2.2.1 Bar Manufacturing process

Two steel manufacturing processes were considered: Microalloying (MA) and Quenching and Self-Tempering (QST). The low-cycle fatigue life of reinforcement is known to depend on metallurgical processing, and inclusion of both bar types allowed evaluation of potential manufacturing process-related differences as well as interaction with the coupling processes.

3.2.2.2 Coupler Type

Various coupler types employing different load-transfer mechanisms that are representative of those commonly available in the U.S. market were tested. To eliminate variability associated with installation process, all couplers were installed by manufacturers.

3.2.2.3 Bar Size

Two bar diameters, #8 (25 mm) and #11 (36 mm), were included to assess the influence of bar size on splice low-cycle fatigue performance. The #8 (25 mm) bars were initially selected because they were used as longitudinal boundary reinforcement in *Part 2-Wall tests*. To enable direct correlation between in-air and in-concrete results, #8 (25 mm) reinforcing bars were therefore adopted as the baseline. In addition, #11 (36 mm) bars were introduced later in the program to investigate potential bar size effects on mechanical splice performance.

3.2.2.4 Bracing condition

Mechanical splice specimens were tested in both unbraced and braced configurations to evaluate the effect of lateral restraint on low-cycle fatigue performance, particularly for those mechanical splice types that could not sustain stable cycling without bracing.

A bracing system was employed in Phase 2 of test program to conduct inelastic cyclic tests on mechanical splices, as shown in Figure 3.3. The bracing device was designed to resist buckling loads and stabilize the specimen under reversed inelastic strain demands.

Figure 3-3-Bracing device system for Phase 2 low cycle fatigue tests

The bracing system consisted of a series of lateral braces connected to the loading frame in two almost orthogonal directions (Figure 3.3). The braces were pinned at their ends using ball-joint ends to avoid introducing forces in the longitudinal specimen direction (Figure 3.4). The braces were connected to the couplers through steel plates and clamps. This configuration permits vertical

movement while effectively preventing lateral buckling and ensures that no axial load is transferred to the bracing system during testing.

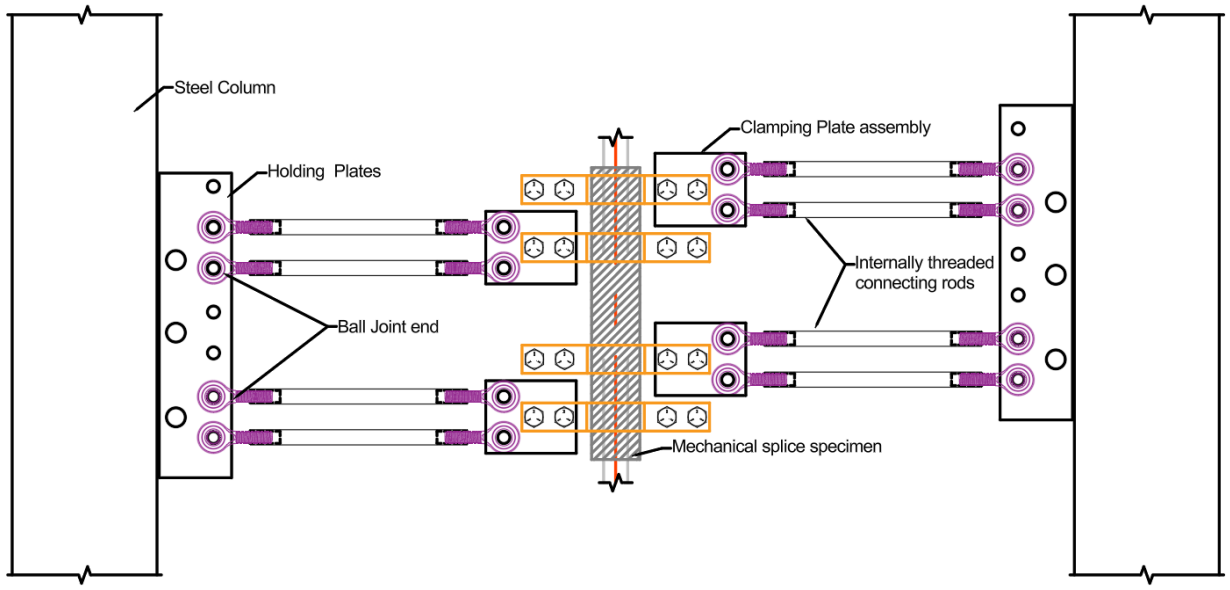

Figure 3-4-Schematic sectional view of bracing system

3.3 Test Procedures

3.3.1 Monotonic tension tests

3.3.1.1 Bar specimens

The mechanical properties of bare bars were determined through monotonic tensile tests conducted in accordance with ASTM A370(ASTM A370-22, 2022) and ASTM E8(ASTM E8/E8M-22, 2022). Complete force-displacement response was recorded throughout the test. Stress was calculated as the applied force divided by the nominal bar area. Strain was measured over an 8-inch (203 mm) gage length , as specified in ASTM A370. The following properties were extracted: elastic modulus, yield strength, ultimate tensile strength, tensile-to-yield strength (T/Y) ratio, uniform strain, and fracture strain. The elastic modulus was determined from the initial linear portion of the stress-strain curve. Yield strength was calculated using the 0.2% offset method per ASTM E8. The ultimate tensile strength was defined as the peak stress during testing, and the T/Y

ratio was computed as the ratio of ultimate to yield strength. Uniform strain is defined as the strain corresponding to the onset of necking, taken as the midpoint of the strain range where stress remained above 99.5% of the peak stress, as specified in ASTM E8. Fracture strain was measured just before load drop and includes both elastic and plastic components. A minimum of three tests were conducted per bar batch.

3.3.1.2 Mechanical splice specimens

For mechanical splice specimens, strains on both bars connected by a coupler were recorded. Monotonic tension tests were performed following the procedure specified in Caltrans Standard Test Method CT 670(Caltrans CT670, 2022). The larger of the bar strains at either end of a specimen at fracture was recorded as the fracture strain. Uniform strain is obtained per ASTM E8/E8M(ASTM E8/E8M-22, 2022) on the bar end that exhibits the larger fracture strain.

For monotonic tension tests, bar strain was measured over an 8-inch (203 mm) gage length along the bare bar segment as shown in Figure 3.5 Target pairs [1,2] were designated as the top gage strain, and [6,7] as the bottom gage strain for mechanical splice specimens. Additionally, targets [3, 4, 5] were placed to monitor slip between couplers and bars and coupler deformations. A minimum of two specimens were tested for each coupler-bar combination.

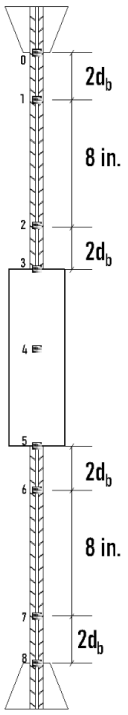

Figure 3-5-Specimens for monotonic tension tests along with target numbering scheme for monotonic tension test

3.3.2 Low-cycle fatigue tests

Low-cycle fatigue (LCF) tests were conducted on bare bar specimens and mechanical splice specimens. The tests were carried out in a uniaxial testing machine under strain control. Aluminum swaging was used to grip bar ends of specimens in the uniaxial machine as shown in Figure 3.6. The aluminum helped reduce stress concentrations at the grips such that fracture could occur away from the grips. Where fracture occurred the grip edge, test results were discarded in this study.

Figure 3-6-Aluminum tube swaging around test specimens

A reversed cyclic strain protocol oscillating between +2.0% in tension and –0.5% in compression was used or all specimens. A sinusoidal waveform was used with a frequency ranging between 0.008 and 0.012 Hz. This loading protocol simulates the strain reversals expected in longitudinal reinforcement of plastic hinge zones during seismic events. A universal testing machine with a capacity of 270 kips that can apply both compression and tension loading was used. Grips with length of 4.75 inches (120.7 mm) were employed at both ends of the specimens to provide rotational fixity. The load cell of the testing machine recorded the applied force during each test.

3.3.2.1 Bar specimens

Real-time strain measurements were obtained using a Digital Image Correlation (DIC) system developed at UTSA ((Rajae et al., 2023)). High-contrast targets were printed on stiff paper and adhered at the end of the bar specimens after mill scale removal to ensure proper bonding and accurate tracking. The DIC system monitored strains between the targets at the edge of the grips in bar specimens and provided those strain readings to the testing machine controller thereby creating a closed feedback control loop based on the surface strains. Specimens were cycled until fracture occurred. For each specimen, the number of half-cycles to fracture and to 80% of the peak strength was recorded.

Figure 3-7-DIC surface targets glued on bare bar specimen for low cycle fatigue testing (1.5db gripping span)

3.3.2.2 Mechanical splice specimens

For mechanical specimens, target pairs [1,2] and [6,7] as shown in Figure 3.8 were placed on the clear bar segments on either side of the coupler to capture the average strain across the clear bar span. The DIC system continuously tracked these targets and fed average strain from the two bar ends to the loading machine controller throughout the test. Additional targets [3,4,5] were

positioned to calculate local deformation across the coupler and slip between the coupler and the bars.

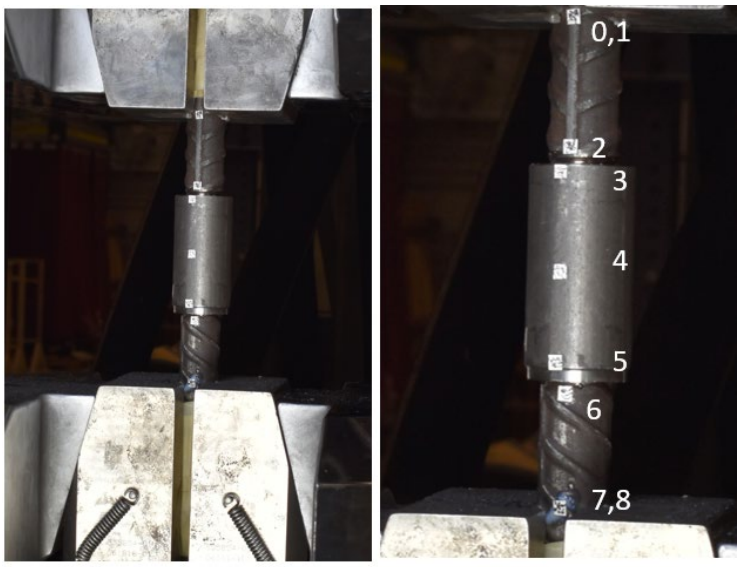

Figure 3-8-Low cycle fatigue target numbering along with DIC surface targets

Testing continued until the specimen fracture, with the number of half-cycles to fracture and 80% of peak strength were recorded. Specimens that failed at the grips were excluded. A minimum of three specimens were tested for each coupler-bar combination.

4 In-Air Testing Results and Observations

4.1 Bare bar specimens

4.1.1 Monotonic tension tests

Monotonic tension tests were conducted on a set of at least three specimens for each combination of bar size, manufacturing process, and steel batch used in the mechanical splice specimens of this study. In total, two bar sizes, #8 [25mm] and #11 [36mm], were tested. The bars satisfied the ASTM A706 supplement 1 specifications for Grade 80 (550MPa) bars and were made using the Microalloying (MA) and Quenched-and-Self-Tempered (QST) processes. The stress-strain behavior of sample specimens are presented in Figure 4.1 for #8 (25mm) and Figure 4.2 for #11 (36mm) bars. The average mechanical properties derived from tension tests are summarized in Table 4.1.

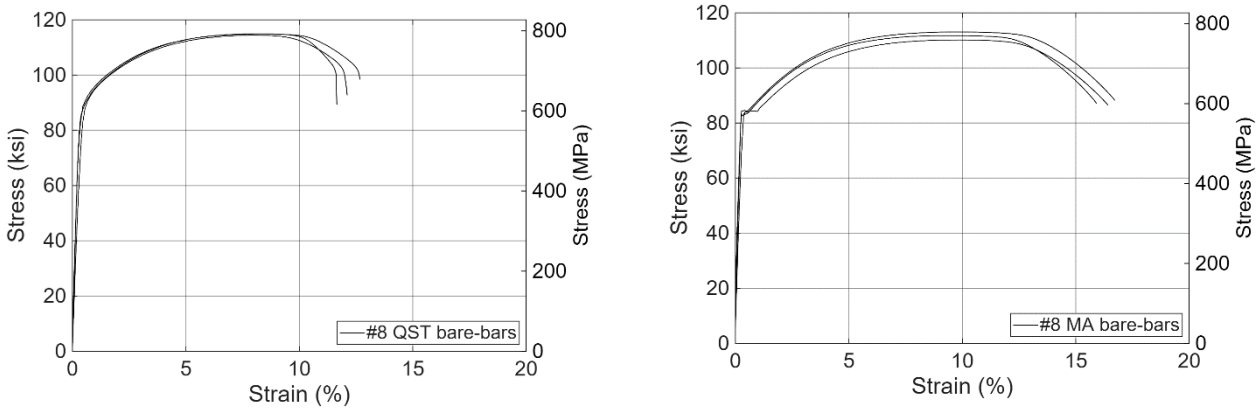

(a) (b)

Figure 4-1-Stress-Strain relationship for #8 (25mm) bars (a) Quenching and Self Tempering (QTB1) bars (b) Micro-alloying (MAB1) bars

As indicated in Table 4.1 , all batches conformed to the requirements of ASTM A706/A706M-25 for Grade 80 (550 MPa) reinforcement. Slight differences were noted in the T/Y ratios and elongation capacities between manufacturing processes, with MA bars generally exhibiting marginally higher values, consistent with findings by Ghannoum and Slavin (2016)(Ghannoum &

Slavin, 2016). The modulus of elasticity for both bar types was below the nominal 29,000 ksi (200,000 MPa) value for reinforcing steel, suggesting the bars may have been rolled on the lower end of the allowable diameter range. Nonetheless, bars satisfied the 7% uniform elongation requirement for #8 (25 mm) Grade 80 reinforcement and 6% uniform elongation requirement for #11 (36mm) per ASTM A706/A706M Supplement 1, as well as the 1.25 minimum required T/Y ratio.

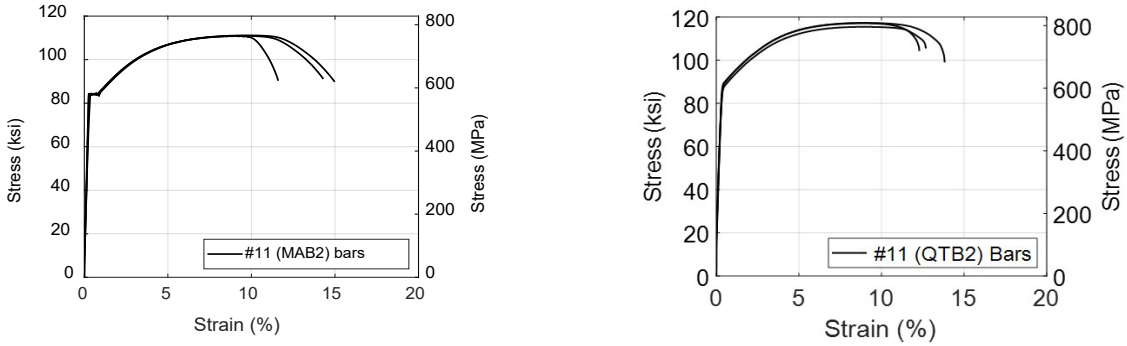

(a) (b)

Figure 4-2-Typical stress-strain plots for #11 (36mm) bars (a) Micro-alloying (MAB2) bars (b)Quenching and Self-tempering (QTB2) bars

Table 4.1-Monotonic tension test results from three specimens per bar type

Bar type	Yield strength, ksi (MPa)		Tensile strength, ksi (MPa)		Tensile/Yield Strength Ratio		Elastic Modulus, ksi (MPa)		Uniform strain, %		Fracture strain, %	
	Mean	COV	Mean	COV	Mean	COV	Mean	COV	Mean	COV	Mean	COV
#8 [25 mm] (QTB1) bars	88.40 (613.90)	1.18%	114.7 (790.3)	0.31%	1.28	0.31%	25,300 (174,317)	0.77%	8.00	3.19%	12.10	4.13%
#8 [25 mm] (MAB1) bars	83.90 (578.10)	0.91%	111.6 (768.9)	1.29%	1.48	8.06%	26,700 (183,963)	8.06%	9.72	2.14%	16.40	2.47%
#11[36 mm] (QTB2) bars	88.01 (606.81)	2.07%	116.35 (802.20)	0.76%	1.32	2.46%	23,413.03 (161,427)	4.52%	8.49	8.21%	12.83	4.59%
#11[36 mm] (QTB3) bars	91.85 (633.53)	0.17%	115.96 (799.52)	0.10%	1.26	0.07%	26,274.98 (181,159)	4.73%	7.96	11.31%	12.92	5.02%
#11[36 mm] (MAB2) bars	84.16 (580.26)	0.04%	110.97 (765.11)	0.126%	1.32	0.096%	27,984.78 (192,948)	5.88%	9.18	3.88%	13.62	10.75%

4.1.2 Inelastic Cyclic Tests

Representative stress-strain responses under inelastic cyclic loading for #8 bars used in this study are shown in Figure 4.3. A key observation is the progressive strength degradation exhibited by the QST bars, particularly evident in the cyces prior to fracture [Figure 4.3 (a)]. By contrast, MA bars demonstrated relatively stable peak strengths with minimal degradation before failing abruptly due to low-cycle fatigue. These behavioral trends align with previously documented results from similar investigations(Ghannoum & Slavin, 2016; Gonzalez, 2022; Slavin & Ghannoum, 2015).

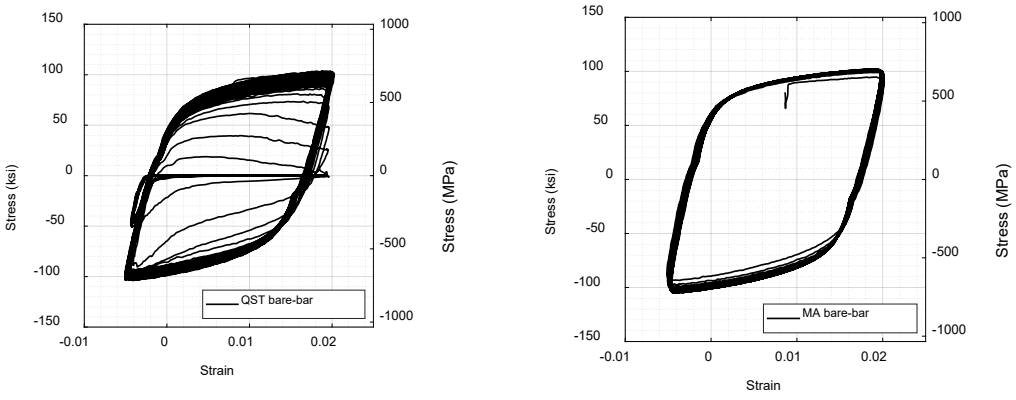

(a) (b)

Figure 4-3-Representative stress–strain relationship from inelastic cyclic test with a 1.5d_b gripping length: (a) #8 (25mm) QST bar; (b) #8 (25mm) MA bar.

Table 4.2 summarizes the low-cycle fatigue results for all bars batches in terms of number of half-cycles to fracture and number of half-cycles recorded until the stress at peak strain drops to 80% of the maximum value.

Table 4.2-Mean half-cycles to fracture or 80% of peak strength for bare bars

Bar Size	Bar Batches	Failure Criteria	Mean-half cycles to fracture		Number of samples tested (N)	
			QST	MA	QST	MA
#8 (25mm)	MAB1 and QTB1	Fracture	206.70	173.60	3	3
		80% of peak strength	172.30	173.60		
#11 (36mm)	MAB2 and QTB2	Fracture	105.01	99.56	3	3
		80% of peak strength	105.01	99.19		
#11 (36mm)	QTB3	Fracture	99.56	-	6	-
		80% of peak strength	99.16	-		

The trend of cyclic strength loss during cycling was also noted in the coupled specimens, which will be discussed in later sections. As reported in prior work by Sokoli et al. (2019) (Sokoli et al., 2019) ,Slavin and Ghannoum (Slavin & Ghannoum, 2015) Ghannoum and Slavin (2016) (Ghannoum & Slavin, 2016), and Gonzalez (2022)(Gonzalez, 2022), fatigue cracks predominantly initiated at the base of the transverse deformations of the bars. Two primary fracture patterns were observed: QST bars tended to fracture along the transverse rib base, with cracks propagating along this feature until final rupture. This mechanism reflects a more ductile failure mode, further supported by the gradual strength degradation during cycling and the slanted and fibrous fracture planes observed in Figure 4.4(a). By contrast, MA bars showed horizontal crack propagation across the bar's core and exhibited a sudden fracture and drop in strength. The resulting smooth fracture surfaces, as seen in Figure 4.4(b), suggest a more brittle fracture.

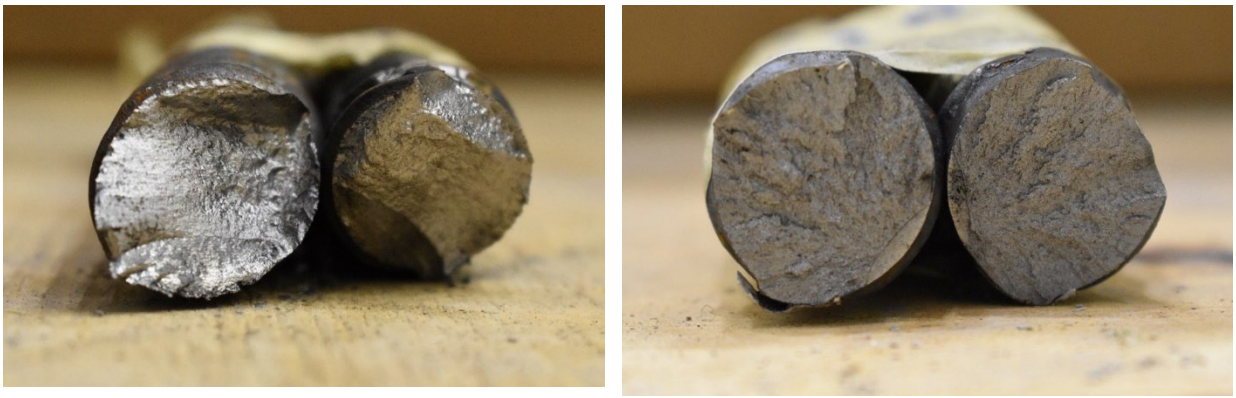

(a) (b)

Figure 4-4-Representative fracture planes for bars: (a) QST bars; and (b) MA bars

On average, #8 (25mm) MA bars fractured after approximately 174 half-cycles, while QST bars withstood about 207 half-cycles before fracture (a shown in Table 4.2). Despite differing failure modes and fracture planes, both bar types demonstrated similar low-cycle fatigue resistance (mean half-cycles to fracture). Notably, the selected MA and QST bars exhibited fatigue lives near the median of published U.S. bar performance (Ghannoum & Slavin, 2016; Sokoli et al., 2019).

Similarly, as presented in Table 4.2 for #11 (36 mm) bars, QST bare bars fractured after approximately 105 half-cycles for batch QTB2 and about 100 half-cycles for batch QTB3, whereas MA bars fractured at slightly lower values of around 100 half-cycles for batch MAB2. Compared to #8 (25 mm) bars, the mean half-cycles to fracture for #11 (36 mm) bars were reduced by 39% for QST bars and 42% for MA bars. These results align with the observations reported by Ghannoum and Slavin (2016).

4.2 Mechanical splice specimens

4.2.1 Monotonic tension tests

All mechanical splice specimens subjected to monotonic tension tests reached stress levels above 100 ksi (690 MPa), as summarized in Table 4.3 and Table 4.4. These results indicate that all tested mechanical splices met the strength criteria for both Type 1 and Type 2 mechanical splice type as defined in ACI 318-19. Specifically, Type 1 splices are required to develop at least 125% of the specified yield strength, while Type 2 splices are required to develop the larger of 125% of the specified yield strength and 100% of the specified tensile strength of the bar. For Grade 80 bars, both criteria result in a requirement of exceeding 100 ksi (690 MPA) before fracture. The peak tensile stresses recorded in the bars of the mechanical splices were within 94% of the corresponding tensile strengths of the parent bare bars.

Stress-strain responses were recorded over an 8 in. (203 mm) gage length on both sides of a mechanical coupler throughout a test, as illustrated in Figure 4.5. Uniform strain is taken as the smaller of the strains at each bar end of a mechanical splice when the specimen reached peak stress.

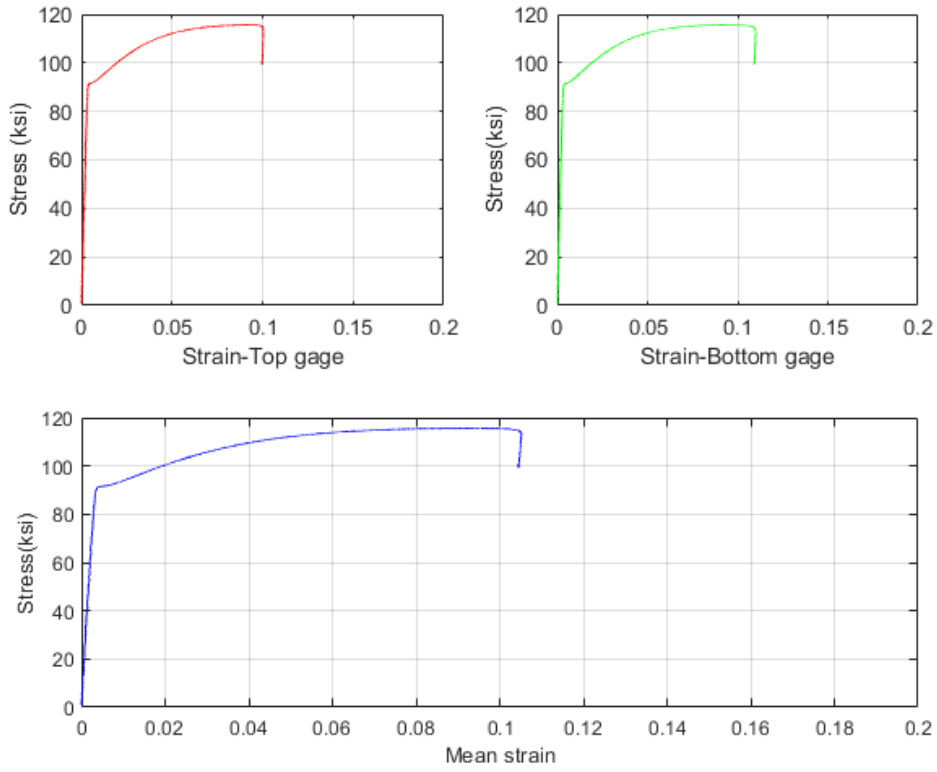

Figure 4-5- Typical stress-strain plots on 8 in. (200 mm) gage lengths on each side of a coupler (1 ksi=6.896 MPa)

Fracture strain was taken as the maximum strain recorded over the bar end where the uniform strain was taken. In cases where fracture occurred outside the instrumented gauge length, fracture strain values were not reported in Table 4.3 and Table 4.4. Coupler fractures were not observed in the #8 (25mm) specimens, whereas about half of Grouted-1 and Grouted-2 #11 (36mm) mechanical specimens experienced coupler fracture at the junction between the bars being coupled (shown in Figure 4.6). However, despite fracture of the coupler itself, the mechanical splice specimens still reached the stress levels required for ACI 318 Type 2 splices. Coupler fractures were not observed in the #11 (36mm) End grip (upset headed) mechanical splice specimens.

While all couplers achieved consistent strength performance, notable variation was observed in their uniform strain capacities. Several mechanical splice systems exceeded the minimum uniform elongation requirements of ASTM A706 supplement 1, namely 7% for #8 (25 mm) bars and 6% for #11 (36 mm) bars. Conversely, some mechanical splice systems exhibited markedly lower ductility. This highlights disparities in ductility among coupler types, despite all of them meeting

the strength criteria of ACI 318-19. These findings therefore indicate that a strength criterion does not guarantee ductility for mechanical splices.

Table 4.3-Monotonic tension test results for #8 (25mm) mechanical splices on QST and MA bar type

Bar Type	Product	Ultimate Stress, ksi (MPa)	Uniform Strain, %	Fracture Strain, %	Fracture Region
QST / Grade 80	*Threaded-1*	107.6 (741.4)	3.24	NA	Coupler-bar interface
		107.9 (743.4)	3.32	NA	Inside coupler
	Swaged	114.6 (789.6)	9.19	13.54	At 8in. gage length
		114.3 (787.5)	6.90	12.79	At 8in. gage length
	Taper Threaded-1	107.6 (741.4)	2.79	NA	Coupler-bar interface
		112.3 (773.7)	4.93	NA	Inside the coupler
	Threaded-2	107.7 (742.1)	3.70	NA	Coupler bar interface
		108.1 (744.8)	3.48	NA	Coupler bar interface
	Friction Welded-2	114.1 (786.1)	8.44	15.08	At 8in. gage length
		113.9 (784.8)	7.82	13.40	At 8in. gage length
	End Grip	114 (785.5)	9.84	13.91	At 8in. gage length
		113.7 (783.4)	9.27	13.64	At 8in. gage length
	Taper Threaded-2	114.5 (788.9)	8.79	12.97	At 8in. gage length
		114.3 (787.5)	8.91	12.65	At 8in. gage length
	Grouted/Threaded	114.1 (786.1)	8.91	12.51	At 8in. gage length
		114.5 (788.9)	8.73	NA	Outside gage length
	Friction Welded-1	114.4 (788.2)	9.36	11.72	At 8in. gage length
		114.3 (787.5)	10.51	12.63	At 8in. gage length
	Grouted-2	114.3 (787.5)	8.85	13.35	At 8in. gage length
		114.4 (788.2)	7.56	12.75	At 8in. gage length
	Grouted-1	113.8 (784.1)	6.76	10.39	At 8in. gage length
		114.5 (788.9)	7.80	15.99	At 8in. gage length
MA / Grade 80	*Threaded-1*	107.4 (739.7)	4.60	5.82	Coupler-bar interface
		109.2 (752.6)	5.62	6.35	Coupler-bar interface
	Swaged	111.9 (770.6)	10.22	17.41	At 8in. gage length
		109 (750.9)	6.06	20.59	At 8in. gage length
	Taper Threaded-1	109.2 (752.7)	6.90	NA	Inside coupler
		110.9 (763.8)	4.13	NA	Outside gage length
	Threaded-2	109.6 (755)	5.69	NA	Outside gage length
		107.8 (742.9)	5.29	NA	Outside gage length
	Friction Welded-2	112.2 (773.3)	8.00	14.15	At 8in. gage length
		111.7 (769.3)	4.41	16.33	At 8in. gage length
	End Grip	112 (771.7)	7.80	15.75	At 8in. gage length
		110.6 (762)	7.43	14.48	At 8in. gage length

	Taper Threaded-2	109.9 (756.9)	11.99	17.33	At 8in. gage length
		111.2 (766.4)	10.64	16.03	At 8in. gage length
	Grouted/Threaded	110.7 (762.6)	6.87	17.19	At 8in. gage length
		111.9 (771.3)	8.87	18.19	At 8in. gage length
	Friction Welded-1	112.8 (777.3)	8.51	15.85	At 8in. gage length
		114.8 (791.2)	11.5	16.32	At 8in. gage length
	Grouted-2	111.8 (770)	9.41	14.05	At 8in. gage length
		110.4 (760.8)	7.45	17.65	At 8in. gage length
	Grouted-1	113.9 (784.6)	11.87	NA	Outside gage length
		110.1 (758.9)	6.91	18.82	At 8in. gage length

Figure 4-6-Coupler fracture for #11 (36mm) grouted mechanical splice specimens

Table 4.4-Monotonic tension test results for #11 (36mm) mechanical splice specimens

Bar Size	Coupler Manufacturer	Coupler	Ultimate Stress, ksi (MPa)	Uniform Strain, %	Fracture Strain, %	Fracture Region
#11 (36 mm)	**M3**	*End Grip (QST)*	115.25 (794.07)	9.25	14.02	At 8 in. gage length
			115.66 (796.89)	9.05	11.07	At 8 in. gage length
	M5	*Grouted-1 (MA)*	110.75 (763.62)	12.86	13.22	Coupler fracture at bar junction
			112.58 (776.21)	12.95	14.92	At 8 in. gage length
		Grouted-1(QST)	117.58 (810.71)	9.21	13.94	At 8 in. gage length
			103.09 (710.79)	1.83	2.209	Coupler fracture at bar junction
		Grouted-2 (MA)	111.82 (770.96)	9.88	11.43	At 8 in. gage length
			112.25 (773.95)	9.19	15.67	At 8 in. gage length
		Grouted-2(QST)	112.60 (776.36)	4.19	4.953	Coupler fracture at bar junction
			114.71 (790.93)	5.12	5.28	Coupler fracture at bar junction

4.2.2 Inelastic reversed cyclic tests

4.2.2.1 Phase 1: Unbraced fatigue performance with #8 (25mm) bars

Figure 4.7 shows the total half-cycle count to fracture for #8 (25mm) specimens tested in Phase 1 of this study under the (+2%, –0.5%) strain protocol with a clear gripping span of $1.5d_b$.

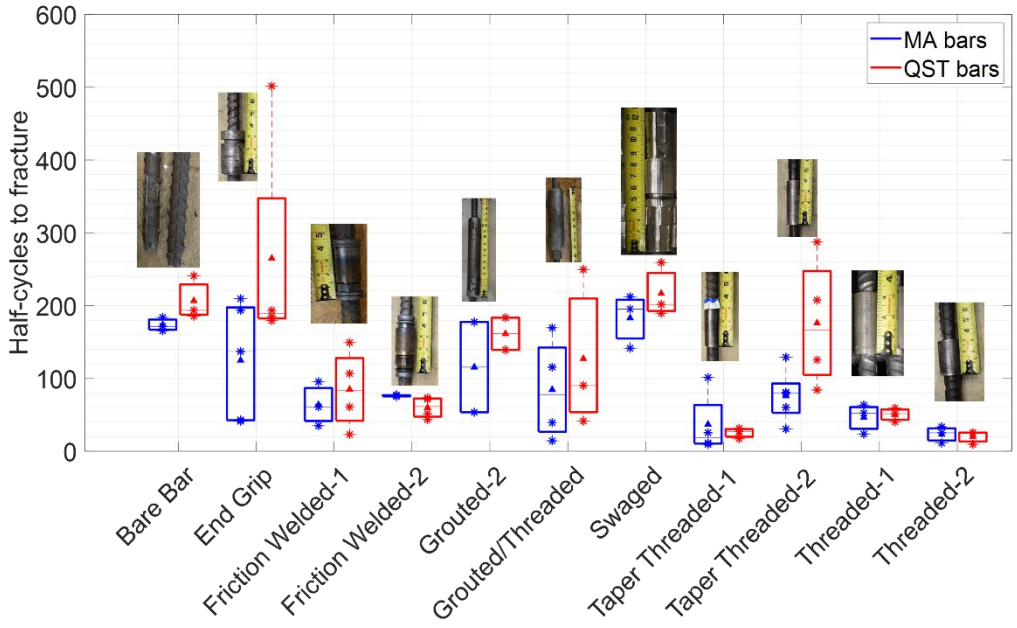

Figure 4-7- Half-cycles to fracture for bare bar and mechanical splice specimens under the (+2%, –0.5%) strain protocol ($1.5d_b$ clear bar gripping span. Asterisk (*) symbols represent individual data points, the two box edges correspond to the 25th and 75th percentiles, the horizontal dashed line denotes the median, and the triangle marker indicates the mean half-cycles.

Table 4.5 summarizes the corresponding half-cycle counts to fracture and to the point where the sustained strength at peak strain dropped to 80% of the peak stress value. The 80% criterion was introduced to address cases, particularly among QST specimens, where strength degradation occurred gradually, resulting in a significant number of cycles at reduced load levels. Figure 4.8 presents the half-cycle counts for the 80% peak strength criterion. These plots show that fatigue life varied widely among splice types, with some mechanical splices achieving values close to 100% of bare-bar fatigue performance and others coming in at only about 10% of the bare bar fatigue life. Pictures of the fractured specimens after testing are presented in Appendix B.

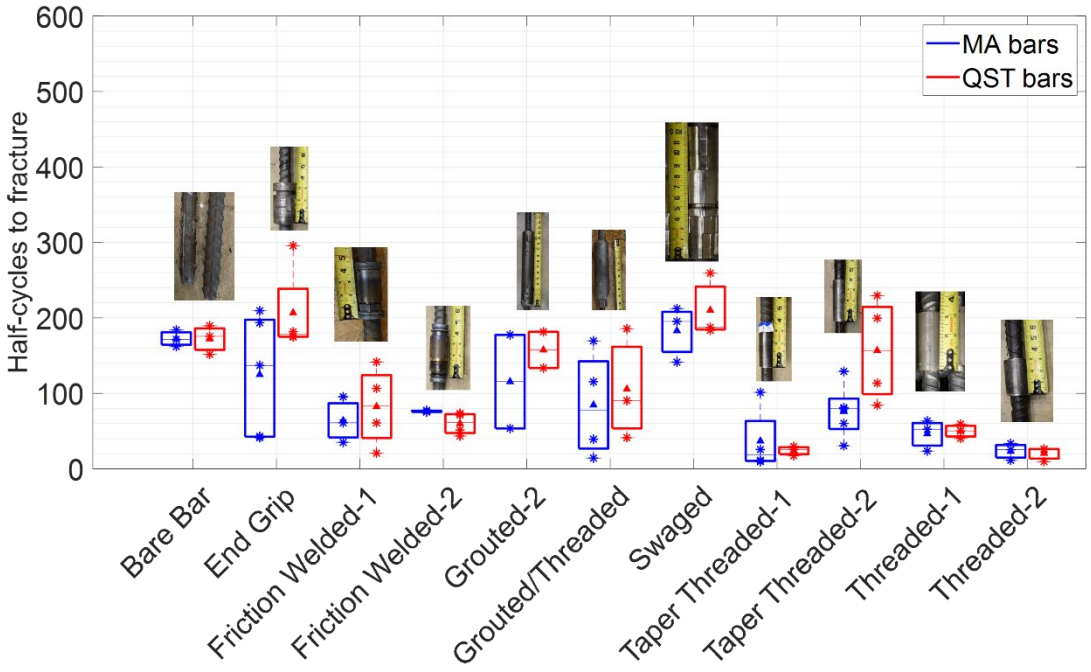

Figure 4-8-Half-cycles to 80% of peak strength for #8 (25mm) bare bar and mechanical splice specimens under the (+2%, –0.5%) strain protocol (1.5db clear bar gripping span). Asterisk (*) symbols represent individual data points, the two box edges correspond to the 25th and 75th percentiles, the horizontal dashed line denotes the median, and the triangle marker indicates the mean.

Table 4.5-Fatigue life for #8 (25mm) specimens of Phase 1 in terms of mean half-cycles to fracture or 80% of peak strength

Product	Failure Criteria	Mean-half cycles to fracture		Number of samples tested (N)		COV (%)	
		QST	MA	QST	MA	QST	MA
Bare Bar	Fracture	206.70	173.60	3	3	14.49	5.47
	80% of peak strength	172.30	173.60			11.15	5.47
Threaded-1	Fracture	50.40	46.50	3	3	18.91	44.22
	80% of peak strength	50.00	46.50			18.97	44.22
Swaged	Fracture	216.80	183.00	3	3	17.15	20.22
	80% of peak strength	210.20	184.00			20.28	20.22
Taper Threaded-1	Fracture	25.37	36.90	3	4	28.56	117.75
	80% of peak strength	24.20	36.90			25.84	117.75
Threaded-2	Fracture	20.20	23.40	3	3	45.72	48.1
	80% of peak strength	20.51	23.40			46.36	48.1
Friction Welded-2	Fracture	59.95	76.10	4	5	24.71	1.54
	80% of peak strength	59.95	76.10			24.71	1.54
End Grip	Fracture	264.90	124.90	5	5	83.17	64.19
	80% of peak strength	165.40	124.90			60.72	64.19
Taper Threaded-2	Fracture	176.10	76.10	4	5	51.18	47.25
	80% of peak strength	156.70	76.10			44.01	47.25
Grouted/Threaded	Fracture	127.10	84.90	3	4	85.6	84.29
	80% of peak strength	105.70	84.90			69.37	84.29
Friction Welded-1	Fracture	84.95	63.90	4	3	64.56	47.53
	80% of peak strength	82.50	63.90			63.97	47.53
Grouted-2	Fracture	161.40	115.50	2	2	19.4	75.88
	80% of peak strength	140.20	115.50			27.41	75.88

To allow direct comparison across splice types, fatigue results were also expressed in normalized form relative to the performance of the corresponding bare-bar for each bar manufacturing type. The normalized plots for fracture and 80% peak strength are presented in Figure 4.9 and Figure 4.10, respectively. For most splice types, MA and QST bars displayed similar normalized performance, with QST specimens generally tending toward slightly higher values. For the *End Grip* and *Taper Threaded-2* configurations, QST specimens demonstrated markedly higher normalized fatigue performance than MA specimens, although no definitive explanation for this difference was identified.

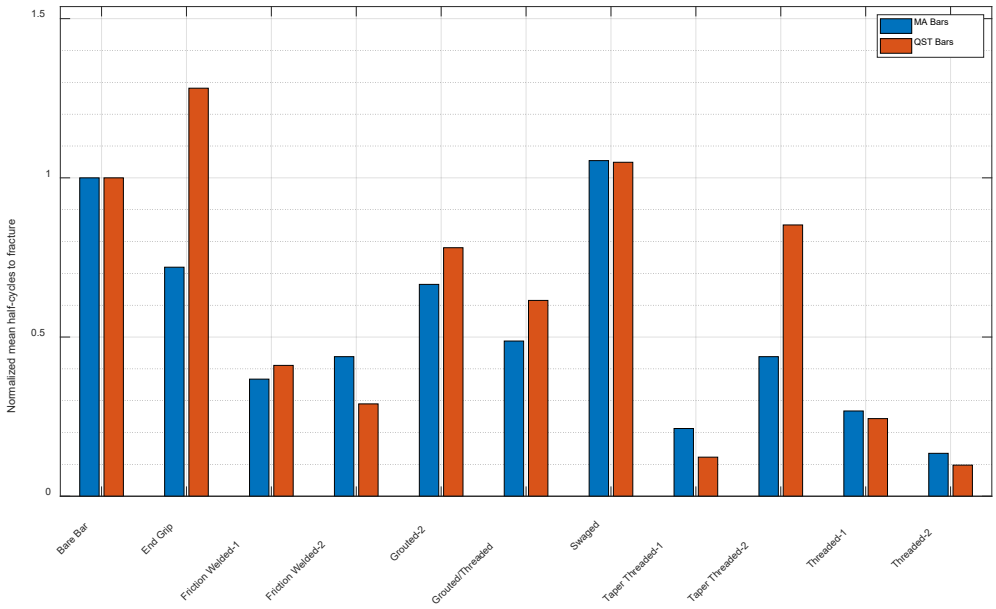

Figure 4-9-Normalized mean half-cycles to fracture performance of mechanical splices relative to bare bar performance

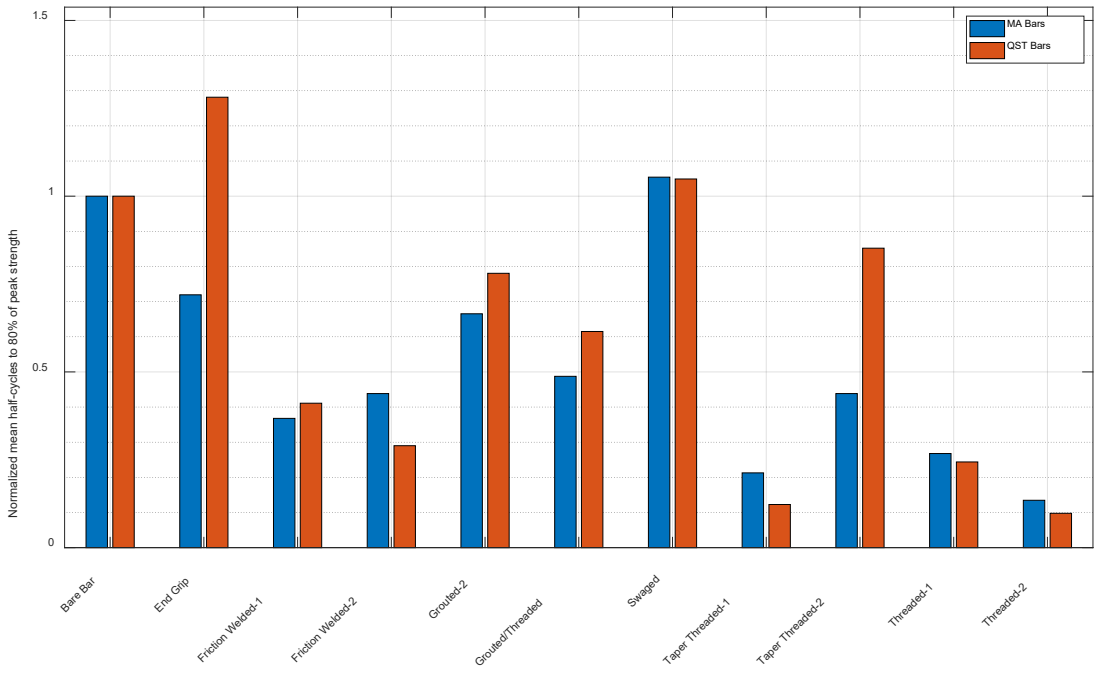

Figure 4-10-Normalized mean half-cycles to 80% peak strength performance of mechanical splices relative to bare bar performance

One notable observation from the normalized plots in Figure 4.9 and Figure 4.10, is that the fatigue performance of specimens with QST bars appears to be more sensitive to mechanical splice coupling processes that disturb the bar material itself, such as friction welding that may alter the original metallurgy of the reinforcing bar, or the taper threading process that can disturb the outer hardened layer of QST bars. This effect is evident through the lower normalized performance of QST specimens compared with their MA counterparts for these splice types: *Friction Welded-1*, *Friction Welded-2*, *Threaded-1*, *Threaded-2* and *Taper Threaded-1*. The *Taper Threaded-2* devices did not show this reduction in performance for QST bars, however.

For all mechanical splice tests conducted in Phase 1 of this study, failure occurred in the reinforcing bars rather than in the coupler assemblies, indicating that the mechanical splice fatigue life is likely correlated with that of the bare bars for a given device types. Since the selected #8 bar batches for Phase 1 had fatigue lives around the median fatigue performance of reinforcing bars in the United States (see Chapter 3), the fatigue performance of the mechanical splice specimens in this Phase 1 is expected to reflect the median response of mechanical splices across various batches of Grade 80 bars in production in the U.S.

4.2.2.2 Phase 1: Correlation Between Uniform Strain and Fatigue Life

A correlation was observed between the uniform strain sustained by mechanical splice specimens during tension testing and the number of half-cycles to fracture, as shown in Figure 4.11. The correlation coefficient of 0.66 indicates a moderately strong positive relationship, suggesting that specimens capable of sustaining higher uniform strain in tension also tend to achieve longer fatigue lives. The associated p-value of 0.027 confirms that this correlation is statistically significant, with less than a 3% probability that the relationship occurred by chance. These findings suggest that similar mechanisms may influence both ductility and fatigue resistance in mechanical splices,

reinforcing the potential for tension strain capacity to possibly serve as an indicator of splice fatigue performance.

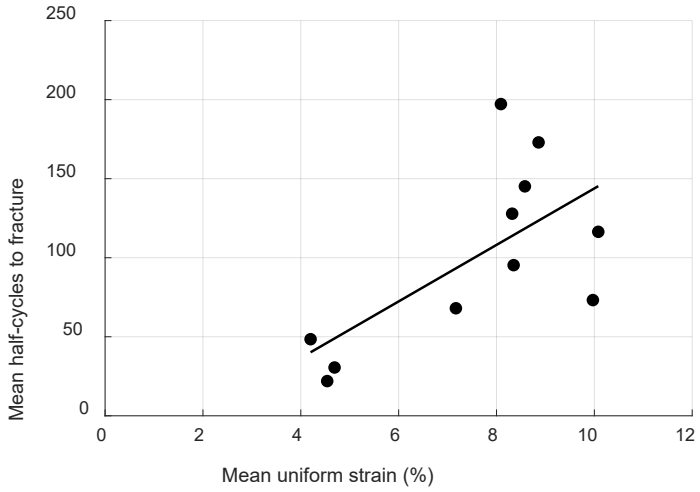

Figure 4-11-Relationship between mean half-cycles to fracture and mean uniform strain sustained in tension testing. Data points represent averages for specimens of the same coupler type and steel production, with a linear regression fit shown to illustrate the correlation.

4.2.2.3 Phase 2: Braced fatigue performance with #8 and #11 bars

In Phase 2, results from braced and unbraced tests with #8 (25mm) bars were compared to investigate the effect of bracing. Grouted-1 and Grouted-2 mechanical splices with #8 (25 mm) bars from the same heats used in Phase 1 were tested with a bracing system described in Chapter 3 to mitigate bar buckling. Their braced cyclic performance was compared with corresponding available unbraced tests from Phase 1 and bare bar behavior in Figure 4.12, Figure 4.15 and Table 4.6. Grouted-2 QST specimens exhibited improvement in fatigue performance when tested with bracing. The braced QST *Grouted-2* specimens sustained an average of 247 half-cycles to fracture compared with 160 mean half-cycles to fracture for the nominally identical unbraced specimens. The braced specimens therefore closely matched the performance of the corresponding #8 (25 mm) bare bars, which fractured after about 205 half-cycles. MA *Grouted-2* specimens followed the same trend, with braced specimens sustaining approximately 140 mean half-cycles to fracture compared with 115 for the unbraced MA specimens. Overall, the results suggest that bracing could contribute to improved fatigue performance of #8 (25 mm) grouted splice specimens tested.

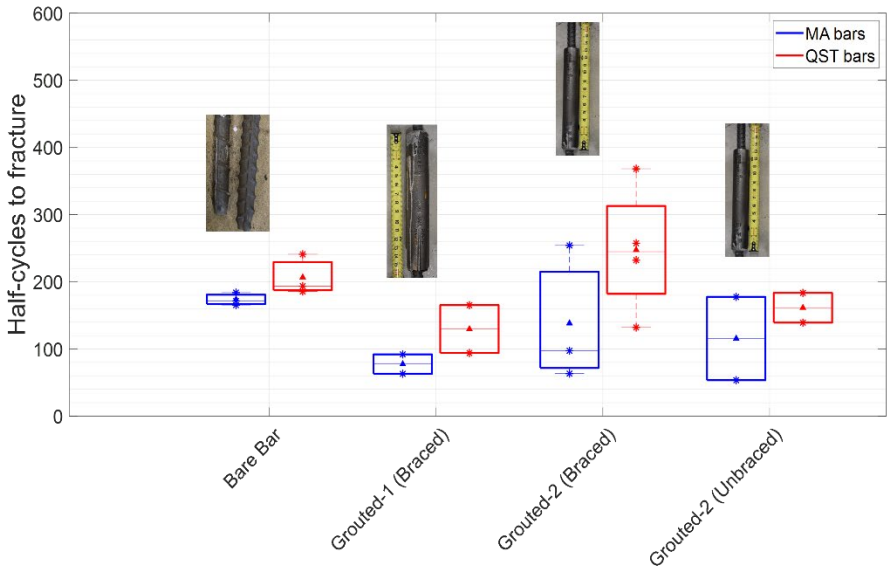

Figure 4-12-Braced inelastic cyclic test results for #8 (25mm) grouted mechanical splices compared with unbraced test. Asterisk (*) symbols represent individual data points, the two box edges correspond to the 25th and 75th percentiles, the horizontal dashed line denotes the median, and the triangle marker indicates the mean.

Table 4.6-Mean half-cycles to fracture for #8 (25mm) and #11 (36mm) braced specimen compared to unbraced specimen

Bracing Condition	Bar Size	Failure Criteria	Mean-half cycles		Number of samples tested (N)		COV (%)	
			QST	MA	QST	MA	QST	MA
Unbraced	#8 (25 mm) *Bare bar*	Fracture	206.70	173.60	3	3	14.49	5.47
		80% of peak strength	172.30	173.60			11.15	5.47
	#11 (36mm) *BB-Grouted-1**	Fracture	105.01	99.56	3	3	44.61	15.12
		80% of peak strength	105.01	99.19			44.61	15.01
	#11 (36mm) *BB-End Grip*	Fracture	99.56	-	6	-	23.95	-
		80% of peak strength	99.16	-			24.95	-
	#8 (25 mm) *Grouted-2*	Fracture	161.40	115.50	2	2	19.40	75.88
		80% of peak strength	140.20	115.50			27.41	75.88
	#8 (25mm) *End Grip*	Fracture	264.90	124.90	5	5	83.17	64.19
		80% of peak strength	165.40	124.90			60.72	64.19
Braced	#8 (25mm) *Grouted-1*	Fracture	130.7	80.98	3	3	27.30	7.43
		80% of peak strength	98.18	80.98			7.03	7.43
	#8 (25mm) *Grouted-2*	Fracture	247.27	139.67	2	2	33.93	59.32
		80% of peak strength	206.57	139.67			23.20	59.32
	#11 (36mm) *Grouted-1*	Fracture	110.01	-	2	-	70.45	
		80% of peak strength	110.01	-			70.45	
	#11 (36mm) *End Grip*	Fracture	85.26	-	4	-	16.50	-
		80% of peak strength	84.65	-			16.80	-

**BB-Grouted-1 and BB-End-Grip represent bare bar performance for bars used in Grouted-1 coupler and End Grip coupler, respectively.*

In addition, braced tests were conducted on mechanical splices with #11(36mm) bars to explore difference in fatigue life of splices with larger bars sizes. For #11 (36 mm) specimens, Figure 4.13, Figure 4.14 and Table 4.6 show that QST *End Grip* splices exhibited performance within the range of their corresponding bare bars, with *End Grip* specimens averaging about 85 half-cycles compared to bare bar means of approximately 110 half-cycles. By contrast, the QST *Grouted-1* specimens exceeded the bare bar performance on average, although their results displayed considerable variability across test specimens with coefficient of variance of 70%.

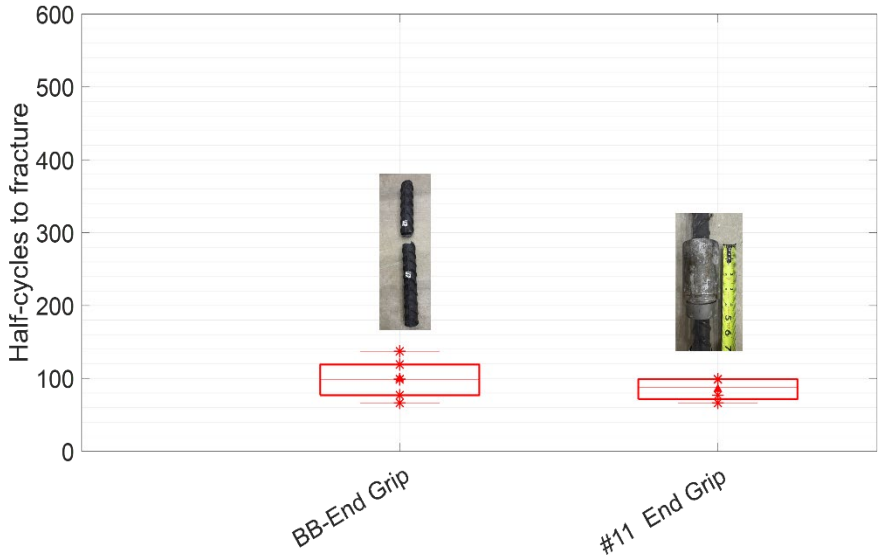

Figure 4-13-Half-cycles to fracture for #11 (36mm) bare and corresponding #11 (36mm) End Grip mechanical splice. Asterisk (*) symbols represent individual data points, the two box edges correspond to the 25th and 75th percentiles, the horizontal dashed line denotes the median, and the triangle marker indicates the mean..

It should be noted that all #11 (36mm) bare bar and mechanical splice specimens were tested without aluminum swaging due to width limitations in the available machine grips at the research facility. Similarly, grouted spalling was observed even under limited buckling during the braced low-cycle fatigue tests, which increased clear bar gripping for these types of test specimens.

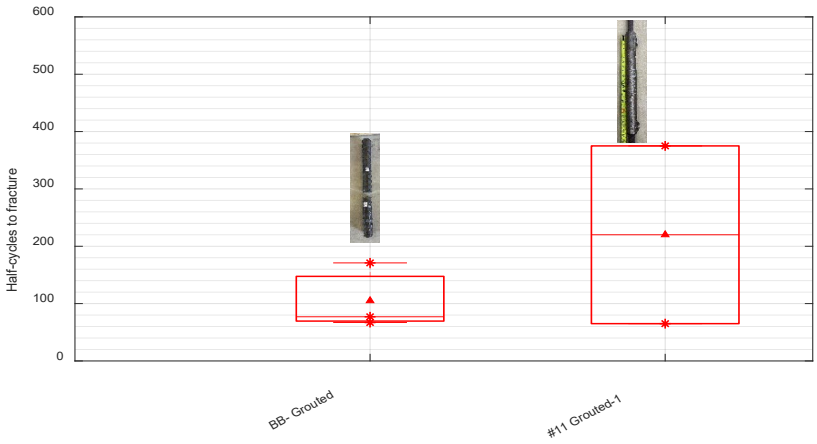

Figure 4-14-Half-cycles to fracture for #11 (36mm) bare bar and corresponding #11 (36mm) Grouted-1 mechanical splice

Normalized mechanical splice performance relative to corresponding bare bar fatigue life, as shown in Figure 4.15, showed distinct trends with bracing and bar size. For #8 (25 mm) specimens, bracing had a strong positive effect on *Grouted-2* splices, raising their unbraced performance from below bare bar levels (0.78 for QST and 0.67 for MA) to values approaching or exceeding par (1.20 for QST and 0.81 for MA). By contrast, *Grouted-1* splices remained below bare bar performance even when braced (0.63 for QST and 0.47 for MA), indicating limited benefit from bracing for this type of splice type.

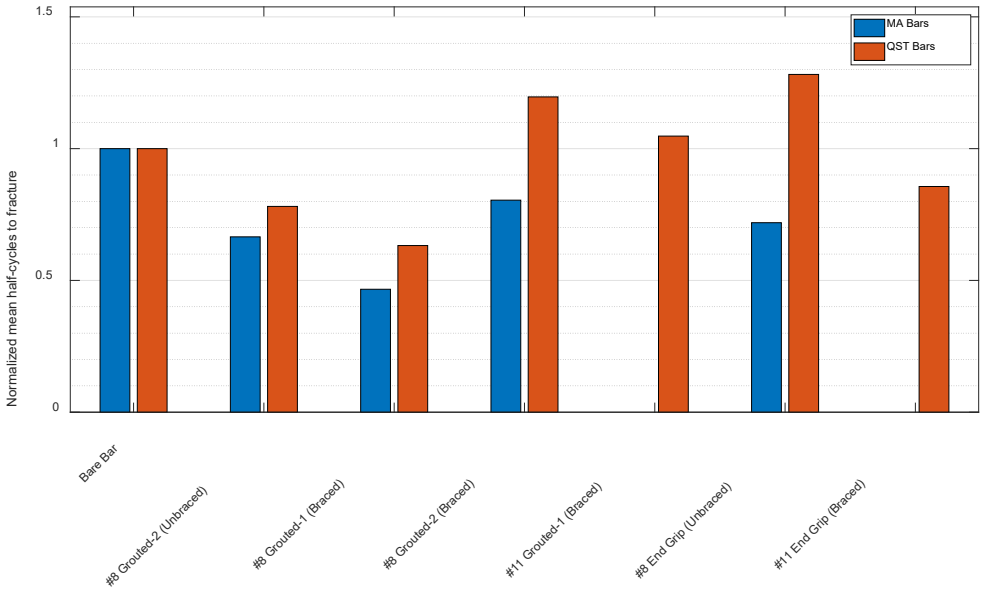

Figure 4-15-Normalized mean half-cycles to fracture performance relative to corresponding bare bar performance

On the other hand, the effect of bar size was not consistent across splice types. Grouted-1 splices showed improved fatigue performance on #11 bars compared to #8 specimens, reaching parity with the #11 QST bare bars (Figure 4.15). However, #11 Grouted-1 fatigue performance showed relatively high variability with a coefficient of variation of approximately 70%, suggesting inconsistent performance across specimens (Figure 4.15 and Table 4.6). By contrast, End Grip splices performed better in unbraced #8 specimens (1.28 of bare bar performance for QST and 0.72 for MA), but dropped to 0.86 for QST in braced #11 specimens (Figure 4.15 and

Table 4.6), indicating that the increase in bar size did not translate into improved performance despite the addition of bracing.

4.2.2.4 Fracture surface and locations

As illustrated in Figure 4.16, fracture due to low-cycle fatigue occurred at several locations: in the exposed bar length between the coupler and the machine grips, at the bar–coupler junction, within the grout, and in some cases the coupler itself fractured. Table 4.7 and Table 4.8 provide a comprehensive list of fracture locations and the corresponding fracture planes in mechanical splice specimens connecting both MA and QST reinforcing bars. Instances of bar pullout from the grout were also observed. For #8 (25mm) specimens, coupler body fractures were not recorded. However, two cases of coupler fracture were observed in #11 (36 mm) grouted splice specimens where the two bars being connected met (Figure A.6). Additional fracture images for tests are presented in Appendix B.

Most bar fractures developed near the bar–coupler interface. This trend is attributed to localized stress concentration resulting from abrupt changes in cross-sectional geometry and potential surface disruptions introduced during installation. Such stress concentrations were especially evident in threaded and friction-welded splice systems.

Another notable observation was that disturbances generated in the bars during coupler installation tended to shift the fracture behavior of QST bars from a ductile behavior to a more brittle behavior. As discussed previously, QST bars tended to exhibit a more ductile fracture plane than MA bars. However, it appears that some coupler installations shifted that behavior towards a more brittle one as illustrated in Figure 4.17 to Figure 4.20. The products that caused this shift in behavior were taper-threaded, threaded, and friction-welded splice systems.

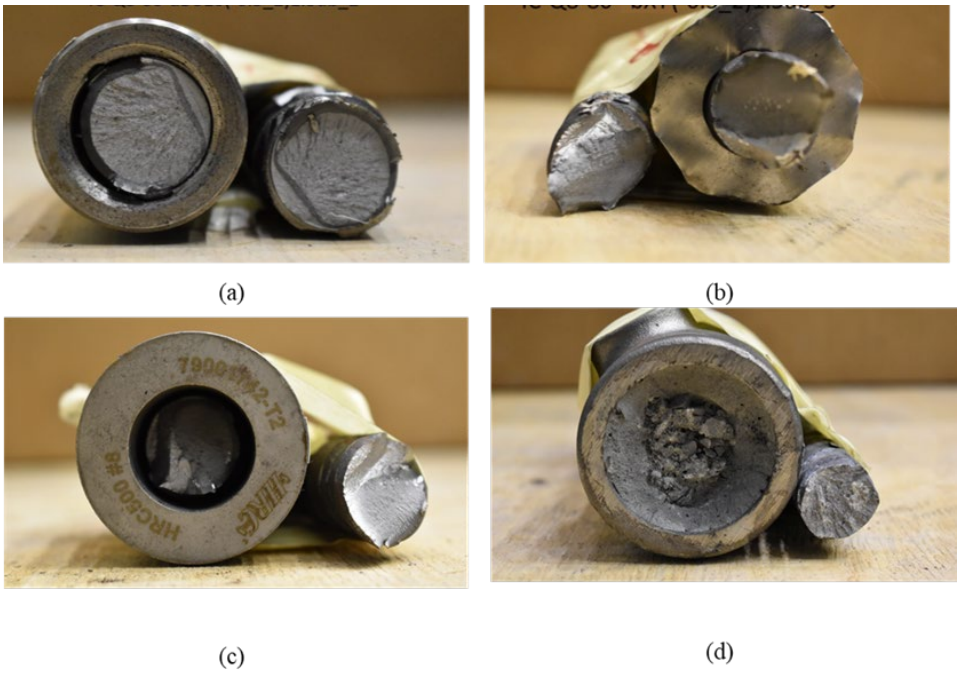

Figure 4-16-Failure locations in mechanical splice specimens: (a) fracture at the coupler junction; (b) fracture between the coupler and the grip; (c) fracture occurring within the coupler; and (d) fracture occurring within the coupler sleeve

Table 4.7- Fracture locations in #8 (25mm) mechanical splice specimens connecting MA Bars

Manufacturer (Bar type)	Mechanical splice specimen	Fracture Location	Fracture plane
Grouted-1 (MA)	IC-M8-80-Grouted-1(-0.5_2)1.5db_2	0.75d_b outside coupler edge	Brittle
	IC-M8-80-Grouted-1(-0.5_2)1.5db_3	0.75 d_b outside coupler edge	Brittle
Friction Welded-1 (MA)	IC-M8-80-Friction Welded-1(-0.5_2)1.5db_1	At the friction weld on coupler side	Brittle
	IC-M8-80-Friction Welded-1(-0.5_2)1.5db_2	At the friction weld on coupler side	Brittle
	IC-M8-80-Friction Welded-1(-0.5_2)1.5db_3	At the friction weld on coupler side	Brittle
Grouted/Threaded (MA)	IC-M8-80-Grouted/Threaded(-0.5_2)1.5db_1	At threaded end	Brittle
	IC-M8-80-Grouted/Threaded(-0.5_2)1.5db_2	Inside coupler	Brittle
	IC-M8-80-Grouted/Threaded(-0.5_2)1.5db_3	Bar pullout	-
	IC-M8-80-Grouted/Threaded(-0.5_2)1.5db_4	Inside coupler	Brittle
Taper Threaded-2 (MA)	IC-M8-80-Taper Threaded-2(-0.5_2)1.5db_1	Inside the coupler (on threads)	Brittle
	IC-M8-80-Taper Threaded-2(-0.5_2)1.5db_2	Inside the coupler (on threads)	Brittle
	IC-M8-80-Taper Threaded-2(-0.5_2)1.5db_3	Edge of coupler (on threads)	Brittle
	IC-M8-80-Taper Threaded-2(-0.5_2)1.5db_4	Edge of coupler (on threads)	Brittle
	IC-M8-80-Taper Threaded-2(-0.5_2)1.5db_5	Edge of coupler (on threads)	Brittle
End Grip (MA)	IC-M8-80-End Grip(-0.5_2)1.5db_1	Inside coupler	Brittle
	IC-M8-80-End Grip(-0.5_2)1.5db_3	Edge of coupler	Brittle
	IC-M8-80-End Grip(-0.5_2)1.5db_4	Inside coupler	Brittle
	IC-M8-80-End Grip(-0.5_2)1.5db_5	Approx. 0.75d_b outside coupler edge	Brittle
	IC-M8-80-End Grip(-0.5_2)1.5db_6	Inside coupler	Brittle
Friction Welded-2 (MA)	IC-M8-80-Frictio Welded-2(-0.5_2)1.5db_1	At the friction weld on coupler side	Brittle
	IC-M8-80-Frictio Welded-2(-0.5_2)1.5db_2	At the friction weld on coupler side	Brittle
	IC-M8-80-Frictio Welded-2(-0.5_2)1.5db_3	At the friction weld on coupler side	Brittle
Threaed-2 (MA)	IC-M8-80-Threaded-2(-0.5_2)1.5db_1	Coupler edge (on threads)	Brittle
	IC-M8-80-Threaded-2(-0.5_2)1.5db_2	Coupler edge (on threads)	Brittle
	IC-M8-80-Threaded-2(-0.5_2)1.5db_3	Coupler edge (on threads)	Brittle
Taper Threaded-1 (MA)	IC-M8-80-Taper Threaded-1(-0.5_2)1.5db_1	Coupler edge (on threads)	Brittle
	IC-M8-80-Taper Threaded-1(-0.5_2)1.5db_2	Coupler edge (on threads)	Brittle
	IC-M8-80-Taper Threaded-1(-0.5_2)1.5db_3	Coupler edge (on threads)	Brittle
	IC-M8-80-Taper Threaded-1(-0.5_2)1.5db_4	Coupler edge (on threads)	Brittle
Swaged (MA)	IC-M8-80-Swaged(-0.5_2)1.5db_1	Approx. 0.25d_b outside coupler edge	Brittle
	IC-M8-80-Swaged(-0.5_2)1.5db_2	Approx. 0.25d_b outside coupler edge	Brittle
	IC-M8-80-Swaged(-0.5_2)1.5db_3	Approx. 0.25d_b outside coupler edge	Brittle
Threaded-1 (MA)	IC-M8-80-Threaded-1(-0.5_2)1.5db_1	Edge of coupler	Brittle
	IC-M8-80-Threaded-1(-0.5_2)1.5db_2	Edge of coupler	Brittle
	IC-M8-80-Threaded-1(-0.5_2)1.5db_3	Edge of coupler	Brittle

Table 4.8-Common fracture locations in mechanical splice specimens connecting (QST) Bars

Manufacturer (Bar type)	Mechanical splice specimen	Fracture location	Fracture plane
Grouted-1 (QST)	IC_Q8-80-Grouted-1(-0.5_2)1.5db1	Approx. 0.25d_b outside coupler edge	Ductile
Grouted-2 (QST)	IC-Q8-80-Grouted-2(-0.5_2)1.5db_2	Coupler edge	Ductile
Friction Welded-1 (QST)	IC-Q8-80-Friction Welded-1-(-0.5-2)-1.5db1	At the friction weld on coupler side	Brittle
	IC-Q8-80-Friction Welded-1-(-0.5-2)-1.5db2	At the friction weld on coupler side	Brittle
	IC-Q8-80-Friction Welded-1-(-0.5-2)-1.5db3	Coupler edge	Brittle
Grouted/Threaded (QST)	IC-Q8-80-Grouted/Threaded-(-0.5-2)-1.5db2	Approx. 0.25d_b outside coupler edge	Ductile
	IC-Q8-80-Grouted/Threaded-(-0.5-2)-1.5db6	Approx. 0.25d_b from coupler edge	Ductile
	IC-Q8-80-Grouted/Threaded-(-0.5-2)-1.5db7	Approx. 0.25d_b from coupler edge	Ductile
Taper Threaded-2 (QST)	IC-Q8-80-Taper Threaded-2(-0.5_2)1.5db_1	Edge of coupler (on threads)	Brittle
	IC-Q8-80-Taper Threaded-2(-0.5_2)1.5db_2	Edge of coupler	Ductile
	IC-Q8-80-Taper Threaded-2(-0.5_2)1.5db_3	Bar pullout	-
	IC-Q8-80-Taper Threaded-2(-0.5_2)1.5db_4	Edge of coupler	-
End Grip (QST)	IC-Q8-80-End Grip(-0.5_2)1.5db_1	Inside coupler	Ductile
	IC-Q8-80-End Grip(-0.5_2)1.5db_3	-	-
	IC-Q8-80-End Grip(-0.5_2)1.5db_4	Approx. 0.5d_b of the coupler	Ductile
	IC-Q8-80-End Grip(-0.5_2)1.5db_5	Inside Coupler	Ductile
	IC-Q8-80-End Grip(-0.5_2)1.5db_6	Inside Coupler	Ductile
Friction Welded-2 (QST)	IC-Q8-80-Friction Welded-2(-0.5_2)1.5db_1	At the friction weld on coupler side	Brittle
	IC-Q8-80-Friction Welded-2(-0.5_2)1.5db_2	At the friction weld on coupler side	Brittle
	IC-Q8-80-Friction Welded-2(-0.5_2)1.5db_3	At the friction weld on coupler side	Brittle
	IC-Q8-80-Friction Welded-2(-0.5_2)1.5db_4	At the friction weld on coupler side	Brittle
Threaded-2 (QST)	IC-Q8-80-Threaded-2(-0.5_2)1.5db_1	Coupler edge (on threads)	Brittle
	IC-Q8-80-Threaded-2(-0.5_2)1.5db_2	Coupler edge (on threads)	Brittle
	IC-Q8-80-Threaded-2(-0.5_2)1.5db_3	Coupler edge (on threads)	Brittle
Taper Threaded-1 (QST)	IC-Q8-80-Taper Threaded-1(-0.5_2)1.5db_1	Coupler edge (on threads)	Brittle
	IC-Q8-80-Taper Threaded-1(-0.5_2)1.5db_2	Coupler edge (on threads)	Brittle
	IC-Q8-80-Taper Threaded-1(-0.5_2)1.5db_3	Coupler edge (on threads)	Brittle
Swaged (QST)	IC-Q8-80-Swaged(-0.5_2)1.5db_1	Approx. 0.25d_b outside coupler edge	Ductile
	IC-Q8-80-Swaged(-0.5_2)1.5db_2	Approx. 0.25d_b outside coupler edge	Ductile
	IC-Q8-80-Swaged(-0.5_2)1.5db_3	Approx. 0.25d_b outside coupler edge	Ductile
Threaded-1 (QST)	IC-Q8-80-Threaded-1(-0.5_2)1.5db_1	Edge of coupler	Ductile
	IC-Q8-80-Threaded-1(-0.5_2)1.5db_2	Edge of coupler	Ductile
	IC-Q8-80-Threaded-1(-0.5_2)1.5db_3	Edge of coupler	Ductile

Figure 4-17-Brittle fracture plane on QST Threaded-1 specimen

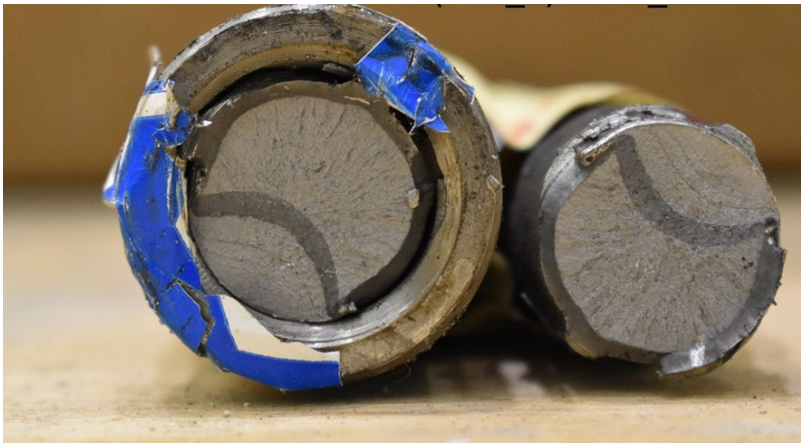

Figure 4-18-Brittle fracture plane on QST Taper Threaded-1 specimen

Figure 4-19-Brittle fracture plane on QST Friction Welded-2 specimen

Figure 4-20-Brittle fracture plane on QST Friction Welded-1 specimen

Figure 4-21-Coupler fracture in #11 (36mm) Grouted-1 mechanical splice specimen

4.2.2.5 Inelastic deformation across couplers

Surface targets attached to the coupler and to the reinforcing bar near the coupler edges were monitored using the DIC system throughout the tests to quantify inelastic deformations across the splice. Total splice deformation (Δ_{total}) was measured between targets on the bars adjacent to the couplers (targets 2 and 6 in Figure 3.8). Localized deformation components were separated as follows: slip between the coupler and the top bar (Δ_{ct}, between targets 2 and 3), slip between the

coupler and the bottom bar (Δ_{cb}, between targets 5 and 6), and deformation of the coupler body itself (Δ_c, between targets 3 and 5).

Representative deformation profiles are shown in Figure 4.23 (a) and Figure 4.23 (b) for End Grip and Taper Threaded-2 couplers on #8 (25mm) MA bars, which capture the range of observed behaviors respectively. Friction-welded devices were not included in this comparison, as they are essentially rigidly connected to the bar and therefore exhibit no slip between coupler and bars. The End Grip coupler displayed the largest deformations among all splice types, whereas the Taper Threaded-2 coupler exhibited the least.

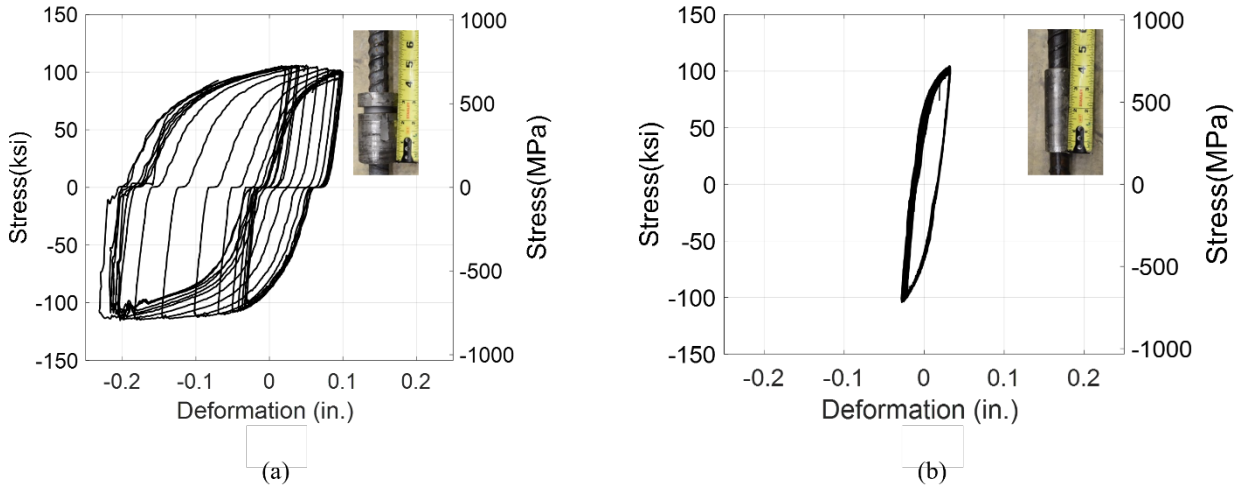

Figure 4-22- Representative deformation responses across couplers (measured between targets 2 and 6, Δ_{total}) for: (a) End Grip; and (b) Taper Threaded-2 on MA bars. (Note: 1 in. = 25.4 mm.)

Deformation measures are presented in for specimens tested in Phase 1 for #8 (25mm) mechanical specimens. Overall, the couplers could be categorized into two groups: those exhibiting limited slip and body deformation, and those exhibiting significant slip and/or body deformation (Table 4.9). For all splice types, body deformation (Δ_c) remained relatively small compared to slip deformations. Notably, Deformation magnitudes at the top and bottom interfaces differed considerably for most specimens, suggesting that slip during inelastic bar loading is generally more pronounced at one end of the coupler than the other.

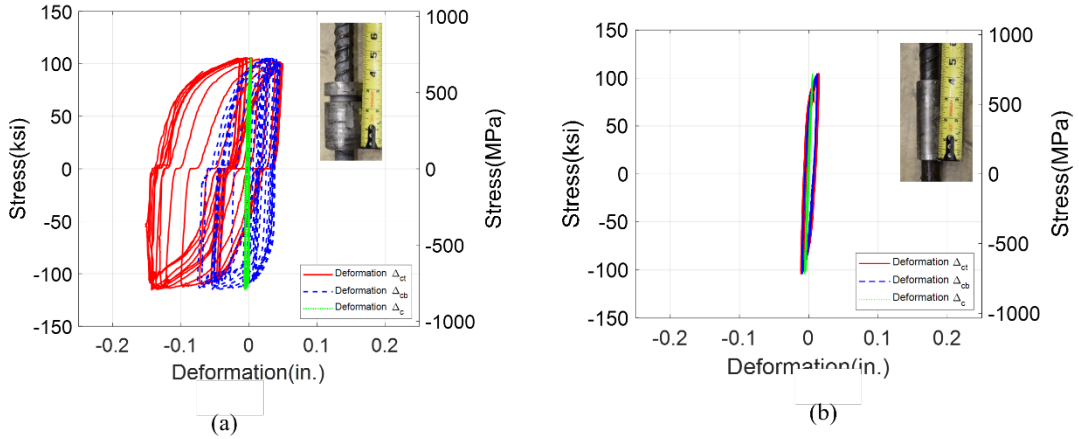

Figure 4-23-Representative deformation behavior of mechanical splices, with deformations across the top, bottom and coupler body highlighted: Δ_{ct}, Δ_{cb}, and Δ_{c}, respectively. (a) End Grip (b) Taper Threaded-2. (Note: 1 in.=25.4mm)

Table 4.9-Measured maximum deformations across #8 (25mm) mechanical splice specimens

Bar Type	Coupler	Δ_{ct}, in.(mm)	Δ_{cb}, in.(mm)	Δ_{c}, in. (mm)	Δ_{total}, in. (mm)
Micro-alloying (MA) bars	*Threaded-1*	0.040 (1.008)	0.042 (1.067)	0.008 (0.195)	0.084 (2.142)
	Swaged	0.065 (1.659)	0.030 (0.762)	0.028 (0.703)	0.107 (2.709)
	Taper Threaded-1	0.032 (0.819)	0.028 (0.718)	0.009 (0.222)	0.065 (1.664)
	Threaded-2	0.042 (1.067)	0.039 (0.991)	0.007 (0.178)	0.084 (2.142)
	Friction Welded-2	0.013 (0.330)	0.018 (0.449)	0.009 (0.229)	0.033 (0.821)
	End Grip	0.0682 (1.732)	0.053 (1.338)	0.005 (0.132)	0.107 (2.725)
	Taper Threaded-2	0.017 (0.432)	0.016 (0.394)	0.007 (0.178)	0.031 (0.781)
	Grouted/Threaded	0.065 (1.643)	0.165 (4.199)	0.014 (0.356)	0.227 (5.757)
	Friction Welded-1	0.010 (0.262)	0.013 (0.339)	0.010 (0.254)	0.028 (0.711)
	Grouted-2	0.086 (2.193)	0.089 (2.252)	0.018 (0.457)	0.186 (4.733)
Quenched and Self-tempered (QST) bars	*Threaded-1*	0.063 (1.592)	0.454 (11.532)	0.007 (0.195)	0.513 (13.030)
	Swaged	0.172 (4.377)	0.029 (0.745)	0.018 (0.457)	0.207 (5.275)
	Taper Threaded-1	0.050 (1.278)	0.034 (0.864)	0.007 (0.178)	0.085 (2.167)
	Threaded-2	0.060 (1.516)	0.056 (1.422)	0.006 (0.161)	0.118 (2.980)
	Friction Welded-2	0.014 (0.362)	0.017 (0.438)	0.009 (0.229)	0.035 (0.883)
	End Grip	0.752 (19.11)	0.052 (1.321)	0.004 (0.112)	0.778 (19.761)
	Taper Threaded-2	0.015 (0.389)	0.218 (5.546)	0.007 (0.186)	0.136 (3.463)
	Grouted/Thread	0.0425 (1.079)	0.0496 (1.257)	0.011 (0.292)	0.096 (2.451)

	Friction Welded-1	0.0135 (0.343)	0.0562 (1.422)	0.009 (0.241)	0.068 (1.752)
	Grouted-2	0.112 (2.853)	0.1691 (4.301)	0.076 (1.938)	0.237 (6.028)

In addition, the relatively high scatter in deformation responses among specimens of the same splice type highlights the complex factors influencing the inelastic cyclic performance of mechanical splices.

4.3 Pre-Qualification Testing Recommendations for Mechanical Splices in Hinge Regions

The study recommends the following pre-qualification testing for mechanical splices that are intended for use in seismic hinge regions. These recommendations are based on observed performance under monotonic and low-cycle fatigue tests, and are aimed at ensuring adequate strength, ductility, and fatigue resistance consistent with the demands placed on longitudinal reinforcement in special seismic members.

4.3.1 Monotonic Tension Testing

4.3.1.1 Test Protocols

- Monotonic tension tests should be conducted on mechanical splices to confirm that they can develop both strength and elongation requirements.
- Tension testing should be carried out until specimen fracture.
- Strains on mechanical splices during monotonic tests should be measured over 8 in. (200 mm) gage lengths on both connecting bars. The gage lengths should be located at least $2d_b$ away from the disturbed zones, namely the machine grips and the coupler edges.

4.3.1.2 Acceptance Criteria

Mechanical splices used in seismic hinge regions should be able to reliably transfer tensile forces while maintaining ductility comparable to the ductility of the bars they connect.

- STRENGTH: mechanical splices should develop at least the specified minimum tensile strength of the bars they couple. Several mechanical splice devices were able to achieve this performance criterion in the study.
- DUCTILITY: mechanical splices should achieve a uniform strain level in the bars that is at least the specified elongation capacity of the bars, as specified in ASTM A706 Supplement 1. Several mechanical splice devises were able to achieve this performance criterion in the study.
- Any specimen that fractures at or near the machine grip should be excluded from results.

4.3.2 Low-Cycle Fatigue Testing

4.3.2.1 Test Protocols

- Low-cycle fatigue tests should be conducted to ensure that splices exhibit adequate performance under reversed inelastic strain demands representative of demands in seismic hinge regions.
- A fully reversed strain amplitude of 2.5% (+2% in tension and -0.5% in compression) was found to be effective for qualification and representative of demands in hinge regions of special seismic members.
- Low-cycle fatigue tests should be conducted with a clear bar gripping span equal to 1.5 to 2 times the bar diameter ($1.5d_b$ to $2.0d_b$), with identical spans used at both ends of each specimen to maintain symmetry. The short griping span is advised to mitigate specimen buckling during testing. A short gripping span was found to preclude the need for lateral bracing for most splice specimens. Avoiding lateral bracing facilitates testing.
- The use of lateral bracing can be used to mitigate lateral buckling of specimens and ensure stability under cyclic loading. The bracing system should not introduce forces in the longitudinal directions of the splice specimens.
- Low-cycle fatigue tests should be conducted under a closed-loop strain-controlled loading protocol. The average strain measured across the two clear bar spans on either side of the coupler should serve as the feedback signal to the loading controller. Measuring strain

directly on bars is essential to eliminate erroneous reading due to slip in the machine grips and the coupling system.

4.3.2.2 Acceptance Criteria

- During low-cycle fatigue testing, performance should be evaluated by recording both the mean number of half-cycles to fracture and the number of half-cycles at which the specimen strength reduces to 80% of its peak strength. The former metric provides the primary measure of fatigue life, while the latter metric serves as an indicator of strength degradation prior to failure.
- The required minimum number of half-cycles to fracture may be set to match the performance of companion bare bars tested under the same conditions, since several splice types demonstrated the ability to achieve this threshold.
- A lower requirement of mean half-cycles to fracture may be acceptable when supported by satisfactory performance in special structural members. Based on the results of the wall testing program presented in *Part II Wall test* of this study, a mean half-cycles to fracture life of approximately 60 half-cycles provides a justified lower bound threshold for qualification.
- Any specimen that fractures at or near the grip should be excluded from results.

4.3.3 Specimen Preparation

1. Aluminum swaging is recommended around the bars at machine grips to reduce stress concentrations and fracture at the grips.
2. Bars outside the coupler device should not be modified.
3. Each coupler–bar combination, including different bar sizes, grades, and steel manufacturing processes, should be tested. Companion bare bar specimens from the same batch and heat should be tested to provide as a baseline performance for comparison with splice specimen performance.

PART II
WALL TESTING

5 Wall Experimental Program

5.1 Introduction

Four full-scale rectangular walls were subjected to reversed cyclic displacements and compressive axial load in this experimental program. The objectives of this study were: 1) to evaluate the performance of mechanical splices in hinge regions where relatively large reversed inelastic strain demands occur, 2) to explore correlations between in-air test performance and in-concrete test performance of mechanical splices, and 3) to help set a minimum in-air inelastic cyclic performance requirement for mechanical splices used in the hinge regions based on acceptable performance in walls.

The first test was dubbed the control wall and did not have splices along the longitudinal bars. All other walls had all their boundary longitudinal bars spliced using mechanical couplers at 2.5 in. (63 mm) above the top of footing where strain demands and effects of cyclic loading were most severe. The mechanical coupler types used in the walls were tested in-air in a testing machine under inelastic cyclic loading (*Part I In-Air Testing)*. The couplers were selected from the in-air testing program and consisted of taper-threaded, friction welded, swaged-threaded, grouted, and end grip. In each wall with mechanical couplers, the coupler type was different in each boundary region to allow for testing of more coupler types. In addition to that, the longitudinal bars of the boundary region were sourced from the same two batches used in the in-air tests and consisted of #8 (25mm) grade 80 (550 MPa) A706 bars that were produced either using a quenching and self-tempering (QST) or micro-alloying (MA) process. By using the same steel batches in-air and in-concrete, the variability in bar mechanical and fatigue properties was thus controlled in the study.

5.2 Test Matrix

5.2.1 Fixed Parameters

To allow for more direct comparison between the hinge region performance of the various mechanical couplers, the following wall parameters were fixed for all wall tests:

1. Wall dimensions

The length of the wall specimen was 84 in. (2133.6 mm), and the height was 204 in. (5181.6 mm) from top of footing to centerline of actuators. The thickness of the wall specimens was 16 in. (406.4 mm).

2. Concrete compressive strength

The same concrete design mix was used in all wall specimens. The specified concrete strength of the mix was 6 ksi (41.37 MPa). Based on the historic mix performance, the expected concrete strength was about 8ksi (55.16 MPa).

3. Longitudinal and web reinforcement

All walls used grade 80 (550 MPa) A706 longitudinal reinforcing bars. The specified yield strength of steel was 80 ksi (551.2 MPa). The boundary regions contained 7#8 (25 mm) grade 80 (550 MPa) A706 longitudinal bars produced either by micro-alloying and quenching and self-tempering process. The web had two curtains of #5 (16mm) vertical and horizontal bars produced by the quenching and self-tempering process spaced at 9 in. (228.6 mm) center to center. The web also contained #5 (16mm) cross-ties with seismic hooks at both ends as required by ACI 318-19.

In all four walls, MA bars were taken from the same batch of steel, while QST #8 (25 mm) bars were taken from the same batch and QST #5 (16 mm) bars were also taken from the same batch. This was done to minimize the effects of variability in bar strength and low-cycle fatigue performance on study outcomes. In this way, more direct comparisons could be made between the low-cycle fatigue performance of mechanical splices

4. Boundary transverse reinforcement

The boundary transverse reinforcement consisted of #5 (16 mm) hoops with 135-degree hooks alternating positions along wall height. The hoops were spaced at 4.5 in. (114.3 mm) center to center. Seismic cross ties with 135-degree hooks spaced at 4.5 in (114.3 mm) center to center were also placed in the boundary regions. The transverse web reinforcement consisted of 2#5 (16 mm) horizontal ties at 9 in. (228.6 mm) spacing center to center. The web also contained crossties with 135-degree hooks on both sides as required by ACI 318-19[9] for special structural walls up to a

wall height of 91 in. (2311.4 mm). Above that level crossties had alternating 90 degrees, and 135-degree hooks up to a height of 101 in. (2565.4 mm).

5. Axial load

A compressive axial load of 350 kips (1556.87 KN) was targeted which corresponds to 3.5 % axial load ratio based on the expected concrete compressive strength of concrete of 8ksi (55.16 MPa) for wall specimens.

6. Location of couplers

All the mechanical couplers used in this study were located at 2.5 in. (63 mm) from the top of the footing.

5.2.2 Variable Parameters

This study focused on varying the coupler types and the manufacturing process of the grade 80 (550 MPa) A706 longitudinal bars in the boundary regions. Boundary reinforcement consisted of 7#8 (25mm) grade 80 (550Mpa) A706 micro-alloying or quenching and self-tempering longitudinal bars. Table 5.1 summarizes the coupler types and bar manufacturing processes used in the wall boundaries. Photos of the coupler types used in the wall are presented in Figure 5.1.

Table 5.1: Mechanical coupler details

Wall Test	North					South				
	Bar Size (mm)	**Bar Manuf. Process**	**Mechanical Coupler Type***	**Coupler Dia., in. (mm)**	**Coupler Length, in. (mm)**	**Bar Size (mm)**	**Bar Manuf. Proc.**	**Mechanical Coupler Type***	**Coupler Dia., in. (mm)**	**Coupler Length, in. (mm)**
Control Wall	#8 (25.4 mm)	QST	-		-	#8 (25.4 mm)	MA	-		-
Wall 2	#8 (25.4 mm)	QST	Friction welded-2	1.5 (38.08 mm)	3.75 (95.25 mm)	#8 (25.4 mm)	MA	Taper threaded-2	1.5 (38.08 mm)	3.0 (76.2 mm)
Wall 3	#8 (25.4 mm)	QST	Swaged	2.0 (50.8 mm)	13.0 (330.2 mm)	#8 (25.4 mm)	MA	Grouted-2	2.0 (50.8 mm)	13.5 (342.9 mm)
Wall 4	#8 (25.4 mm)	MA	Friction welded-2	1.5 (38.08 mm)	3.75 (95.25 mm)	#8 (25.4 mm)	MA	End-grip	2.5 (62.5 mm)	3.0 (76.2 mm)

* Mechanical coupler naming is based on coupling mechanism *Part I In-Air Testing*.

Figure 5-1: Photos of couplers used in walls starting from left: a) Friction welded-2, (b) Grouted-2, (c) End Grip, (d) Swaged, and e) Taper-threaded-2

5.3 Wall Reinforcing Details

Figure 5.2 to Figure 5.6 show the elevation, reinforcement layouts and sections of the four walls. Wall specimens had an overall height of 252 in. (6400 mm) from bottom of footing to top of top beam. More detailed drawings of the specimens and reinforcement layouts at presented in Detailed Drawing and Reinforcement Layouts. Lateral loads were applied at 204 in. (5182 mm) above the top of footing. The walls were 84 in. (2134mm) long having a span to section depth ratio of 2.43 and a 16 in. (406.4 mm) thickness. A concrete clear cover to transverse reinforcement of 1.5 in. (38.01 mm) was selected to achieve a minimum clear cover of 0.75 in. (19 mm) around the couplers. All longitudinal and transverse reinforcement bar bend diameters satisfied ACI 318-19 bend diameters. Table 5.2 summarizes the wall boundary reinforcement details.

Table 5.2: Summary of wall boundary reinforcement details

	Control Wall	Wall 2	Wall 3	Wall 4
Longitudinal reinforcement (Boundary region)	7#8 ρ_l = 2.13%	7#8 ρ_l = 2.13%	7#8 ρ_l = 2.13%	7#8 ρ_l = 2.13%
Transverse reinforcement (Boundary region)	3 legs #5 @4.5in 4.5d_b ρ_t=1.29%	3 legs #5 @4.5in 4.5d_b ρ_t=1.29%	3 legs #5 @4.5in 4.5d_b ρ_t=1.29%	3 legs #5 @4.5in 4.5d_b ρ_t=1.29%

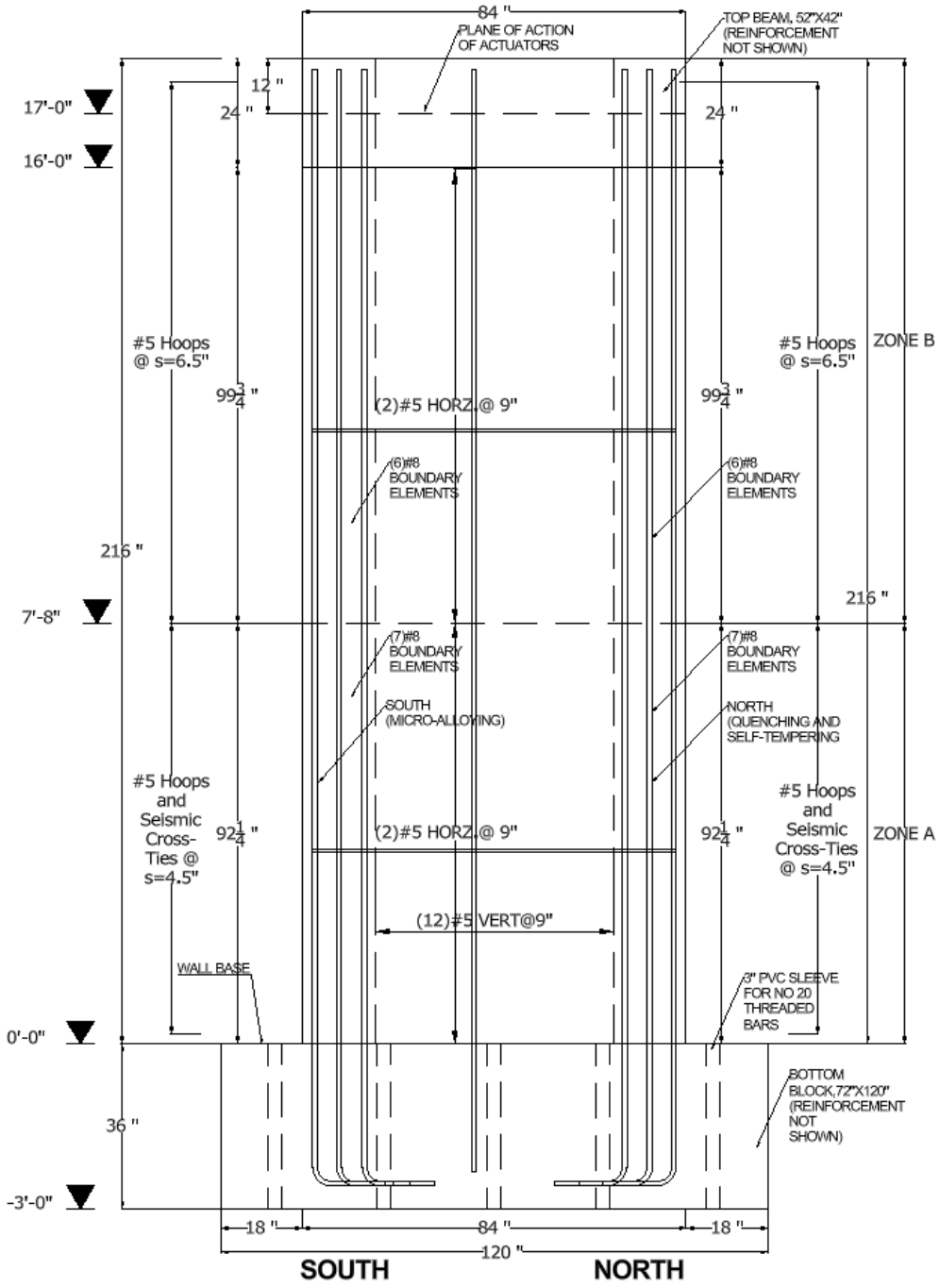

Figure 5-2: Control wall elevation and reinforcement layout (1in.=25.4mm)

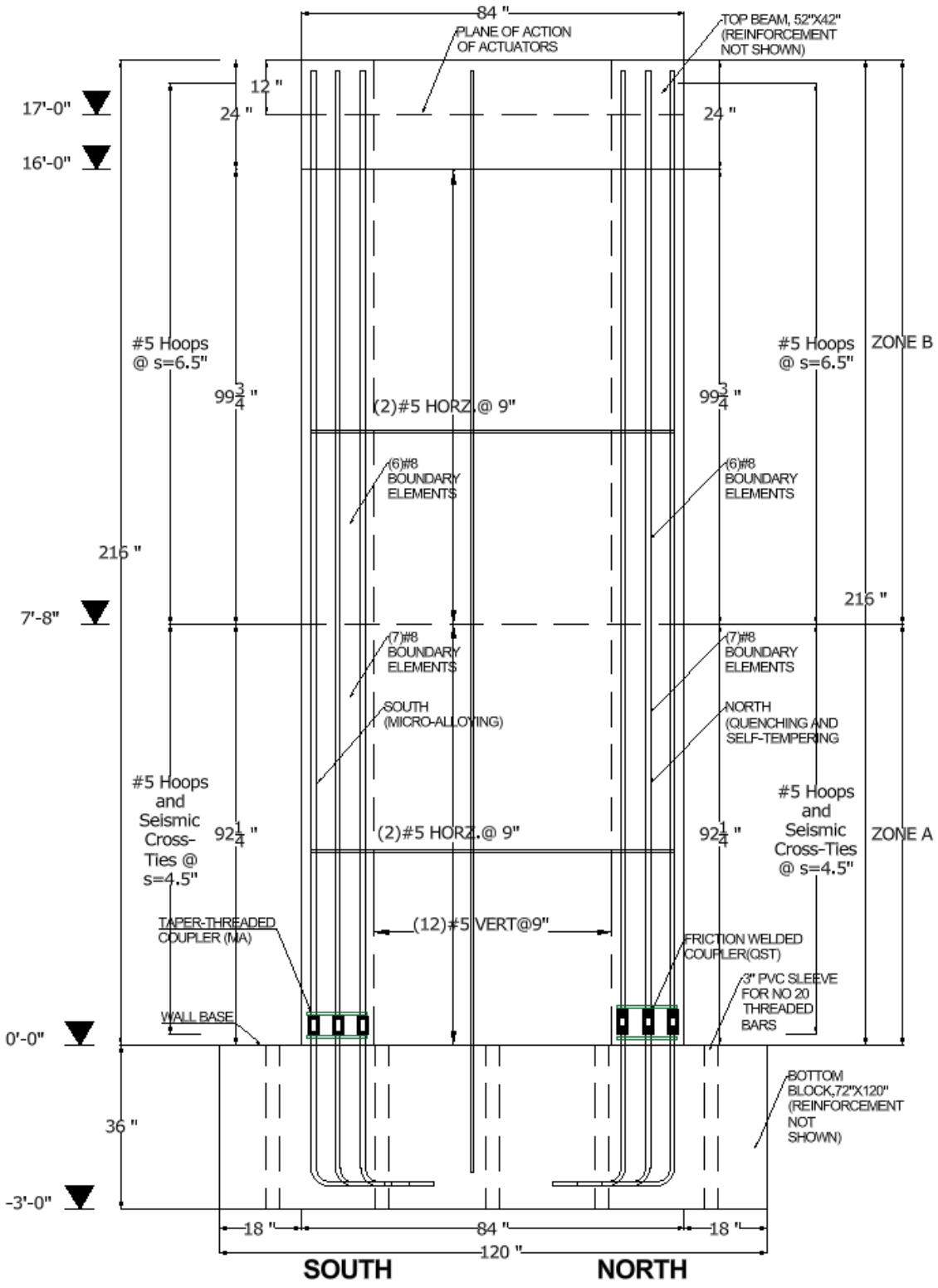

Figure 5-3: Wall 2 elevation, reinforcement layout and mechanical splice in boundary region

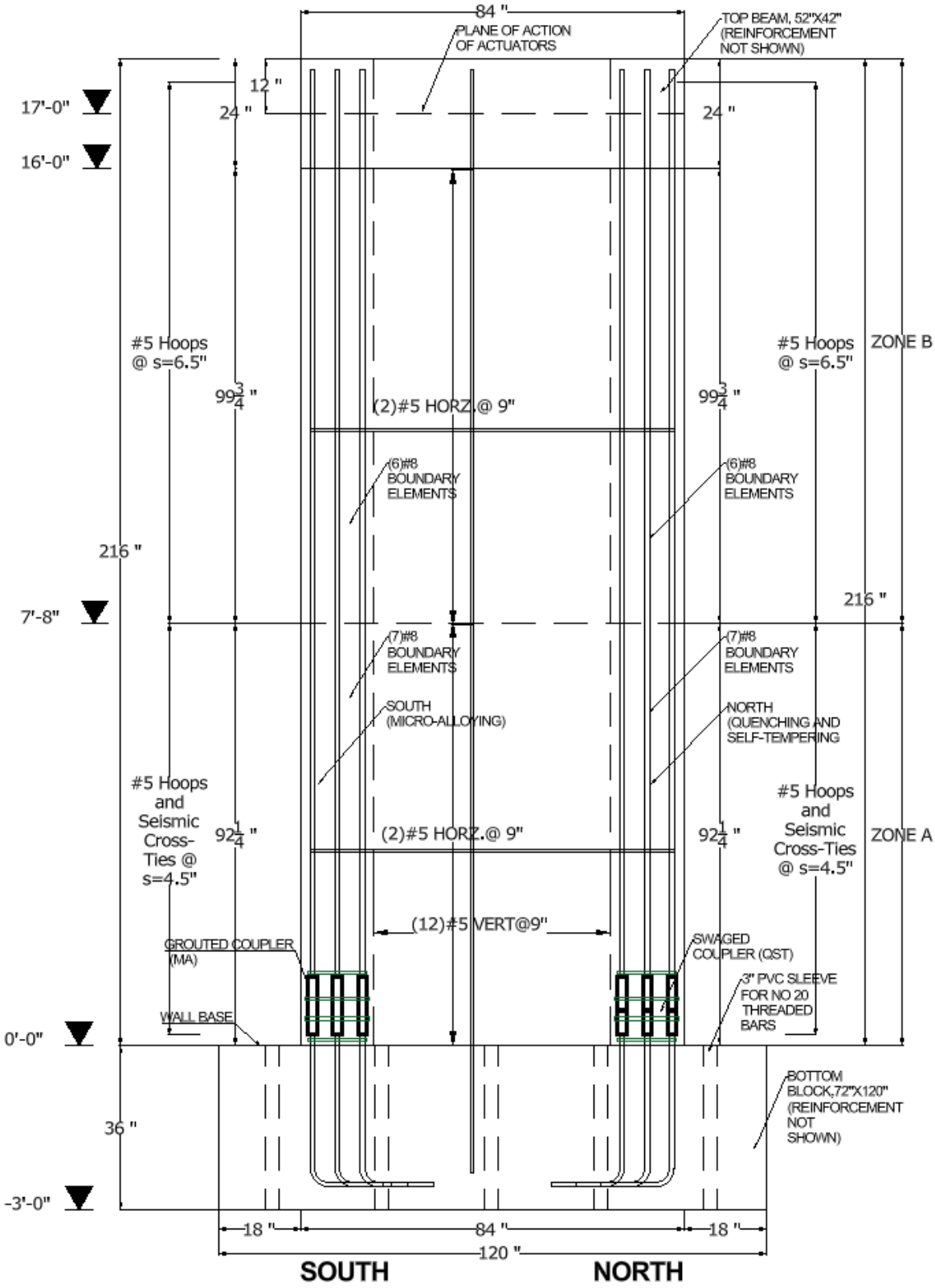

Figure 5-4: Wall 3 elevation, reinforcement layout and mechanical splice in boundary region

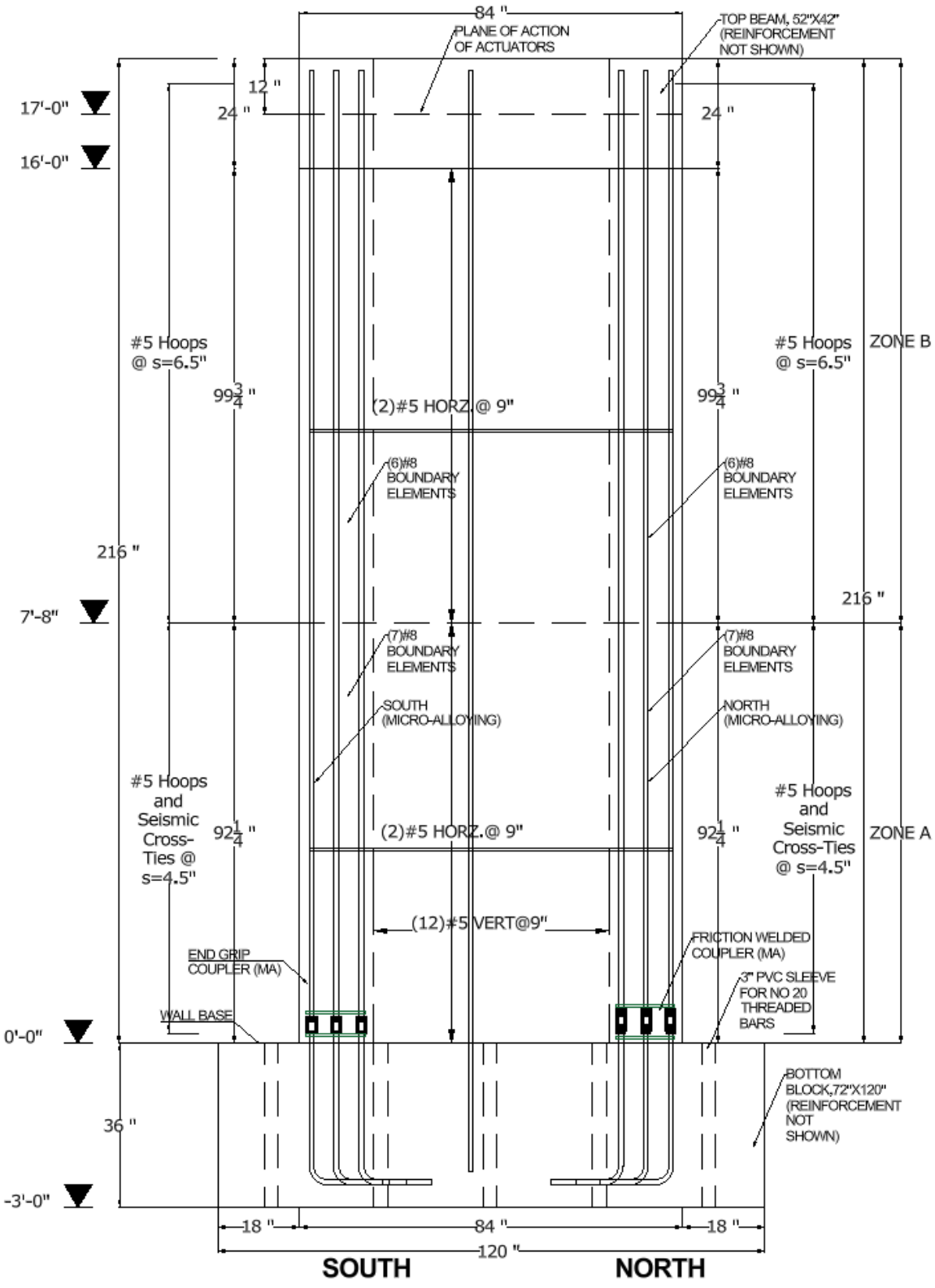

Figure 5-5: Wall 4 elevation, reinforcement layout and mechanical splice in boundary region

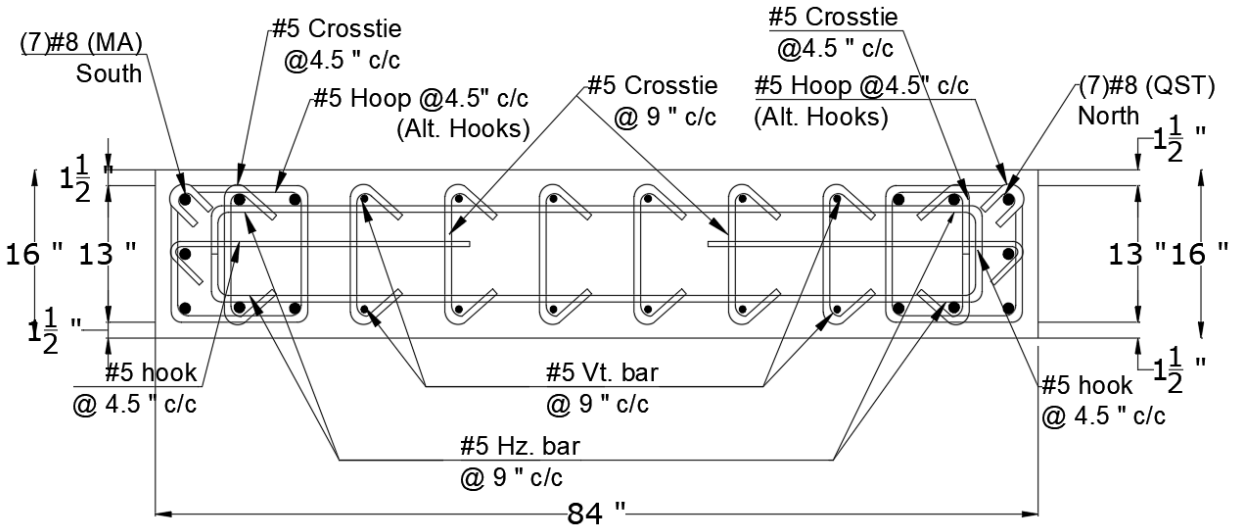

a) Control wall boundary region details at splice

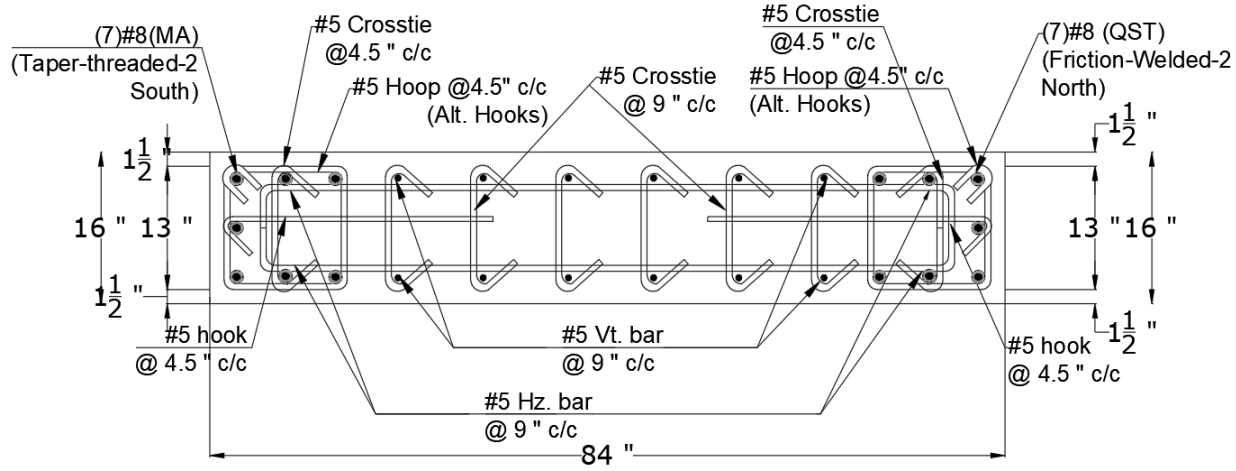

b) Wall 2 boundary region details at splice

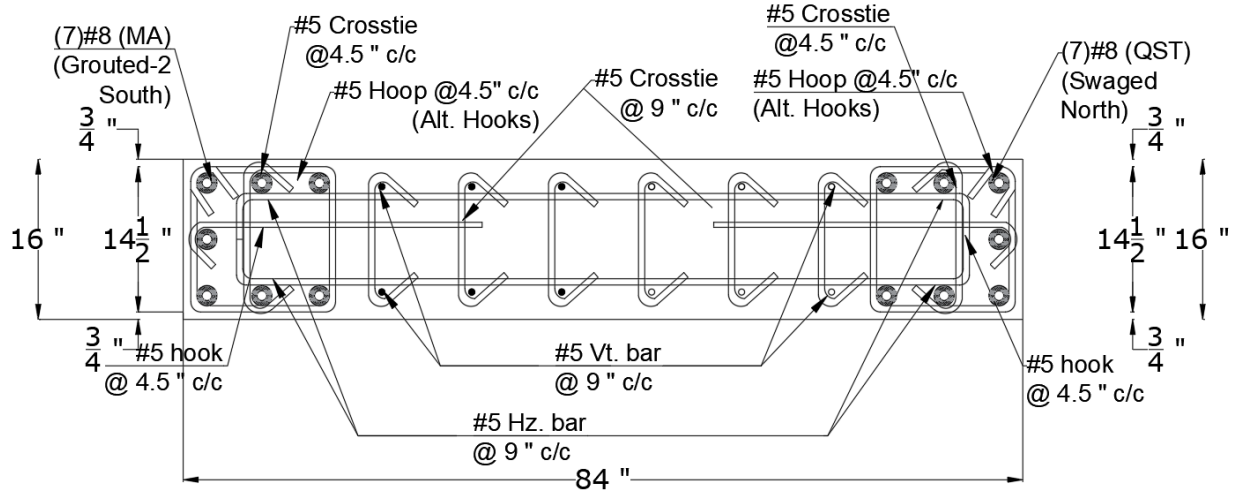

c) Wall 3 boundary region details at splice

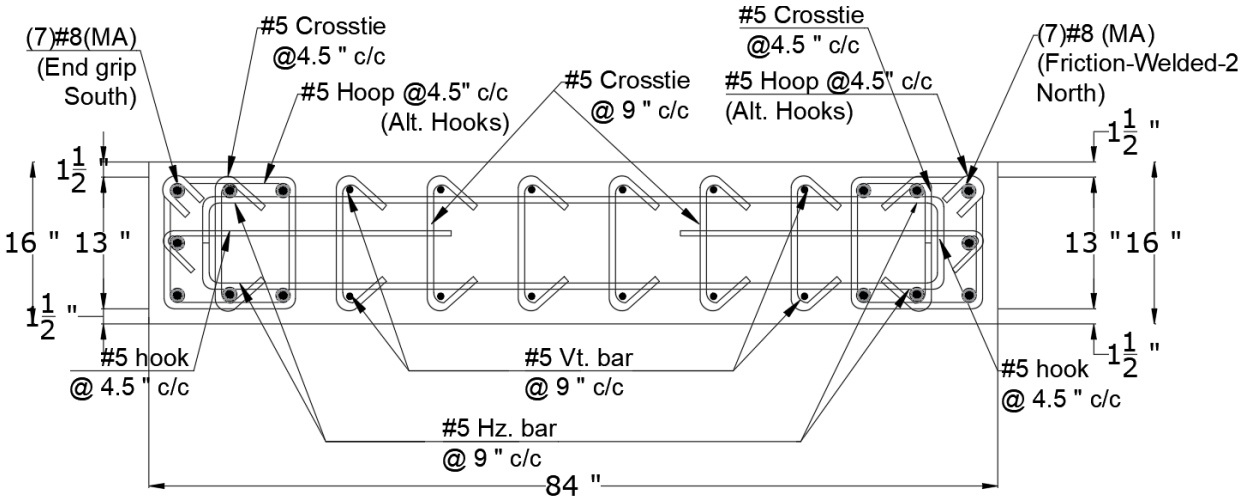

d) Wall 4 boundary region details at splice

Figure 5-6: Confined boundary elements for wall specimens (1 in.=25.4 mm, 1ft =305 mm)

5.4 Specimen Design

Walls were designed to impart large strain demands on the longitudinal bars and mechanical couplers in the plastic hinge region. The walls satisfied ACI 318-19(Institute, 2019) design and detailing requirements for special structural walls. A constant compressive axial load of 350 kips (1568 KN) was targeted for application to the walls. This axial load corresponds to an axial load ratio of about 3.5% applied to rectangular walls. The axial load ratio is defined here as axial load

divided by the product of gross sectional area and measured concrete compressive strength. Wall specimens were designed and tested at full-scale. To fit within the laboratory strength limits, the target design ultimate lateral strength of walls was 350 kips (1568 KN), which corresponds to a target moment strength at the base of wall of 5950 kip-ft (8126.23 KN-m). A shear demand of $3.0\sqrt{f_c'}$ in psi units ($0.023\sqrt{f_c'}$ in MPa units) was therefore targeted in the study.

The axial load versus ultimate moment strength diagram (P-M diagram) is given for the walls in Figure 5.7. The ultimate moment strength of the walls, M_u, was calculated using an expected concrete strength of 7.5 ksi (51.45 MPa) from measured properties of concrete, 1.15 times the expected yield strength of the longitudinal bars (f_{yE}=83.9 ksi for MA bars, f_{yE}=88.4 ksi for #8 (25mm) QST bars, and f_{yE} =88.4 ksi for #5 (16mm) QST bars , from Table 5.5). At an axial load of 350 kips (1556.87 KN), M_u was estimated to be 5780.83-ft (KN-m), which corresponds to the applied lateral force of 339.64 kips (1510.38 kN). Shear friction strength per ACI 318-19 at the base of the wall was calculated to be 816.46 kips (3631.78 kN). Sliding at the base of the wall was not expected.

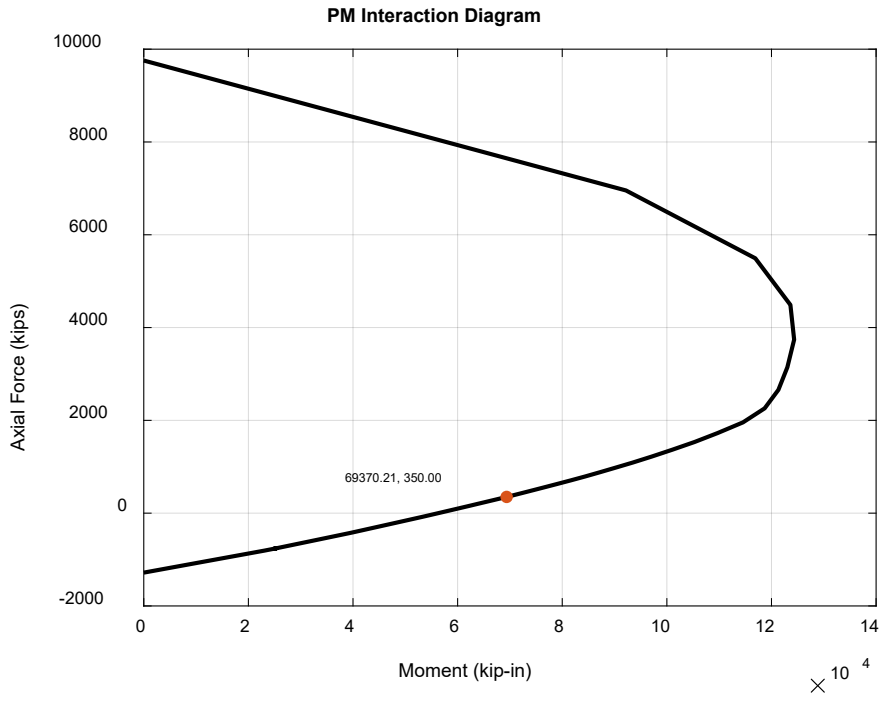

Figure 5-7: Ultimate moment versus axial load interaction diagram (Mu)

(1 kips = 4.45 kN, 1 kip-in. = 0.113 kN-m)

5.5 Specimen Construction

Walls were cast in an upright position in two staged following a typical construction sequence. The bottom footing, wall and top beam cages were tied separately (Figure 5.8). The footing cage was placed in forms along with the PVC pipes that created the holes necessary to post-tension the footing to the strong floor (also shown in Figure 5.8). The wall cage was then inserted into the footing cage and levelled and centered before the footing was cast as shown in Figure 5.8. The interface between the wall and footing was then roughened to a least a ¼ in. (6.35 mm) amplitude. The footing was allowed to be cured for several days before the wall and top beam were cast. In all walls, the top beam was formed and cast with the wall. The top beam contained eight horizontal PVC pipes to create holes for attaching the actuators to the specimens. At least 28 days were allowed to elapse from the day of the casting before each wall was tested, except for Wall 4. Only 14 days, elapsed from wall casting to testing for Wall 4. Concrete cylinders were prepared for each cast and stored near the specimens in laboratory conditions.

Figure 5-8: Wall casting process

5.6 Material Properties

5.6.1 Concrete

The concrete mix had a specified compressive strength of 6 ksi (41.37 MPa) and a 6 in. (152.4 mm) slump. Mix design quantities are presented in Table 5.3.

Table 5.3: Concrete mix design quantities

MATERIAL	**DESIGN QUANTITIES**
STC Type I/II	**500 lb/yd^3**
Fly ash- Class C	**158 lb/yd^3**
Limestone Sand(85%)	**1108 lb/yd^3**
Silica Sand (15%)	**199 lb/yd^3**
3/4" aggregate (limestone)	**1775 lb/yd^3**
Water	**30 gal/yd^3**
ADMIXTURES	
Plastocrete C494 Type A	**19.7 lb/yd^3**
Plastiment C494 Type D	**19.7 lb/yd^3**
ADVA 190 C494 Type F	**32.9 lb/yd^3**

Cylinders with a 4 in. (101.6 mm) diameter were prepared for each cast and stored near the specimens to cure in the same environmental conditions. Concrete cylinders were removed from the plastic cylinders the same day the formwork was removed for each test. Concrete cylinders were tested in compression on 7, 14, 28 and the day of testing. Testing was conducted in accordance with ASTM C39-C39M as shown in Figure 5.9. Concrete compressive strength on day of testing are presented in Table 5.4.

Figure 5-9: Slump test and concrete test as per ASTM C39

Table 5.4: Concrete compressive strengths of walls on day of testing

	Cylinder 1 ksi (MPa)	Cylinder 2 ksi (MPa)	Cylinder 3 ksi (MPa)	Average ksi (MPa)
Control Wall	7.95 (54.81)	7.25 (49.99)	7.96 (54.88)	7.72 (53.23)
Wall 2	7.25 (49.99)	7.96 (54.88)	7.59 (52.33)	7.60 (52.40)
Wall 3	7.0 (48.27)	7.5 (51.56)	7.0 (48.43)	7.17 (49.42)
Wall 4	7.32 (50.46)	7.4 (51.02)	7.80 (53.75)	7.51 (51.75)

5.6.2 Reinforcing Steel

5.6.2.1 Tensile Properties

Sample reinforcing bars used in wall specimens were tested monotonically in tension to fracture in accordance with ASTM A370(ASTM A370-22, 2022). Walls were reinforced with grade 80 (550 MPa) A706 bars from different manufacturers(ASTM Standard A706/A706M-24, 2024). All bar satisfied the ASTM A706 supplement 1 requirements (S1): Low-Alloy Steel Deformed Bars for Seismic Applications. Manufacturer 1 produces the bars mainly through a micro-alloying process while Manufacturer 2 achieved higher strength mainly through a quenching and self-tempering process. Transverse bars were grade 80 A706 as well and sourced from the mill using the quenching and self-tempering process. In all four walls, MA bars in all four walls were taken

from the same batches of steel, while QST #8 (25 mm) bars were taken from the same batch and QST #5 (16 mm) bars were also taken from the same batch.

The stress versus strain response of the bars was recorded during each monotonic tension test. Stresses were calculated as the applied force divided by the nominal bar area. Strains used to generate stress-strain relations were measured over an 8 in. (203.2 mm) gauge length as specified in ASTM A370(ASTM A370-22, 2022). For bars that exhibit a distinct yield plateau, the yield strength and strain at the elastic limit were taken at the visible end of linear response. The yield strength and strain at the elastic limit was calculated using the 0.2% offset method ASTM E8/E8M for the bars that did not exhibit distinct yield plateau (ASTM E8/E8M-22, 2022). The modulus of elasticity was measured as the slope of the initial elastic region of the stress-strain curve between stresses of 20% f_{ye} and 60% f_{ye}. The ultimate tensile strength was measured as the maximum stress recorded in a test. The tensile to yield strength ratio (T/Y ratio) was taken as the ratio of the ultimate tensile strength to the yield strength. Uniform strain is defined as the strain reached at the tensile strength and immediately prior to the initiation of necking. Uniform elongation strain was determined per ASTM (ASTM E8/E8M-22, 2022)s. Fracture elongation strain was measured as the largest measured strain prior to fracture and therefore includes both the plastic and elastic components of strain. Bar testing results and material properties obtained are summarized in Table 5.5. Stress strain relationships for #8 (25 mm) QST bars, #5 (16 mm) QST bars, and #8 (25 mm) MA bars are shown in Figure 5.10.

Table 5.5: Tension test results averaged over a minimum of three tests per bar type from Part I In-Air testing

Manuf. process (Batch)	Bar Size	Yield Strength, ksi (MPa) [COV]	Tensile Strength, ksi (MPa) [COV]	Tensile /yield strength ratio [COV]	Elastic Modulus ksi (MPa) [COV]	Uniform strain, % [COV]	Fracture strain, % [COV]
QST (QTB1)	#8 (25 mm)	88.4(613.9) [1.18%]	114.7(790.3) [0.31%]	1.29 [0.77%]	25,300(174,317) [5.57%]	8.0 [3.19%]	12.1 [4.13%]
QST	#5 (16 mm)	88.4(609.3) [0.48%]	112.6(777.1) [0.23%]	1.29 [0.56%]	28,140(194,000) [4.20%]	7.2 [7.3%]	11.1 [13.6%]
MA (MAB1)	#8 (25 mm)	83.9(578.1) [0.91%]	111.6(768.9) [1.29%]	1.33 [0.77%]	26,700(183,963) [8.06%]	9.72 [2.14%]	16.4 [2.47%]

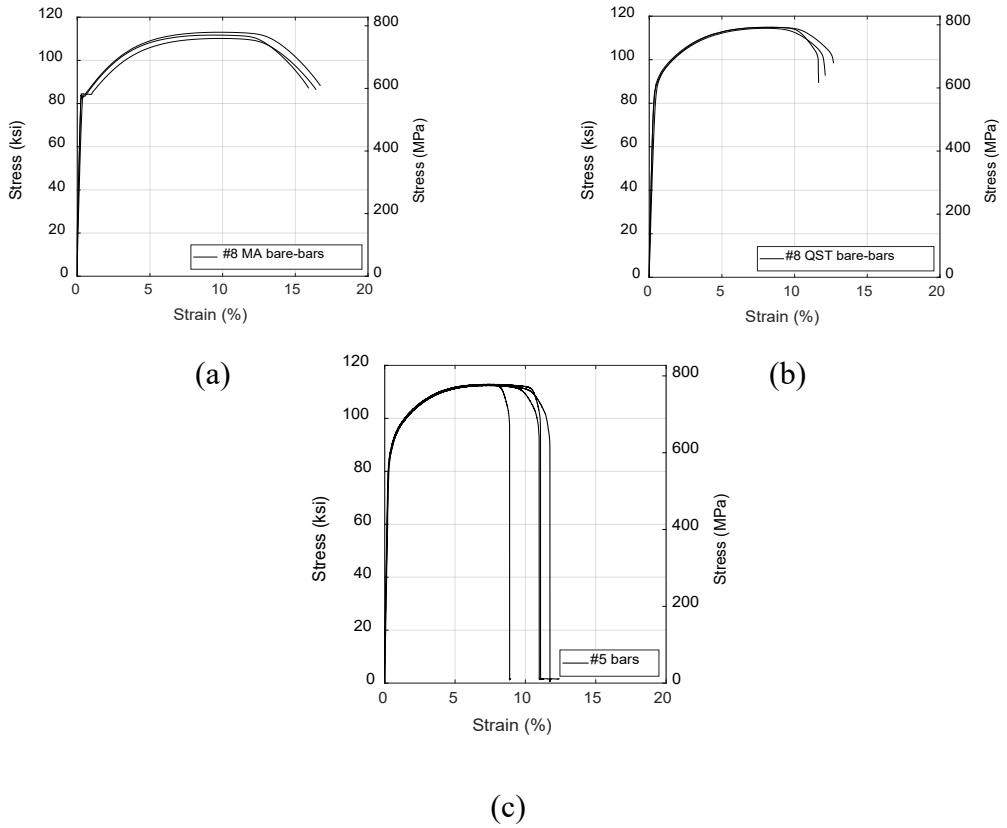

Figure 5-10: Stress strain relationships for #8 (25mm) MA and QST bars and #5 (16mm) QST bars from monotonic tension tests adapted from Part I In-Air testing

5.6.2.2 Low-cycle Fatigue Properties

To obtain the low-cycle fatigue life of bars, bar specimens were tested under reversed inelastic strain demands as described in (Ghannoum & Slavin, 2016; Sharma et al., 2025). The strain amplitude used in the tests was from +2% strain in tension to -0.5% strain compression. The clear gripping span between machine grips was 3 bar diameters. Bars were cycled until the fracture. Strains were measured during testing using a DIC system(Sokoli et., 2014), which monitored the location of two targets placed at edge of the top and bottom machine grips (Figure 5.11). The DIC system(Sokoli et., 2014) continuously provided strain readings to the testing machine, which controlled the crosshead movement under strain control. The number of half-cycles to fracture or to a strength drop to 80% of peak were recorded. Table 5.6 summarizes test results for each bar type during inelastic cyclic testing.

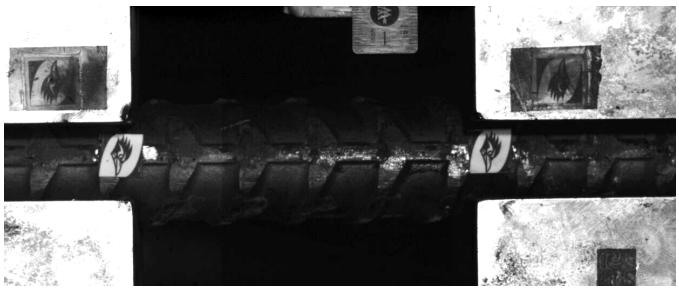

Figure 5-11: Bar sample with paper targets used to monitor strain during a low-cycle fatigue test

Table 5.6: Mean half cycles to fracture or to 80% of peak strength, from Part I In-Air testing

Failure criteria	**Mean half-cycles to fracture**		**Number of tested samples [N]**		**COV %**	
	QST	**MA**	**QST**	**MA**	**QST**	**MA**
Fracture	206.7	173.6	3	3	14.49	5.47
80% of peak strength	172.3	173.6			11.15	5.47

5.6.3 Mechanical Splices

5.6.3.1 Tensile Properties

Mechanical splices were tested under monotonic tension loading until the fracture of the bars. For monotonic tension tests, bar strain was measured using the DIC system over an 8 in. (200 mm) gauge length along the two bare bar segments surrounding a coupler (shown in Figure 5.12). Target pairs [1,2] provided the top gauge strain, and pair [5,6] the bottom gauge strain. Additionally, targets [3, 4] were placed to monitor slip between couplers and bars. Table 5.7summarizes the results from monotonic tension test results for mechanical splices on QST and MA #8 (25mm) bars.

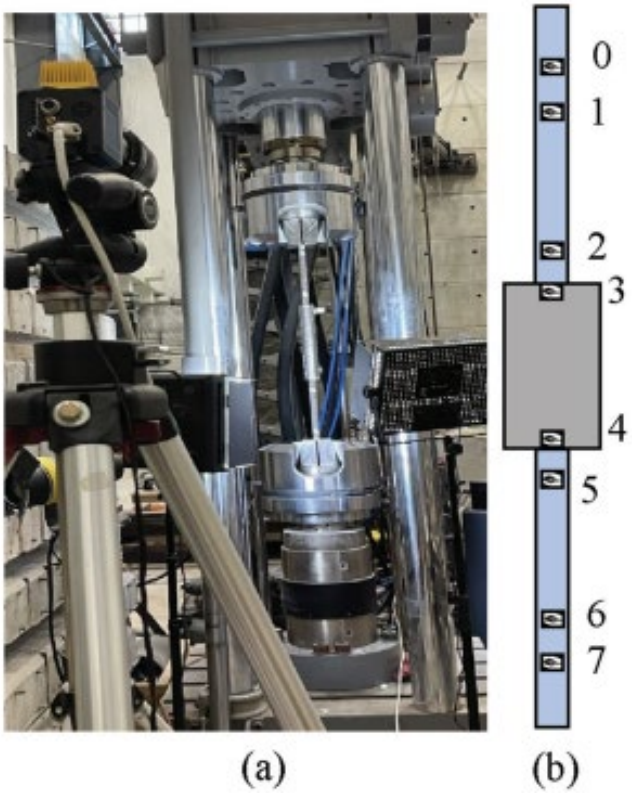

Figure 5-12: (a) Mechanical splice specimen installed in uniaxial testing machine; and (b) typical surface target layout and their numbering along coupled specimens during monotonic tension tests, adapted from Part I In-Air Testing

Table 5.7: Monotonic tension test results for mechanical splices on QST and MA bars from Part I In-Air Testing

Id.	Bar Type	Coupler Type	Bar Size	Coupler Dia. in. (mm)	Ultimate stress ksi, (MPa)	Uniform strain,%	Fracture strain,%	Fracture region
Wall 2	QST	Friction Welded-2	#.8 (25 mm)	1.38 (35.05)	114.1 (786.1)	8.44	15.08	Above the coupler
			#.8 (25 mm)	1.38 (35.05)	113.9 (784.8)	7.82	13.4	Above the coupler
	MA	Taper Threaded-2	#.8 (25 mm)	1.38 (35.05)	109.2 (752.7)	6.9	NA	Inside coupler
			#.8 (25 mm)	1.38 (35.05)	110.9 (763.8)	4.13	NA	Outside gauge length
Wall 3	QST	Swaged	#.8 (25 mm)	2 (50.8)	114.6 (789.6)	9.19	13.54	Above the coupler
			#.8 (25 mm)	2 (50.8)	114.3 (787.5)	6.9	12.79	Below the coupler
	MA	Grouted	#.8 (25 mm)	2 (50.8)	110.7 (762.6)	6.87	17.19	Above the coupler
			#.8 (25 mm)	2 (50.8)	111.9 (771.3)	8.87	18.19	Below the coupler
Wall 4	MA	Friction Welded-2	#.8 (25 mm)	1.38 (35.05)	112.2 (773.3)	8	14.15	Below the coupler
			#.8 (25 mm)	1.38 (35.05)	111.7 (769.3)	4.41	16.33	Above the coupler
	MA	End grip	#.8 (25 mm)	2.5 (63.5)	112 (771.7)	7.8	15.75	Below the coupler
			#.8 (25 mm)	2.5 (63.5)	110.6 (762)	7.43	14.48	Above the coupler

5.6.3.2 Low-cycle Fatigue Properties

Low-cycle fatigue testing of mechanical splice specimens was conducted similarly to testing on bare bars. A Digital Image Correlation (DIC) system monitored strains of the two clear bar spans at either end of a coupler during testing. The clear bar span between coupler and machine grips was 1.5 bar diameter on each side of the coupler. The DIC system(Sokoli et., 2014) averaged the strains of the two clear spans through the deformation of designated surface targets (Figure 5.12). Target pairs [1,2] and [6,7] were used to obtain bar strain during testing as shown in Figure 5.13 .Average bar strains were fed to the testing machine controller, which in turn controlled the crosshead movement based on those strains to achieve a strain control protocol. The machine controller enforced a loading protocol with strain peaks and valleys of +2% in tension and -0.5% in compression. Additional targets [3,4,5] were positioned to calculate local deformation and inelastic slip across the coupler.

Testing continued until the specimen fracture, with the number of half-cycles to fracture or 80% of peak strength were recorded. Deformations across the coupler, including bar-coupler slip and coupler body elongation, were monitored throughout. Specimens that failed outside the gauge length or near the grips were excluded. A minimum of three specimens were tested for each coupler-bar combination. Mean half cycles to fracture or to 80% peak stress for mechanical couplers used in wall tests are summarized in Table 5.8.

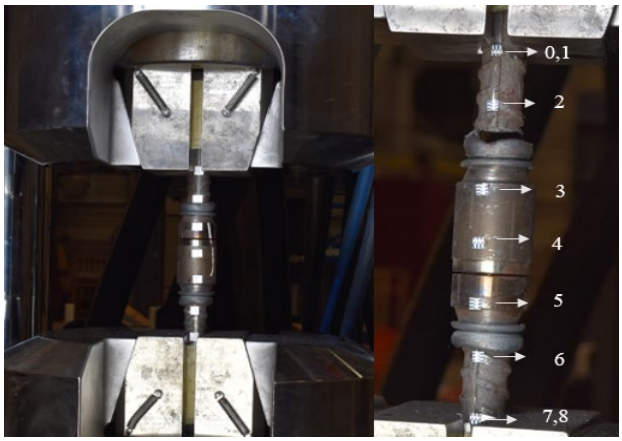

(a) (b)

Figure 5-13: (a) Specimen with 1.5d_b clear gripping span on each side of the coupler; and (b) typical monitored surface targets and their numbering along coupled specimens during inelastic cyclic tests adapted from Part I In Air testing

Table 5.8: Mean half cycles to fracture or 80% peak strength, from Part I In-Air Testing

Id	Product	Failure criteria	Mean half-cycles to fracture [% bare bar]		Number of tested samples, [N]		COV,%	
			QST	MA	QST	MA	QST	MA
Wall 2	Taper Threaded-2	Fracture	176.1 [85%]	76.1 [44%]	4	5	51.18	47.25
		80% of peak stress	156.7 [90.9%]	84.9 [49%]			44.01	47.25
Wall 3	Swaged	Fracture	216.8 [105%]	183 [105%]	3	3	17.15	20.22
		80% of peak stress	210.2 [121.9%]	184 [105%]			20.28	20.22
Wall 2 and Wall 4	Friction Welded-2	Fracture	59.95 [29%]	76.1 [44%]	4	5	24.71	1.54
		80% of peak stress	59.95 [29%]	76.1 [44%]			24.71	1.54
Wall 4	End Grip	Fracture	264.9 [128%]	124.9 [72%]	5	5	83.17	64.19
		80% of peak stress	165.4 [95.6%]	124.9 [72%]			60.72	64.19
Wall 3	Grouted-2	Fracture	161.4 [78%]	115.5 [67%]	2	2	19.4	75.88
		80% of peak stress	140.2 [81.4%]	115.5 [67%]			27.41	75.88

5.7 Test Procedures

Wall specimens were post-tensioned to a strong floor using nine #20 (75 mm) grade 100 (690 MPa) threaded bars that were each post-tensioned to 350 kips to minimize horizontal sliding during testing. Non-shrink grout was used at all contact surfaces between the external apparatus and the specimens to avoid stress concentration at the interface and facilitate specimen leveling. Lateral force was applied using two servo controlled hydraulic actuators with 220kip (978.6 KN) force capacity and an overall stroke length of 40 in. (1020 mm). Actuators were connected to a concrete reaction wall and angled about 20 degrees from the longitudinal axis of wall specimens to provide bracing against transverse movement as shown in Figure 5.14. The compressive axial load of about 350 kips (1557 KN) was applied to the walls using hydraulic rams connected to electric pumps.

Axial load was regulated through a pressure release valve and a pump that triggered the pump to increase the pressure below a threshold value as shown in Figure 5.14. This automatic pressure regulation system was able to maintain the desired pressure level within +/- 200 psi (1378.9 kPa). For each ram, the effective pressure area was 40.45 in^2 (0.026097 m^2). Therefore, the axial load tolerance on the specimens was +/- 8.09 kip (35.98 KN). However, prior to significant damage to the walls, hydraulic pressure on the walls remained nearly constant during the experiments (see Chapter 4). Wall specimens were subjected to three fully reversed lateral cycles to target drift ratios of increasing amplitudes. Drift ratio is defined as the ratio of lateral drift to wall height, taken from the top of the footing to the level of actuators (204 in., 5181.6 mm). The target lateral drift ratios were 0.2%,0.3%,0.5%,0.75%,1.0%,1.5%,2.0%,3.0% and 4%. Lateral loading continued until a significant loss of lateral strength and was stopped when wall specimens were at risk of lateral instability. Walls could not be pushed to axial collapse due to concern about their lateral stability after substantial damage was imparted.

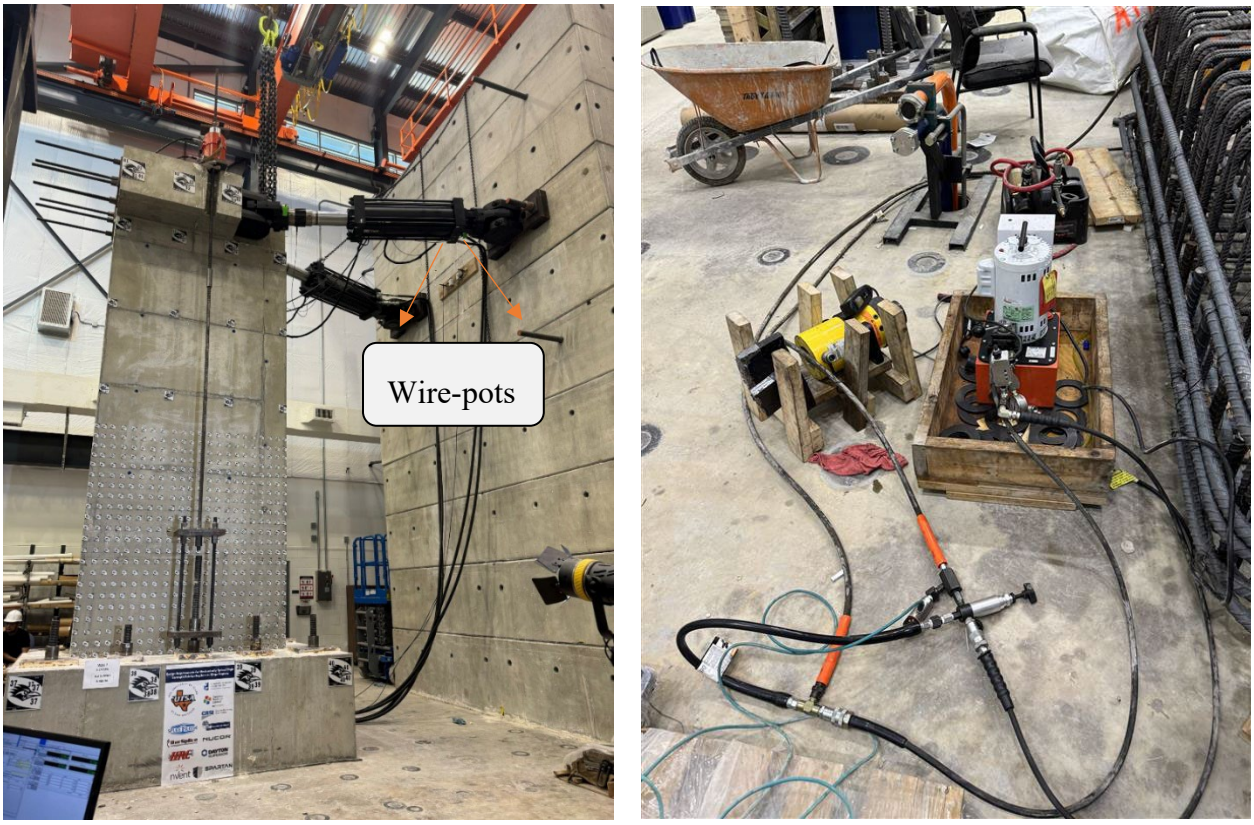

Figure 5-14: (a)Loads applied from actuators and hydraulic rams and, (b) axial load regulated through electric pump and release valve

5.8 Instrumentation

Instruments used in the tests included wire pots measuring lateral displacement at the lateral loading level, load cells in the actuators measuring applied lateral loads, a pressure gauge monitoring the axial load set up hydraulic pressure, strain gauges on the longitudinal and transverse reinforcing bars and a Digital Image Correlation System (DIC)(Sokoli et al., 2014) that monitored the surface deformations of the specimens. At the peak target drift ratio of every loading cycle, the actuator stroke remained stationary for 10 seconds to allow for data averaging at peak drifts.

The lateral load was calculated from the load cell reading of the actuators. An axial load was derived from a digital pressure gauge connected to the rams applying the axial load. The lateral load and hydraulic pressure applied using hydraulic rams were recorded during testing at a frequency of 10 Hz using a National Instruments data (NI) acquisition system. Two wire-pots were

used to measure the lateral displacements of wall specimens and were placed at the level of actuators as shown in Figure 5.14. Strain gauges were installed on the corner and middle longitudinal bars in boundary regions, as well as on the hoops and crossties that encompasses the length of the plastic hinge region as illustrated in Figure 5.15 to Figure 5.19. Strain gauges were labeled based on their three-dimensional coordinates in inches from the north-east wall corner at the footing interface. The x-coordinate aligned with the north-south direction, the y-coordinate was vertical, while the z-coordinate aligned with the east-west direction. Strain gauge labels also started with "L" for boundary longitudinal bars, "V" for vertical web bars, and "T" for transverse bars. Strain gauge installation followed manufacturer's recommended procedures. Steel bars were ground to achieve a smooth surface at the location of strain gauge. Care was taken not to reduce bar cross-section in grinding process. The surface was then treated to remove any grease or dirt and polished with #220 sandpaper followed by #400 paper and wiped with acetone or alcohol wipes. CN-Y(Cyanoacrylate) adhesive was used to glue gauges to bars, and it was wrapped with protective layers (shown in Figure 5.20). Wire pot and strain gauge data recorded at a 10Hz sampling frequency using the NI data acquisition system.

A DIC camera system dubbed the CIV developed at UTSA (Ghannoum et al., 2021; Rajae et al., 2023; Sokoli et., 2014) was used to measure the three-dimensional movement of paper targets glued on the east surface of wall specimens as shown in Figure 5.21. This system used two high-resolution cameras, digital image correlation (DIC), a triangulation software developed by the research team (Ghannoum et al., 2021; Rajae et al., 2023; Sokoli et., 2014) as shown in Figure 5.22. The system tracks target locations in each recorded frame using a Digital Image Correlation Algorithm. A calibration procedure adjusts for lens distortion and provides necessary extrinsic and intrinsic camera parameters for the three-dimensional triangulation of target locations. Wall deformations were obtained from targets placed on a 3.75 in.x3.75 in. (95.25 mm x95.25mm) grid over the east surface of the wall. The CIV system recorded image frames at a frame rate of 3Hz during the tests. Targets lost for short periods were linearly interpolated over the missing frames and targets permanently lost due to the spalling of concrete were ignored after being lost. CIV and NI data were synchronized through their time stamps.

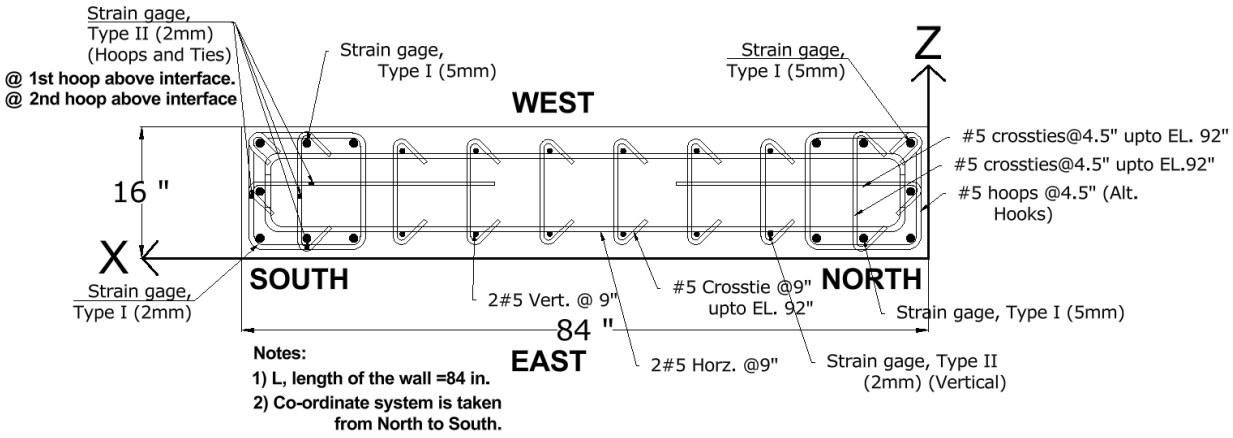

Figure 5-15: Wall cross-section, strain gauge location in plan and reinforcing bar labels

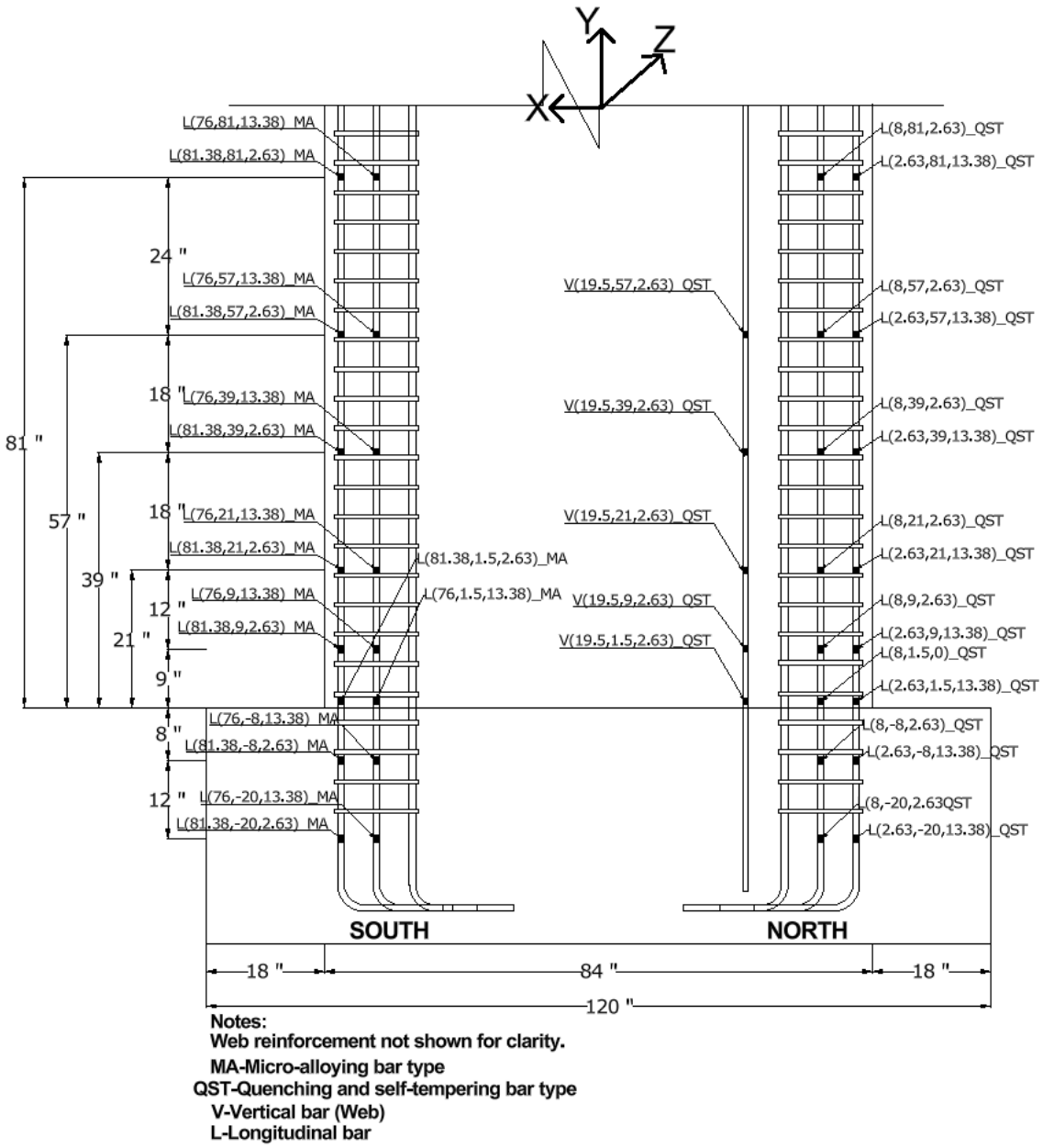

Figure 5-16: Control wall strain gauge location in elevation

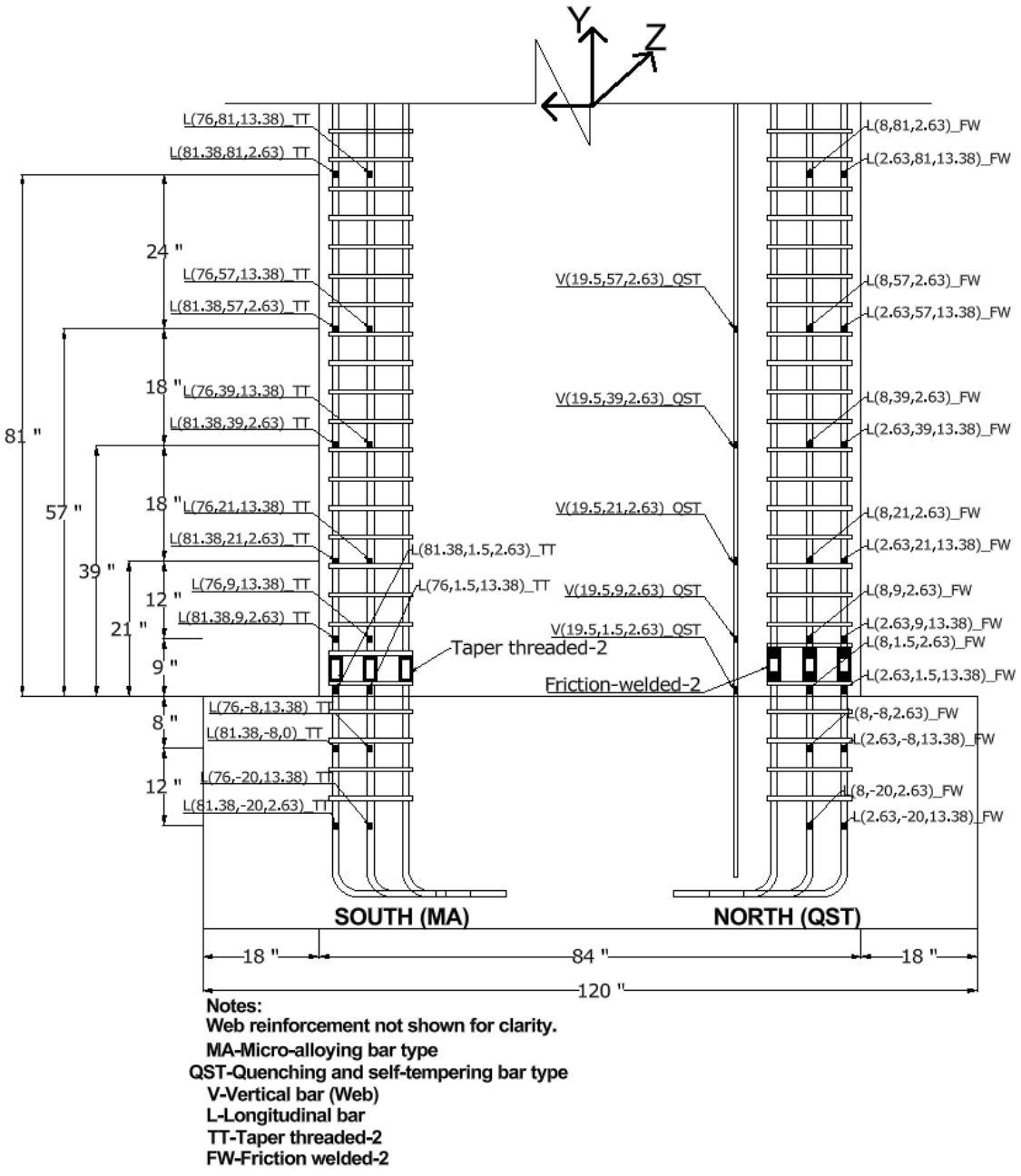

Figure 5-17: Wall 2 strain gauge location in elevation

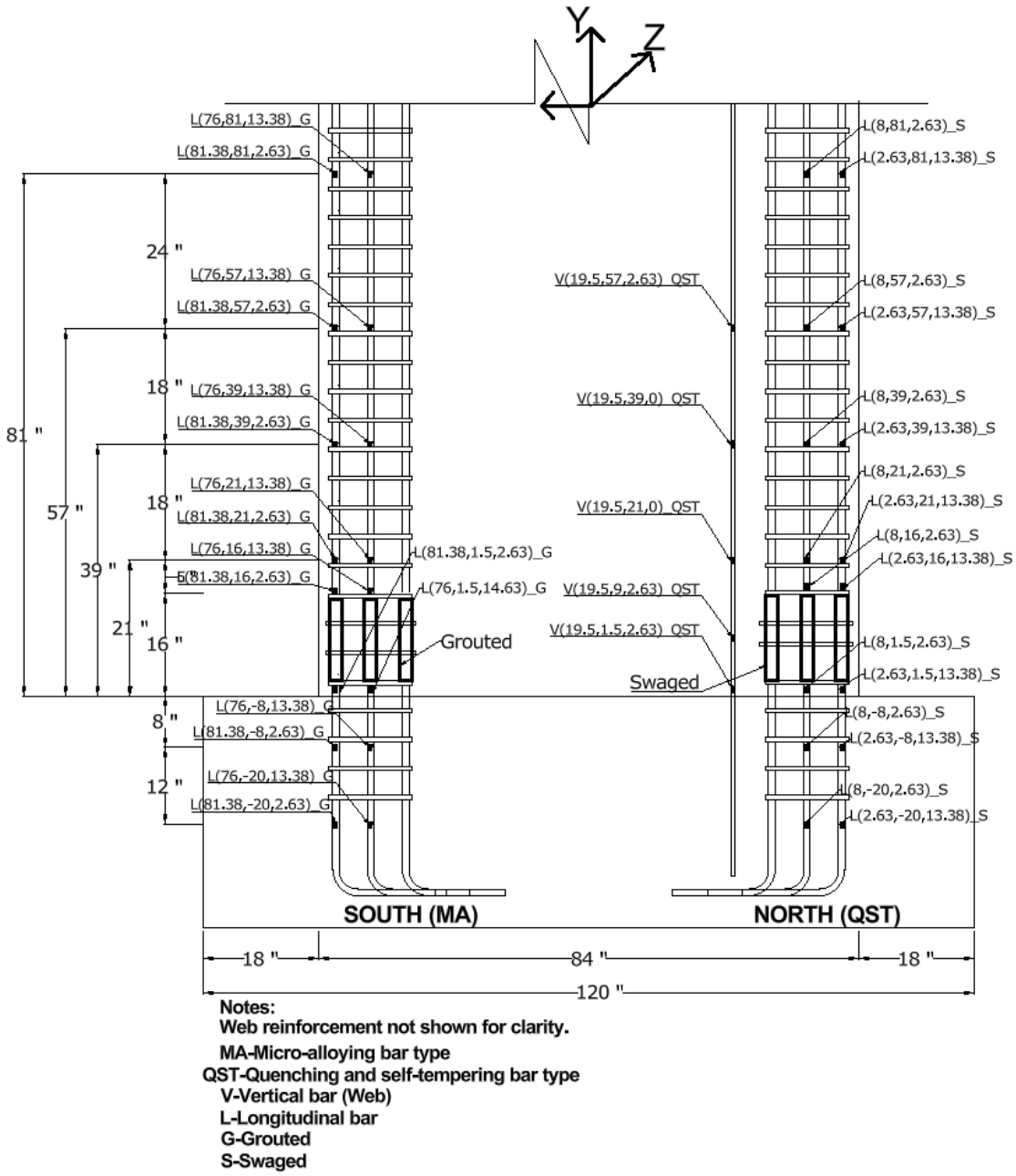

Figure 5-18: Wall 3 strain gauge location in elevation

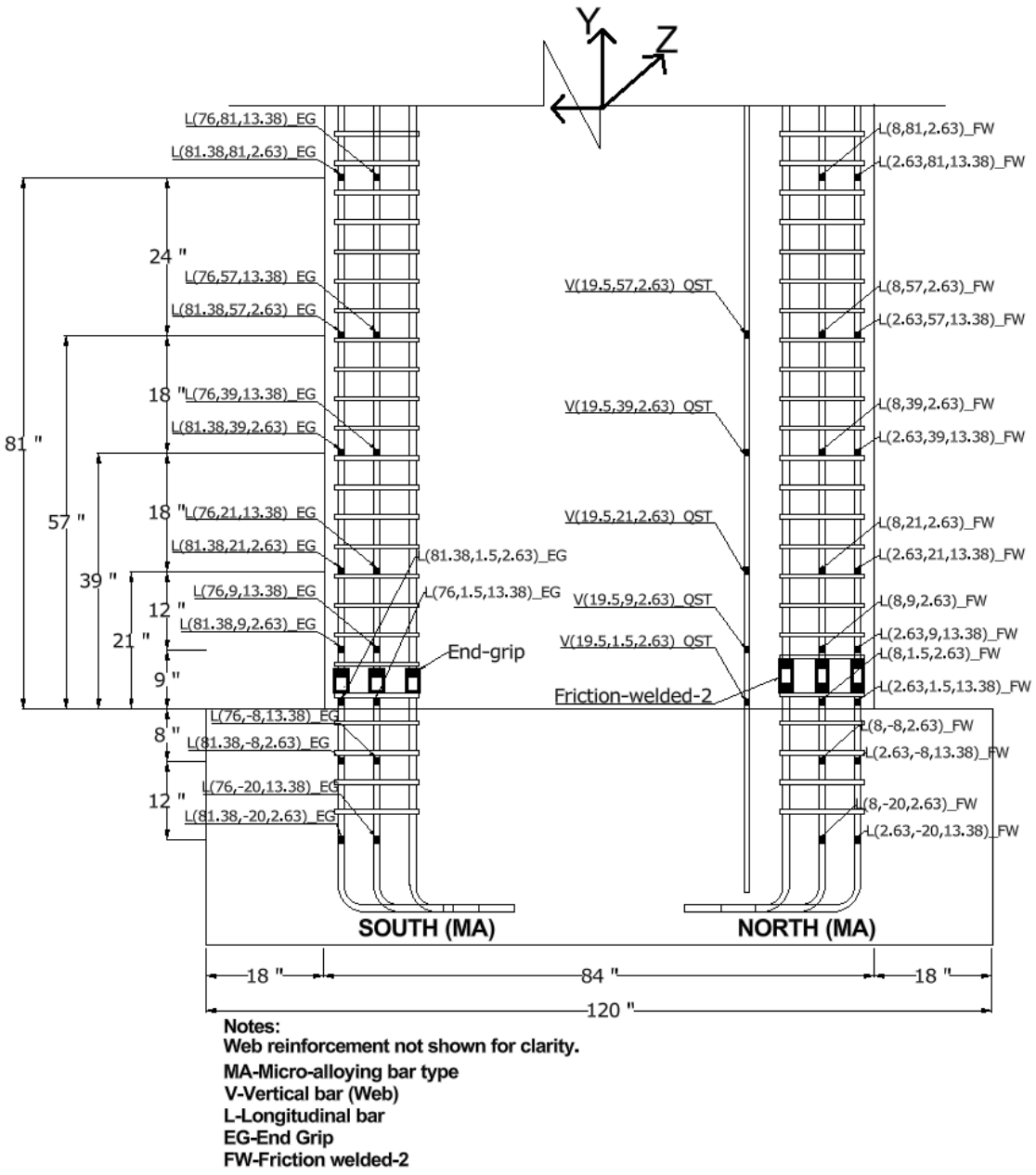

Figure 5-19: Wall 4 strain gauge location in elevation

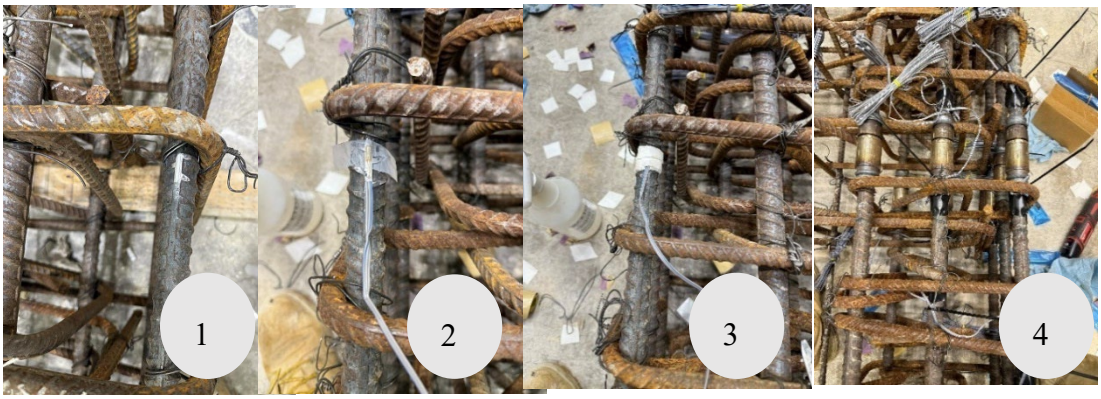

Figure 5-20: Strain Gauge installation process

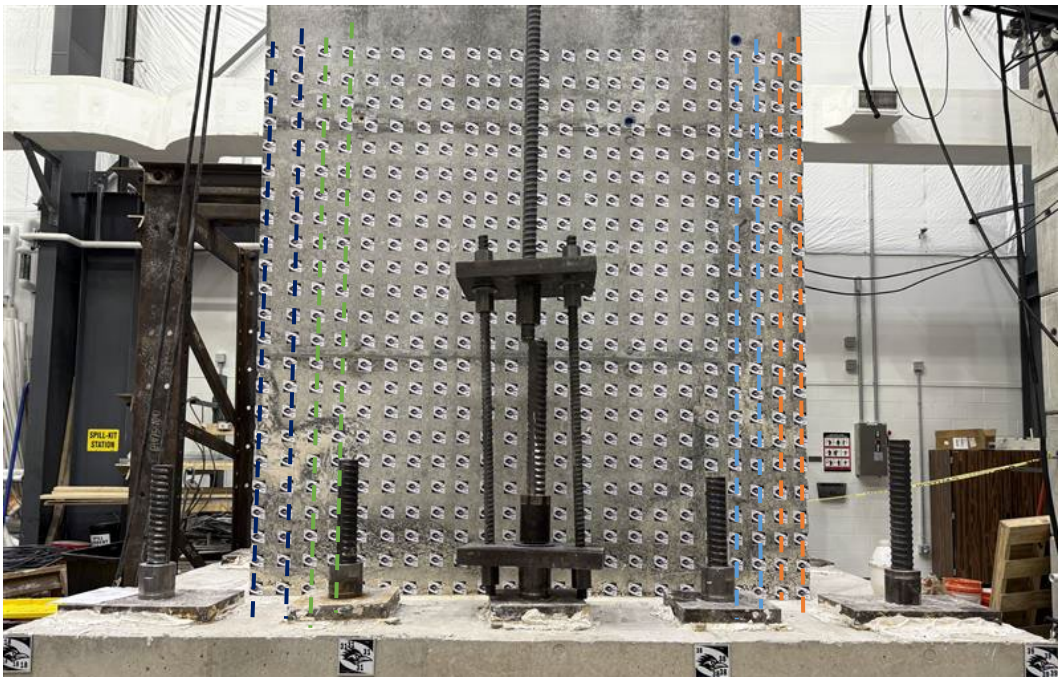

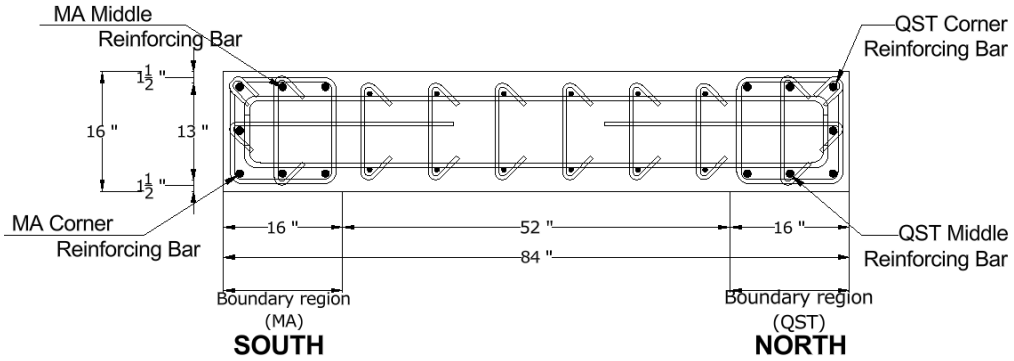

Figure 5-21: Glued paper targets on test monitored by CIV system

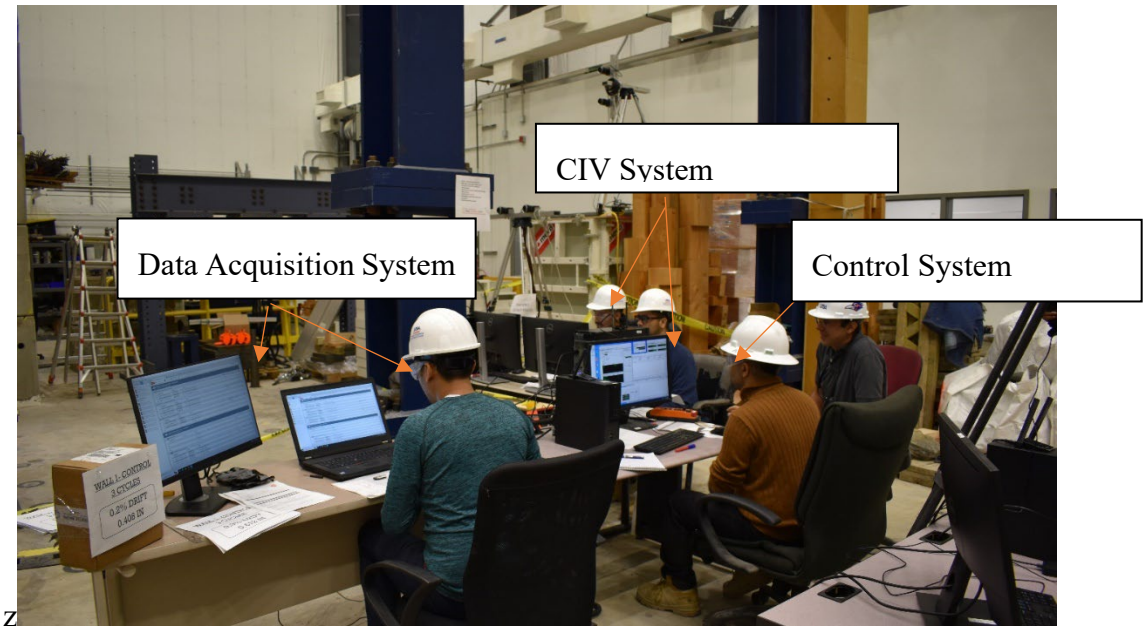

Z

Figure 5-22: Computer systems used in test

6 Wall Experimental Test Results

This chapter presents test data for each of the four full scale wall tests. The subsequent chapter provides a comparison between the four walls. Post processing of collected experimental data is explained in this chapter. The general behavior of each wall is summarized and results regarding lateral force versus deformation, longitudinal reinforcement strain demands, surface strain profiles along the height of specimens are presented.

6.1 Data Processing

6.1.1 Lateral Displacement

Displacement readings from the wire-pots placed at the level of the actuators were zeroed at the beginning of each test. Lateral displacements from the two wire-pots were averaged to calculate the lateral displacement of test specimens. The displacement data were filtered using a low-pass Butter filter (Ref (MathWorks, 2024)) to remove high frequency noise from displacement signals.

6.1.2 Axial Force

The hydraulic pressure applied to the vertical rams recorded using the data acquisition system was multiplied with the effective area for the rams to calculate the applied compressive axial load during the tests.

6.1.3 Lateral Force

The applied lateral force was calculated from the load cells of two servo-controlled hydraulic actuators. The locations of the actuator's ends were measured prior to the test for the calculation of initial angles of the actuators with respect to the wall longitudinal axis. Applied wall forces (shear and axial) were computed using large deformation equilibrium accounting for the inclination of actuators and considering the P-delta effect generated by the axial load setup. For the calculation of the P-Δ effect, the total length of threaded bars was assumed to be constant and the pivot point for rotation was assumed to be the clear distance between the nut at the top of the rams and the nut at the bottom of the single rods dropping from the rams, as can be seen in. The free body diagram and the static equilibrium equations are presented in Free Body Diagrams and Static Equilibrium Equations.

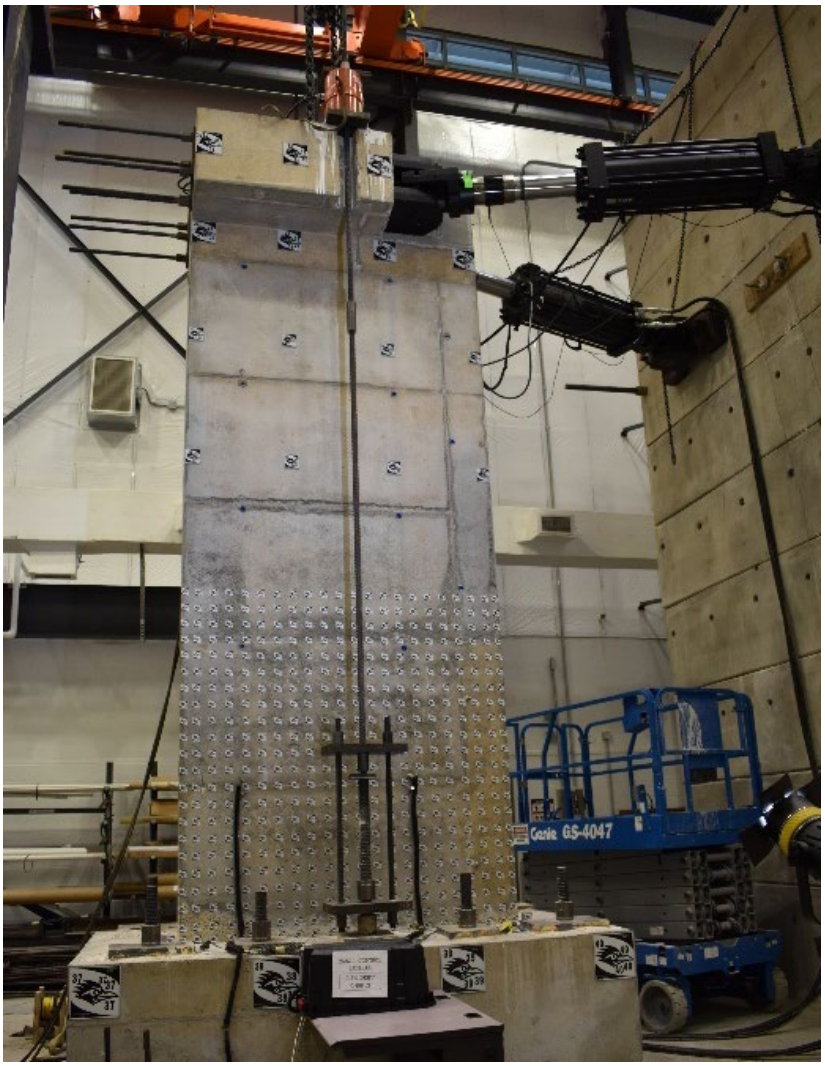

Figure 6-1: Picture of wall specimen with loading apparatus

6.1.4 Reinforcing Bar Strains

At the peak target drift ratio of every cycle, the actuator stroke remained stationary for 10 seconds to allow for data averaging at peak drifts. The recorded strain data from the strain gauges placed on reinforcing bars were averaged over the stationary period of each peak drift to obtain the strain demands in the reinforcing bars at peak drifts. The peak drift strains were used to generate strain profiles along the height of test specimen up to a height of 81in (2057.4 mm) from the base of the walls.

During each test, some strain gages failed due to surrounding damage. Strain data are only reported to loss of strain gauges.

6.1.5 Surface Strains

Test images recorded using the CIV system were reprocessed to extract the coordinates of surface targets from the start to the end of each test. The measurements of three-dimensional movements of targets on a test specimen were used to calculate surface strains on the concrete. The calculated surface strain data were averaged over the stationary loading period of each peak drift to obtain the surface strain demands at peak drifts, assuming the surface strains varied linearly between targets, the following surfaces were calculated; the x-directional or horizontal strains (εx) and the y-directional or vertical strain (εy). To compare the vertical strains from both DIC system and strain gauges, vertical strains from the first two columns of targets from wall edges, which were spaced at 3.75 in. (95.25 mm) on center, were averaged to produce vertical strain profiles along specimen height. Likewise, the vertical strains of the next two columns of targets were averaged to produce vertical strain profiles along specimen height. The surface strain profiles are compared in subsequent sections with the strain data of corner and middle longitudinal reinforcing bars at the wall boundaries. DIC measurement of surface strains were also used to estimate longitudinal reinforcement strains from concrete surface strains where strain gauges failed prematurely. At the base of walls, strain penetration effects of the longitudinal bars into the footing generate slip between the longitudinal bars in the footing concrete, which in tun generates relatively large cracks at the wall to footing interface. The crack width at the interface is obtained through vertical movement of surface targets at the base of the wall. To allow for the relative comparison between the vertical movement at the wall to footing interface and vertical elongation over the height of the wall, the crack width at the wall base is converted to a strain by dividing vertical movement of targets at the wall base by the typical target vertical spacing of 3.75 in. (95.25 mm).

6.1.6 Behavioral Milestones

First yielding in longitudinal reinforcement was identified from strain gauges installed at the interfaces of walls and footings where the demands were expected to be largest. First flexural cracking and first inclined cracking were identified by monitoring the wall surface strains for the first occurrence of strains above the concrete cracking strain. The formation of the first cover

splitting crack was identified from surface x-direction (horizontal) strains at the vertical edges of wall specimens. Bar buckling was identified from the pictures taken at the end of each half-cycle. Bar buckling markers are placed at the end of half cycles during which buckling is initiated. Bar fractures were noted down during the test and were tracked through the recorded data from strain gauges and visual observations.

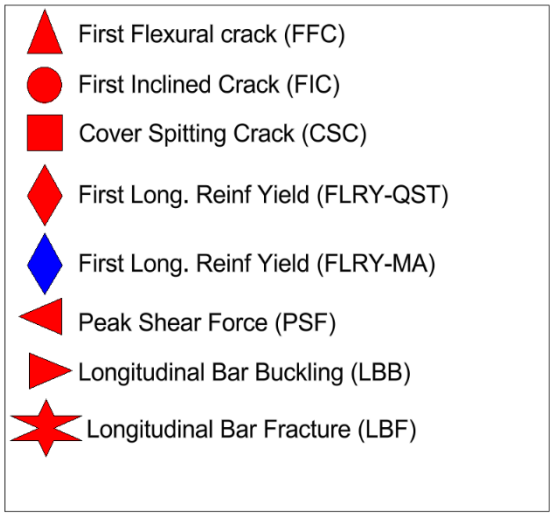

Figure 6-2: Behavioral milestones and corresponding markers

6.2 Test Results for Control Wall

The control wall had no mechanical splices or lap splices. The control wall was tested under quasi-static cyclic lateral loading as described in Chapter 3. A compressive axial load of 350 kips (1556.87 KN) was targeted which corresponds to 3.4% axial load ratio based on the measured compressive strength of concrete on day of testing of 7.72ksi for this wall. The axial load was maintained between about 300 kips (1334.46 KN) and 400 kips (1779.28 KN) throughout the test as shown in Figure 6.4.

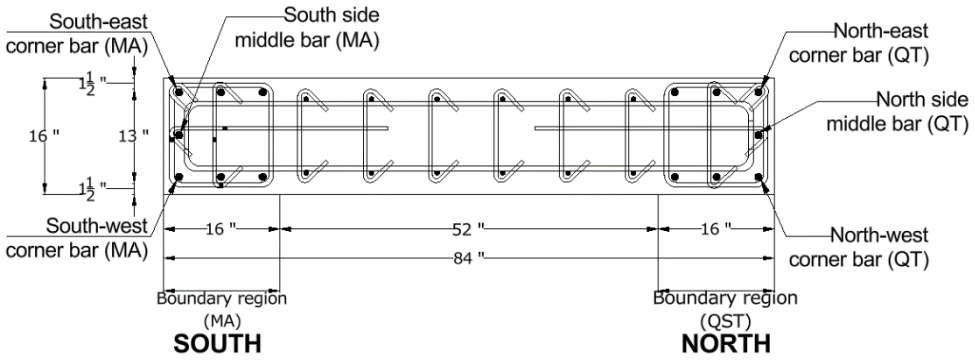

Figure 6-3: Control wall cross-section

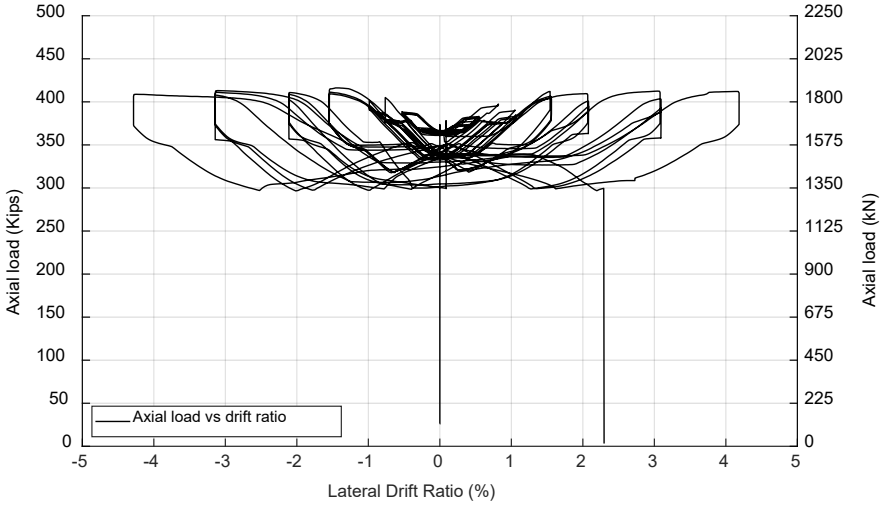

Figure 6-4: Control wall axial load versus drift ratio

6.2.1 General Behavior

presents the lateral force versus drift envelope (backbone) response of the wall. This wall was pushed first in the negative drift direction i.e., to the south. Table 6.1 summarizes the lateral force and drift values for all milestones for the control wall specimen. The first flexural cracks formed towards the end of the first cycle to -0.2% drift ratio while the first inclined crack was observed during the first cycle of -0.5% drift ratio. The first yield in the longitudinal reinforcement was identified from strain gauge readings towards the end of the first cycle to a drift ratio of -0.75%. The maximum applied lateral force of 326.82 kips (1453.76 KN) was recorded at the end of the

first cycle to a drift ratio of +3.0 %. Beyond that drift cycle, the lateral load diminished gradually until bar fractures occurred. Significant bar buckling occurred before bars fractured above the wall to footing interface during the first excursions to a -4% drift ratio. During the first excursion to -4% drift ratio, the middle longitudinal reinforcing bar at the north end (Figure 6.3) fractured in between the third and fourth hoops from footing interface. On the first excursion to +4% drift ratio, the middle longitudinal reinforcing bar on the south end fractured in between second and third hoops from wall-footing interface in the south boundary element of the wall. The test was stopped after the completion of first cycle of 4% drift due to stability concerns as the compression boundary began buckling while axial deformations increased (Figure 6.9).

The control wall therefore maintained lateral strength and stability to a drift ratio of 3%, which is deemed sufficient for special concrete seismic systems under an MCE level event (ASCE/SEI 7(American Society of Civil Engineers (ASCE), 2022)).

Table 6.1-Control wall-behavioral milestones

Milestone	**Drift Ratio (%)**	**Lateral Load (kips)**
First Flexural Crack	-0.2	-160.91 (715.76 KN)
First Inclined Crack	-0.49	-225.17 (1001.60 KN)
First Long. Reinf. Yield	-0.63	-263.5 (1172.1 KN)
Cover Splitting Crack	-0.75	-281.39 (1251.68 KN)
Peak Shear Force	+3.0	+326.82 (1453.76 KN)
Longitudinal Bar Buckling	-3.0	-320.8 (1426.98 KN)
Longitudinal Bar Fracture (QST)	-3.7	-291.65 (1297.32 KN)
	-3.0	
Longitudinal Bar Fracture (MA)	+1.31	+197.34 (877.81 KN)
	+3.0	

Note: for bar buckling and bar fracture, the maximum prior drift ratio and the actual drift at which milestone occurred are reported; the top value reports actual drift and the bottom value reports maximum prior drift ratio.

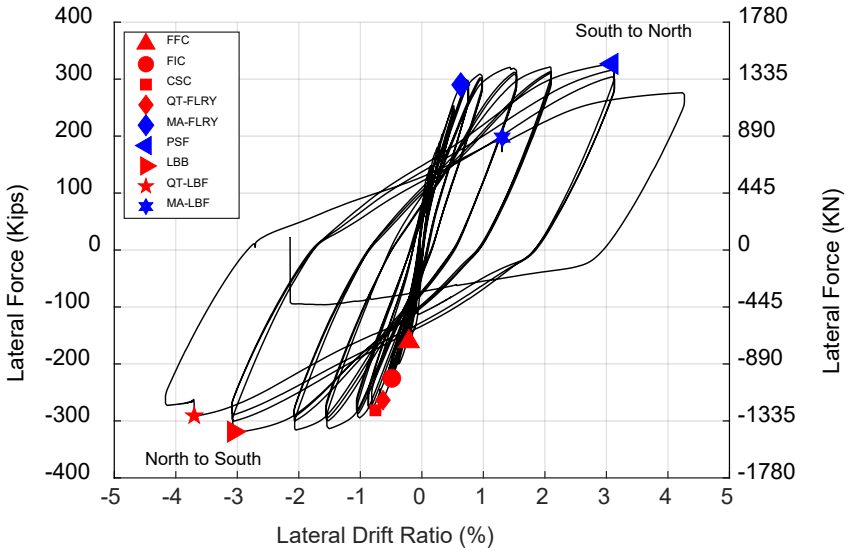

Figure 6-5: Control wall -latera force versus drift ratio response

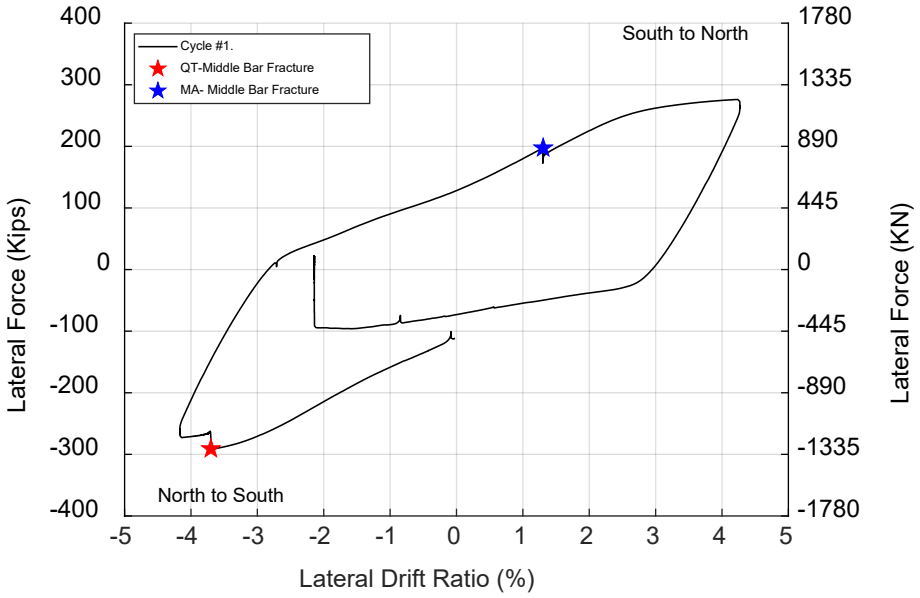

Figure 6-6: Control wall- last cycle response

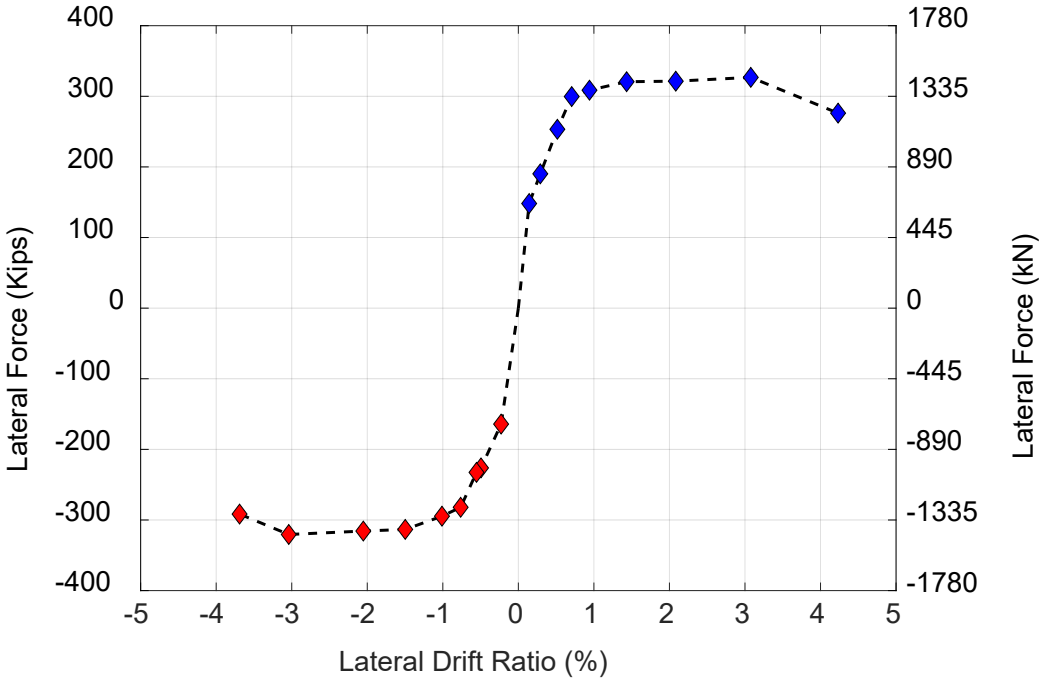

Figure 6-7: Control wall- backbone response

6.2.2 Test Pictures- Control Wall

Figure 6.8 and Figure 6.9 show pictures of the control wall at various stages of loading and damage.

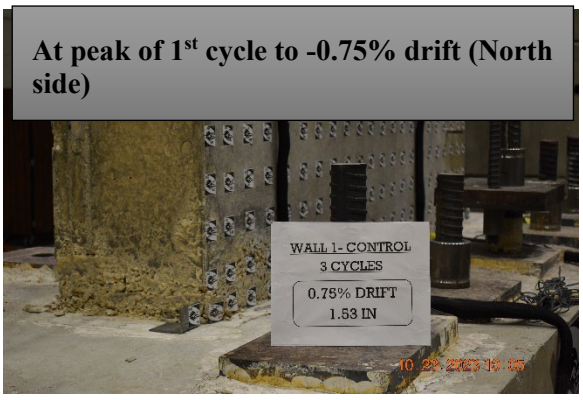

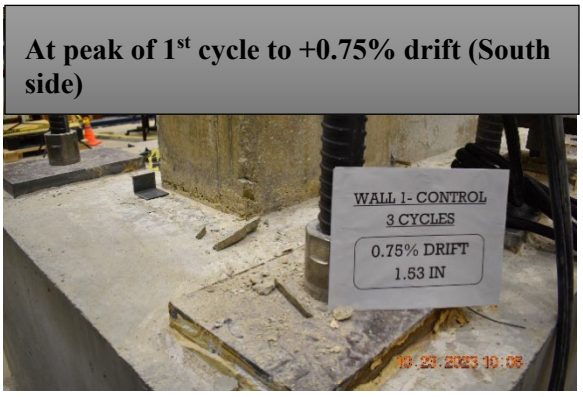

At peak of 3rd cycle to +1.0% drift (South side), spalling of concrete

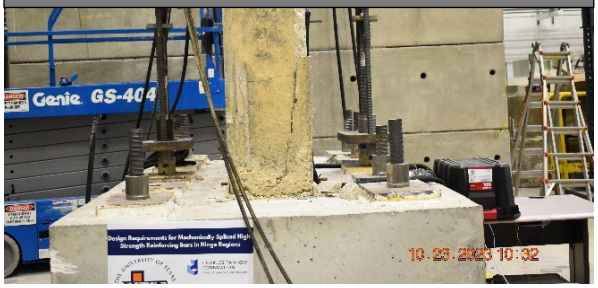

At peak of 1st cycle to +1.5% drift (North side), spalling of concrete

At peak second cycle to 2.0% drift, flexural cracks propagated leading to formation of inclined cracks

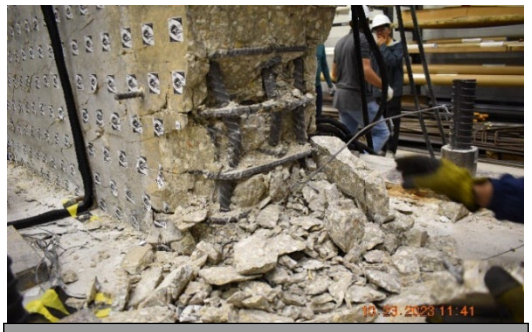

At peak of 3rd cycle to +3.0% drift, buckling of longitudinal bars on North side

Figure 6-8: Control wall test pictures at the peak of various drift targets

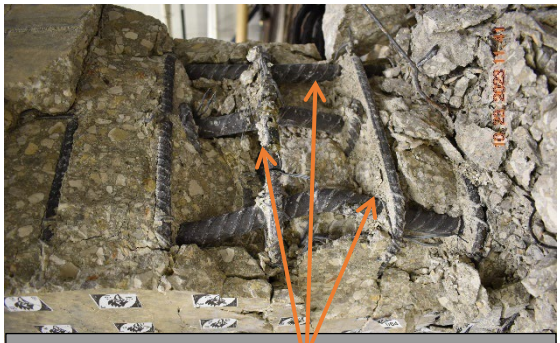

Buckling of longitudinal bars North side (QST)

First middle bar fracture North side (QST)

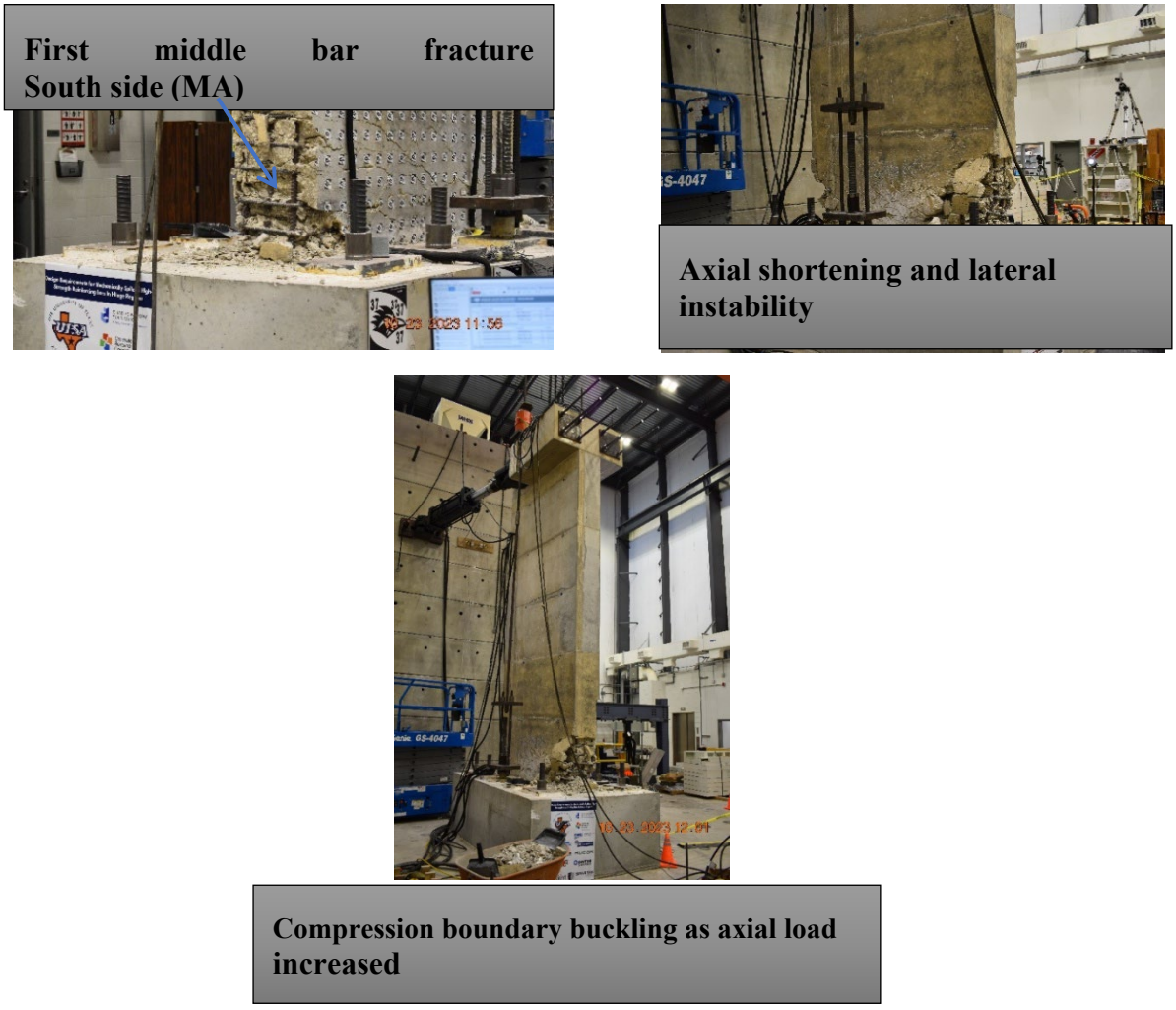

Figure 6-9: Control wall -pictures of buckled and fractured bars at the end of the test at the peak of + or - 4% drift

6.2.3 Strain Histories

Maximum strain demands were recorded at the interfaces between the wall and footing. Figure 6.10 and Figure 6.11 show typical strain versus lateral drift ratio responses for a corner and a middle boundary bar 9 in. (228.6 mm) above the wall-footing interface, where strain readings were reliable to larger drifts. The #8 (25 mm) bars used as longitudinal reinforcement in the boundary region had a yield strain of 0.0035 for quenching and self-tempered (QST) bars and 0.0031 for micro-alloying (MA) bars as obtained from material tests. This strain was first reached at a drift ratio of about + or -0.75%.

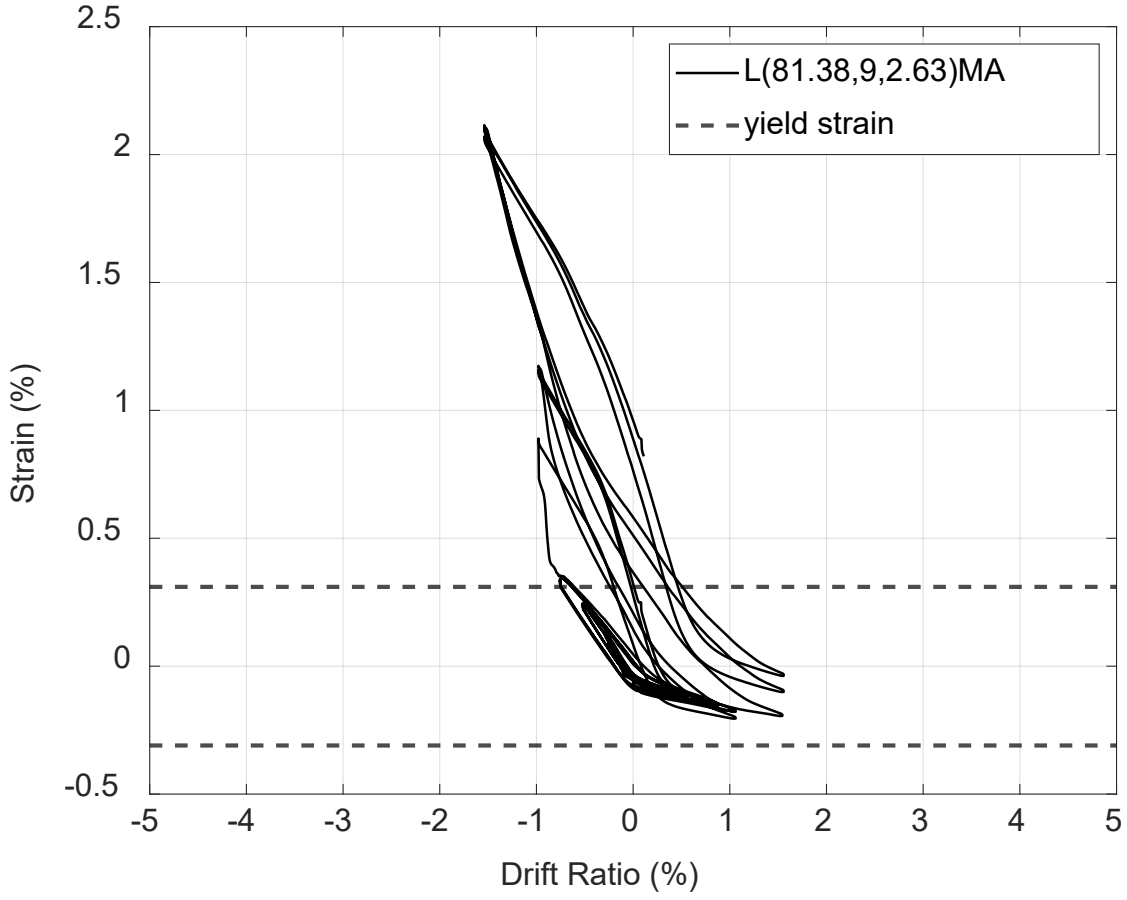

Figure 6-10: Control wall strain gauge at 9 inches (228.6 mm) from the wall to footing interface for the south end MA corner reinforcing bar

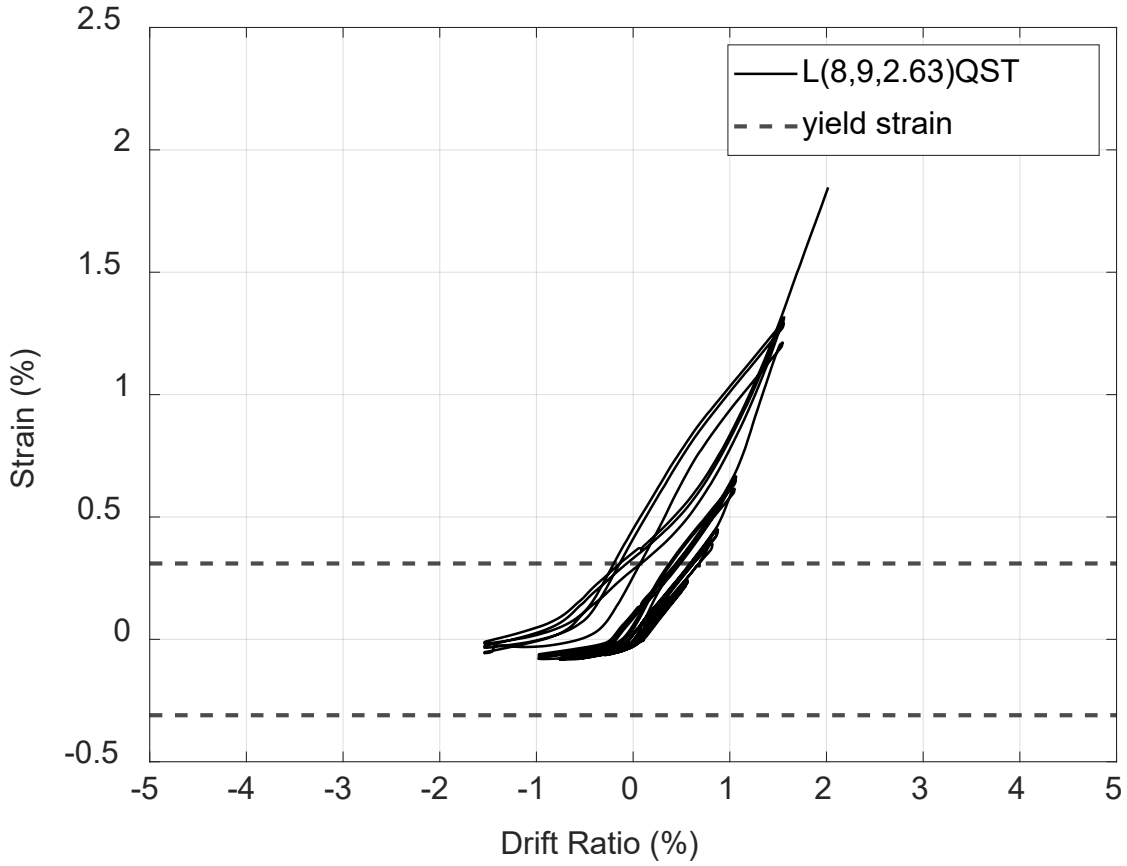

Figure 6-11: Control wall strain gauge at 9 inches (228.6 mm) from the wall to footing interface for the north end QST middle reinforcing bar

6.2.4 Longitudinal Reinforcing Bar Strain Demands

Recorded strain data on a sample longitudinal bar from all three cycles applying tension at each target drift were averaged and then plotted against the lateral drift ratio in Figure 6.12. After yielding, the strain demands increased in longitudinal reinforcing bars more rapidly with respect to lateral drift.

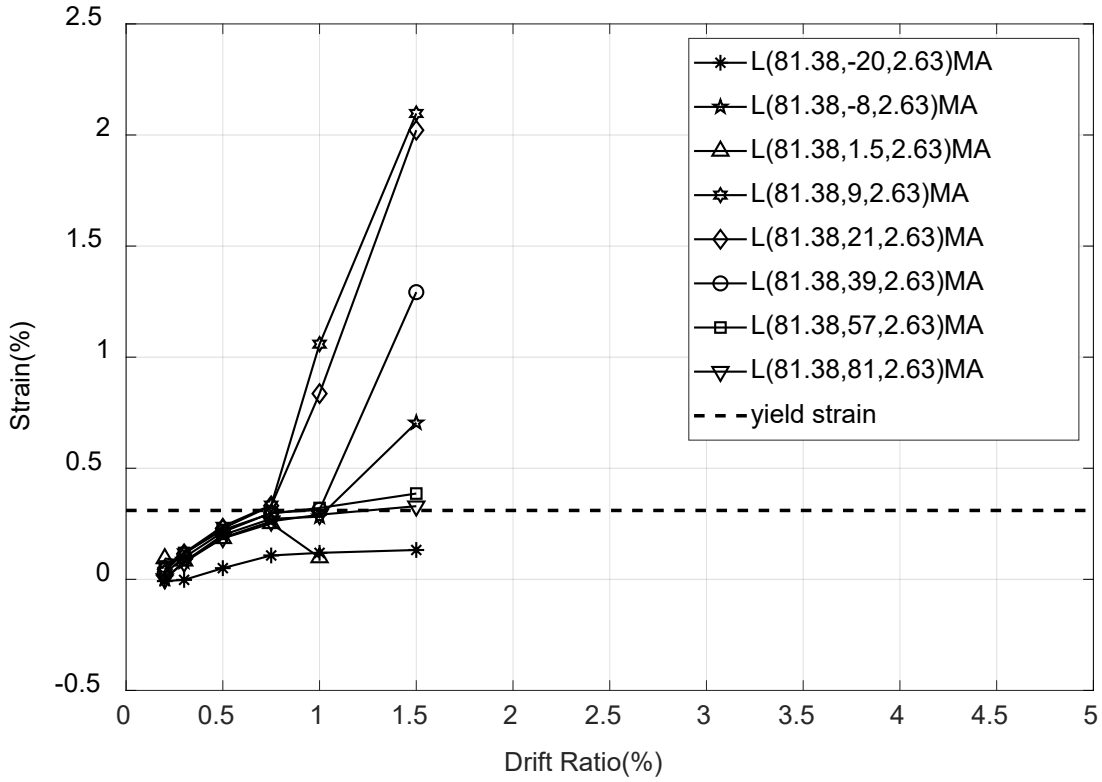

Figure 6-12 :Control wall longitudinal reinforcement strain demands at drift targets for the south end MA corner reinforcing bar

6.2.5 Strain Gauge Profiles along Height

Strain readings over the height of longitudinal reinforcing bars in each of the boundary regions are given in Figure 6.13 ,Figure 6.14 and Figure 6.15. Unfortunately, all the strain gauges at the wall to footing interface were lost prematurely in this test and therefore their values could not be reported as damage progressed.

As the wall was pushed past the first yield to higher drifts, inelastic strains were able to spread at least 81 in. (2057.4 mm) from the base of the wall for MA bars and about 70 in. (1778.4 mm) for QST bars. Plasticity spread up the wall height was therefore more pronounced for the MA bars than for the QST bars. This may partly be attributed to the higher tensile-to-yield strength ratio of MA bars (1.33) versus QST bars (1.29).

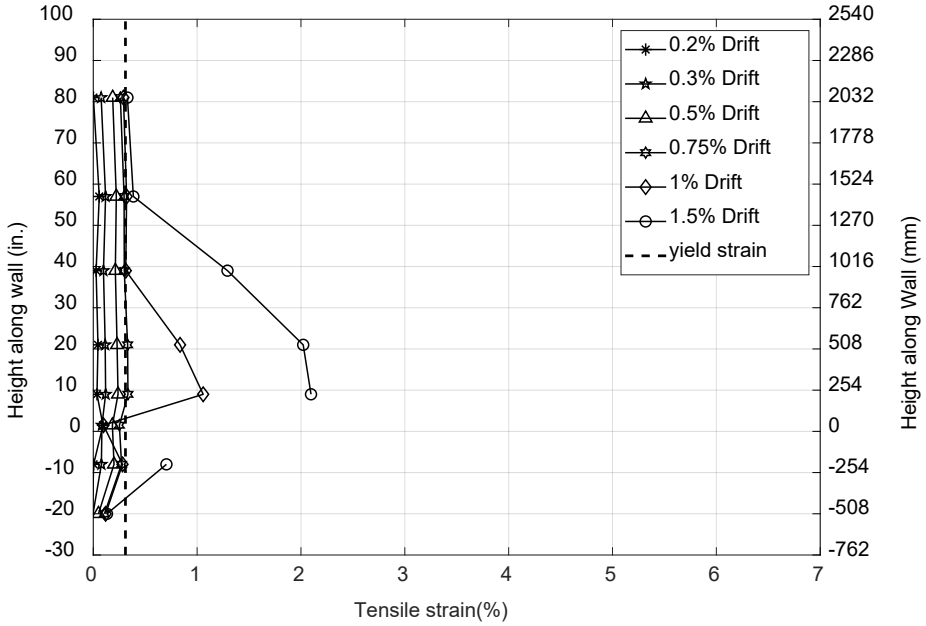

Figure 6-13: Control wall longitudinal reinforcement strain profiles over height at peak drift targets (Micro-alloying corner bar)

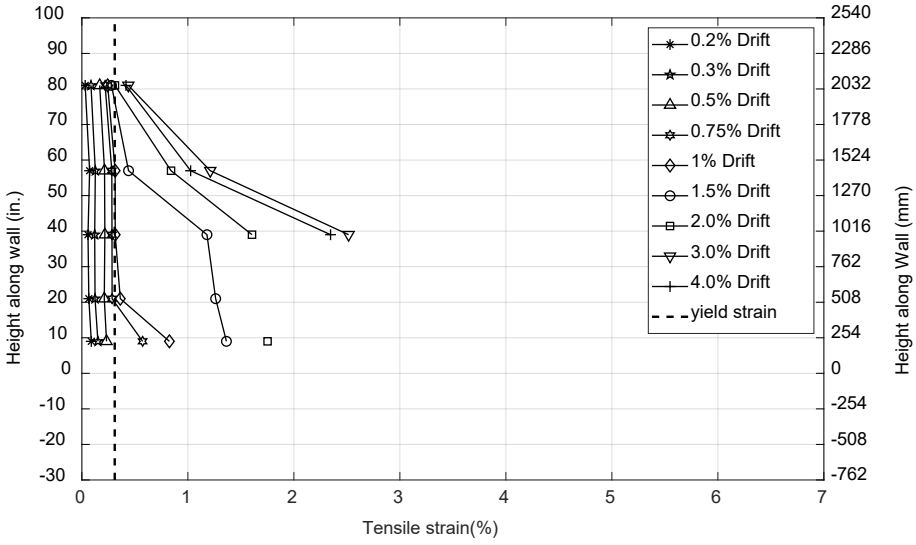

Figure 6-14-Control wall longitudinal reinforcement strain profiles over height at peak drift targets (Micro-alloying middle bar)

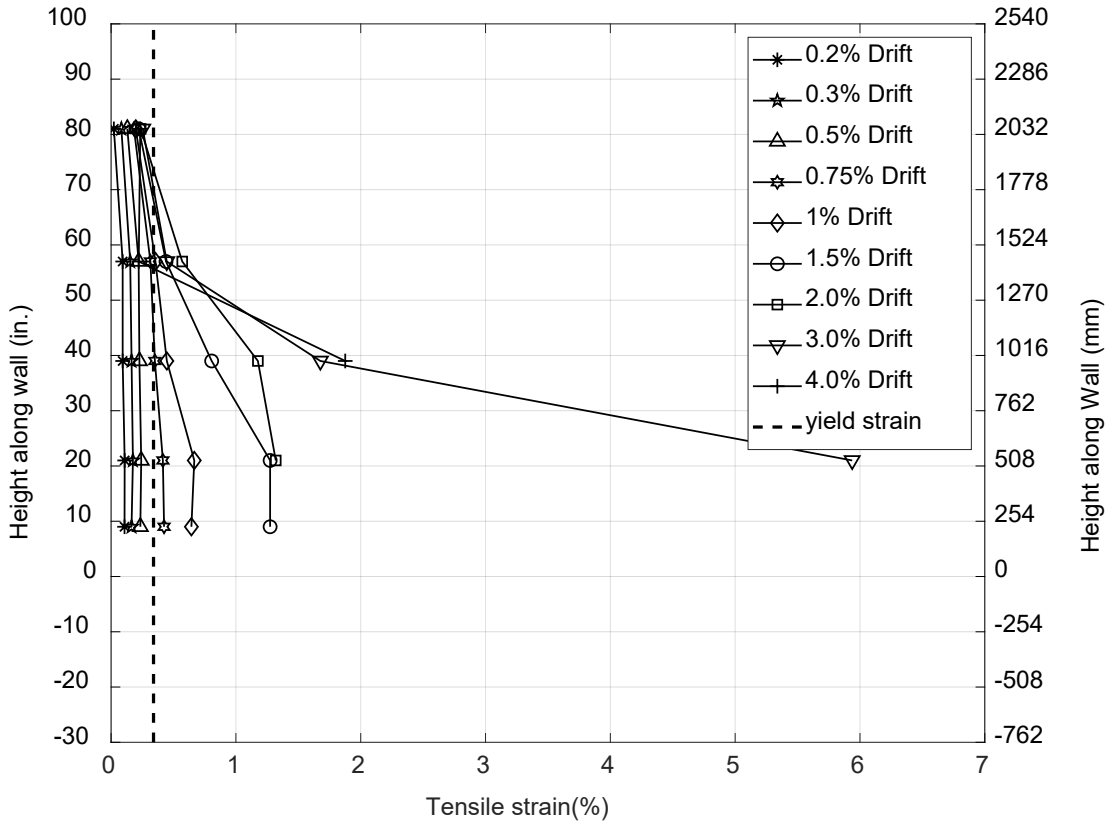

Figure 6-15-Control wall longitudinal reinforcement strain profiles over height at peak drift targets (Quenching and self-tempering middle bar)

4.3.6 Surface Strain along Height (DIC system)

Vertical surface strains along the height of the wall specimen at the boundary regions were calculated from the recorded target displacements as described in section 6.1.5 .Surface strain profiles are presented for targets facing the longitudinal bars that were strain gauged. Figure 6.16 and Figure 6.17 show vertical surface strains along the height of the test specimen for the concrete facing the micro-alloyed longitudinal corner and middle reinforcing bars in the south the boundary region. Figure 6.18 and Figure 6.19 show vertical surface strains along the height of the test specimen for concrete facing the quenching and self-tempered longitudinal reinforcing bars in the north boundary region. Based on surface strains, inelastic strains are seen to spread up to 65 in. (1651 mm) from the base of the wall around MA bars, and 60 in. (1524 mm) around QST bars. The lower observed plasticity spread at the QST boundary region corroborates the lower plasticity spread observed from strain gauge data on the bars.

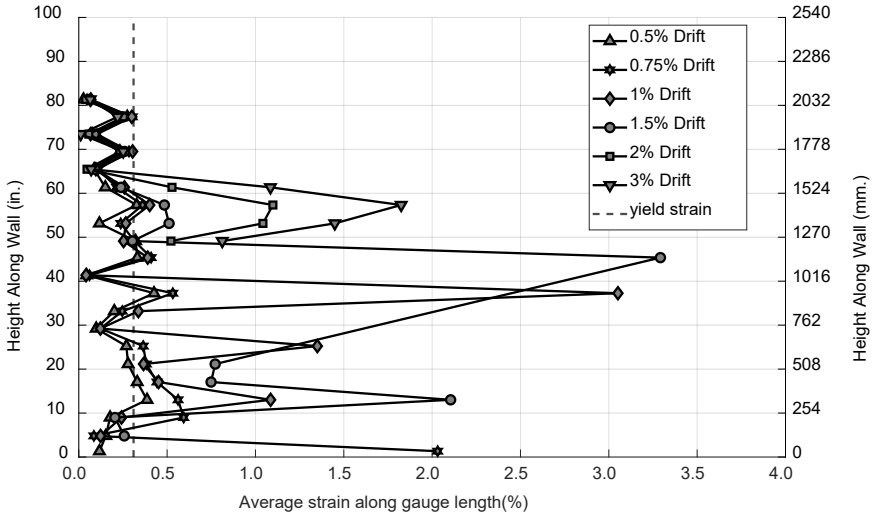

Figure 6-16: Vertical strain profiles from surface targets facing the south end MA corner reinforcing bar

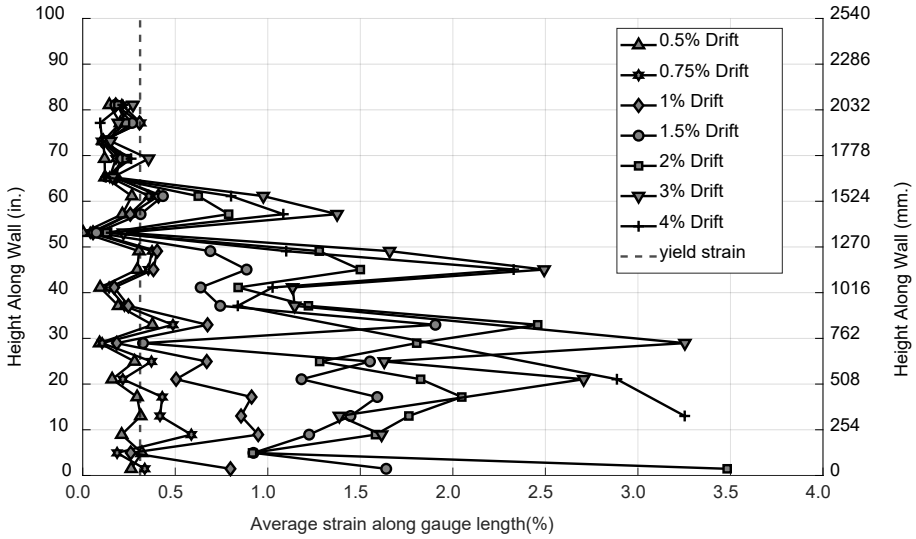

Figure 6-17- Vertical strain profiles from surface targets facing the south end MA middle reinforcing bar

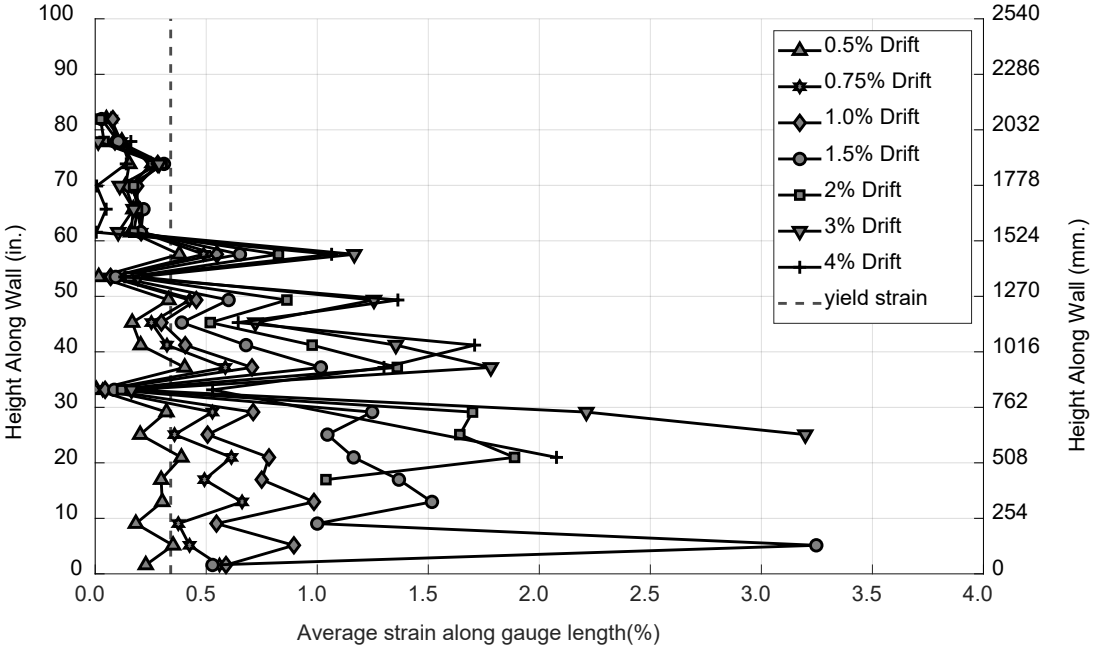

Figure 6-18:Vertical strain profiles from surface targets facing the north end QST corner reinforcing bar

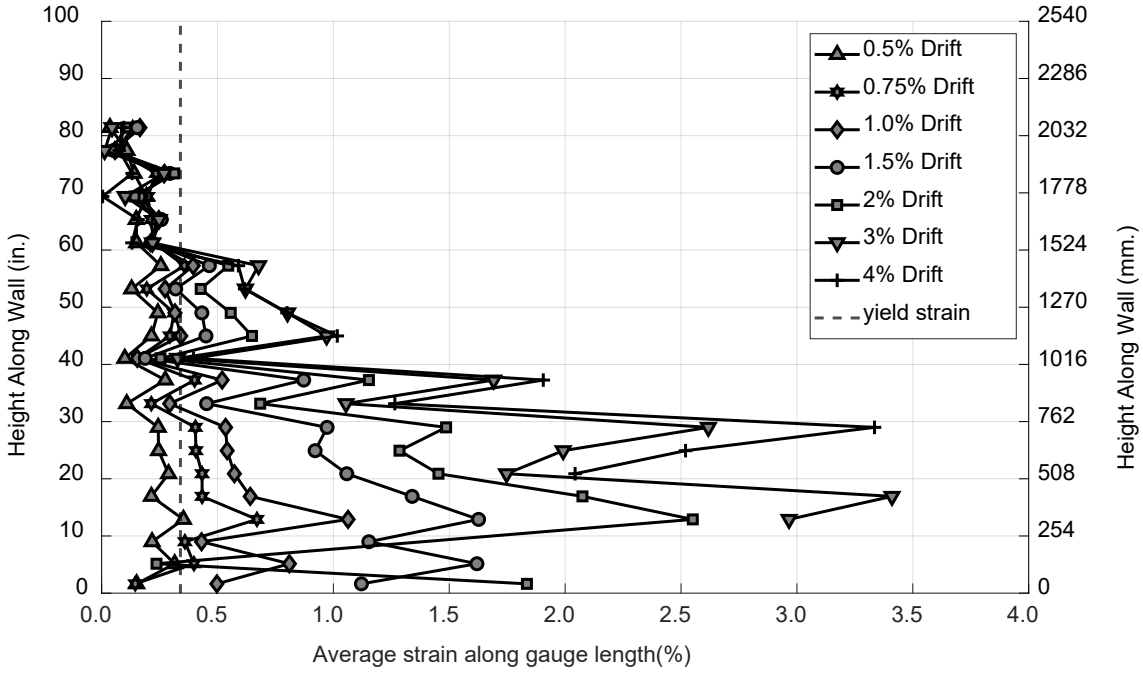

Figure 6-19: Vertical strain profiles from surface targets facing the north end QST corner reinforcing bar

6.2.6 Comparisons between Vertical Strains from DIC System and Strain Gauges

Longitudinal bar strain readings are compared with the surface vertical strain readings from the targets closest to the bars in Figure 6.20 and Figure 6.21 for the boundary region with MA bars and in Figure 6.22 and Figure 6.23 for the boundary region with QST bars. Section 6.1.5 explains how the surface strains were obtained, and which surface targets were used.

As can be seen in the figures, vertical surface strains match longitudinal bar strains reasonably well where strain gauge readings could be obtained, i.e., before strain gauge failure. This indicates that surface strains could be used to estimate longitudinal bar strains where strain gauges failed during testing.

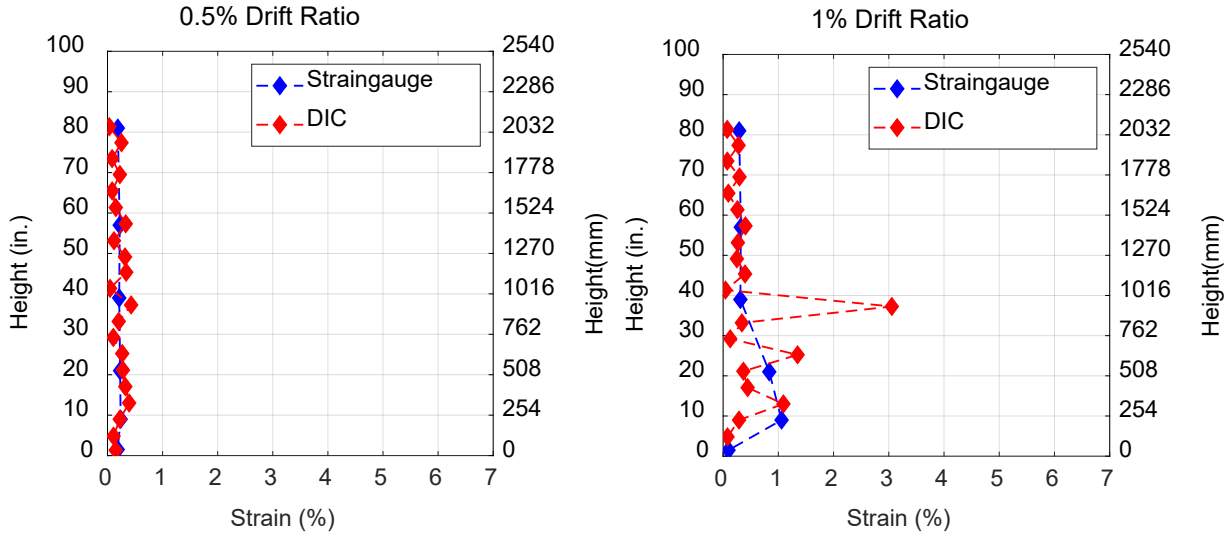

Figure 6-20: Strain profiles from strain gauges and DIC system for the south end MA corner bar

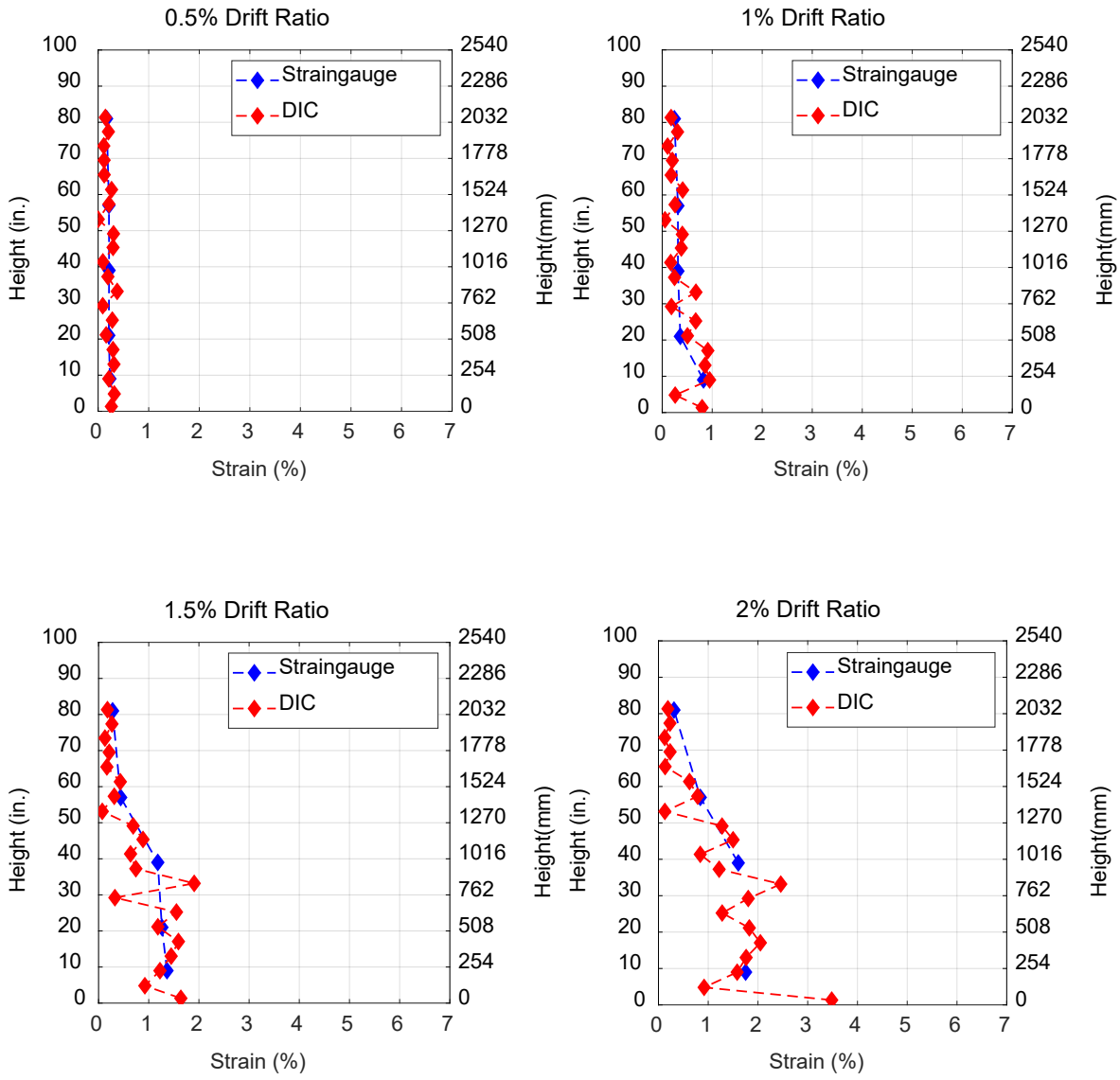

Figure 6-21- Strain profiles from strain gauges and DIC system for south end MA middle bar

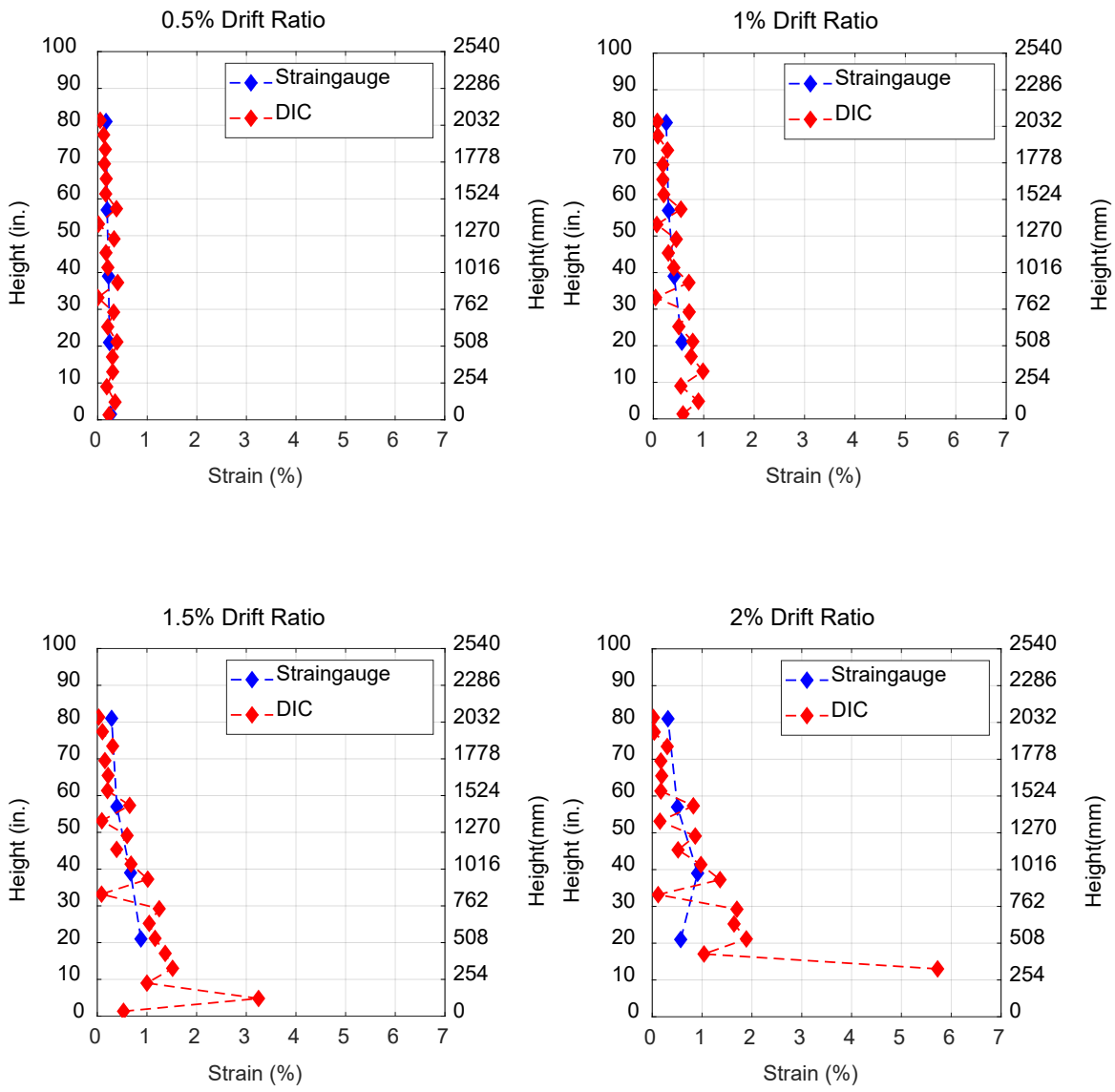

Figure 6-22: Strain profiles from strain gauges and DIC system for north end QST corner bar

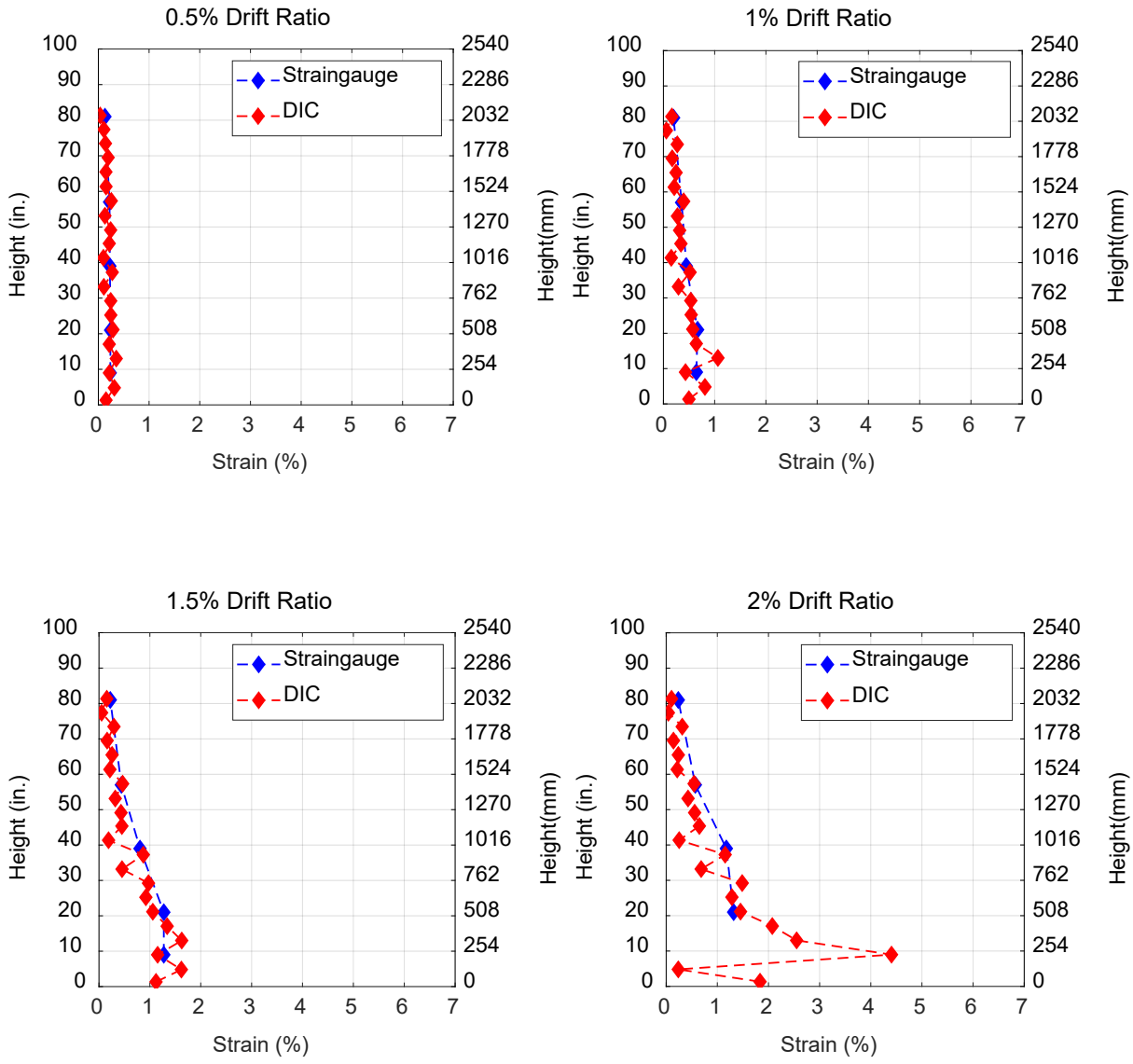

Figure 6-23: Strain profiles from strain gauges and DIC system for north end QST middle bar

6.2.7 Energy Dissipation

The energy dissipated in each full loading cycle is plotted in Figure 6.24. The first, second and third cycles to the same drift target are treated separately in the figure. The amount of energy dissipated in the first and second cycles was similar for control wall. During the third cycle to the drift ratio of 3.0%, the amount of energy dissipated was about 11% lower than first and second cycle to 3.0% drift.

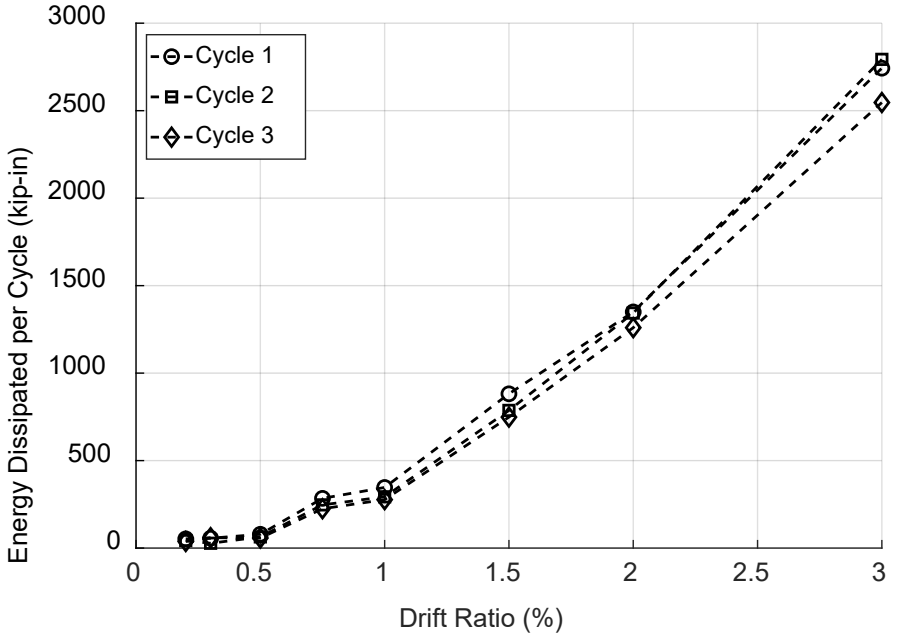

Figure 6-24: Energy dissipated in each full loading cycle

6.3 Test Results for Wall 2

Micro-alloying south boundary bars were spliced with high strength taper threaded couplers and quenching and self-tempered north boundary bars were spliced with friction welded couplers. These couplers were relatively short with lengths equal to 3.5 to 3.75 in. (76.2 to 95.25 mm) and relatively slim with diameters equal to 1.38 in. (35.05 mm). The specimen was tested under quasi-static cyclic lateral loading as described in Chapter 3. A compressive axial load of 350 kips (1556.87 KN) was targeted which corresponds to 3.59% axial load ratio based on the measured compressive strength of concrete of 7.25ksi for this wall. The axial load was maintained between about 300 kips (1334.46 KN) and 400 kips (1779.28 KN) throughout the test as shown in Figure 6.26.

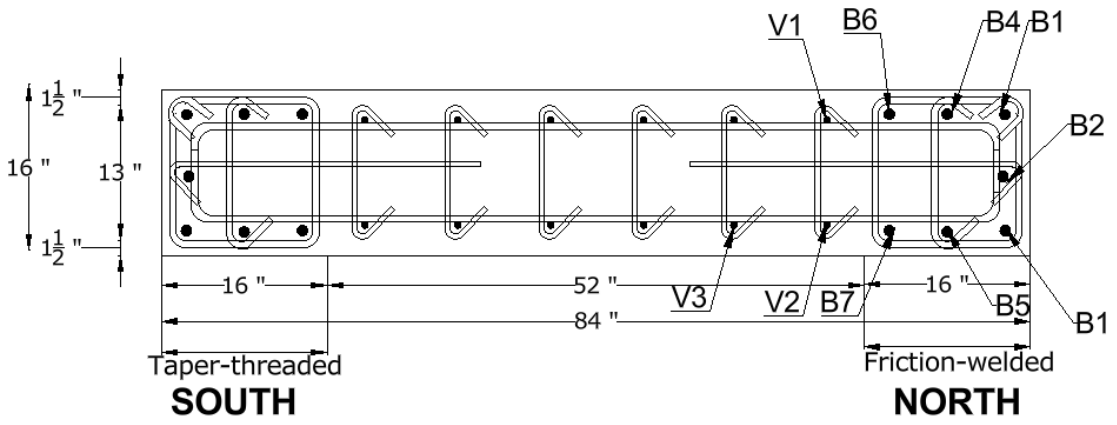

Figure 6-25: Wall 2- cross section and boundary reinforcing bar location; the designations of bars that fractured during the test are shown

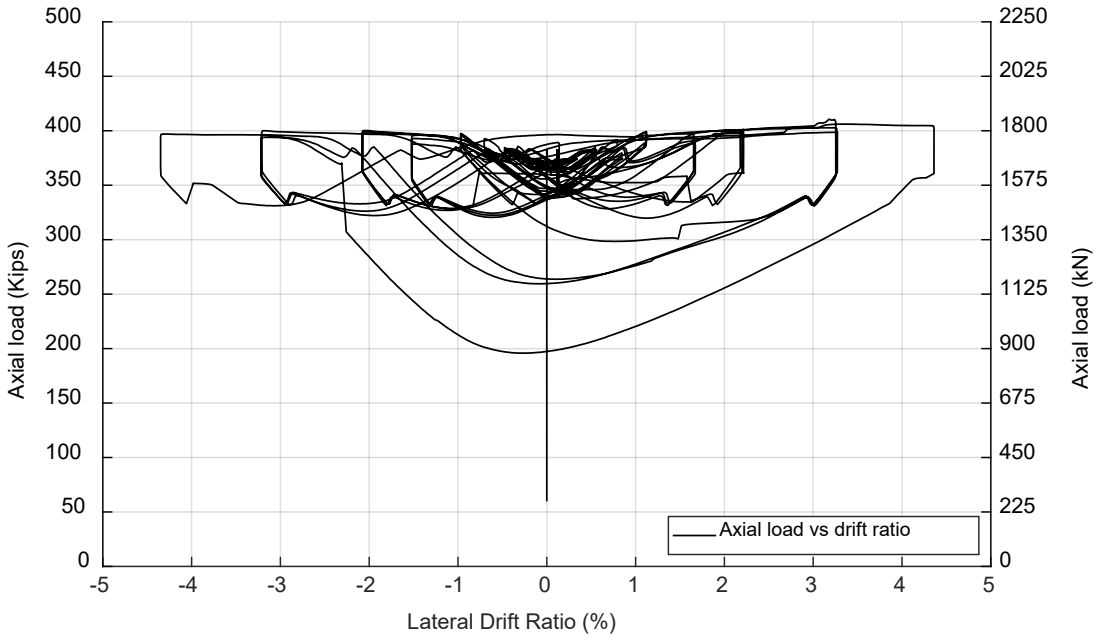

Figure 6-26: Wall 2- applied axial load versus drift ratio

6.3.1 General Behavior

Wall2 was pushed to the south or negative drift values then to the north or positive drift values for each drift target. The recorded lateral force versus drift ratio response of Wall 2 is plotted in Figure 6.27 and Figure 6.28. Figure 6.29 presents the lateral force versus drift envelope (backbone) response of Wall 2.

Table 6.2 summarizes the lateral force and drift values for all milestones for Wall 2 specimen. The first flexural cracks formed at the end of the first cycle to -0.2% drift ratio while the first inclined crack was observed during the first cycle of -0.75% drift ratio. The first yield in the longitudinal reinforcement was identified from the strain gauge readings at the end of the first cycle to a drift ratio of + or - 0.5%. The maximum applied lateral force of 330.10 kips (1468.35 KN) was recorded at the end of the first cycle to a drift ratio of -2.0%. The lateral load resistance of the wall remained relatively stable up to the first cycle of -2.0% drift ratio. During the second cycle to -2.0% drift ratio, two QST longitudinal reinforcing bars in the north boundary region spliced with friction welded couplers suffered fracture away from the coupler. As the wall was pushed to the third cycle of -2.0% drift ratio, two additional longitudinal reinforcing bars in the north boundary fractured. During the first cycle to drift ratio of -3.0%, the remaining longitudinal bars in the north boundary fractured below the coupler. The lateral strength at this point dropped below 50% of the peak strength. It is noteworthy that all the bar fractures occurred at the friction welds at the edge of couplers. As the test continued and went to the second cycle of -3.0% drift ratio, longitudinal reinforcing bars in the web region of the wall specimen suffered fracture at the wall footing interface. None of the bars spliced with taper-threaded couplers fractured in the south boundary region. The test was stopped after several longitudinal reinforcing bars in web region were fractured and the wall showed signs of lateral instability. The wall was able to carry the targeted axial load throughout the test.

Wall 2 did not maintained lateral strength to a drift ratio of 3%, which is deemed necessary for special concrete seismic systems under an MCE level event (ASCE/SEI 7(American Society of Civil Engineers (ASCE), 2022)). This wall is therefore deemed not to have performed as needed for regions of high seismicity.

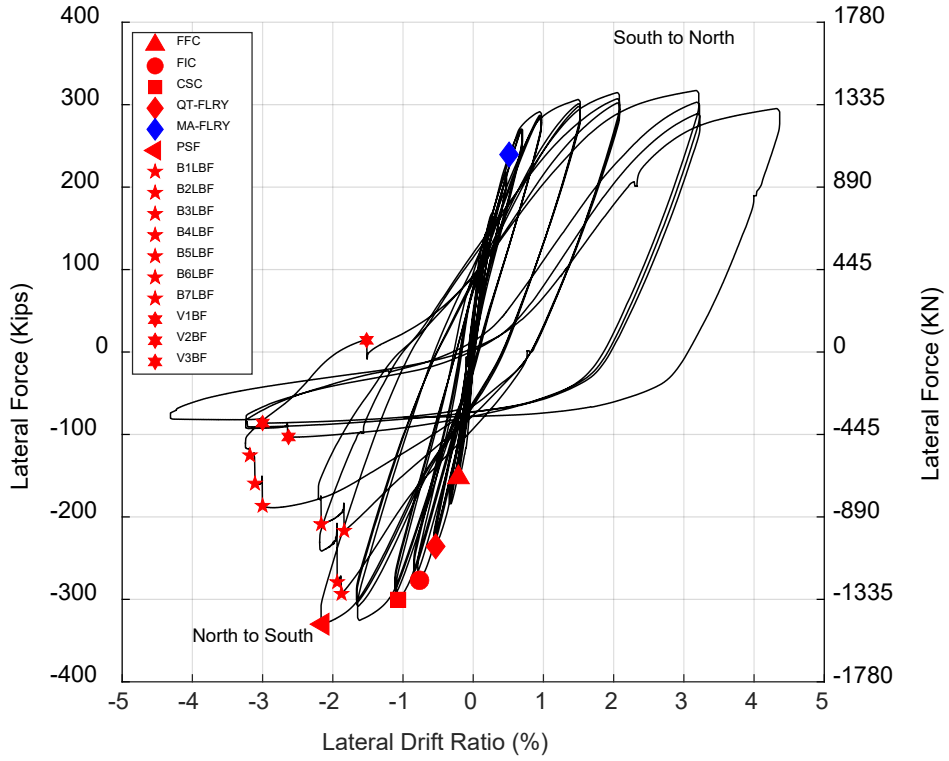

Figure 6-27: Wall 2 -lateral load versus drift ratio response

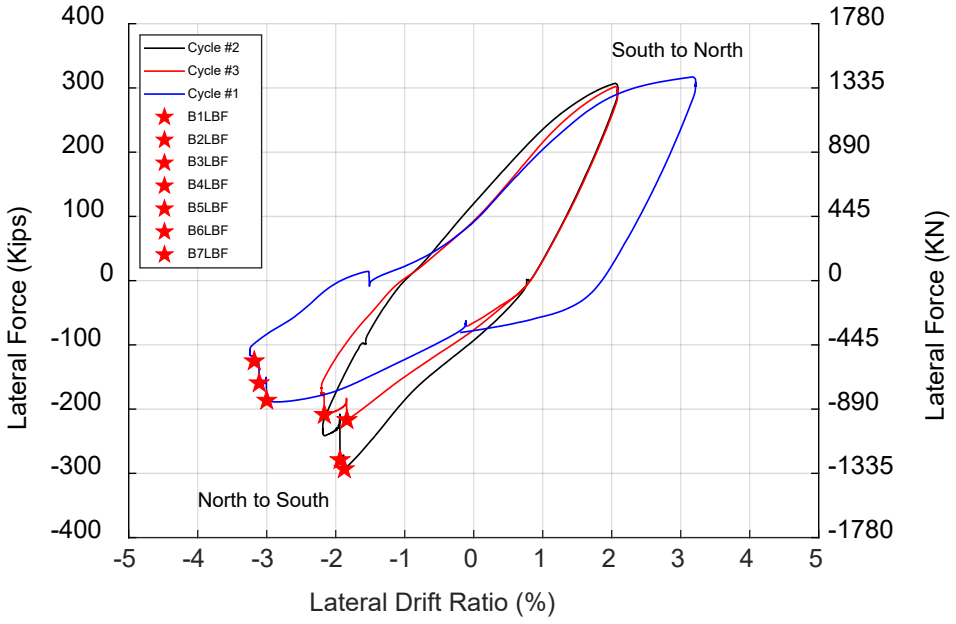

Figure 6-28: Wall 2 -last cycle response

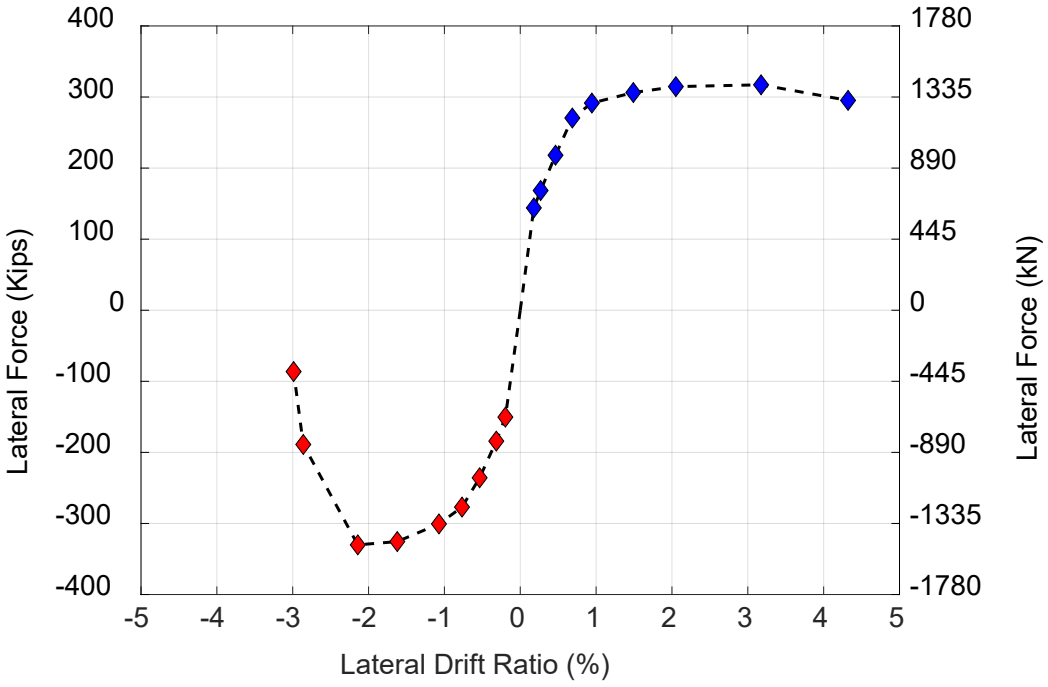

Figure 6-29: Wall 2 -backbone response

Table 6.2 :Wall 2-behavioral milestones

Milestone	Drift Ratio (%)	Lateral Load (kips)
First Flexural Crack	-0.21	-152.12 (676.66 KN)
First Inclined Crack	-0.75	-276.87 (1231.57 KN)
First Long. Reinf. Yield (QST)	-0.50	-235.74 (1048.62 KN)
First Long. Reinf. Yield (MA)	+0.50	+239.48 (1065.25 KN)
Cover Splitting Crack (CSC)	-1.06	-300.55 (1336.91 KN)
Peak Shear Force (PSF)	+2.00	+330.10 (1468.35 KN)
Longitudinal Bar Fracture (B1-LBF)	-1.87 -2.0	-293.35 (1304.88 KN)
Longitudinal Bar Fracture (B2-LBF)	-1.94 -2.0	-279.12 (1241.58 KN)
Longitudinal Bar Fracture (B3-LBF)	-1.84 -2.0	-216.84 (964.55 KN)
Longitudinal Bar Fracture (B4-LBF)	-2.16 -2.0	-208.72 (928.43 KN)
Longitudinal Bar Fracture (B5-LBF)	-3.0 -3.0	-186.50 (829.59 KN)
Longitudinal Bar Fracture (B6-LBF)	-3.10 -3.0	-159.50 (709.49 KN)
Longitudinal Bar Fracture (B7-LBF)	-3.18 -3.0	-125.29 (557.32 KN)
Longitudinal Bar Fracture (V1-LBF)	-2.63 -3.0	-103.03 (458.29 KN)
Longitudinal Bar Fracture (V2-LBF)	-3.0 -3.0	-86.16 (383.26 KN)
Longitudinal Bar Fracture (V3-LBF)	-1.5 +3.0	-14.23 (63.30 KN)

Note: for bar buckling and bar fracture, the maximum prior drift ratio and the actual drift at which milestone occurred are reported; the top value reports actual drift and the bottom value reports maximum prior drift ratio.

6.3.2 Test Pictures of Wall 2

Figure 6.30 to Figure 6.31 show pictures of the control wall at various stages of loading and damage.

At peak of 1st cycle to -1.0% drift (South side)

At peak of 2nd cycle to +1.5% drift (South side)

At peak of 1st cycle of +2.0% drift, Inclined cracks seen from

At peak of 1st cycle of +2.0% drift, Inclined cracks seen from east

Figure 6-30: Wall 2-test pictures at peak of drift targets

At the peak of 2nd cycle of -2.0% drift, first bar fracture (QST) (Northeast corner)

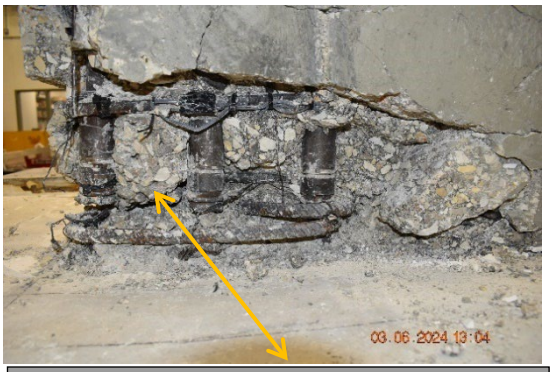

At the peak of 2nd cycle of -2.0% drift, second bar fracture (QST) (Northwest corner)

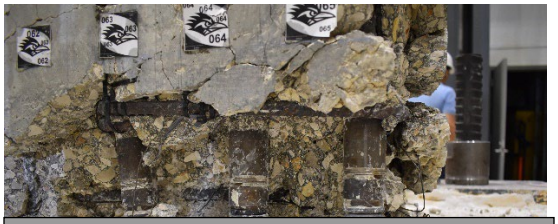

At the peak of 3rd cycle of -2.0% drift, middle bars fracture (QST) -east and west side

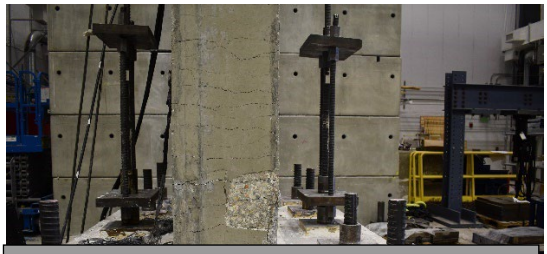

No bar fracture
South side boundary region

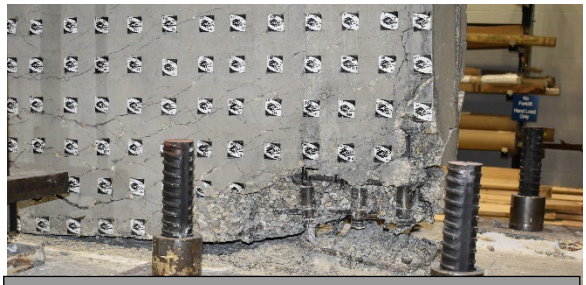

At the peak of 1st cycle of -3.0% drift, web bars fracture (QST)

Figure 6-31: Wall 2-pictures of buckled and fractured bars at the peak of 2.0% drift ratio (second and third cycles)

6.3.3 Strain Histories

Maximum strain demands were recorded above the taper threaded couplers used with micro-alloying bars and below the friction welded couplers used with quenching and self-tempered bars up to a drift ratio of 1.5%. Beyond that drift, strain demands above the couplers were largest.

Figure 6.32, Figure 6.33,Figure 6.34 and Figure 6.35 show a typical strain versus lateral drift response in boundary regions below the couplers at 1.5 in. (38.1 mm) from top of footing, and above couplers at 9 in. (228.6 mm) from footing. In the figures, strain gauge naming includes the two-letter abbreviation of the coupler name splicing the instrumented bars. As can be seen on the figures, strain values reached 6% in tension in some cases (Figure 6.33). The first yield of longitudinal reinforcement strain was recorded at + or – 0.5% drift ratio. Figure 6.34 and Figure 6.35 indicate that after bar fractured at the QST north end during the 2% drift ratio cycles, strains in the MA longitudinal bars at the south end no longer reversed into compression, reversing only to +0.5% to 2% tension strains while their boundary region was under compressive stresses. In other words, due to the loss of tension strength at the QST north boundary, the south boundary strains could no longer be reversed into compression. This alleviated the cyclic strain demands on the MA bars and their couplers at the north boundary.

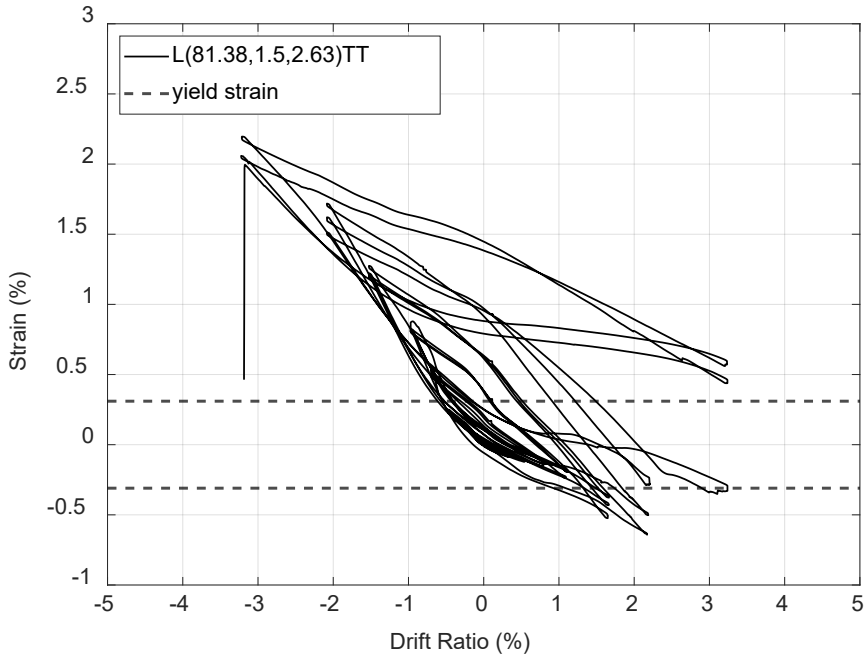

Figure 6-32: Wall 2 strain gauge at 1.5 in. (38.01 mm) from the wall to footing interface for the south end MA corner reinforcing bar spliced with a taper threaded coupler

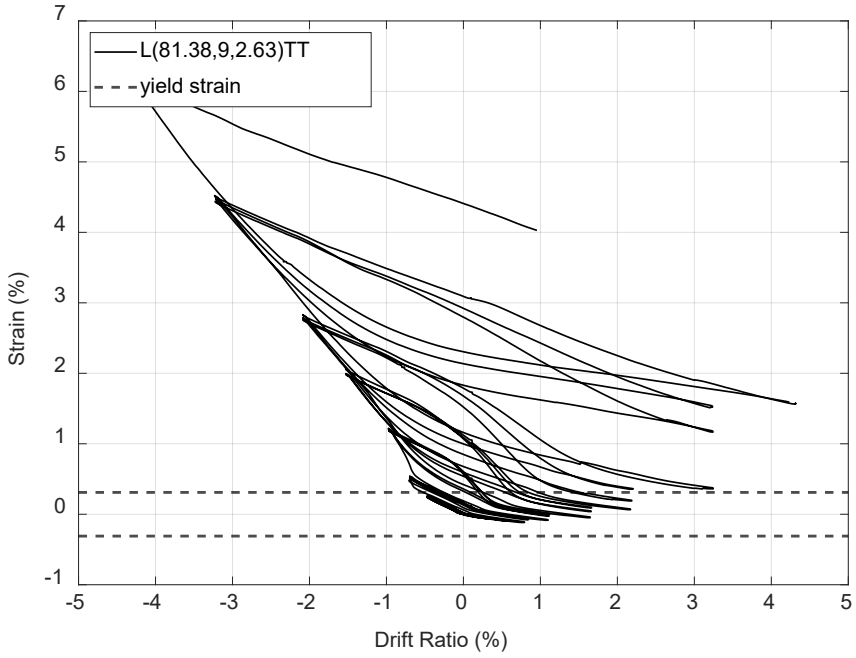

Figure 6-33: Wall 2 strain gauge at 9 in. (228.06 mm) from the wall to footing interface for the south end MA corner reinforcing bar spliced with a taper threaded coupler

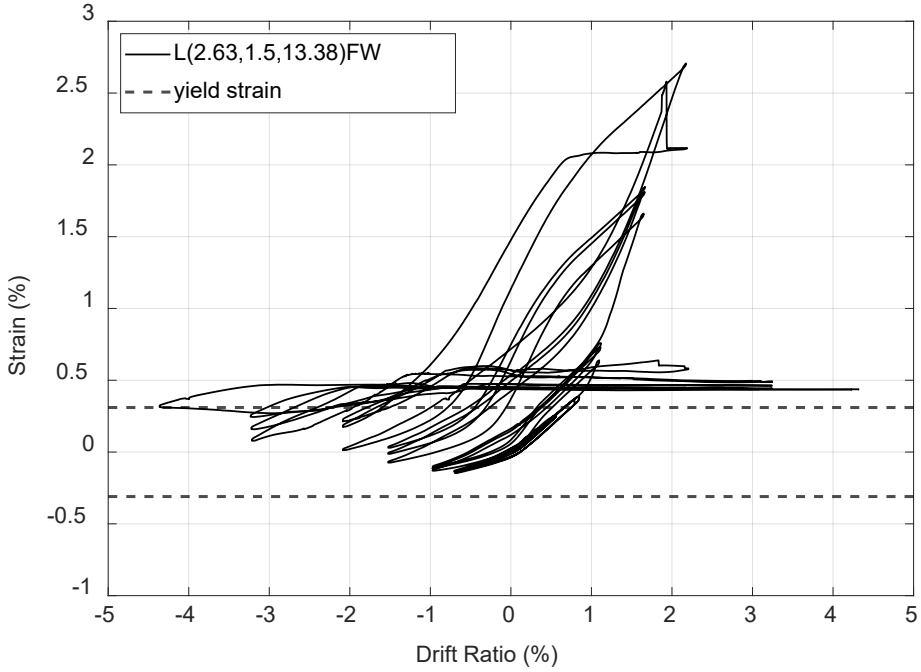

Figure 6-34: Wall 2 strain gauge at 1.5 in. (38.01 mm) from the wall to footing interface for the north end QST corner reinforcing bar spliced with a friction welded coupler

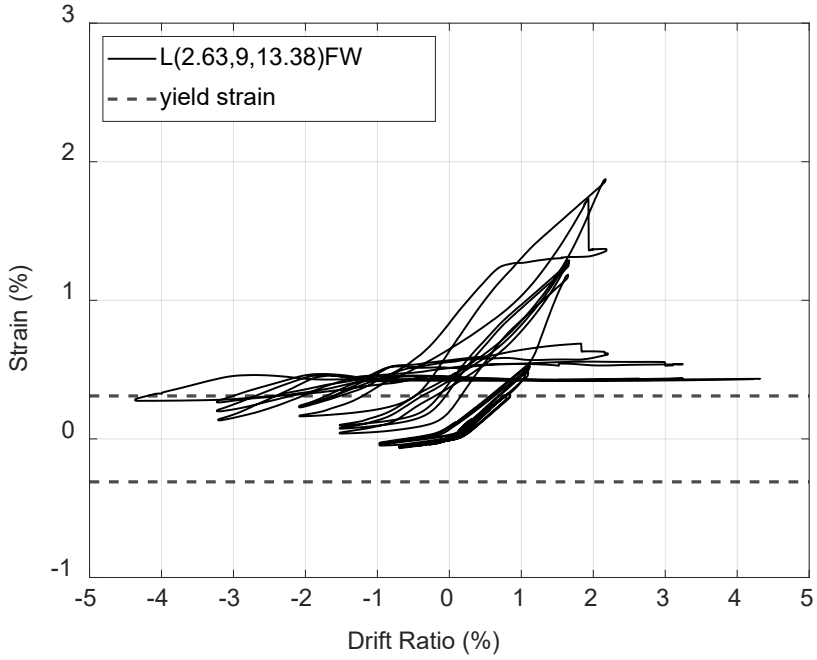

Figure 6-35: Wall 2 strain gauge at 9 in. (228.06 mm) from the wall to footing interface for the north end QST corner reinforcing bar spliced with a friction welded coupler

6.3.4 Longitudinal Reinforcing Bar Strain Demands

The recorded tension strain data from all three cycles were averaged and then plotted against the lateral drift ratio. Figure 6.36 and Figure 6.37 show the strain demands versus drift ratio of corner longitudinal reinforcing bar for both boundary regions. After yielding, the strain demands increased more rapidly with increasing drifts in longitudinal reinforcing bars. For the south end MA bar with a TT (taper threaded) coupler, strain demands were consistently larger just above the coupler than below it. For the north end QST bar with a FW (friction welded) coupler, strain demands were larger below the coupler up to a drift ratio of 1.5% but then became larger above the coupler at larger drifts. Strains continued to increase in the south end MA bars with taper threaded couplers as drift increased until the end of the test. However, strain demands increased in the QST corner bar until a drift ratio of 2.0% and subsequently dropped due to QST bar fracture that occurred during the second cycle at the 2.0% drift ratio.

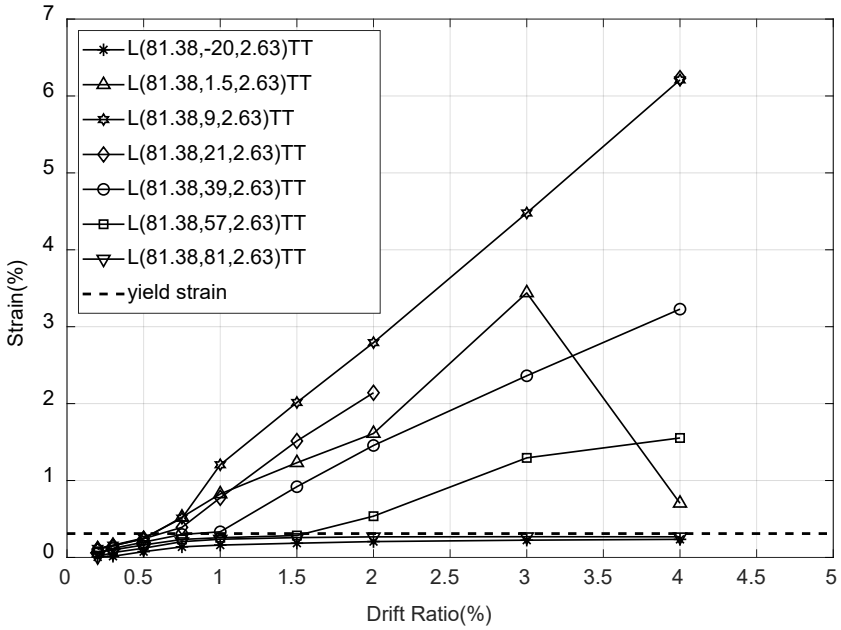

Figure 6-36: Wall 2 longitudinal reinforcement strain demands at drift targets for the south end MA corner reinforcing bar spliced with a taper threaded coupler

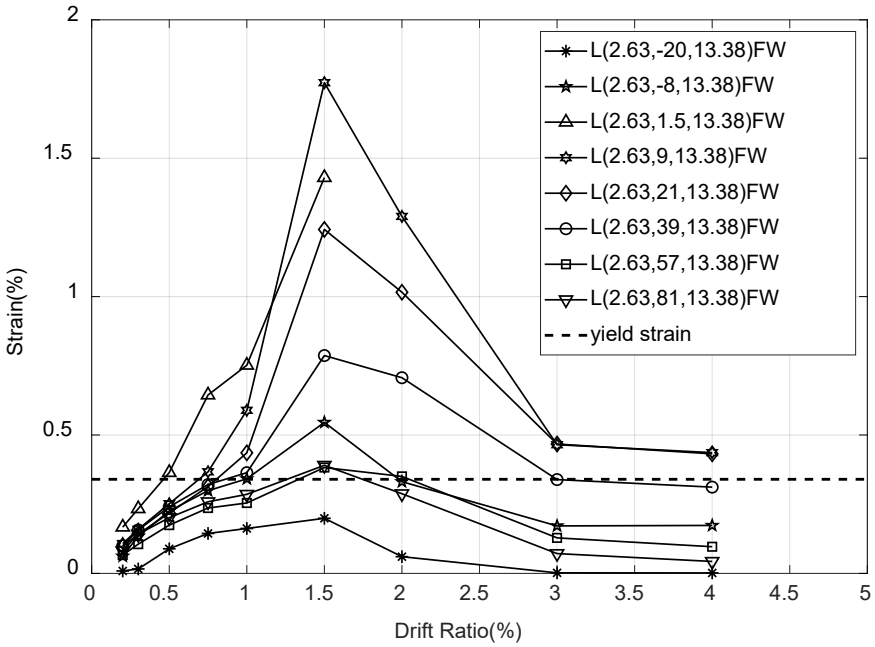

Figure 6-37: Wall 2 longitudinal reinforcement strain demands at drift targets for the north end QST corner reinforcing bar spliced with a friction welded coupler

6.3.5 Strain Gauge Profiles along Height

Tension strain readings over the height of longitudinal reinforcing bar in boundary regions are given in Figure 6.38 and Figure 6.39. As the wall was pushed past the first yield to higher drifts, inelastic strains were able to spread at least 81 in. (2057.54 mm) from the end of the wall. At both ends of the wall, strain demands can be seen in Figure 6.38, Figure 6.39 to be largest above the couplers from a drift ratio of 1.5% and not at the wall-footing interface. A possible explanation is that as the bars are pulled in tension from the loading points, the couplers essentially act as heads in that they resist upward movement due to their geometry, which in turn reduces stress and strain demands on the bars below them.

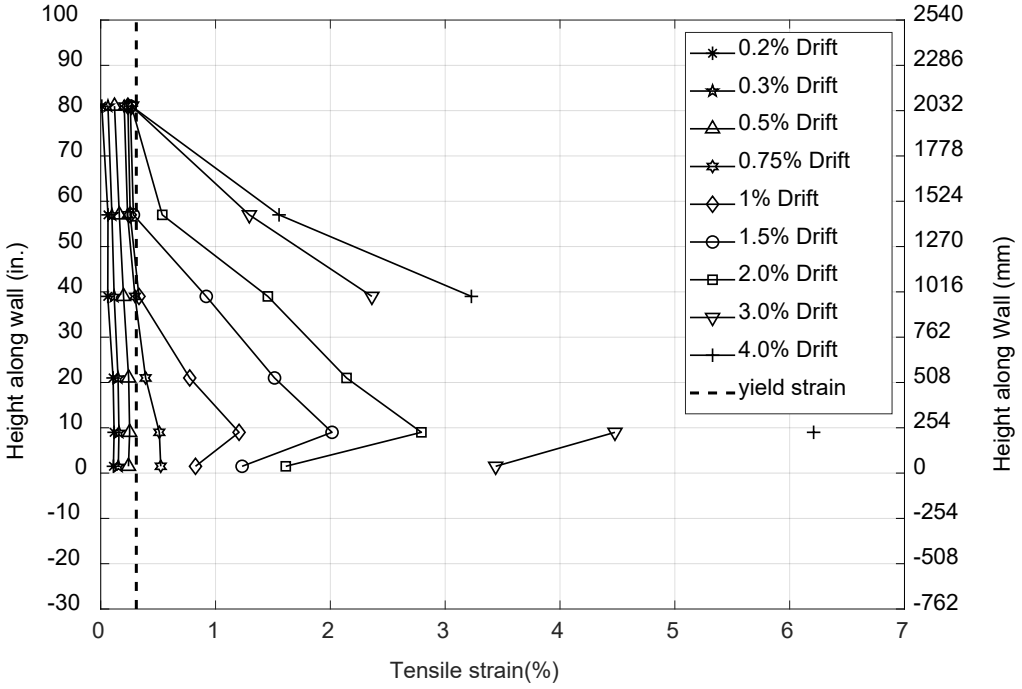

Figure 6-38: Wall 2 longitudinal reinforcement strain profiles for the south end MA corner bar spliced with a taper threaded coupler

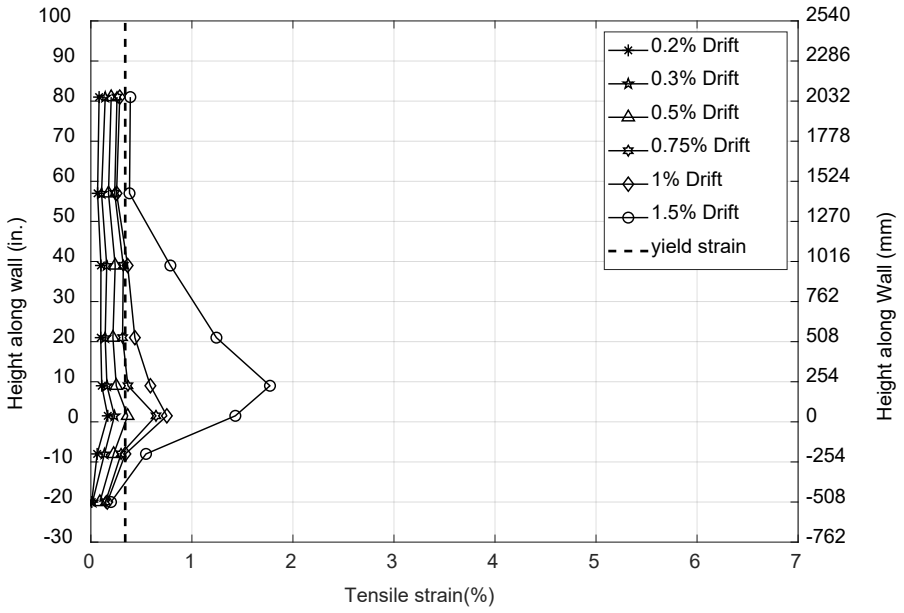

Figure 6-39-: Wall 2 longitudinal reinforcement strain profiles for the north end QST corner bar spliced with a friction welded coupler

6.3.6 Surface Strain along Height (DIC system)

Unfortunately, cameras during Wall 2 testing stopped functioning early in the test. Surface strain along the height from DIC system is unavailable for Wall 2.

6.3.7 Energy Dissipation

Energy dissipated for all three cycles versus drift ratio is plotted in Figure 6.40.The energy dissipated during the second cycle to a drift ratio of 2.0% was about 10% higher than the first cycle to 2.0% drift, after which longitudinal bar fractures were observed which resulted in lower than expected energy dissipation during subsequent cycles. After bars began to fracture, the hysteresis loop area was significantly larger when pushing to the north, placing the south boundary region in tension compared with the area of loop when pushing in the other direction (**Figure 6.27**). This contributed to the relatively stable energy dissipation during the first cycle to 3.0% drift ratio. By the second and third cycle to drift ratio of 3.0%, all the boundary bars fractured on the north side, which resulted in about 40% less energy dissipation per cycle.

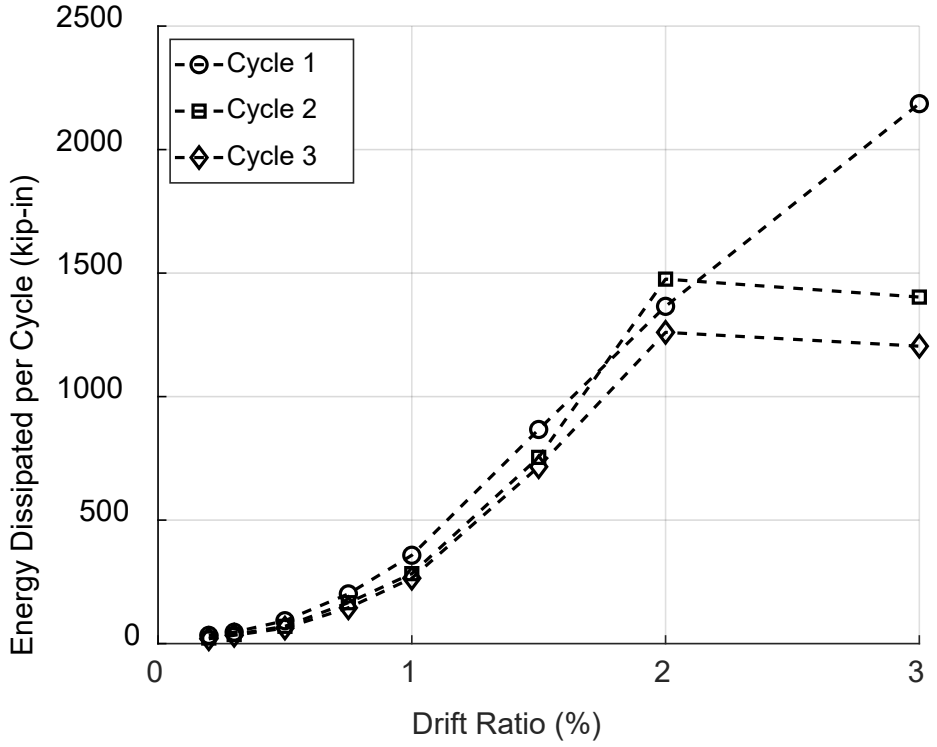

Figure 6-40: Wall 2 -energy dissipated in each full loading cycle

6.4 Test Results for Wall 3

Wall 3 was pushed to the south or negative drift values first and then to the north or positive drift values for each target drift. Micro-alloying boundary bars were spliced with grouted couplers at the south end and quenching and self-tempered boundary bars were spliced with swaged couplers at the north end (Figure 5.4 and Figure 5.6). These couplers were relatively long 12 to 13 in. (304.8 to 330.2 mm) and relatively thick with diameters around 2 in (50.8 mm). The axial load on the specimen was maintained between about 300 kips (1334.46 KN) and 400 kips (1779.28 KN) throughout the test as shown in Figure 6.42.

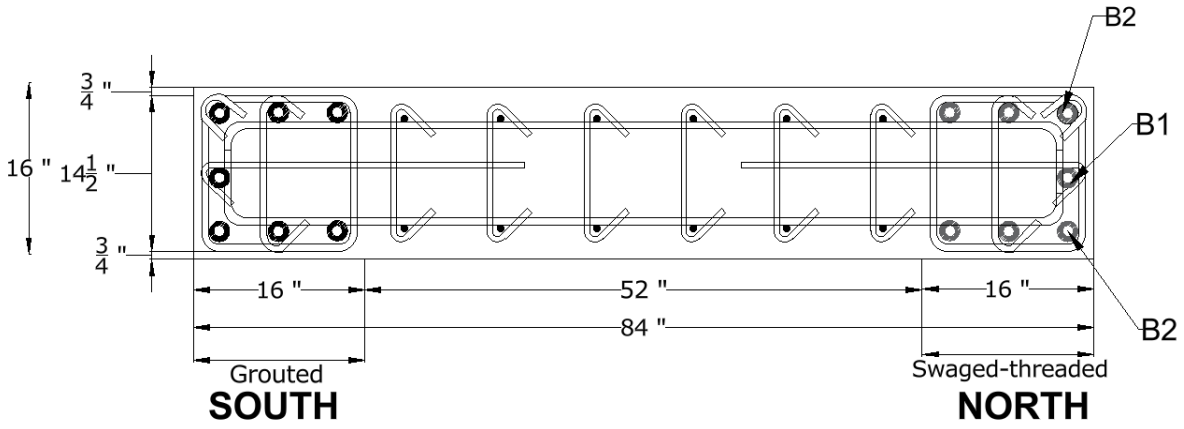

Figure 6-41: Wall 3- cross section and reinforcing bar location; the designation of the bars that fractured during test is shown

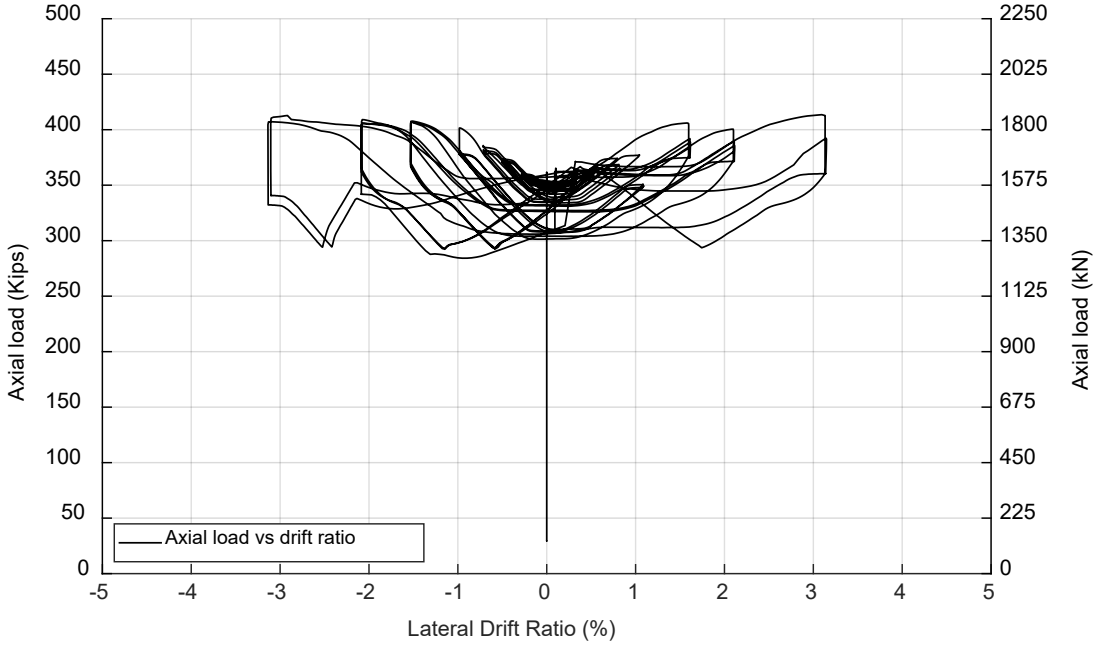

Figure 6-42: Wall 3- applied axial load versus drift ratio

6.4.1 General Behavior

The recorded lateral force versus drift ratio response of Wall 3 is plotted in Figure 6.43and Figure 6.44 . Figure 6.45 presents the lateral force versus drift envelope (backbone) response of Wall 3. Table 6.3 summarizes the lateral force and drift values for all milestones for Wall 3 specimen. The first flexural cracks formed at the end of the first cycle to -0.20% drift ratio. The first yield in the longitudinal reinforcement in the south end boundary region was identified from the strain gauge readings at the end of the first cycle to a drift ratio of + 0.50%. Flexural cracks then propagated leading to the formation of the first inclined crack at a drift ratio of -1.0%. As the wall was further pushed to drift ratio of -1.5%, spalling of concrete cover was observed. The maximum applied lateral force of 333.91 kips (1485.30 KN) was recorded at the end of the first cycle to a drift ratio of +3.0%. During the first cycle to +3.0% drift ratio, a corner longitudinal reinforcing bars in the south end boundary region spliced with the grouted couplers suffered fracture (

Figure 6.47). It was noteworthy that the fracture occurred away from the coupler. On the first excursion to -3.0% drift ratio, a corner longitudinal reinforcing QST bar fractured away from the coupler in the north boundary element of the wall. As the wall was pushed to the second cycle of +3.0%, the middle longitudinal reinforcing MA bar suffered fracture. The test was stopped after three bars fractured, and the wall became unstable due to boundary region buckling. The wall was able to carry the targeted axial load throughout the test.

Wall 3 maintained lateral strength and stability to a drift ratio of 3%, which is deemed sufficient for special concrete seismic systems under an MCE level event (ASCE/SEI 7(American Society of Civil Engineers (ASCE), 2022)).

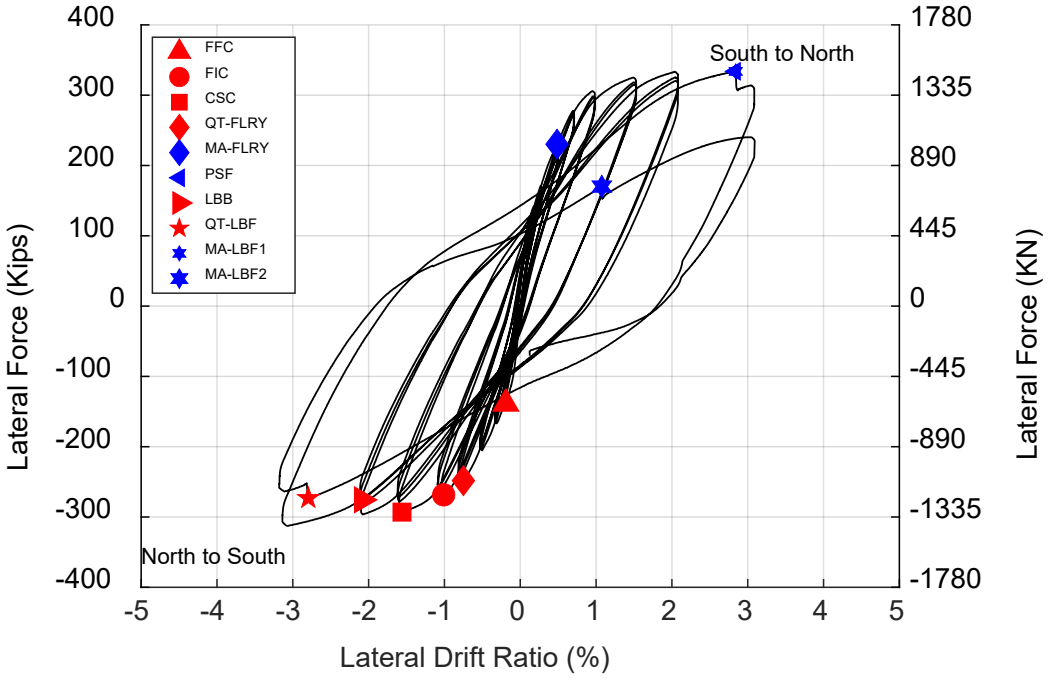

Figure 6-43-Wall 3 -lateral load versus drift ratio response

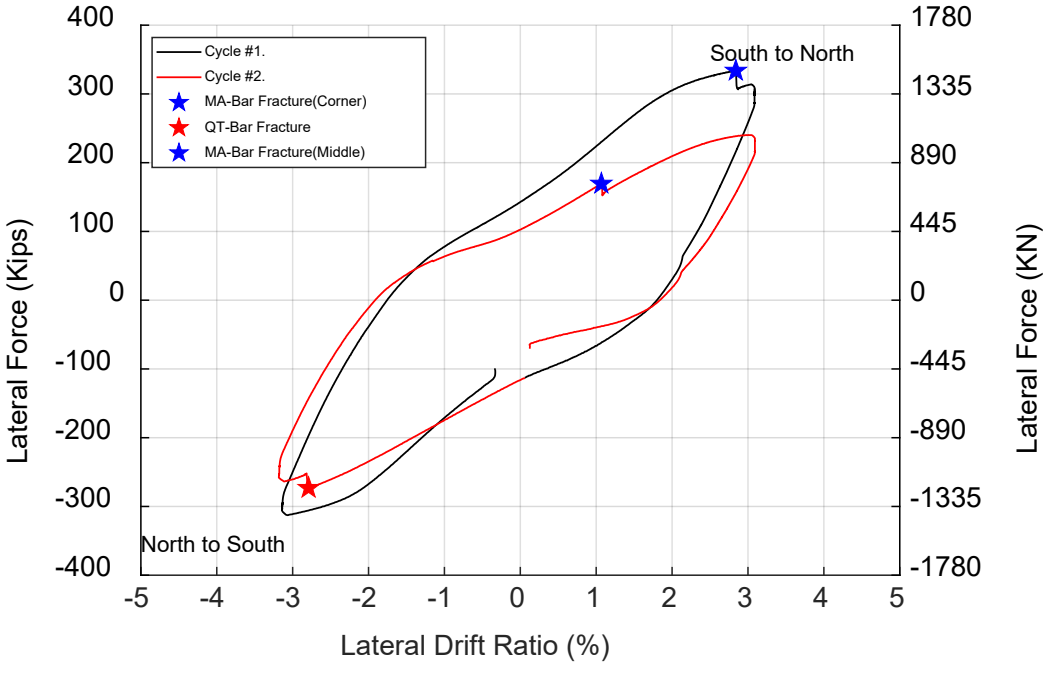

Figure 6-44: Wall 3- last cycles response

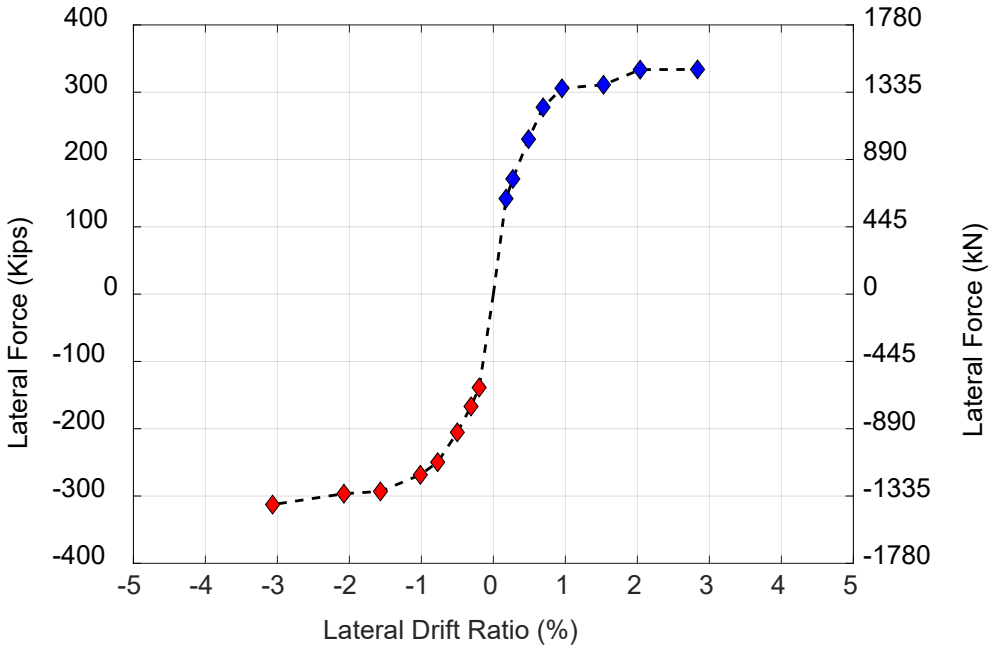

Figure 6-45 : Wall 3- backbone response

Table 6.3: Wall 3 behavioral milestones

Milestone	Drift Ratio (%)	Lateral Load (kips)
First Flexural Crack	-0.19	-138.77 (617.28 KN)
First Inclined Crack	-1.01	-268.47 (1194.21 KN)
First Long. Reinf. Yield (MA)	+0.48	+230.23 (1024.11 KN)
First Long. Reinf. Yield (QST)	-0.75	-248.34 (1104.66 KN)
Cover Splitting Crack	-1.56	-293.06 (1303.59 KN)
Peak Shear Force	+2.80	+333.91 (1485.30 KN)
Longitudinal Bar Buckling	+2.0	+329.80 (1467.02 KN)
Longitudinal Bar Fracture (QST)	-2.83 -2.0	-273.03 (1214.49 KN)
Longitudinal Bar Fracture B2 (MA)	+2.84 +2.0	+333.7 (1484.4 KN)
Longitudinal Bar Fracture B1 (MA)	+1.07 +3.0	+170 (756.19 KN)

Note: for bar buckling and bar fracture, the maximum prior drift ratio and the actual drift at which milestone occurred are reported; the top value reports actual drift and the bottom value reports maximum prior drift ratio.

6.4.2 Test Pictures of Wall 3

Figure 6.46 to Figure 6.47 show the pictures of Wall 3 at various stages of loading and damage.

At peak of 1st cycle of -1.0% drift, Flexural cracks are distinct

At peak of 1st cycle of 1.5 % drift, Spalling of concrete on both ends

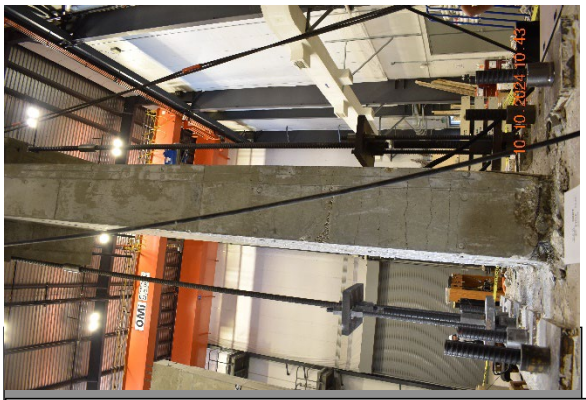

At peak of 1st cycle of -2.0 % drift, Spreading of flexural cracks on north side

At peak of 3rd cycle of +2.0 % drift, Inclined cracks seen from west side

Figure 6-46: Wall 3- pictures at peak of drift targets

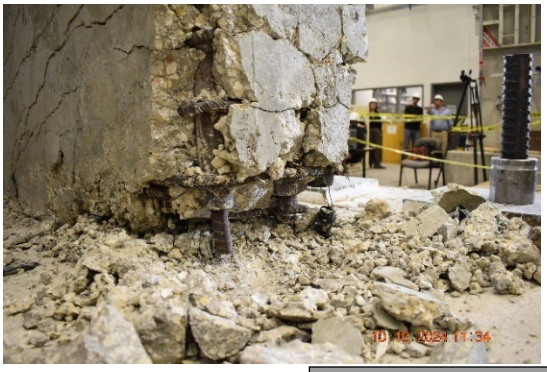

At peak of 1st cycle of +3.0 % drift, MA bars fracture below coupler at

At peak of 2nd cycle of -3.0 % drift, QST bars fracture below coupler at

At peak of 2nd cycle of +3.0 % drift, MA middle bar fracture south side below

Figure 6-47: Wall 3- pictures of fractured and buckled bars at end of test (3% drift ratio)

6.4.3 Strain Histories

Figure 6.48 and Figure 6.49 show a typical strain versus lateral drift ratio on south side boundary region below the couplers at 1.5 in. (38.01 mm) from the top of footing, and above the couplers at 21 in. (533.4 mm) from the wall-footing interface. Figure 6.50 and Figure 6.51 show the typical strain versus lateral drift response recorded on the north side middle reinforcing bar at 1.5 in. (38.01 mm, and 16 in. (406.4 mm) from the wall to footing interface.

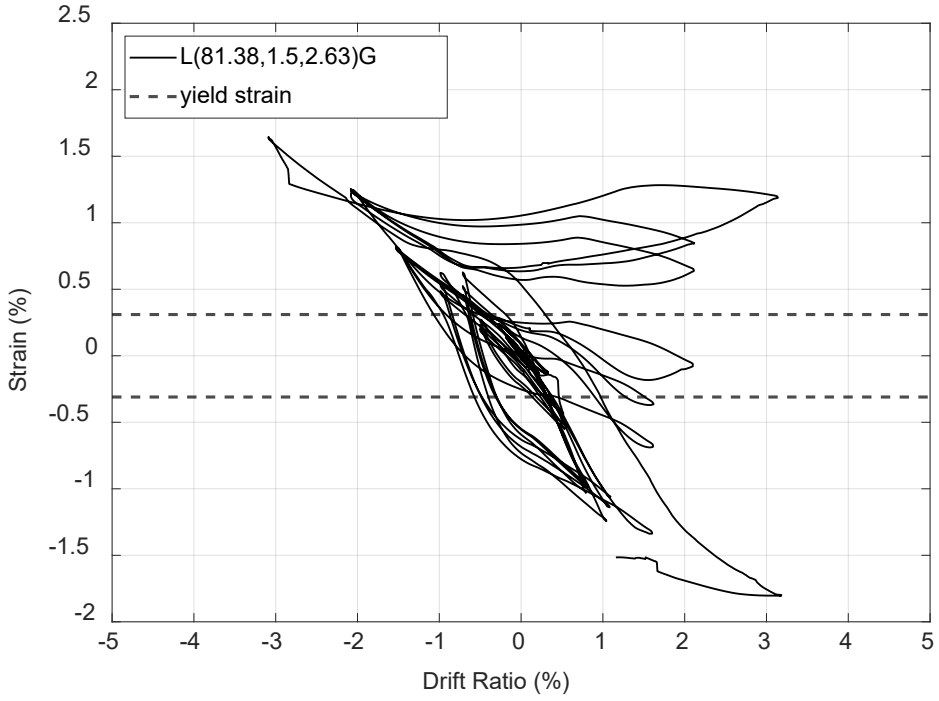

Figure 6-48: Wall 3 strain gauge at 1.5 in. (38.01 mm) from the wall to footing interface for south end MA corner reinforcing bar spliced with a grouted coupler

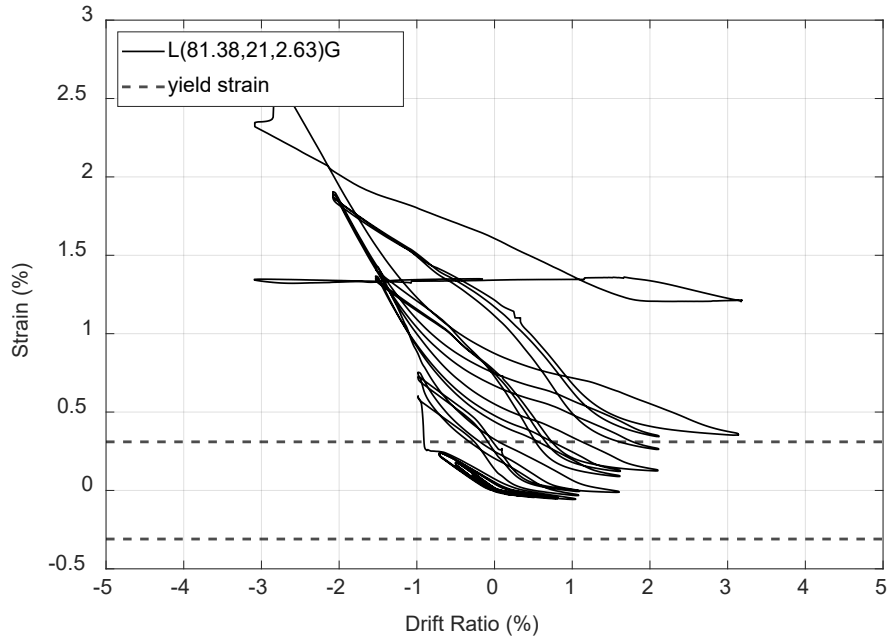

Figure 6-49: Wall 3 strain gauge at 21 in. (533.4 mm) from the wall to footing interface for the south end MA corner reinforcing bar spliced with a grouted coupler

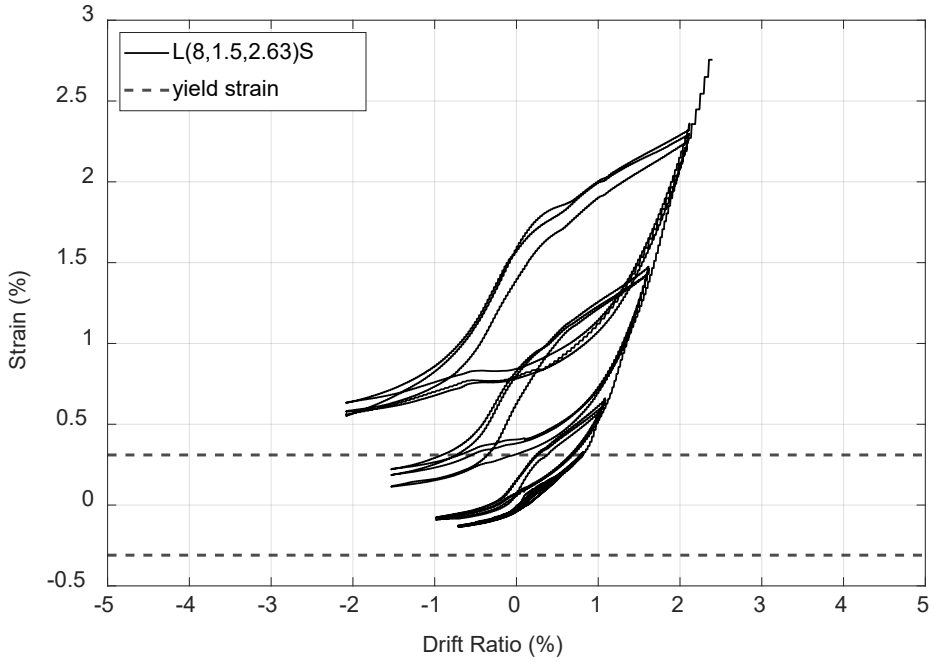

Figure 6-50: Wall 3 strain gauge at 1.5 in. (38.01 mm) from the wall to footing interface for the north end QST middle reinforcing bar spliced with a swaged coupler

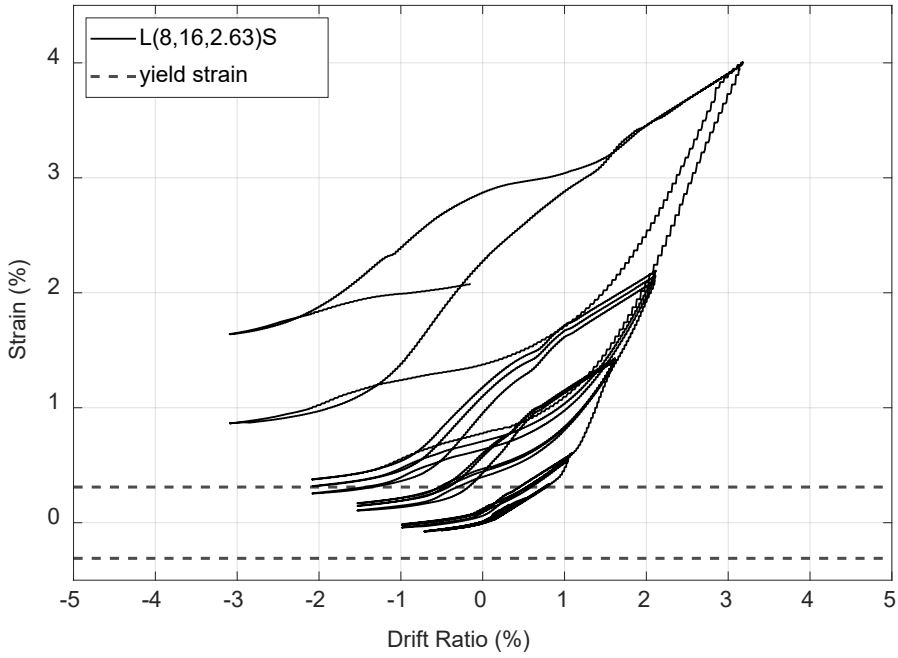

Figure 6-51: Wall 3 strain gauge at 16 in. (406.4 mm) from the wall to footing interface for the QST middle reinforcing bar spliced with a swaged coupler

6.4.4 Longitudinal Reinforcing Bar Strain Demands

Recorded tension strain data from all three cycles were averaged and then plotted against the lateral drift ratio. Figure 6.52 and Figure 6.53 show averaged strain demands versus drift ratio of corner middle longitudinal reinforcing bar for both boundary regions. After yielding, the strain demands increased more rapidly with drift in longitudinal reinforcing bars, with tension strains increasing to higher levels above the couplers rather than at the wall-footing interface. Strain demands appear to stabilize on the MA bars after the 2.0% drift ratio cycles, which may be attributed to the slip in the grouted coupler due to grout damage. The strain demand continued to increase on QST bar with swaged couplers throughout the test (Figure 6.53).

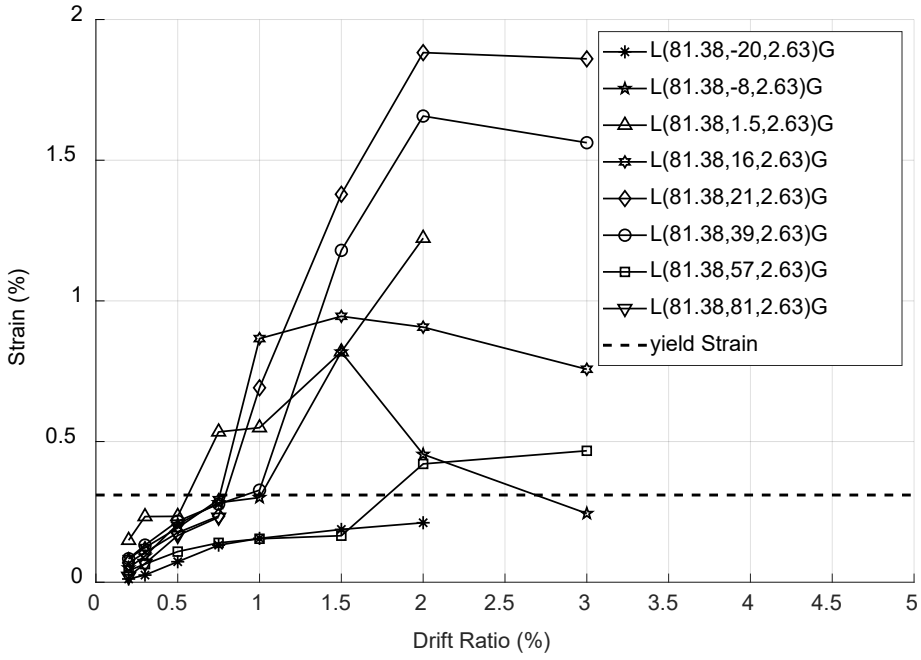

Figure 6-52: Wall 3 longitudinal reinforcement strain demands at drift targets for the south end MA corner reinforcing bar spliced with grouted couplers

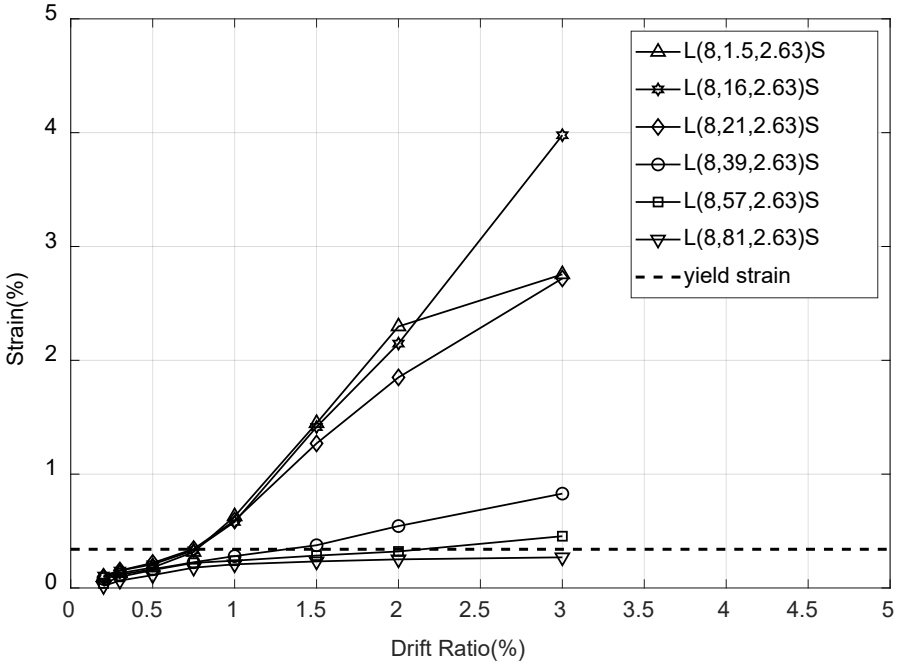

Figure 6-53: Wall 3 longitudinal reinforcement demands at drift targets for the north end QST middle reinforcing bar spliced with a swaged coupler

6.4.5 Strain Gauge Profiles along Height

Strain readings over the height of longitudinal reinforcing bar in boundary region are given in Figure 6.54, Figure 6.55 and Figure 6.56. As the wall was pushed past first yield to higher drifts, inelastic strains were able to spread at least 81 in. (2057.4 mm) for QST bars (Figure 6.56). Due to loss of strain gauges on the MA side, plasticity spread at the larger drifts could not be assessed. At both boundaries, as strain demands increased, they became higher above the couplers than at the wall to footing.

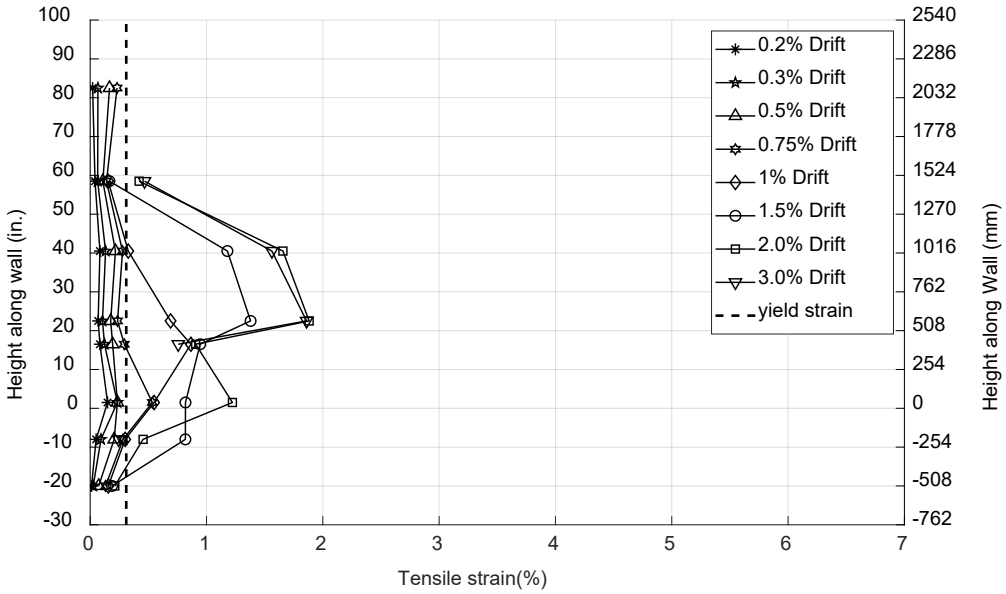

Figure 6-54: Wall 3 longitudinal reinforcement strain profiles for the south end MA corner bar spliced with a grouted coupler

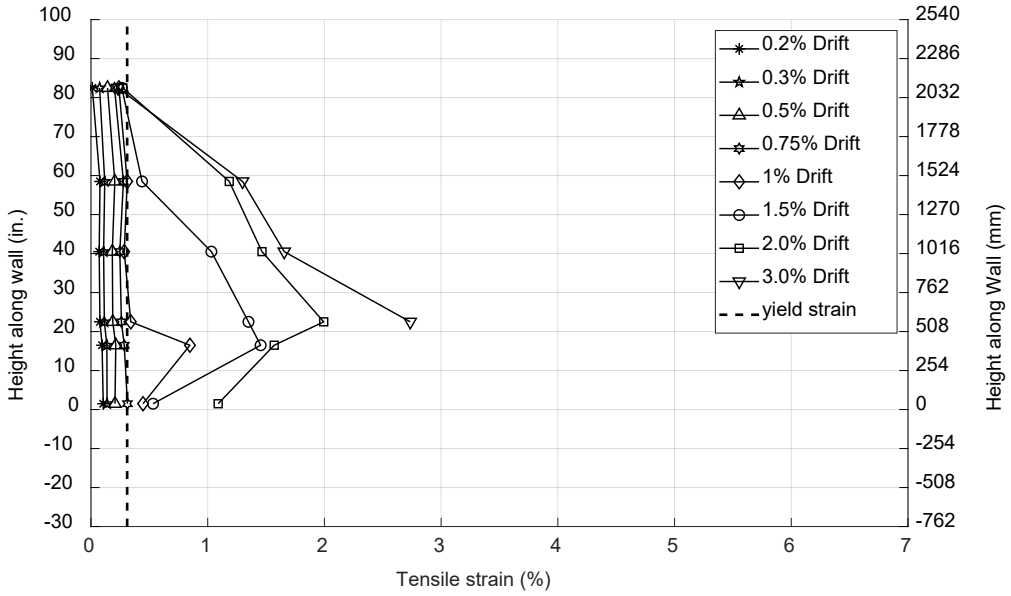

Figure 6-55: Wall 3 longitudinal reinforcement strain profiles for the south end MA middle bar spliced with a swaged coupler

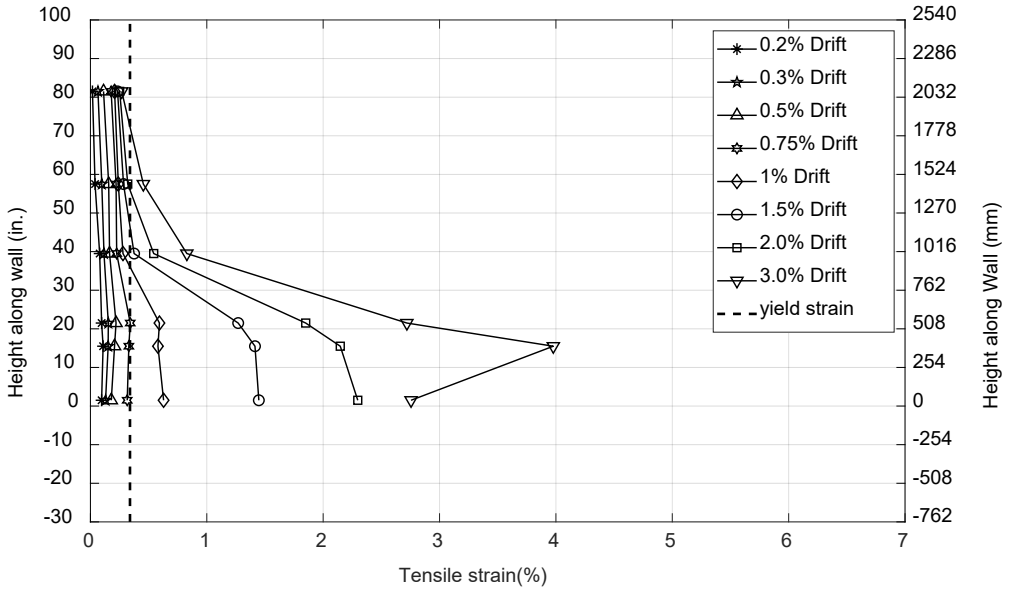

Figure 6-56 : Wall 3 longitudinal reinforcement strain profiles for the north end QST middle bar spliced with a swaged coupler

6.4.6 Surface Strain along Height (DIC System)

Vertical surface strains along the height of the wall specimen at the boundary regions were calculated from the recorded target displacements as described in section 4.1.5. Surface strain profiles are presented for targets facing the longitudinal boundary bars that were strain gauged. Figure 6.57 and Figure 6.58 show vertical surface strains along the height of the test specimen for the concrete facing the micro-alloyed corner and middle reinforcing bars in the south boundary region. Figure 6.59 and Figure 6.60 show vertical surface strains along the height of the test specimen for concrete facing the quenching and self-tempered longitudinal reinforcing bars in the north boundary region. As seen in the figures, tensile strains on the bars were generally higher above the mechanical couplers as was also observed from strain gauge recordings. The tensile strains were lower at the location of mechanical couplers at both boundary regions (Figure 6.56 to Figure 6.60)

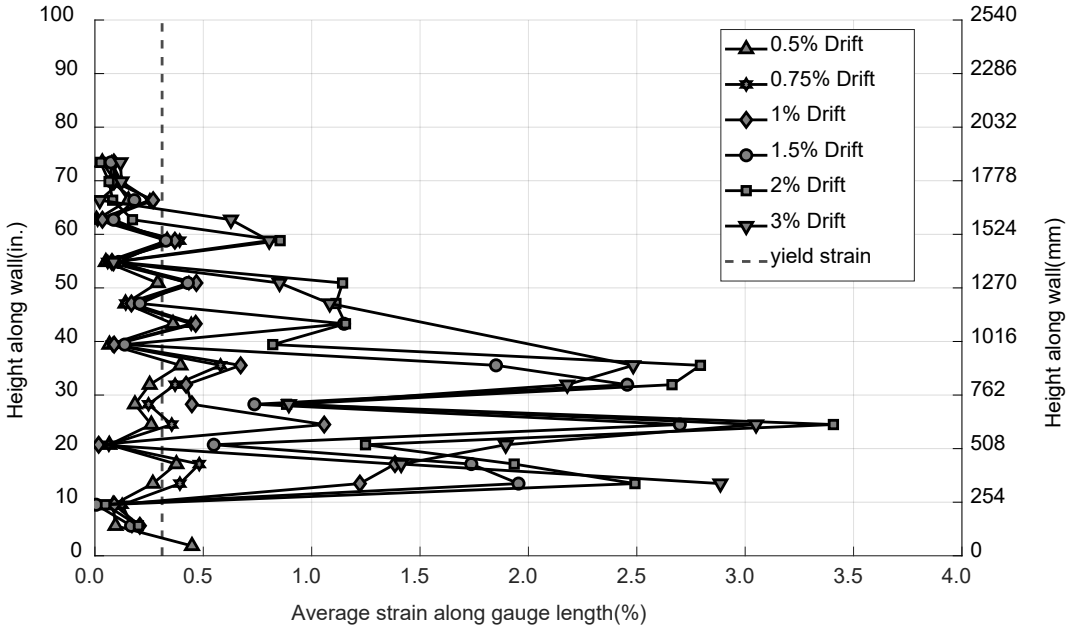

Figure 6-57: Vertical strain profiles from surface targets facing the south end MA corner reinforcing bar with a grouted coupler

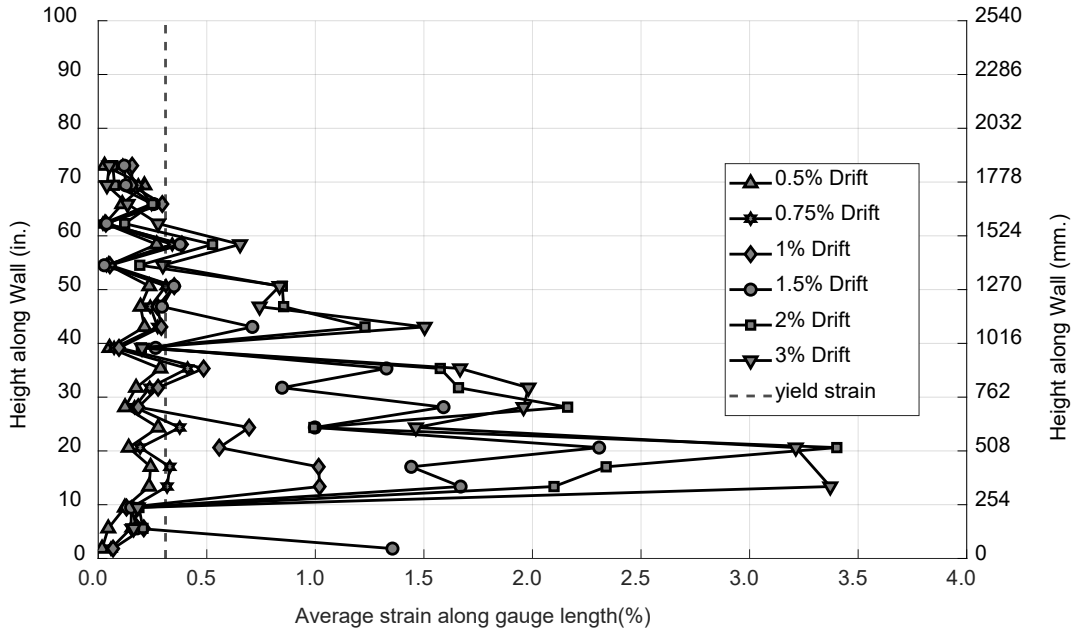

Figure 6-58: Vertical strain profiles from surface targets facing the south end MA middle reinforcing bar with a grouted coupler

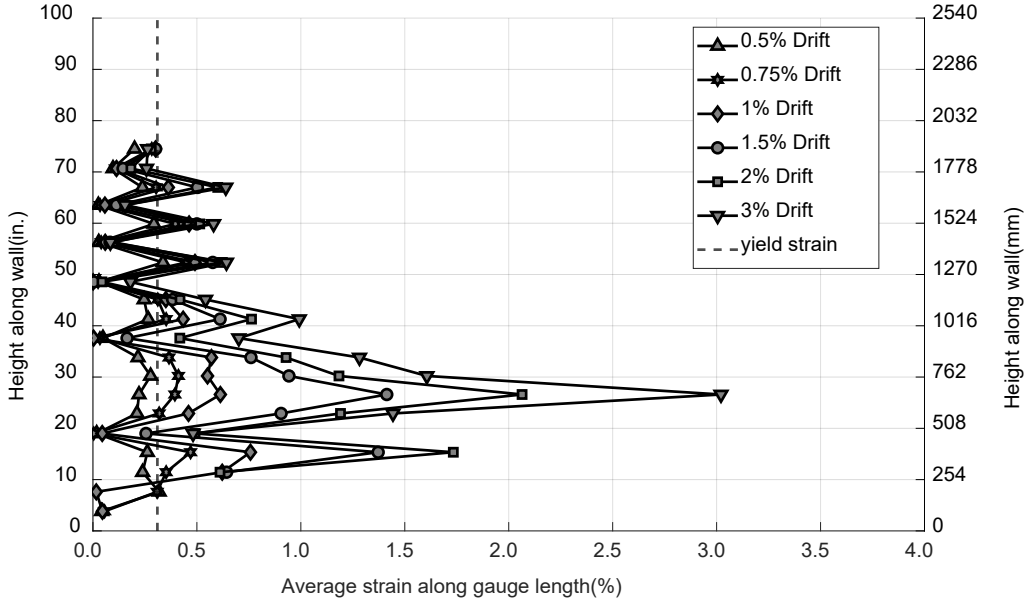

Figure 6-59: Vertical strain profiles from surface targets facing the north end QST corner reinforcing bar with a swaged coupler

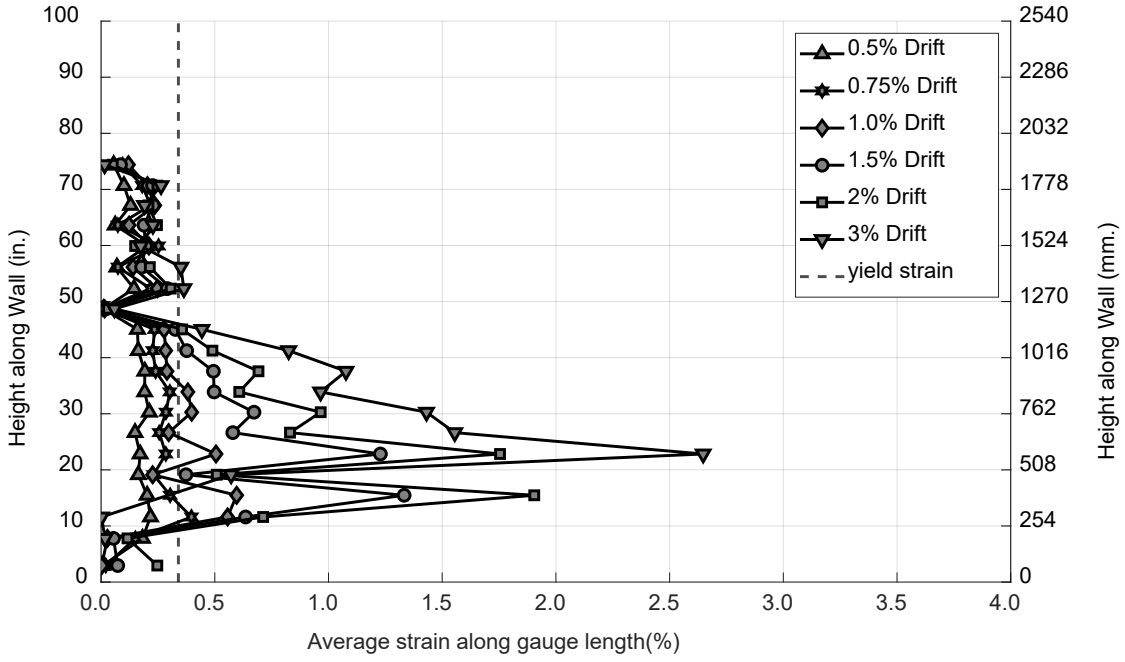

Figure 6-60: Vertical strain profiles from surface targets facing the north end QST middle reinforcing bar with a swaged coupler

6.4.7 Comparisons between Vertical Strains from DIC System and Strain Gauges

Longitudinal bar strain readings are compared with the surface vertical strain readings from the targets closest to the bars in Figure 6.61 and Figure 6.62 for the boundary region with MA bars spliced with grouted couplers and in Figure 6.63 and Figure 6.64 for the boundary region with QST bars spliced with swaged couplers. Section 6.1.5 explains how the surface strains were obtained, and which surface targets were used.

As can be seen in the figures, vertical surface strains match longitudinal bar strains reasonably well where strain gauge readings could be obtained, i.e., before strain gauge failure.

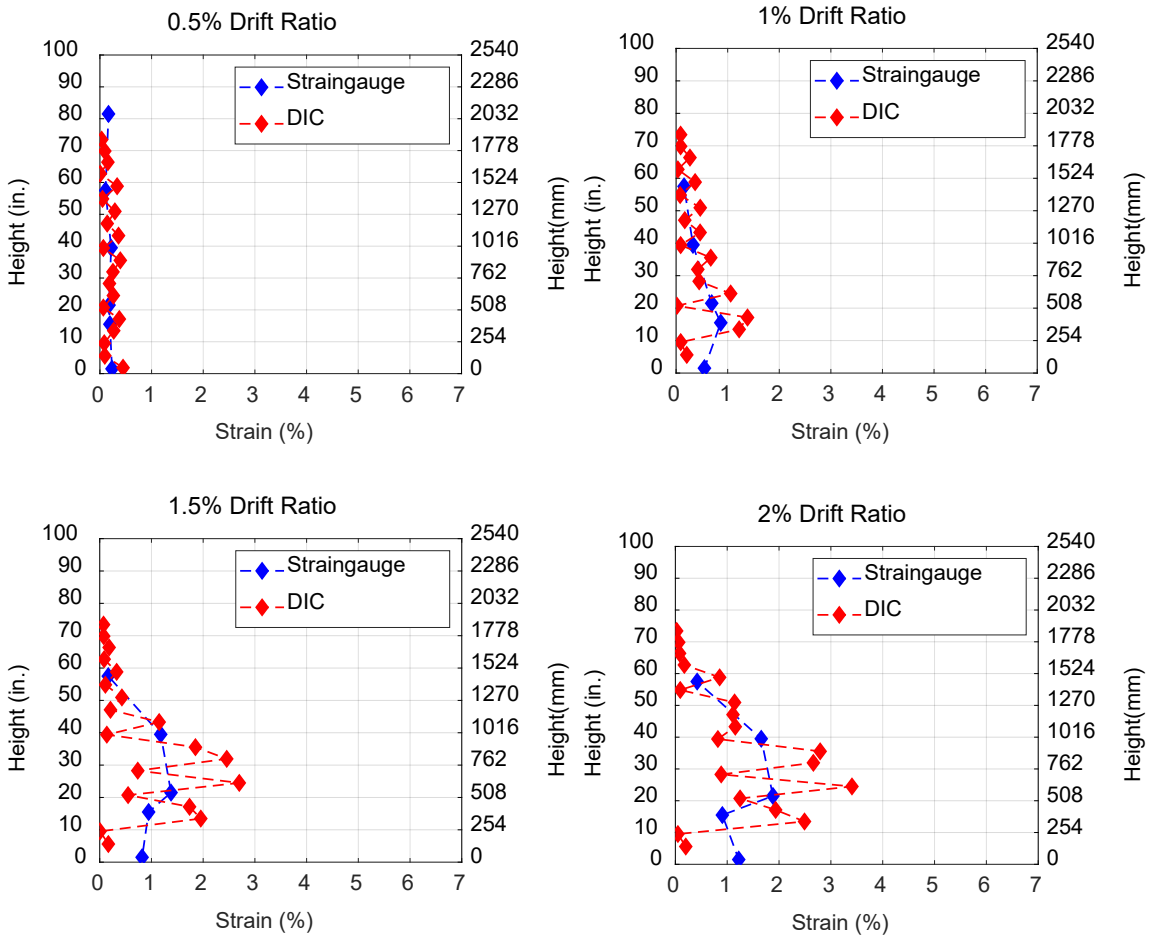

Figure 6-61: Strain profiles from strain gauges and DIC system for the south end MA corner bar spliced with a grouted coupler

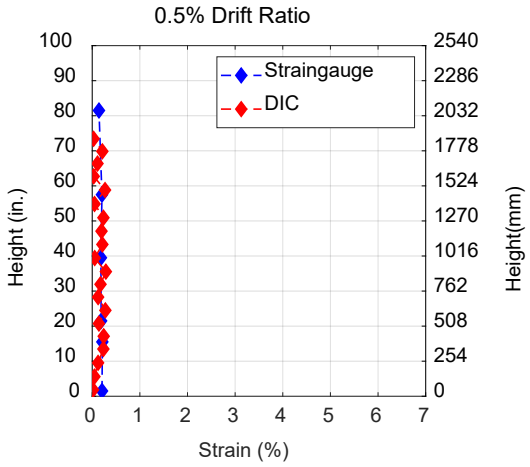

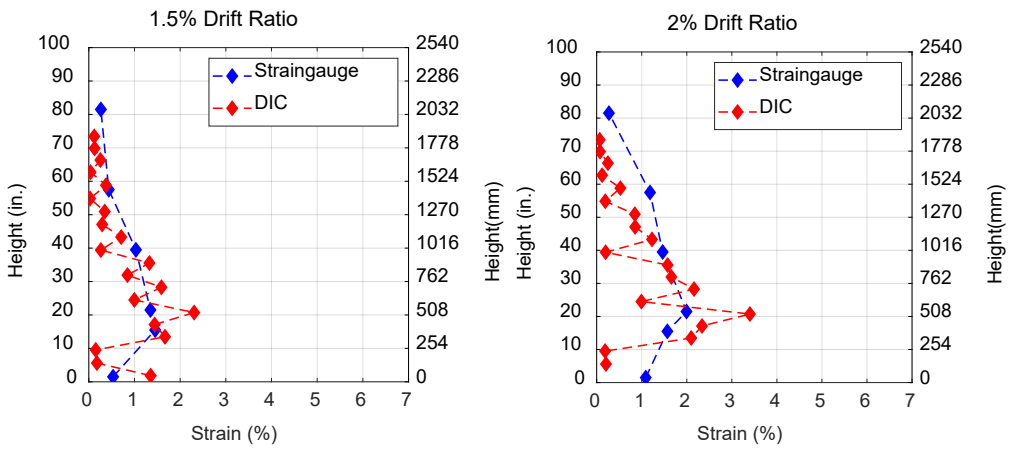

Figure 6-62: Strain profiles from strain gauges and DIC system for the south end MA middle bar spliced with a grouted coupler

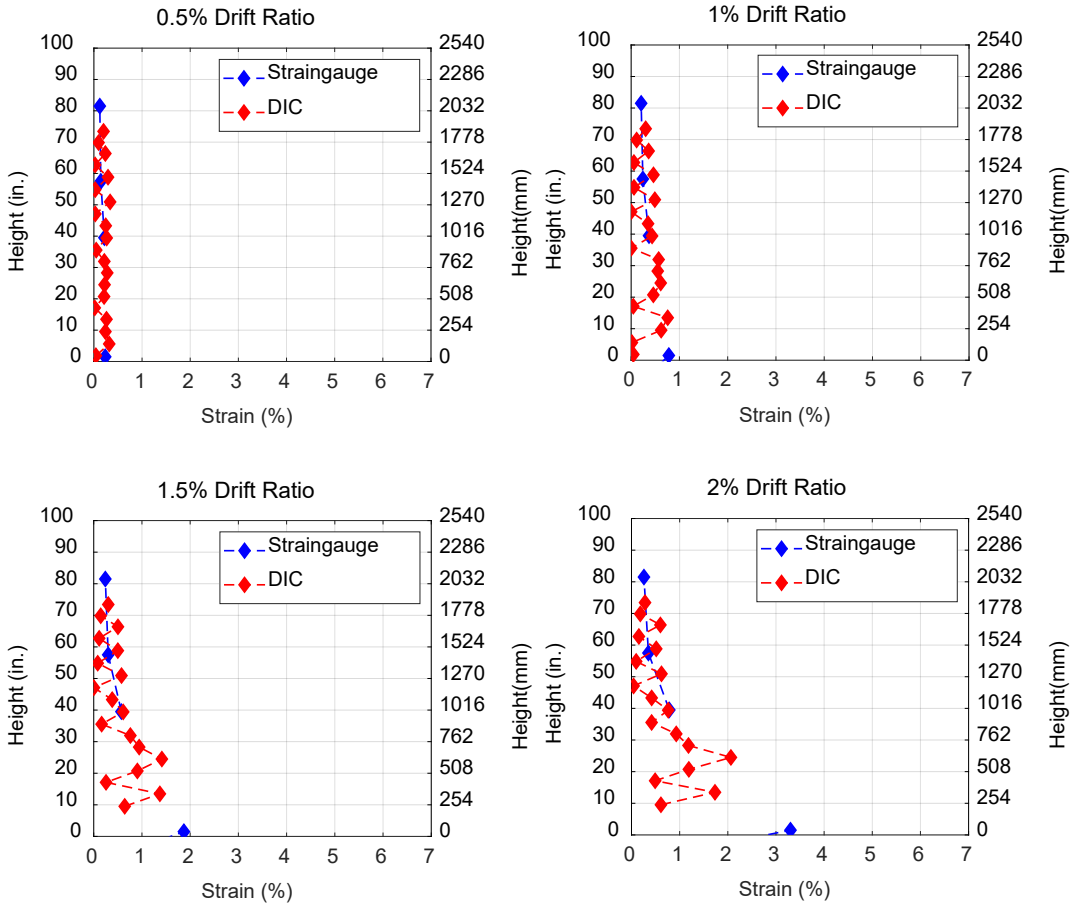

Figure 6-63: Strain profiles from strain gauges and DIC system for the north end QST corner bar spliced with a swaged coupler

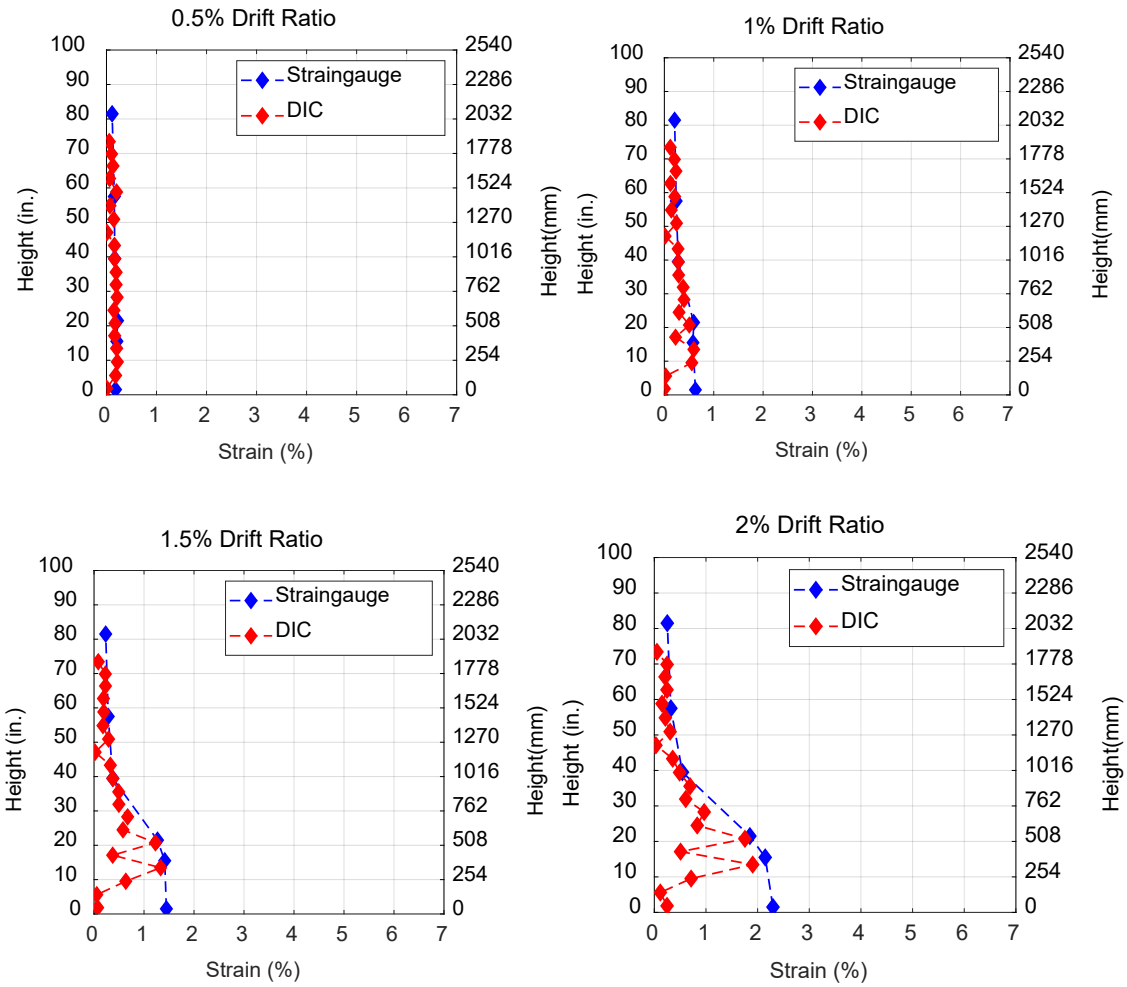

Figure 6-64: Strain profiles from strain gauges and DIC system for north end QST middle bar spliced with a swaged coupler

6.4.8 Energy Dissipation

The energy dissipated by the wall per cycle is shown in Figure 6.65. As can be seen in the figure, the amount of energy dissipated was similar for each cycle to a given drift target for Wall 3. The wall energy dissipation was stable up to a fracture of longitudinal bars in the last cycles (Figure 6.43).

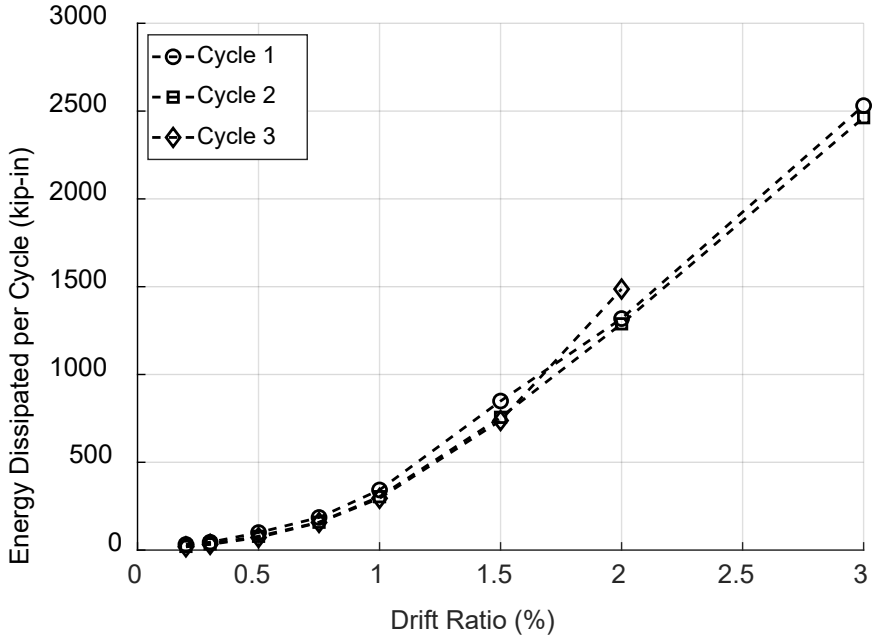

Figure 6-65: Energy dissipated in each full loading cycle (except 3%)

6.5 Test Result for Wall 4

Wall 4 was pushed to the north or positive drift values first and then to the south or negative drift values for each target drift. This was done to apply tension loading to the end grip couplers first for each increasing drift target since those couplers exhibited higher fatigue life than the friction welded couplers during in-air testing (*Part I In-Air Testing*) Micro-alloying boundary bars were used in both boundaries. This was done to explore the effect of bar manufacturing process on the fatigue behavior of friction welded couplers. These couplers exhibited differing low-cycle fatigue performance during in-air testing depending on bar type, with couplers splicing MA bars sustaining larger number of cycles before fracture than the same couplers splicing QST bars (Chapter 4 and *Part I In-Air Testing*). Since the friction welded splices with QST bars fractured relatively early resulting in unacceptable performance for Wall 2, Wall 4 was designed to explore whether the same coupler type with MA bars would result in acceptable wall performance. South end bars were spliced with end grip couplers while north end bars were spliced with friction welded couplers.

Couplers in the wall were relatively short with lengths equal to 3 or 3.75 in. (76.2 or 95.25 mm) and relatively slim with diameters approximately 2.5 or 1.38 in. (62.5 or 35.05 mm). The axial load on the specimen was maintained between about 300 kips (1334.46 KN) and 400 kips (1779.28 KN) throughout the test as shown in Figure 6.67.

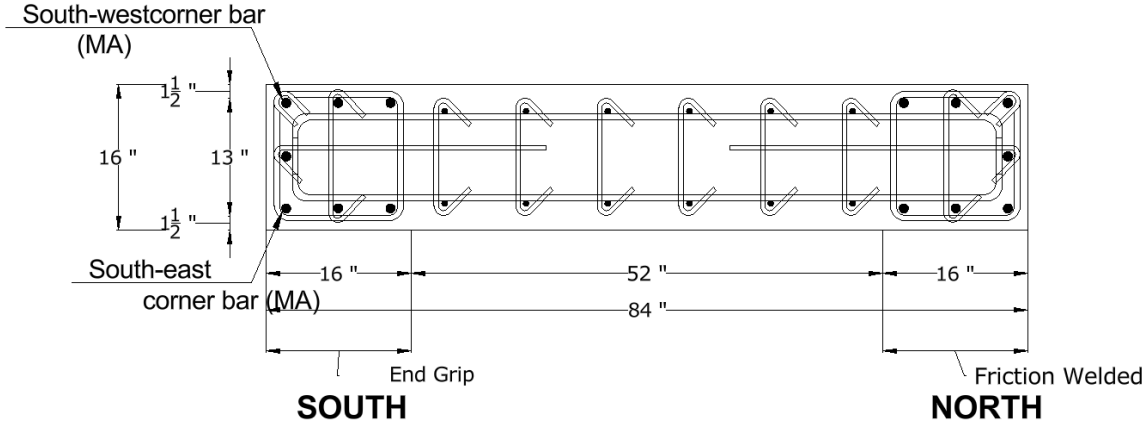

Figure 6-66: Wall 4- cross section and reinforcing bar location; the designation of the bars that fractured during test is shown

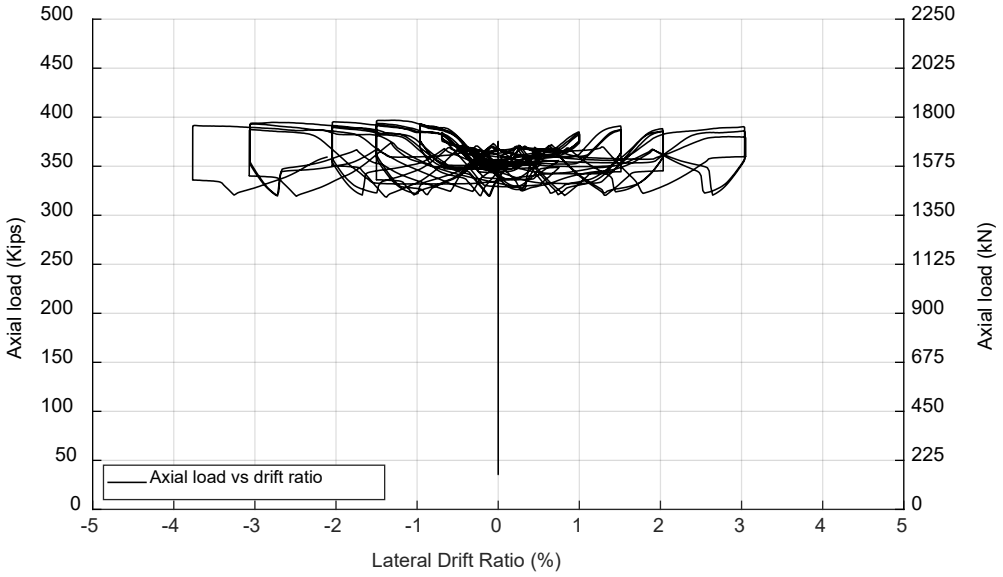

Figure 6-67: Wall 4- axial load versus drift ratio

6.5.1 General Behavior

The recorded lateral force versus drift ratio response of Wall 4 is plotted in Figure 6.68. The last cycle response of Wall 4 is plotted in Figure 6.69. Figure 6.70 presents the lateral force versus drift envelope (backbone) response of Wall 4. Table 6.4 summarizes the lateral force and drift values for all milestones for Wall 4. The first flexural cracks formed at the start of the first cycle to -0.20% drift ratio. The first yield in the longitudinal reinforcement in the south end boundary region was identified from the strain gauge readings at the end of the first cycle to a drift ratio of +0.50%. The flexural cracks then propagated leading to the formation of the first inclined crack at a drift ratio of +0.75%. As the wall was further pushed to a drift ratio of -1.5%, the spalling of concrete cover was observed at the boundary region with friction welded couplers. The maximum applied lateral force of 328.05 kips (1485.30 KN) was recorded at the end of the first cycle to a drift ratio of +3.00%. Buckling of bars were observed as the wall was pushed to a drift ratio of +/- 3.0%. On the first excursion to +4.0% drift ratio, a corner longitudinal reinforcing MA bar with an end grip coupler fractured above the coupler on the west side. As the wall was pushed further, the east corner longitudinal reinforcing MA bar with an end grip coupler fractured below the coupler. Those bars experienced significant buckling and fractured away from the coupler. The test was stopped after significant bar buckling was observed leading to the fracture of longitudinal

bars and the wall became unstable due to boundary region buckling. The wall was able to carry the targeted axial load throughout the test.

Wall 4 maintained lateral strength and stability to a drift ratio of 3%, which is deemed sufficient for special concrete seismic systems under an MCE level event (ASCE/SEI 7(American Society of Civil Engineers (ASCE), 2022)).

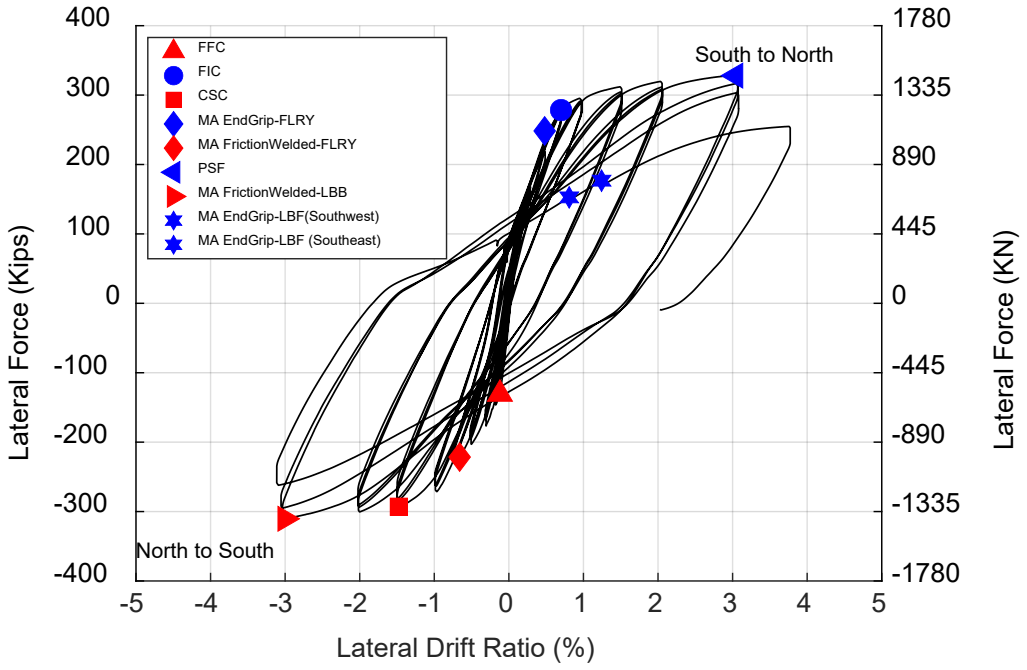

Figure 6-68: Wall 4- lateral force versus drift ratio response

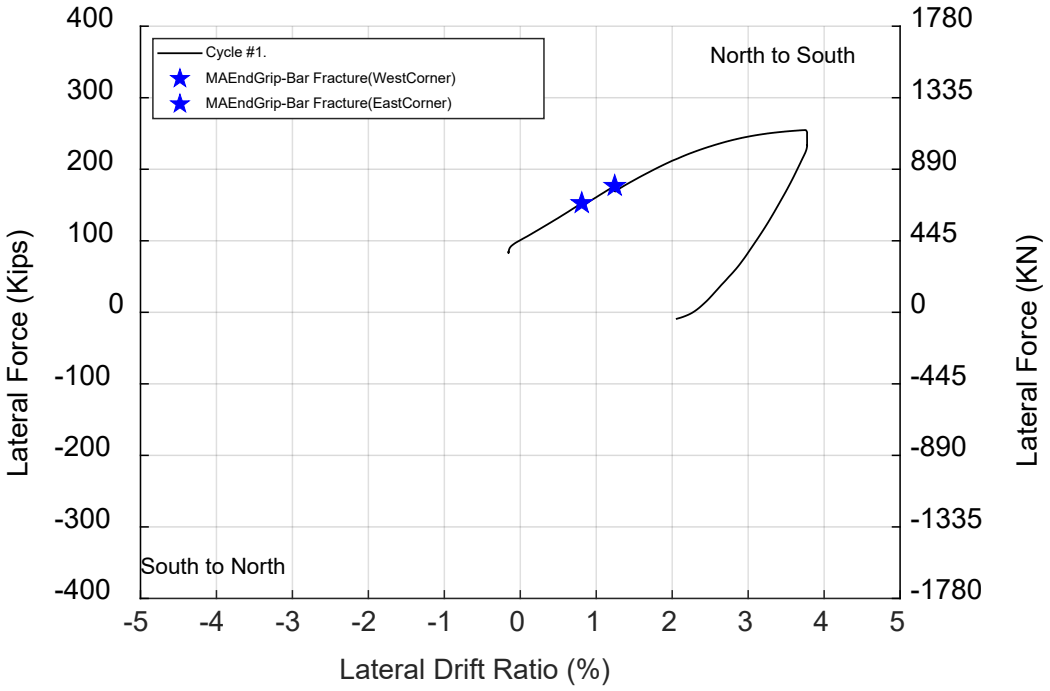

Figure 6-69: Wall 4- last cycle response

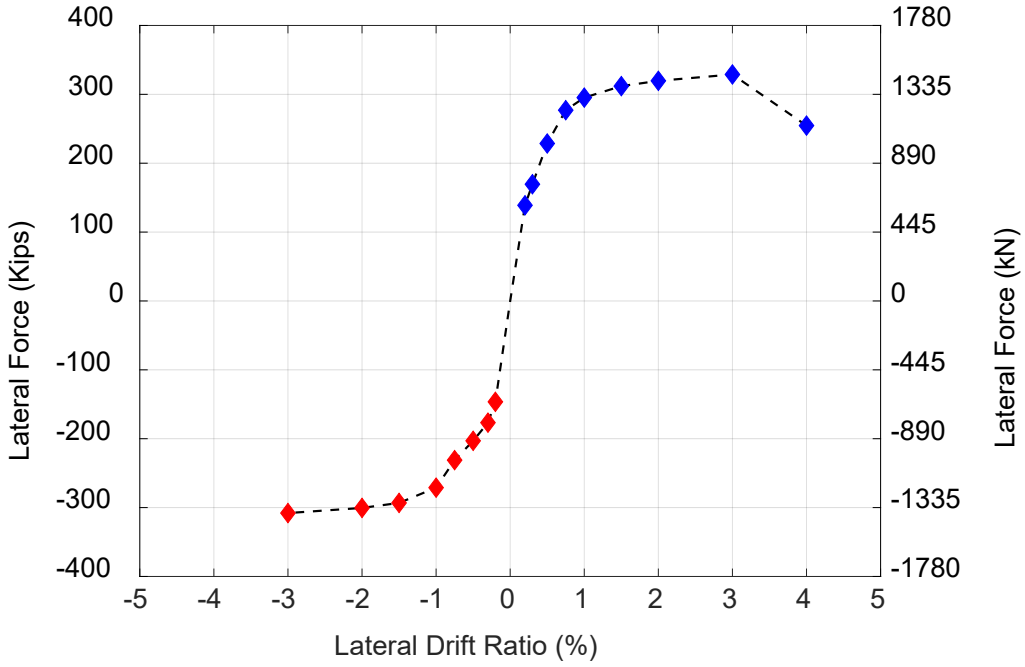

Figure 6-70: Wall 4- backbone response

Table 6.4: Wall4-Behavioral Milestones

Milestone	Drift Ratio (%)	Lateral Load (kips)
First Flexural Crack	-0.12	-130.75 (581.60 KN)
First Inclined Crack	+0.70	+278.37 (1238.24 KN)
First Long. Reinf. Yield	+0.48	+248.34 (1104.67 KN)
Cover Splitting Crack	-1.47	-229.07 (1018.95 KN)
Peak Shear Force	+3.04	+328.05 (1459.23 KN)
Longitudinal Bar Buckling	-3.0	-310.42 (1380.81 KN)
Longitudinal Bar Fracture (MA-End Grip)	+0.81 +3.0	+152.65 (679.02 KN)
Longitudinal Bar Fracture (MA-End Grip)	+1.24 +3.0	+176.69 (785.95 KN)

Note: for bar buckling and bar fracture, the maximum prior drift ratio and the actual drift at which milestone occurred are reported; the first value reports actual drift and the second value reports maximum prior drift ratio.

6.5.2 Test pictures of Wall 4

Figure 6.71 and Figure 6.72 show the pictures of Wall 4 of the wall during various stages of loading and damage.

Spreading of flexural cracks at peak of 3rd cycle of +1.5% drift ratio

Spalling of concrete on north side at peak of 3rd cycle of +1.5% drift ratio

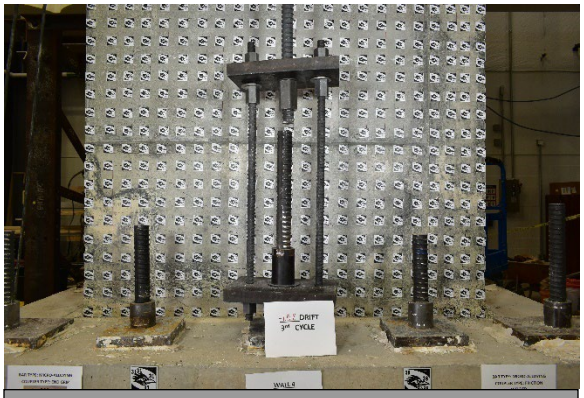

Inclined cracks seen at peak of 3rd cycle of +1.5% drift ratio

Propagation of flexural cracks at peak of 3rd cycle of +2.0% drift ratio

Figure 6-71:Wall 4- test pictures at peak of drift targets

First bar fracture above the coupler on Southwest corner at +4.0% drift

Second bar fracture below the coupler on Southeast corner at +4.0% drift

Buckling of MA bars on North side at peak of +4.0% drift ratio

Compression boundary buckling at +4.0% drift ratio

Figure 6-72: Wall 4- pictures of buckled and fractured bars at the end of test

6.5.3 Strain Histories

Maximum strain demands were recorded above and below the location of splices, where significant bar buckling was observed in both boundary regions. Figure 6.73, Figure 6.74, Figure 6.75 and Figure 6.76 show the strain versus drift response below couplers at 1.5 in. (38.01 mm)

above the wall-footing interface and above the couplers at 9 in. (228.06 mm) from the wall-footing interface. The north side boundary region consisted of MA bars with friction welded couplers and south side boundary region consisted of MA bars with end grip couplers. Compression strains as high as (1.5% to 2%) were recorded on MA bars with end grip and friction welded couplers (Figure 6.74 and Figure 6.75).

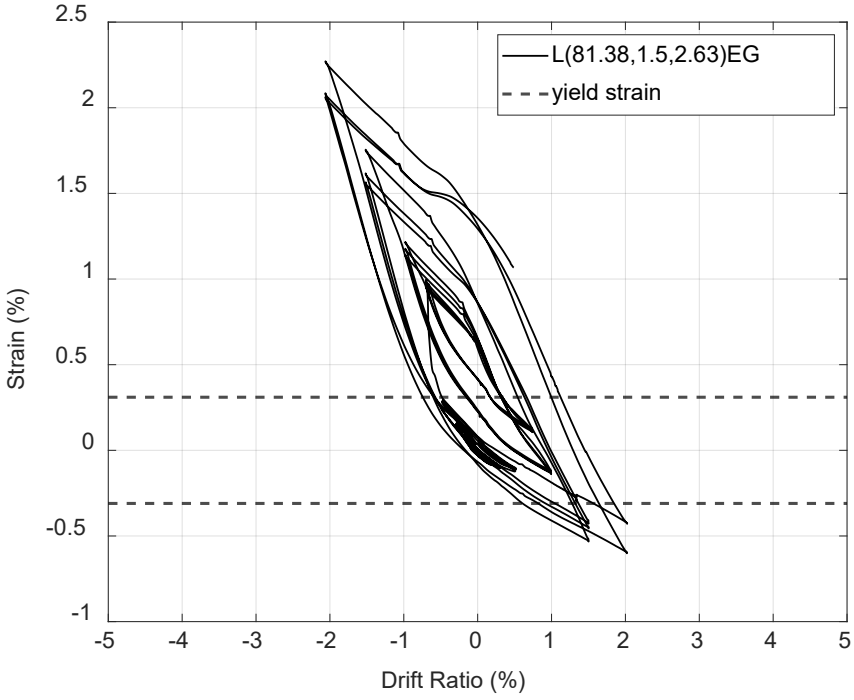

Figure 6-73: Wall 4 strain gauge at 1.5 in. (38.01 mm) from the wall to footing interface for south end MA corner reinforcing bar spliced with an end grip coupler

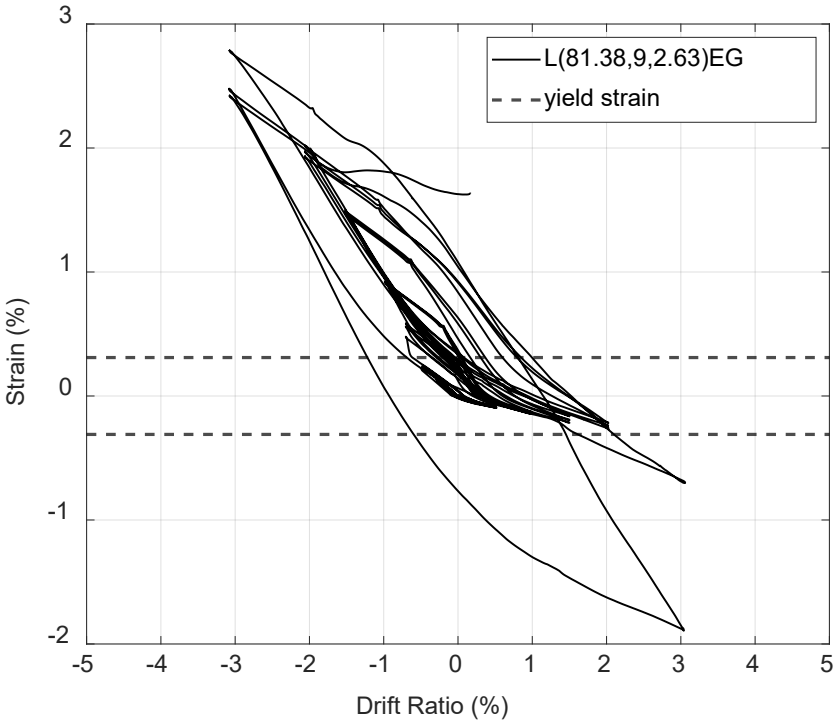

Figure 6-74: Wall 4 strain gauge at 9 in. (228.06 mm) from the wall to footing interface for the south end MA corner reinforcing bar spliced with an end grip coupler

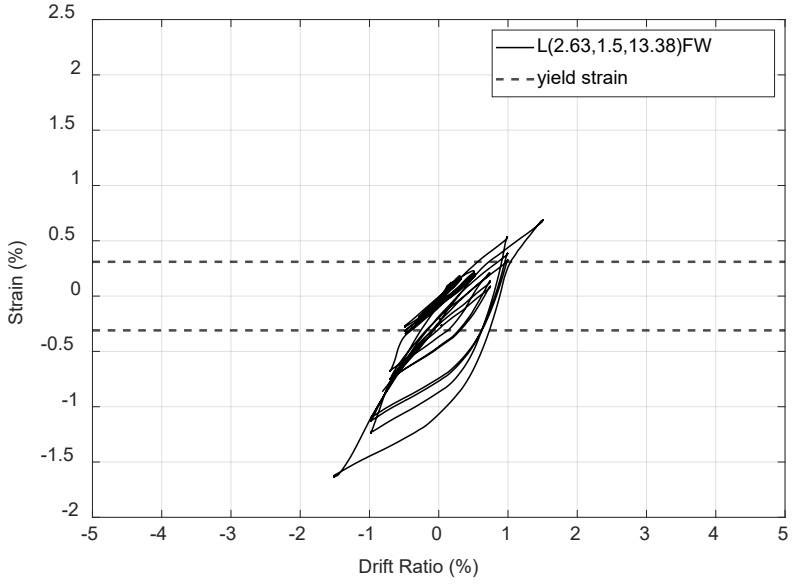

Figure 6-75- Wall 4 strain gauge at 1.5 in. (38.01 mm) from the wall to footing interface for the north end MA corner reinforcing bar spliced with a friction welded coupler

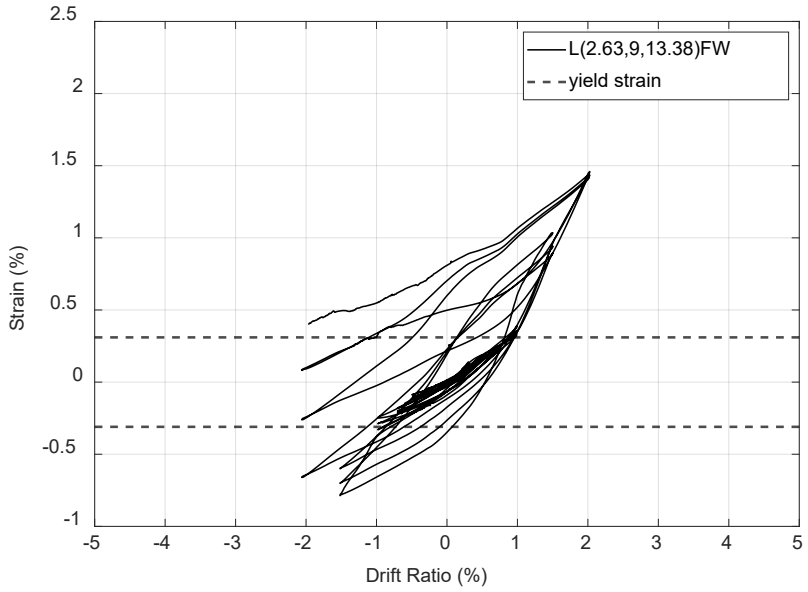

Figure 6-76 : Wall 4 strain gauge at 9 in. (228.6 mm) from the wall to footing interface for the north end MA corner reinforcing bar spliced with friction welded coupler

6.5.4 Longitudinal Reinforcing Bar Strain Demands

The recorded tension strain data from all three cycles to a drift target were averaged and then plotted against the lateral drift ratio. As can be seen in Figure 6.77 and Figure 6.79, strain demands increased with drift up to a drift ratio of 3.0%. They were higher above the couplers in MA bars spliced with end grip couplers up to a drift ratio of 3.0% and then dropped once bar fracture was observed at 4.0% drift. Figure 6.79 and Figure 6.80 show increased strain demands above couplers in MA bars spliced with friction welded couplers. Maximum tension strains reaching 6% were recorded on the MA middle reinforcing bars.

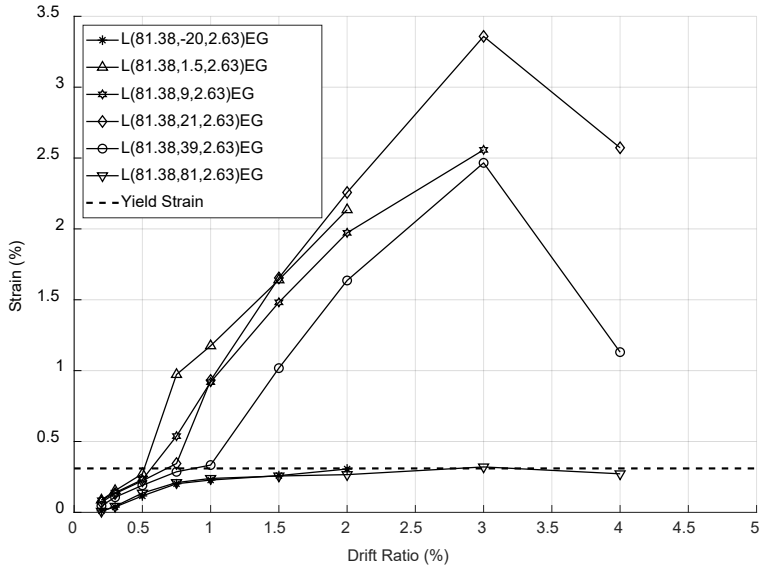

Figure 6-77: Wall 4 longitudinal reinforcement strain demands at drift targets for the south end MA corner reinforcing bar spliced with an end grip coupler

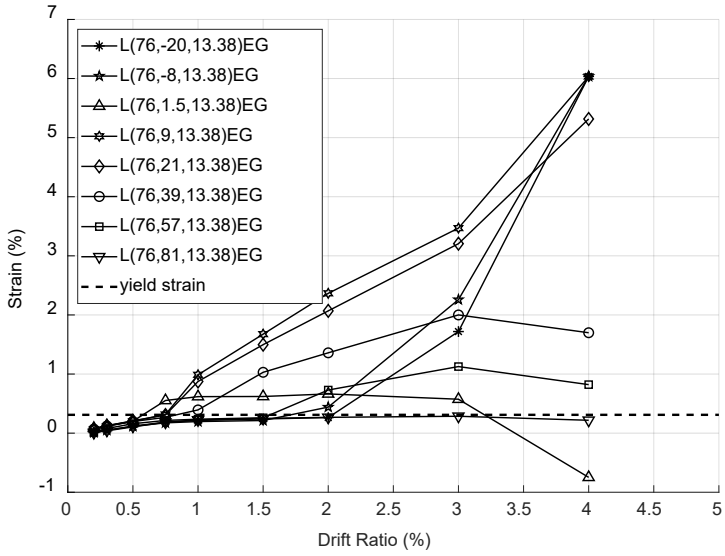

Figure 6-78: Wall 4 longitudinal reinforcement strain demands at drift targets for the south end MA middle reinforcing bar spliced with an end grip coupler

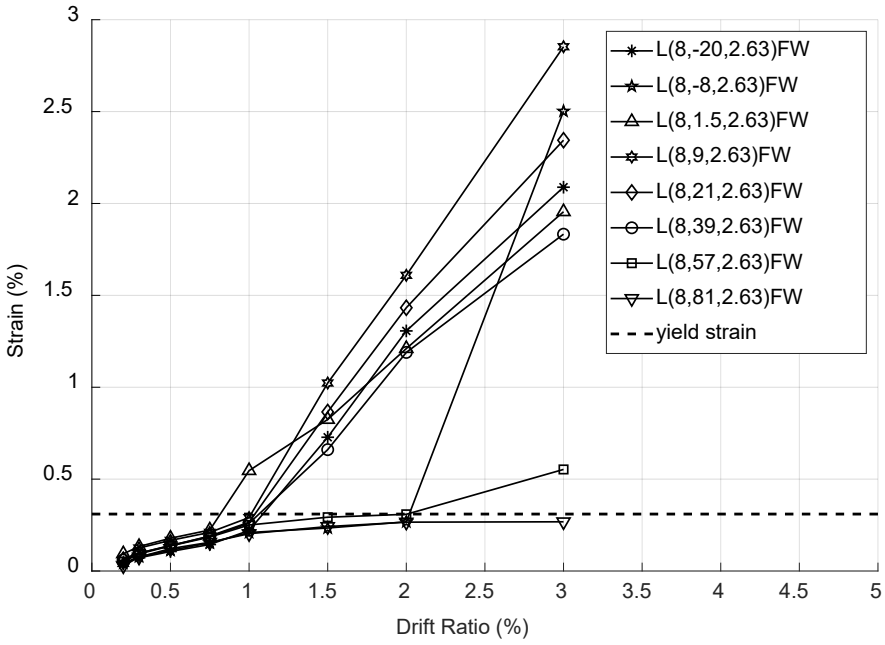

Figure 6-79: Wall 4 longitudinal reinforcement strain demands at drift targets for the north end MA corner reinforcing bar spliced with a friction welded coupler

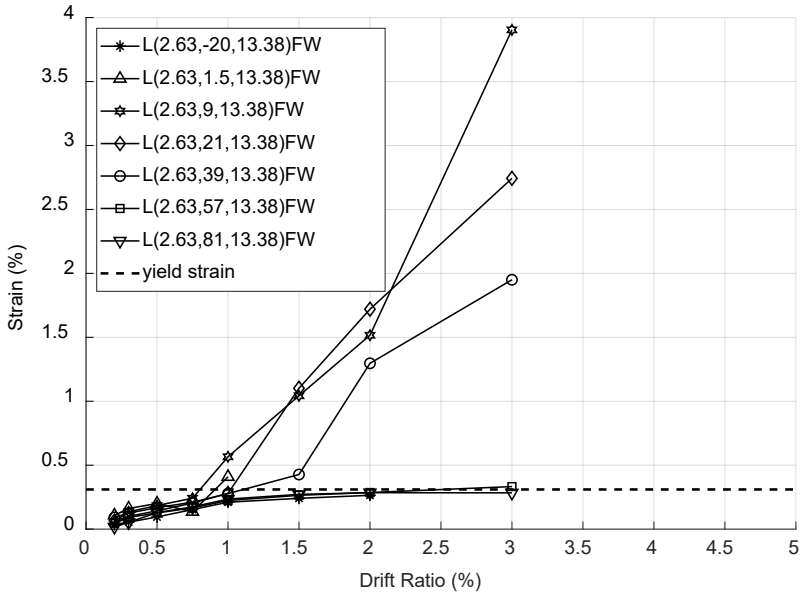

Figure 6-80: Wall 4 longitudinal reinforcement strain demands at drift targets for the north end MA middle reinforcing bar spliced with a friction welded coupler

6.5.5 Strain Gauge Profiles along Height

Strain readings over the height of longitudinal reinforcing bar in boundary region are given in Figure 6.81, Figure 6.82,Figure 6.83Figure 6.55 and Figure 6.84. Unfortunately, strain gauges higher up the wall were lost on the MA corner bar with end grip coupler. As seen in figures, inelastic strains were able to spread at least 80 in. (2032 mm) which can be partly attributed to the relatively high tensile to yield strength (T/Y) ratio of MA bars.

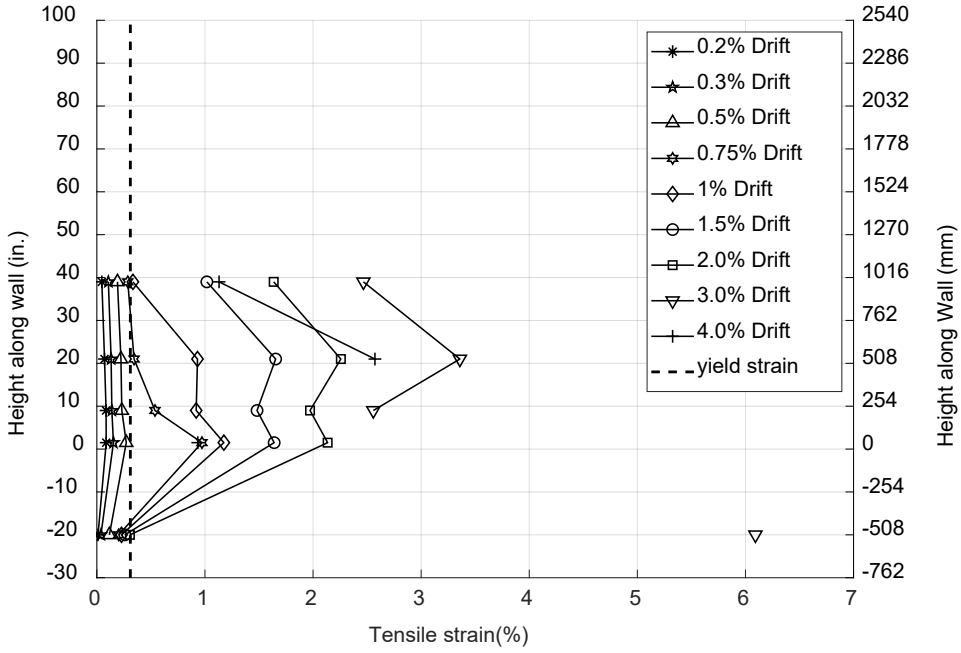

Figure 6-81: Wall 4 longitudinal reinforcement strain profiles for the south end MA corner bar spliced with an end grip coupler

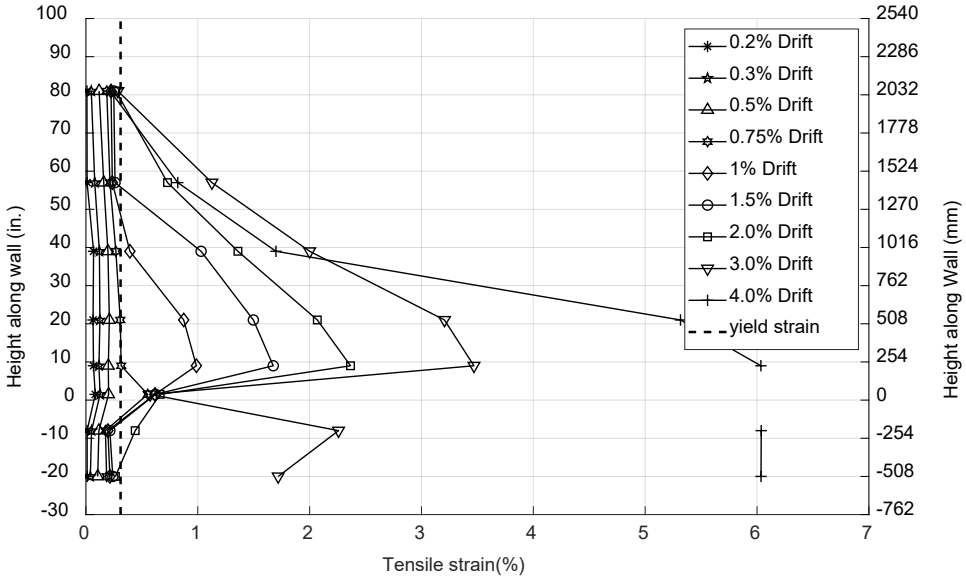

Figure 6-82: Wall 4 longitudinal reinforcement strain profiles for the south end MA middle bar spliced with an end grip coupler

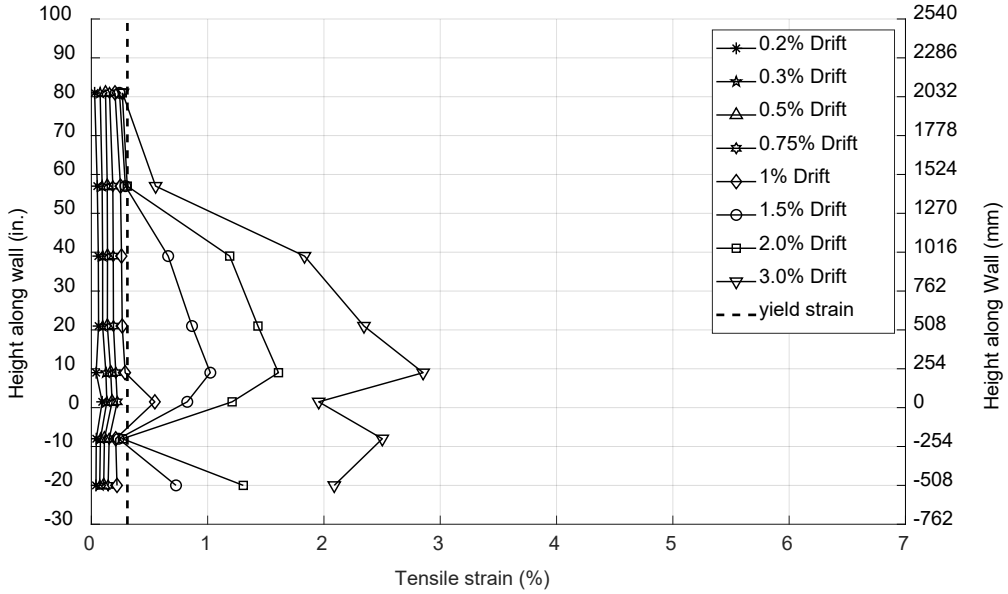

Figure 6-83- Wall 4 longitudinal reinforcement strain profiles for the north end MA middle bar spliced with a friction welded coupler

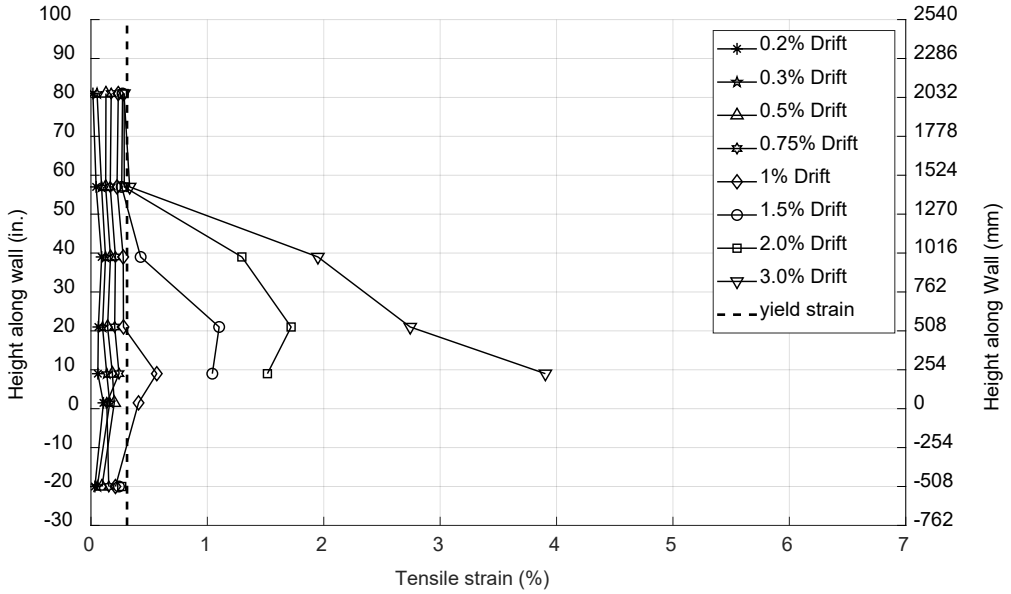

Figure 6-84: Wall 4 longitudinal reinforcement strain profiles for MA corner bar spliced with a friction welded coupler

6.5.6 Surface Strain along Height (DIC System)

Vertical surface strains along the height of the wall specimen at the boundary regions were calculated from the recorded target displacements as described in section 6.1.5. Figure 6.16, Figure 6.85 and Figure 6.86 show vertical surface strains along the height of the test specimen for the concrete facing the micro-alloyed longitudinal corner and middle reinforcing bar in the boundary region spliced with end grip coupler. Figure 6.87Figure 6.18 and Figure 6.88 show vertical surface strains along the height of the test specimen for concrete facing the micro-alloying longitudinal reinforcing bar in the boundary region spliced with friction welded coupler. Based on surface strains, inelastic strains are seen to spread up to 70 in. (1778 mm) from the base of the wall for MA bars spliced with end grip coupler, and at least 81 in. (2057.4 mm) for MA bars spliced with friction welded coupler.

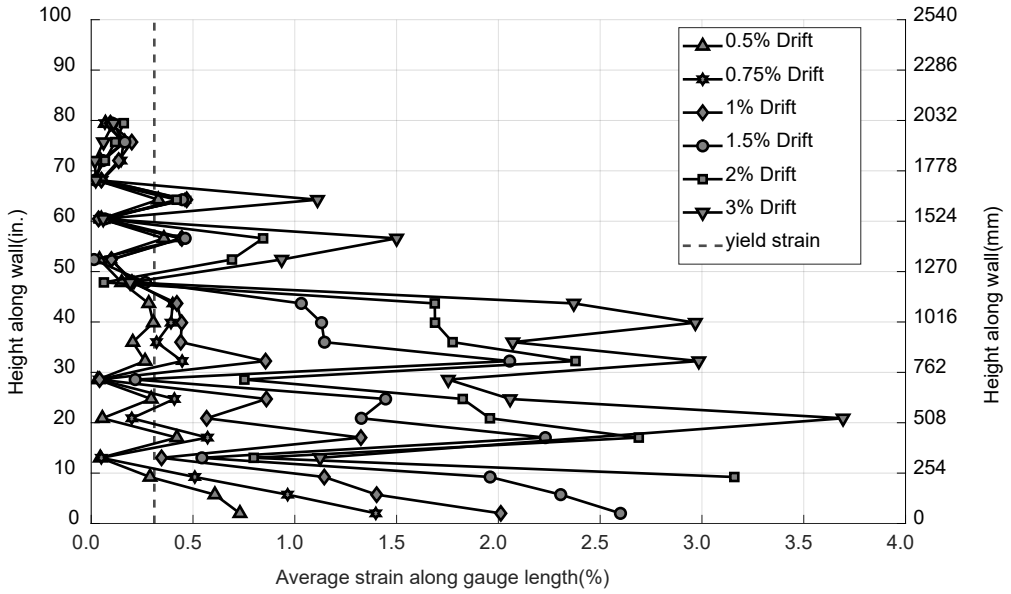

Figure 6-85: Vertical strain profiles from surface targets facing the south end MA corner reinforcing bar with an end grip coupler

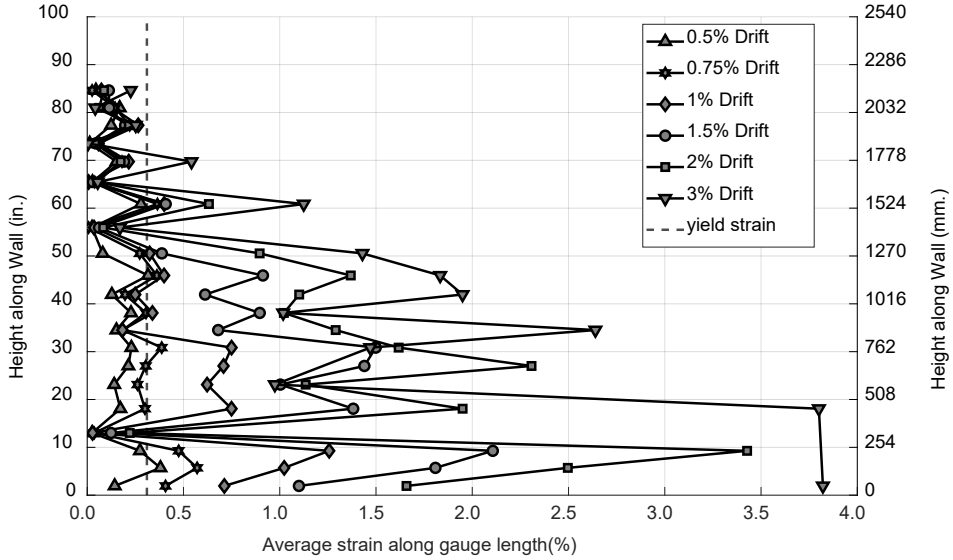

Figure 6-86: Vertical strain profiles from surface targets facing the south end MA middle reinforcing bar with an end grip coupler

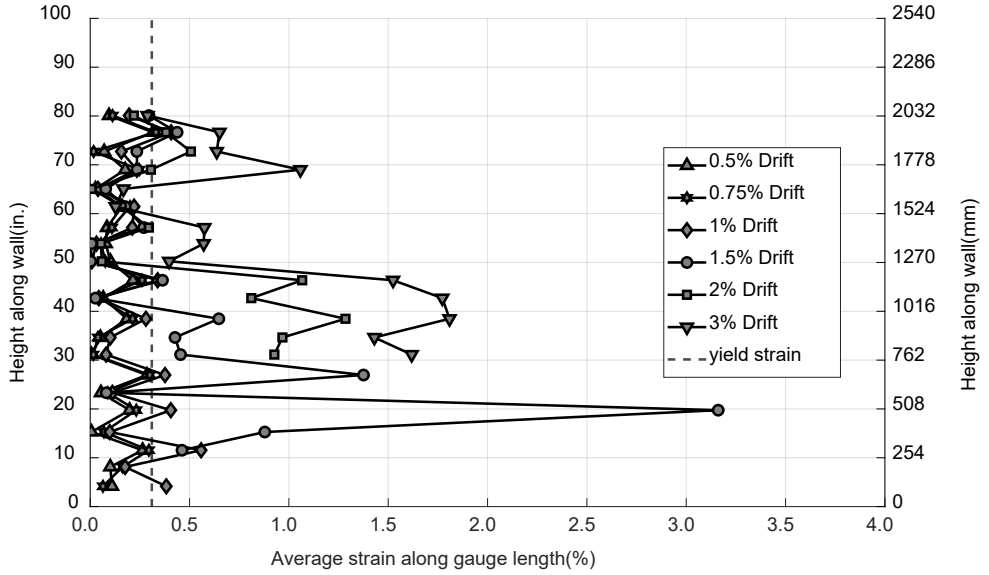

Figure 6-87: Vertical strain profiles from surface targets facing the north end MA corner reinforcing bar with a friction welded coupler

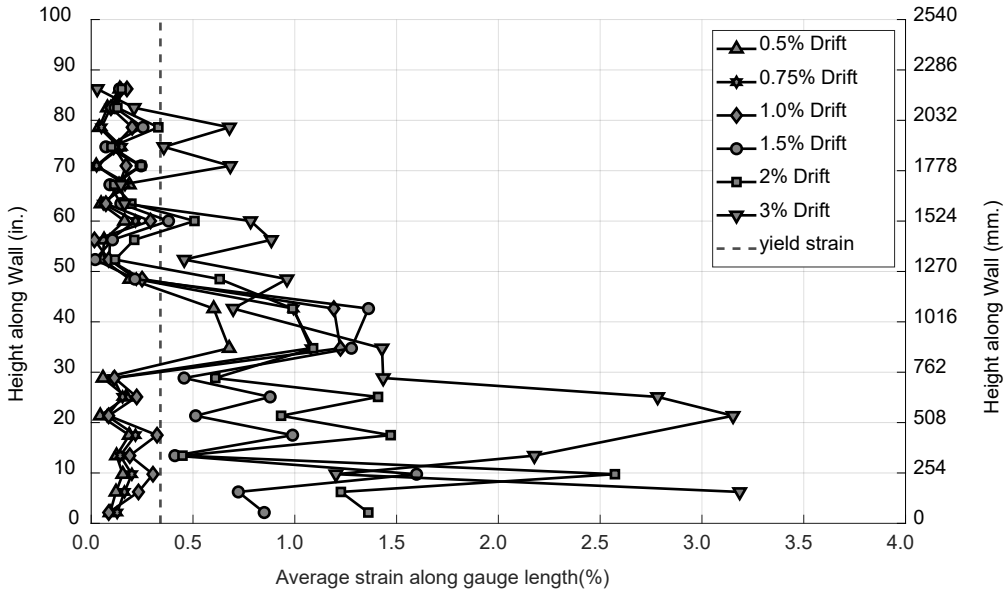

Figure 6-88: Vertical strain profiles from surface targets facing the north end MA middle reinforcing bar with a friction welded coupler

6.5.7 Comparisons between Vertical Strains from DIC System and Strain Gauges

Longitudinal bar strain readings are compared with the surface vertical strain readings from the targets closest to the bars in Figure 6.89 and Figure 6.90 for the boundary region with MA bars spliced with end grip couplers and in

Figure 6.63 and Figure 6.64 for the boundary region with MA bars spliced with friction welded couplers. Section 6.1.5 explains how the surface strains were obtained, and which surface targets were used.

As can be seen in the figures, vertical surface strains match longitudinal bar strains reasonably well where strain gauge readings could be obtained, i.e., before strain gauge failure

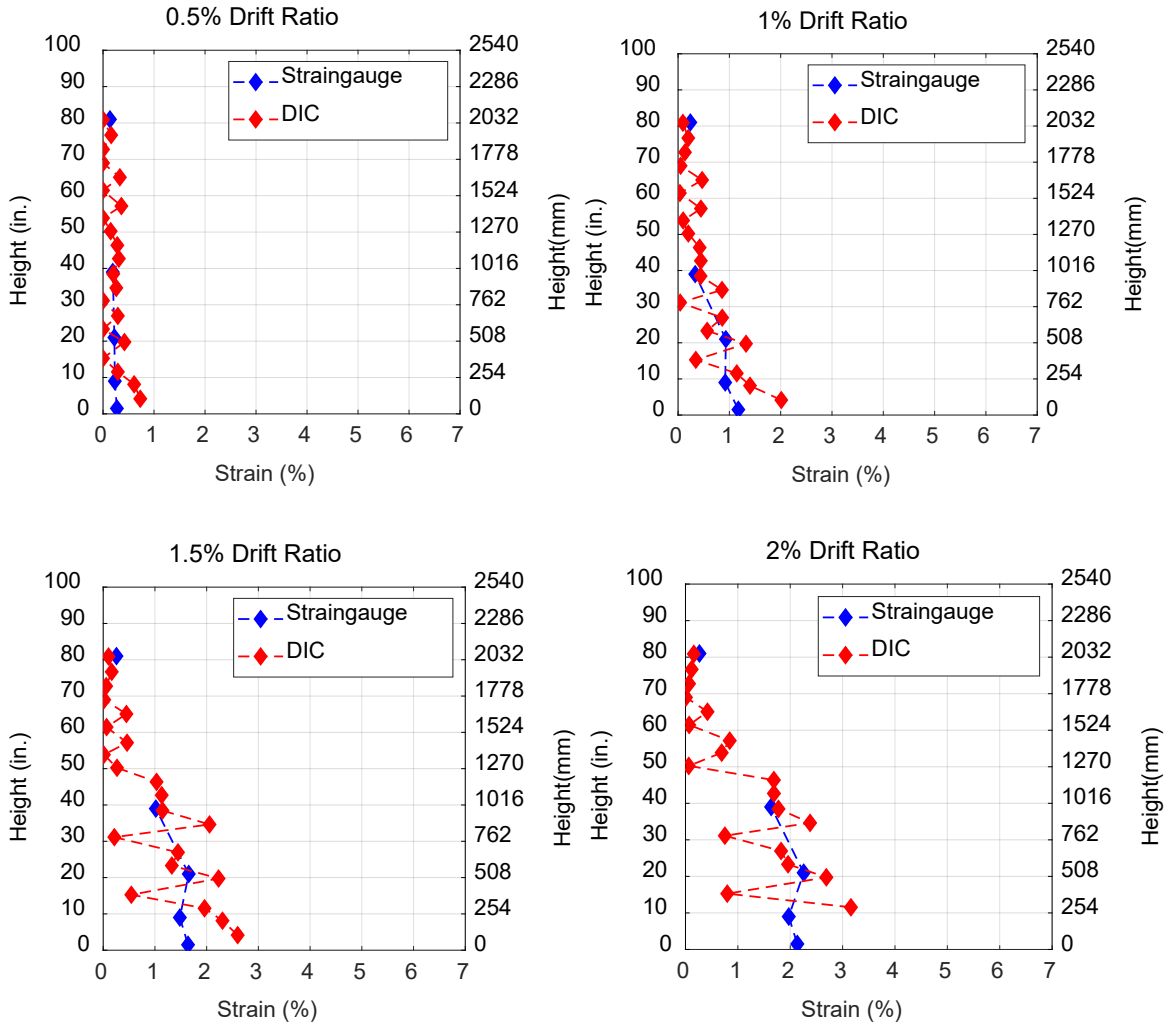

Figure 6-89: Strain profiles from strain gauges and DIC system for the south end MA corner bar spliced with an end grip coupler

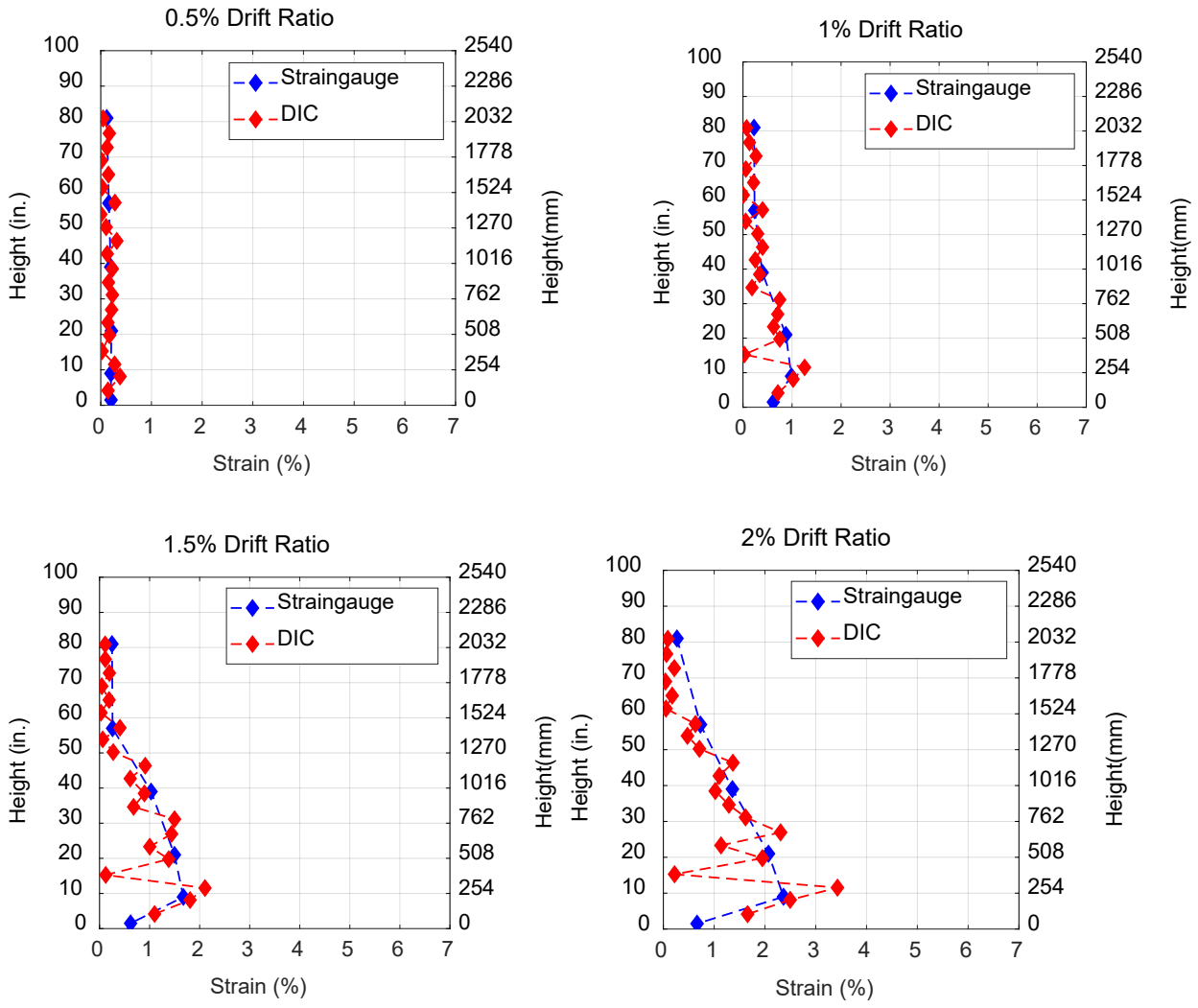

Figure 6-90: Strain profiles from strain gauges and DIC system for the south end MA middle bar spliced with an end grip coupler

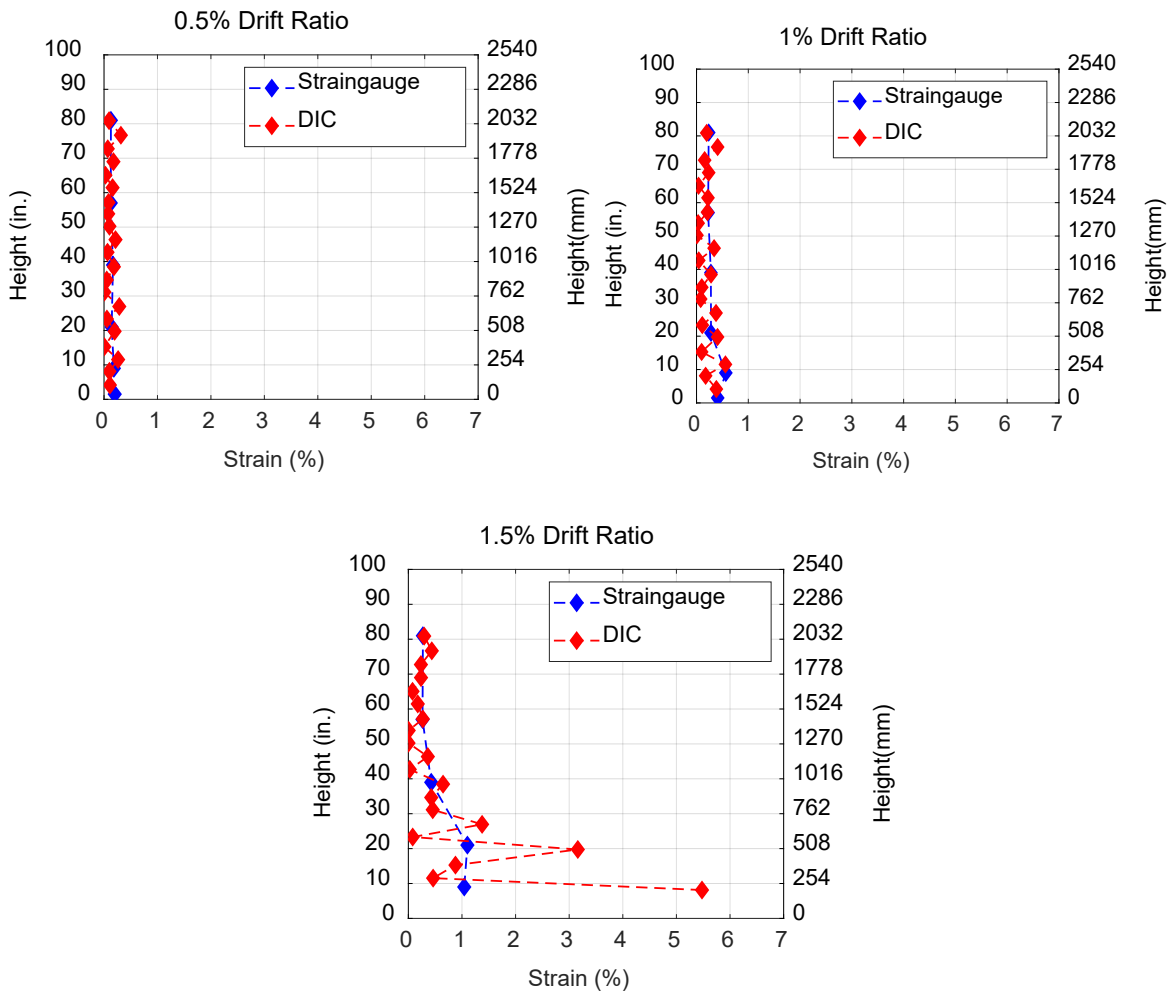

Figure 6-91: Strain profiles from strain gauges and DIC system for the north end MA corner bar spliced with a friction welded coupler

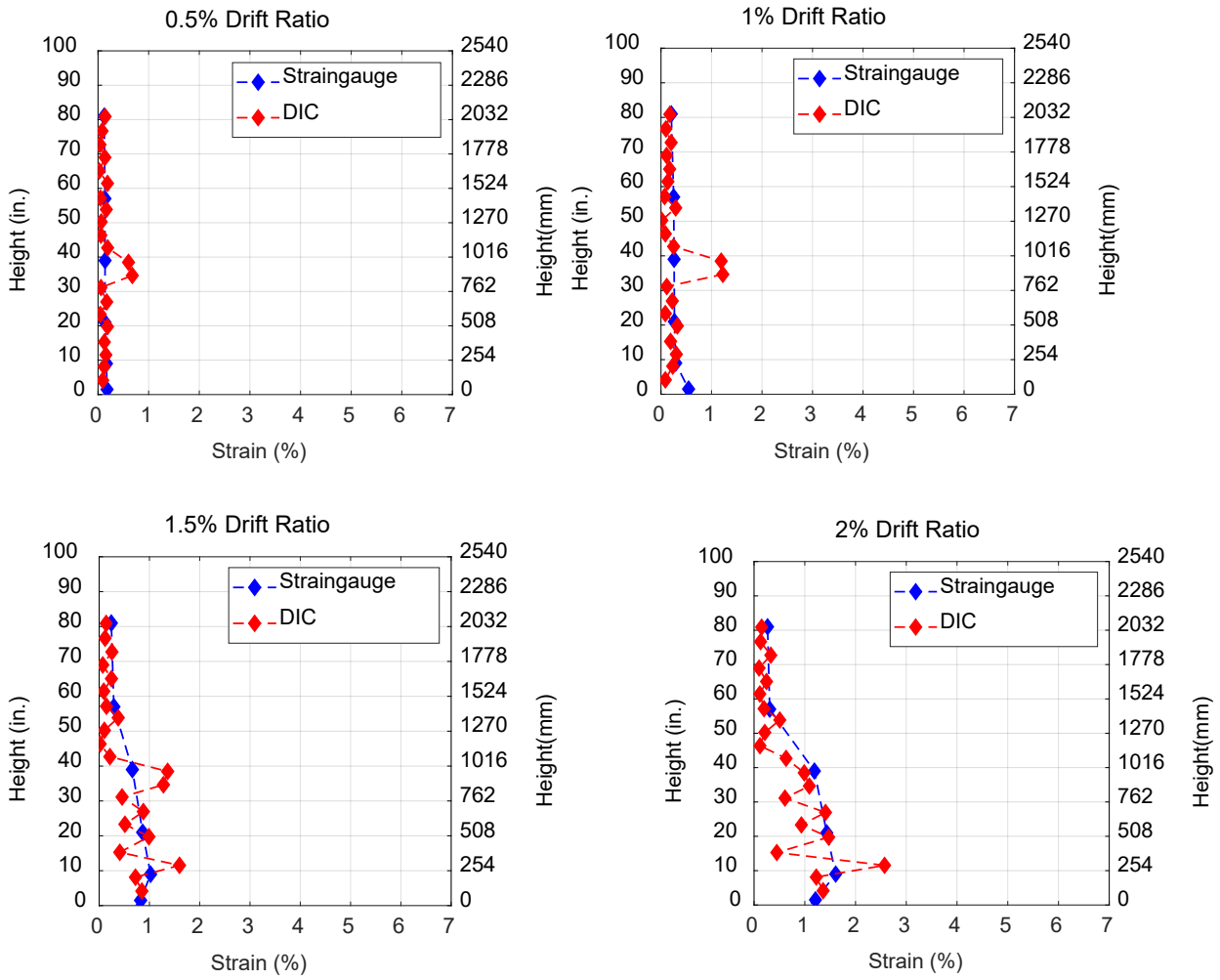

Figure 6-92: Strain profiles from strain gauges and DIC system for the north end MA middle with friction welded coupler

6.5.8 Energy Dissipation

The energy dissipated in each full cycle up to a drift ratio of 3.0% is plotted in Figure 6.93. Boundary region consisted of micro-alloying bars in Wall 4. The hysteresis loop was essentially symmetrical and stable which resulted in minimal degradation across cycles. The energy dissipated for each cycle to the same drift target was almost identical to a drift ratio of 3.0%.

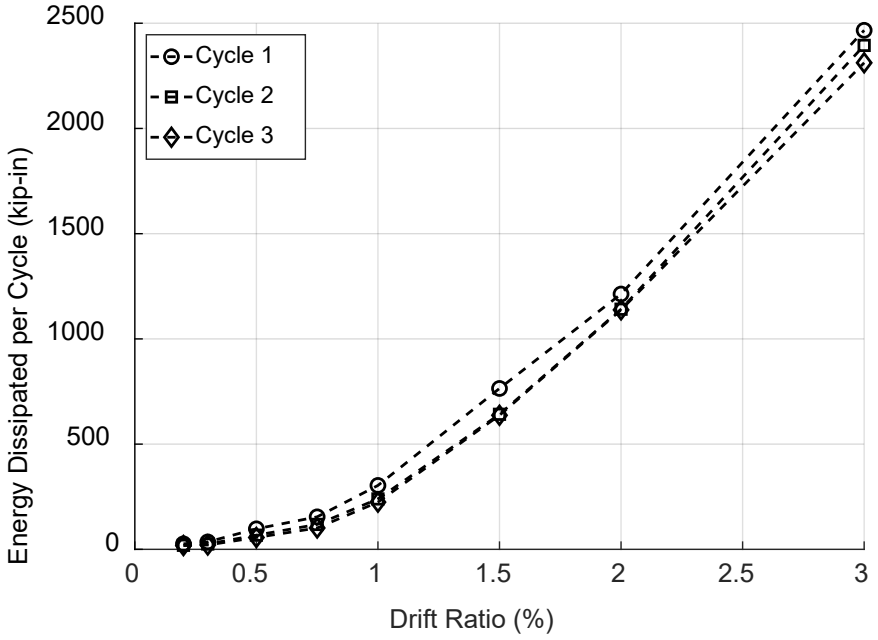

Figure 6-93: Energy dissipated in each full loading cycle

7 Discussion and comparison between wall specimens

7.1 Overall Behavior

The following observations can be made when comparing the overall behavior of the four walls:

- All tested wall specimens exhibited comparable lateral-load behavior up to the first cycle to a drift ratio of 2.0%. Milestones occurred at nearly identical drift levels for all walls, except for the milestone of longitudinal bar fractures (Table 7.1).
- First yield occurred at a larger drift for the control wall (0.63% drift ratio) than for the other walls (~0.5% drift ratio).
- All walls exhibited a flexural mode of strength degradation, characterized by crushing of concrete, followed in most cases by longitudinal bar buckling, and eventually leading to longitudinal bar fracture.
- Bar buckling was observed earlier for Wall 3 (~2% drift ratio), which had relatively long couplers, than for Wall 4 (3% drift) that had relatively short couplers, and the control wall (3% drift) (Table 7.1).Wall 2 bar fractures initiated prior to significant bar buckling on the north end. The fractures at the north end in Wall 2 relieved compression demands on the south end, which may have delayed bar bucking at that end as bar buckling was not observed until wall instability stopped the test.
- Despite bar buckling occurring earlier at a drift ratio of 2%, the amplitude of buckling was lower for Wall 3 than for other walls. Significant bar buckling was observed in the control wall and Wall 4 prior to the onset of the first bar fracture. By the end of the first cycle at a drift ratio of 3.0%, buckling of longitudinal bars was observed in control wall and Wall 4.
- The envelopes of the lateral force-versus-drift response for the first positive and negative half-cycles are presented for all walls in Figure 7.1. Except for Wall 2, the response of the walls did not show significant strength degradation up to the first cycle to a drift ratio of 3.0%. This performance is deemed acceptable for the maximum considered earthquake seismic event (MCE). ASCE/SEI 7-22(American Society of Civil Engineers (ASCE), 2022) limits the story drift ratio for seismically designed building to below 2% for the

design base earthquake (DBE). On the other hand, the MCE ground motion is defined as having 1.5 times larger accelerations than the DBE and therefore would be limited to an inter-story drift ratio of about 3.0%.

- The mechanical couplers in Wall 3 and Wall 4 performed adequately under relatively severe inelastic strain demands imposed in the wall hinge regions. This indicates that their fatigue performance, defined as the number of half-cycles to fracture under the testing protocol proposed by *Part I In-Air Testing*, is sufficient to achieve acceptable seismic performance of concrete walls subjected to an MCE level seismic event.
- Wall 2, in which quenching and self-tempering longitudinal reinforcing bars were mechanically spliced using friction-welded couplers, experienced multiple longitudinal bar fractures before completing the three cycles to a drift ratio of 2.0%. This resulted in a lateral strength loss of approximately 50% from peak before the wall was pushed to the first cycle to a drift ratio of 3.0%. Wall 2 seismic performance was therefore inadequate under an MCE level event due to premature and substantial strength loss.
- On the other hand, no bar fractures were observed in the boundary region of Wall 2 where micro-alloyed longitudinal bars were mechanically spliced with taper-threaded couplers. The lateral strength of Wall 2 when pushed in the direction that placed the MA bars in tension followed the behavior of other walls with stable response to a drift ratio of 3.0%.
- The friction-welded couplers splicing QST bars in Wall 2 therefore performed inadequately under the imposed strain demand reversals. This indicates that their fatigue performance, defined as the number of half-cycles to fracture under the testing protocol proposed by , is not sufficient to achieve acceptable seismic performance of concrete walls subjected to an MCE level seismic event.
- The taper threaded couplers splicing MA bars in Wall 2 performed adequately under relatively severe inelastic strain demands imposed in the wall hinge regions. However, since their strains could not fully reverse into compression once bars fractured at the other end of the wall, it is not possible to directly gage from results of Wall 2 whether their fatigue performance, defined as the number of half-cycles to fracture under the testing

protocol proposed by *Part I In-Air Testing*, is sufficient to achieve acceptable seismic performance of concrete walls subjected to an MCE level seismic event.

- The control wall, Wall 2, Wall 3, and Wall 4 exhibited a typical hysteretic response for seismically detailed concrete members up to bar fractures(Moehle, 2014; D. Sokoli et al., 2020; D. Sokoli et al., 2025), as shown in Figure 7.2. Prior to the yielding of longitudinal bars, hysteretic loops were observed to be essentially linear in loading and unloading. After yielding, plastic strains in the bars kept the flexural cracks open as compressive stresses built on the longitudinal bars. The result is a less stiff force-drift response was observed during reloading. Once flexural cracks closed again during reloading, the section stiffness increased again. Walls showed wide and stable hysteresis loops and exhibited minimal degradation between the cycles up to a drift ratio of 3.0%, except where bar fractures occurred.

Table 7.1: Summary of behavioral milestones for all wall specimens

Milestone*	Control Wall		Wall 2		Wall 3		Wall 4	
	Drift Ratio (%)	**Lateral Load (kips)**	**Drift Ratio (%)**	**Lateral Load (kips)**	**Drift Ratio (%)**	**Lateral Load (kips)**	**Drift Ratio (%)**	**Lateral Load (kips)**
FFC	-0.20	-160.91 (715.76KN)	-0.21	-152.12 (676.66KN)	-0.19	-138.77 (617.28KN)	-0.12	-130.75 (581.60KN)
FIC	-0.49	-225.17 (1001.60KN)	-0.75	-276.87 (1231.57KN)	-1.01	-268.47 (1194.21KN)	0.70	+278.37 (1238.24KN)
FLRY	-0.63	-263.5 (1172.1KN)	-0.5	-235.74 (1048.62KN)	+0.48	+230.23 (1024.11KN)	+0.48	+248.34 (1104.67KN)
CSC	-0.75	-281.39 (1251.68KN)	-1.06	-300.55 (1336.91KN)	-1.56	-293.06 (1303.59KN)	-1.47	-229.07 (1018.95KN)
PSF	+3.0	+326.82 (1453.76KN)	+2.0	+330.1 (1468.35KN)	+2.8	+333.91 (1485.30KN)	+3.04	+328.05 (1459.23KN)
LBB	-3.0	-320.80 (1426.98KN)	NA	NA	+2.07	+329.8 (1467.02KN)	-3.0	-310.42 (1380.81KN)
FLBF (QST)	-3.7 -3.0	-291.65 (1297.32KN)	-1.88 -2.0	-293.35 (1304.88KN)	-2.80 -2.0	-273.03 (1214.49KN)	NA	NA
FLBF (MA)	+1.31 +3.0	+197.34 (877.81KN) NA	NA	NA	+2.84 +2.0	+333.77 (1484.68) NA	+0.81 +3.0	+152.65 (679.02KN) NA

** FFC=First Flexural Crack, FIC=First Inclined Crack, FLRY=First Longitudinal Reinforcement Yield, CSC=Cover Spitting Crack, PSF=Peak Shear Force, LBB=Longitudinal Bar Buckling, FLBF=First Longitudinal Bar Fracture, QST=Quenching and Self-Tempering, MA=Micro-Alloying.*

Note: for bar buckling and bar fracture, the maximum prior drift ratio and the actual drift at which milestone occurred are reported; the first value reports actual drift and the second value reports maximum prior drift ratio. For Wall 2, the first longitudinal bar fracture is reported.

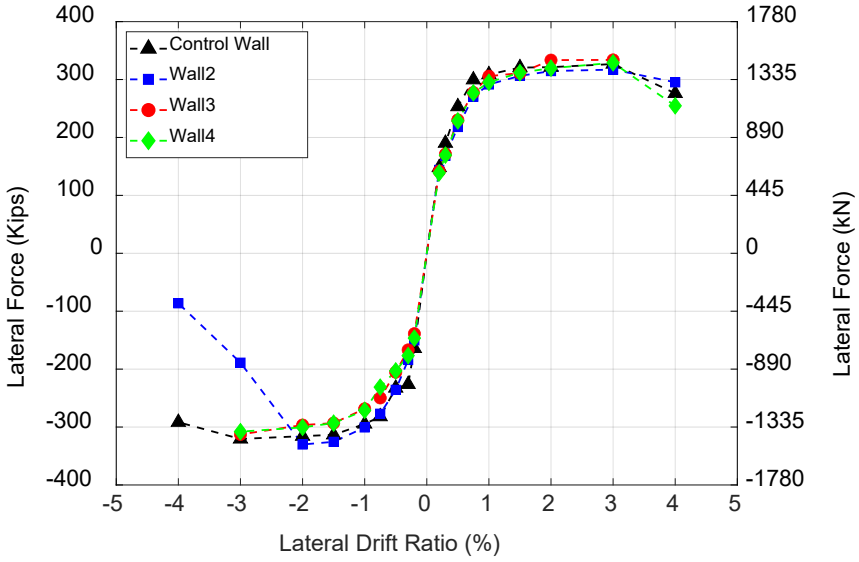

Figure 7-1: Backbone responses for all walls

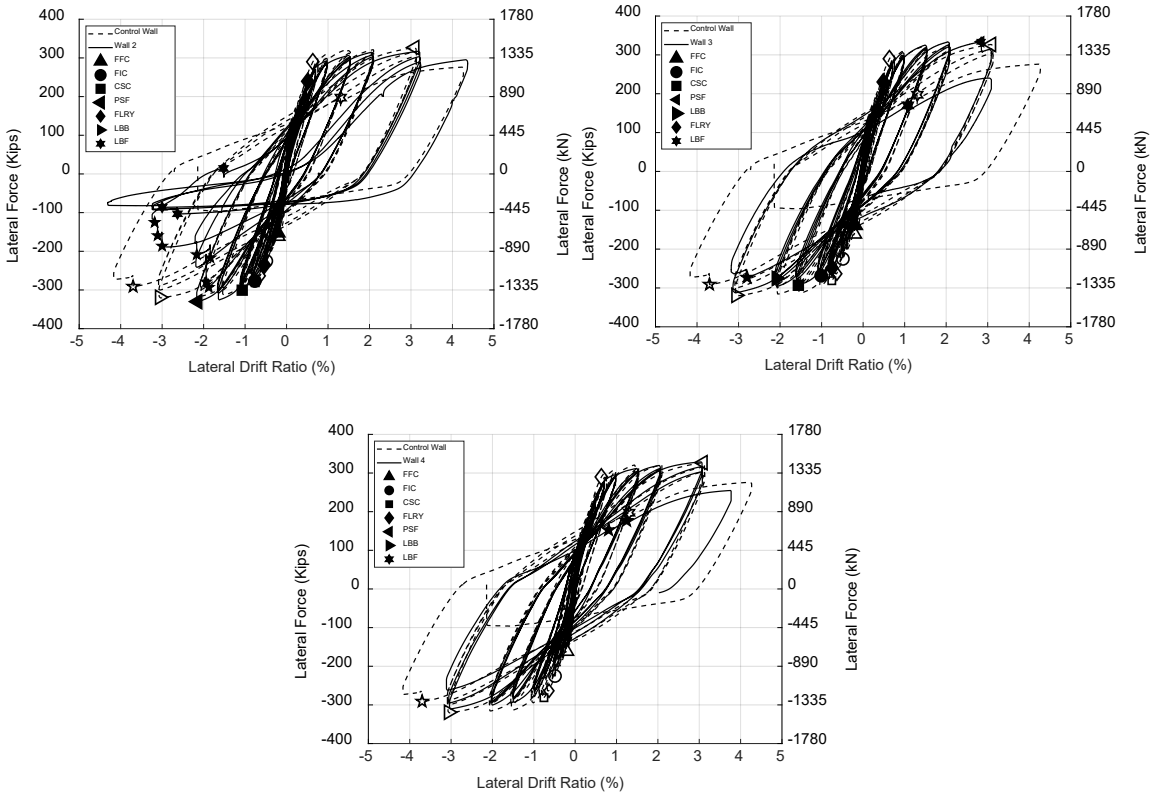

Figure 7-2: Lateral cyclic response of (a) Control wall and Wall 2, (b) Control wall and Wall 3 and (c) Control wall and Wall 4 (Hollow markers for Control wall and filled markers for other walls)

7.2 Strain Demands on Reinforcement

Tensile strains measured on longitudinal reinforcing bars in wall boundary regions are averaged over three cycles per drift target and presented versus drift ratios in Figure 7.3 to Figure 7.5. In these figures, strains are presented at the wall to footing interface just below couplers, just above couplers, and at 21 in. (533.4 mm) height from wall base. Figure 7.6 to Figure 7.9 present tensile strains averaged over three cycles to a drift target versus the height of walls and at different target drift ratios. The data recordings from the strain gauges which were lost are not presented in the plots. The following observations can be made based on strain data and the plots.

- Prior to the first yield of longitudinal bars, tensile strain demands were similar for all walls. In all walls, the first yielding of the longitudinal bar first occurred at the wall-footing interface. Longitudinal bars then exhibited a more rapid increase in tension strain demands after yielding versus drift as can be seen from Figure 7.3 to Figure 7.5.

- For walls with couplers, as wall drifts increased, larger tensile strain demands were generally recorded above the couplers as opposed to below the couplers at the section of maximum moment. A possible explanation is that as the bars are pulled in tension from the loading points, the couplers essentially act as heads in that they resist upward movement due to their geometry, which in turn reduces stress and strain demands on the bars below them.
- Some couplers resulted in larger strain demands than others on bars around the coupler location at any given drift. Coupler size and slip with respect to coupler bars varied considerably between coupler types used in the *Part I In-Air Testing* and may, at least partly, have caused the differences.
- The same friction welded coupler type was used in Wall 2 and Wall 4. In Wall 2, the coupler was applied to QST bars, while in Wall 4 the coupler was applied to MA bars.
- Strain demands were higher on QST bars compared with MA bars spliced with the friction welded as shown in Figure 7.5. The lower tensile to yield strength ratio of the QST bars may have contributed to the higher strains(Drit Sokoli & Wassim M Ghannoum, 2016; Drit Sokoli et al., 2025; Drit Sokoli et al., 2020).
- As seen in Figure 7.6 to Figure 7.9, inelastic strains were recorded from strain gauges reached a height of about the length of wall. MA bars generally spread plasticity higher than QST bars, reaching the highest strain gauge placed at 81 in. (2057.4 mm) above the base of wall. QST bars typically spread plasticity slightly lower sometimes not spreading it past 70 in. (1778 mm) from the base of wall. This may be attributed to the lower tensile to yield strength ratio of QST bars compared with MA bars(Drit Sokoli & Wassim M Ghannoum, 2016; Drit Sokoli et al., 2025; Drit Sokoli et al., 2020).

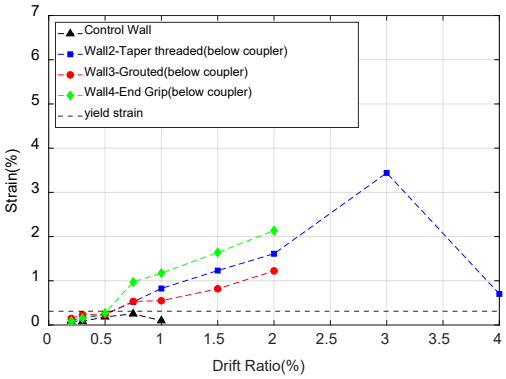

(a)

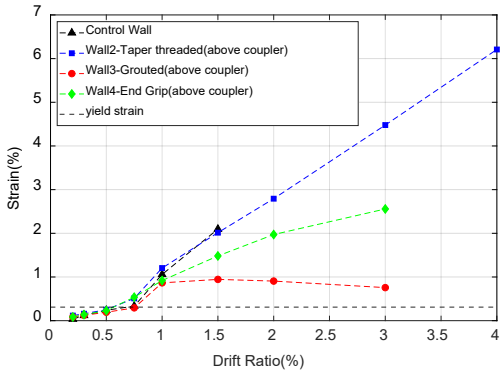

(b)

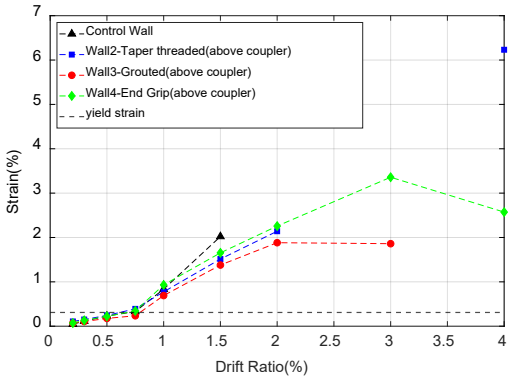

(c)

Figure 7-3: Tensile strain demands averaged across the three cycles to each drift target for the south end MA corner longitudinal bar (a) at wall base below couplers : 1.5 in.(38.01 mm) from base, (b)above couplers: 9 in. (228.6mm) above base for (Wall 2 and Wall 4) or 16 in. (406.4 mm) for Wall 3 , and (c) at 21 in. (533.4 mm) above the wall-footing interface

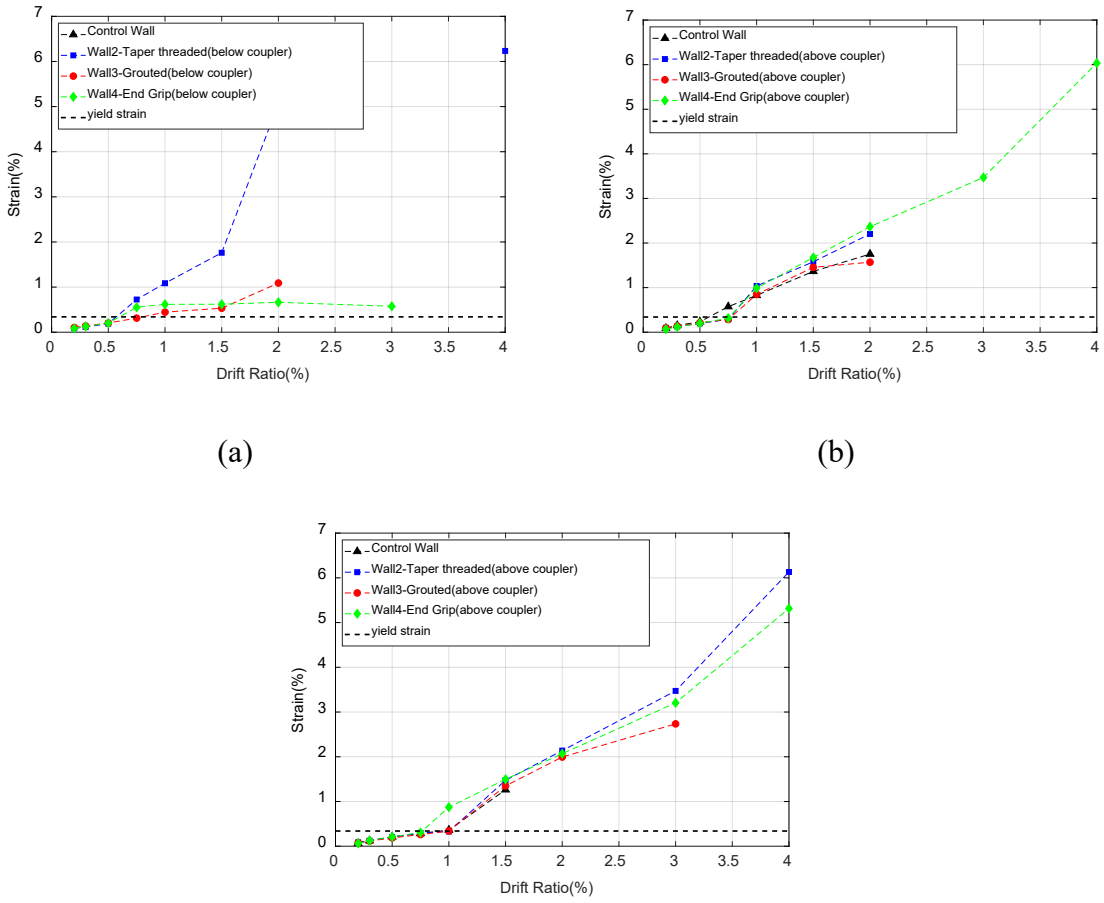

Figure 7-4: Tensile strain demands averaged across the three cycles to each drift target for the south end MA middle longitudinal bar (a) at wall base below couplers : 1.5 in.(38.01 mm) from base, (b)above couplers: 9 in. (228.6mm) above base for (Wall 2 and Wall 4) or 16 in. (406.4 mm) for Wall 3 , and (c) at 21 in. (533.4 mm) above the wall-footing interface

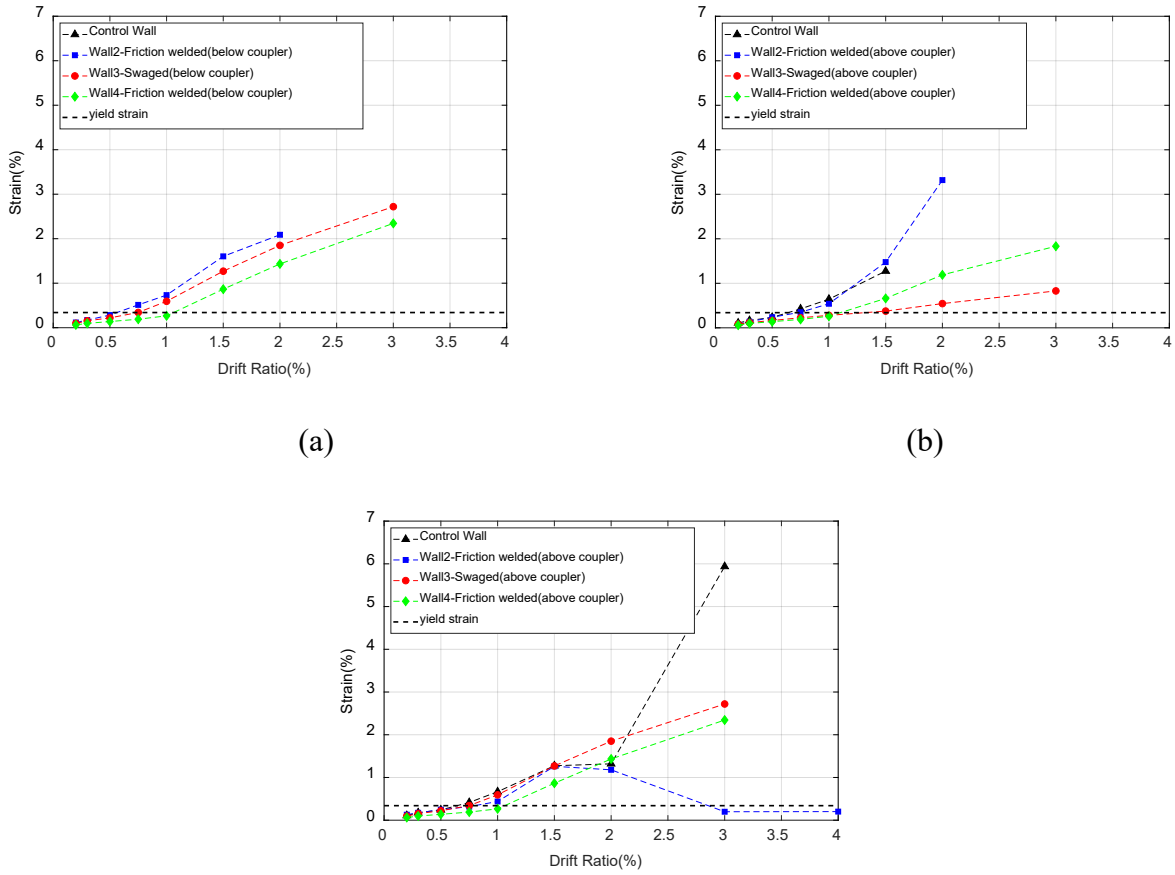

Figure 7-5: Tensile strain demands averaged across the three cycles to each drift target for the north end middle longitudinal bar (a) at wall base below couplers: 1.5 in.(38.01 mm) from base, (b)above couplers: 9 in. (228.6mm) above base for (Wall 2 and Wall 4) or 16 in. (406.4 mm) for Wall 3 , and (c) at 21 in. (533.4 mm) above the wall-footing interface

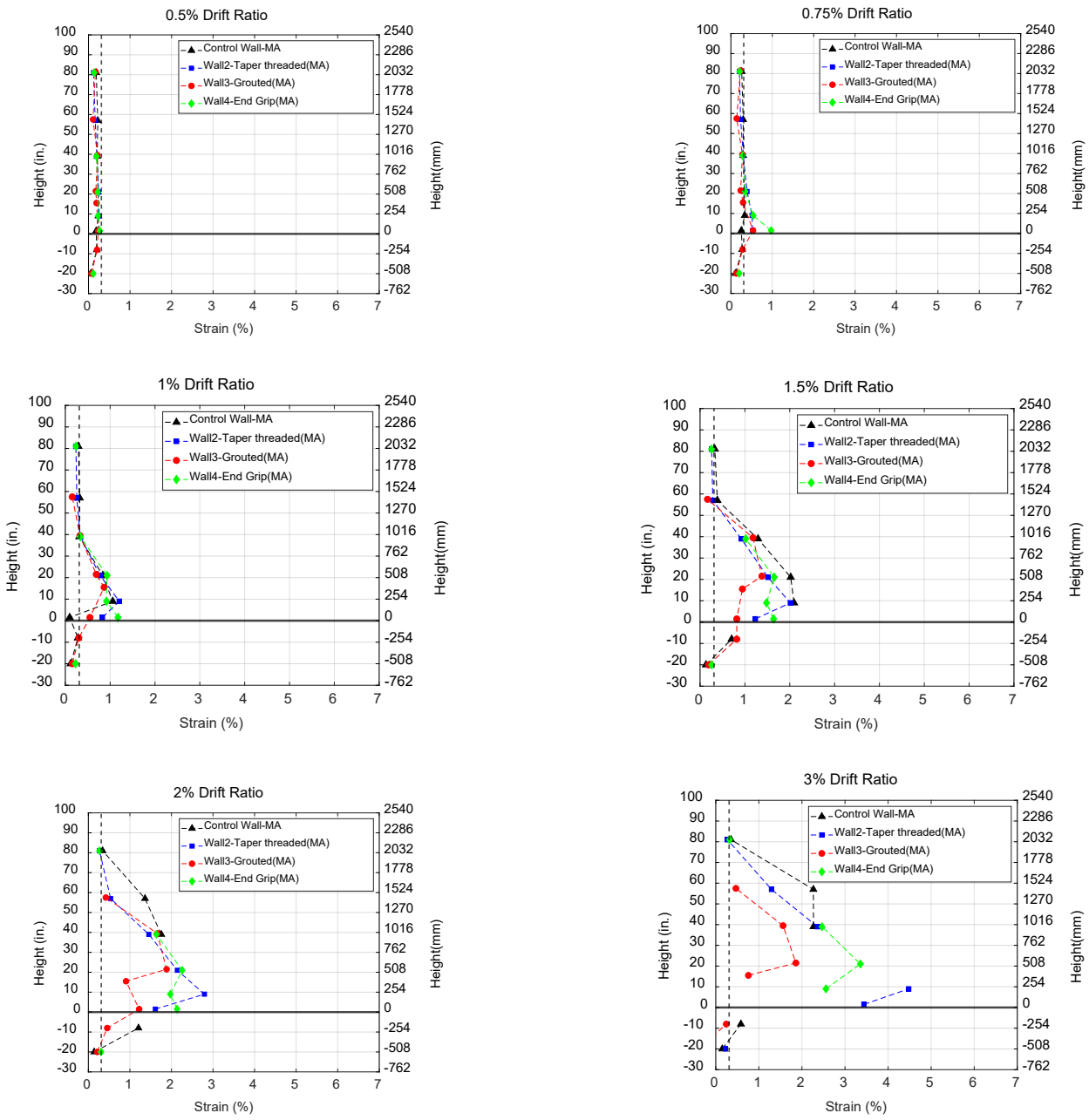

Figure 7-6: Strain profiles along the height for south side MA corner reinforcing bar

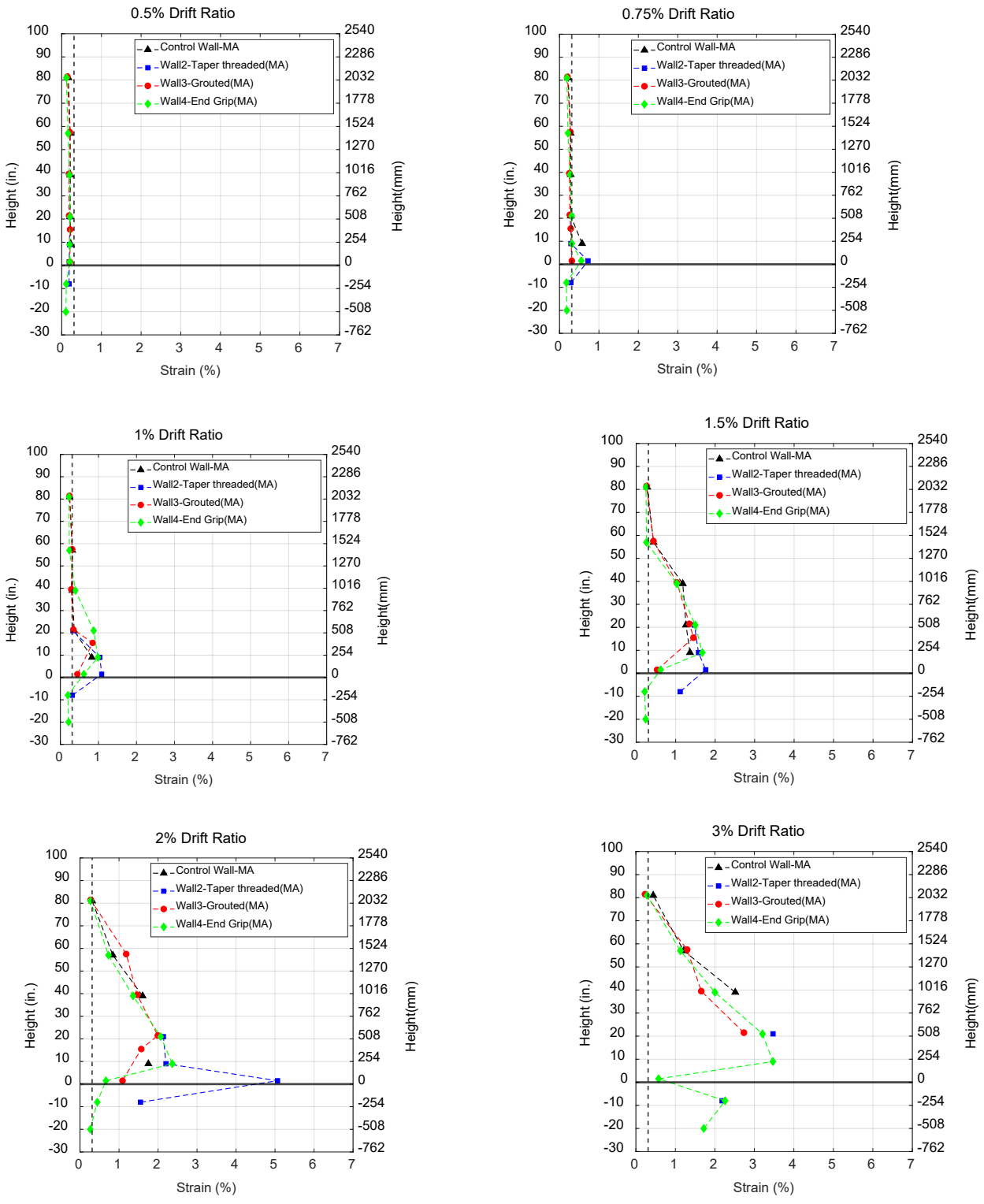

Figure 7-7: Strain profiles along the height for south side MA middle reinforcing bar

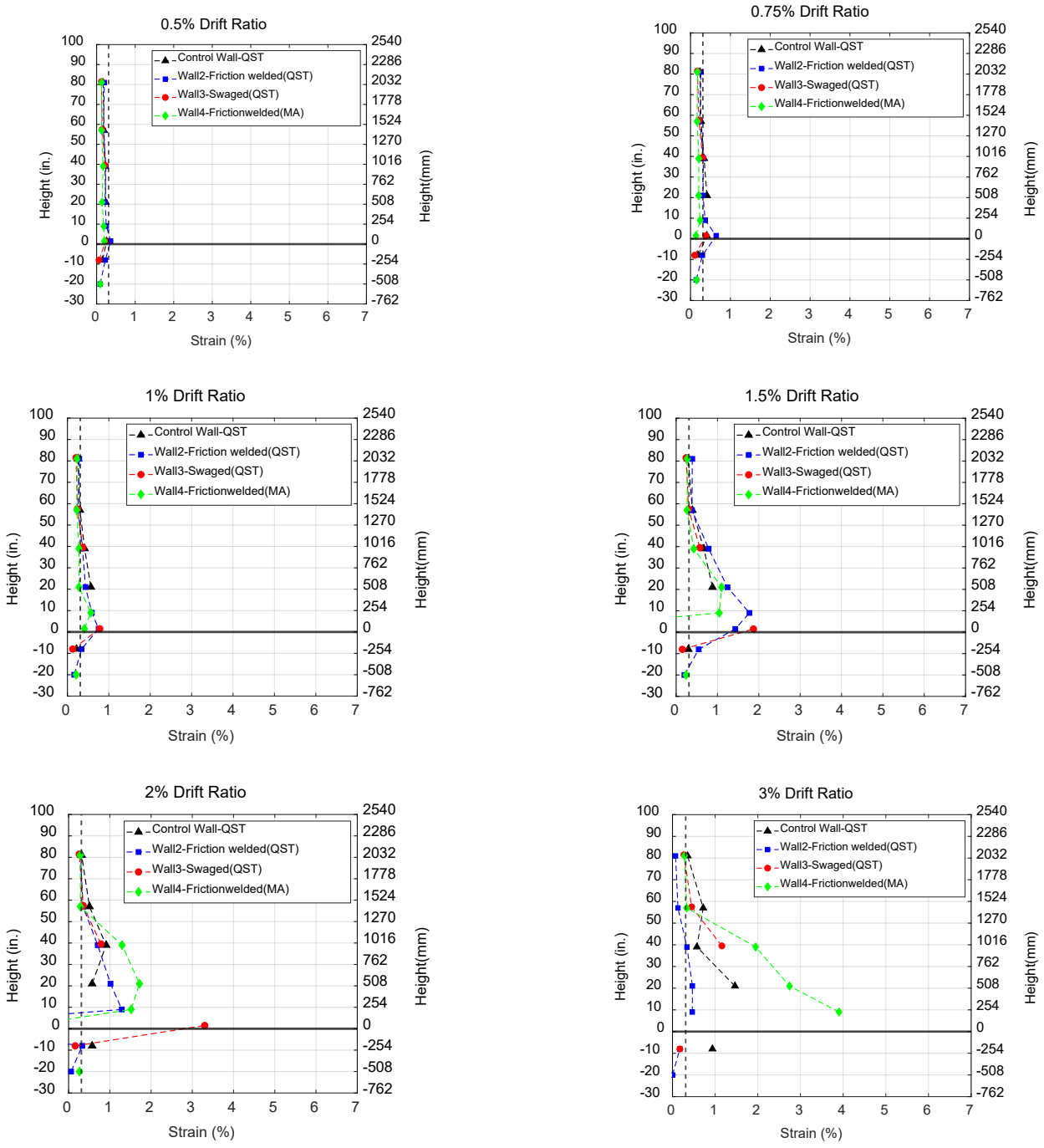

Figure 7-8: Strain profiles along the height for north side corner longitudinal bar (All walls had QST bar except Wall4 on north side)

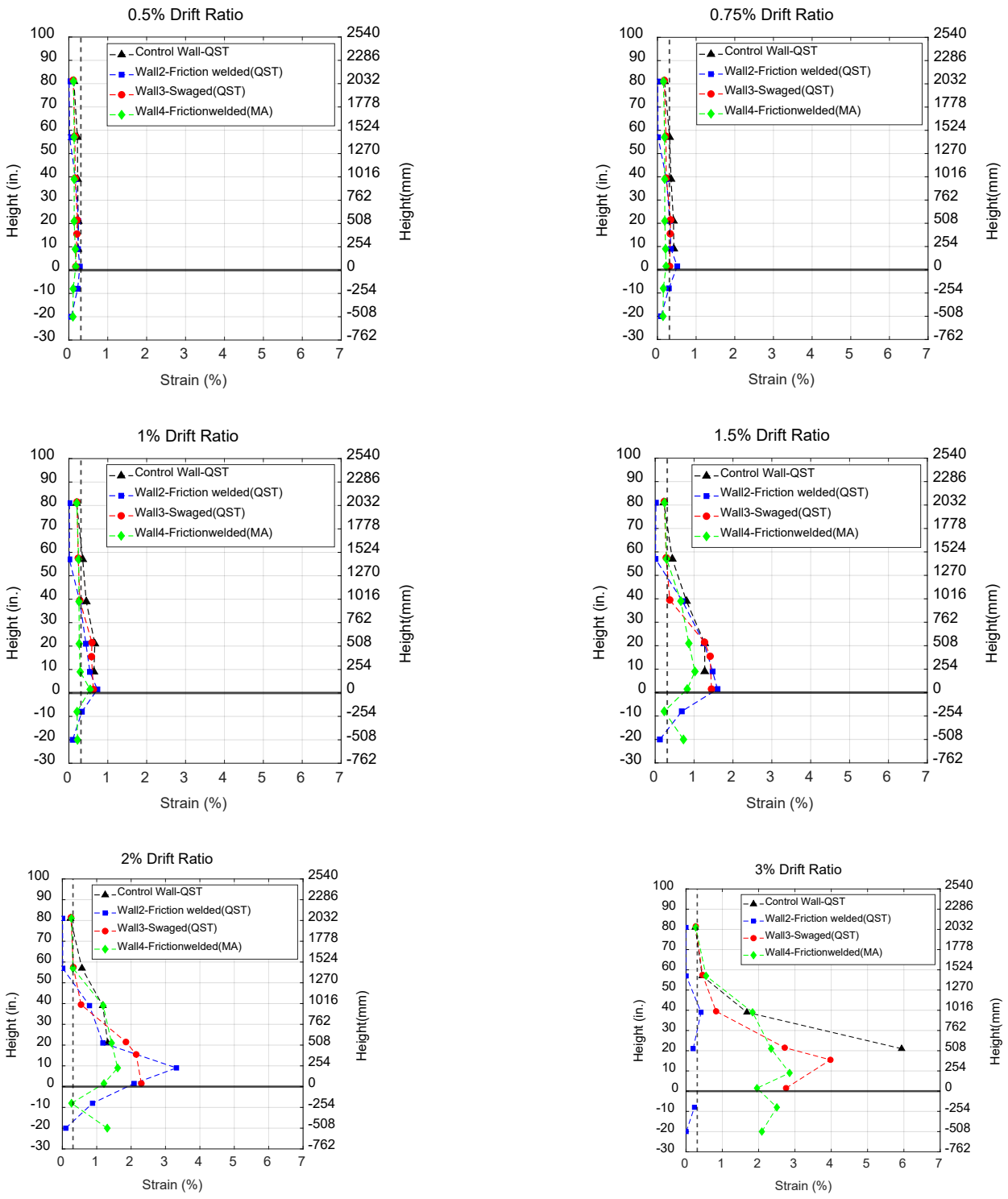

Figure 7-9: Strain profiles along the height for north side middle longitudinal bar (All walls had QST bar except Wall4 on north side)

7.3 Surface Strain Profiles along Height (DIC System)

Figure 7.10 to Figure 7.13 show surface vertical strain profiles along the height of specimen measured using DIC system, calculated as described in section 6.1.5. Unfortunately, cameras during Wall 2 testing stopped functioning early in the test and Wall 2 results are not presented.

As seen in figures, inelastic strains were able to spread at least 75 in. (1905 mm) from the base of wall which is about the length of wall.

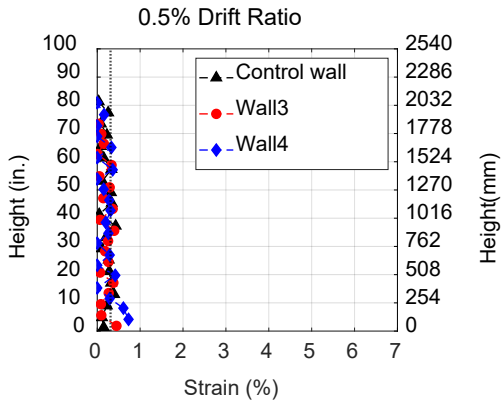

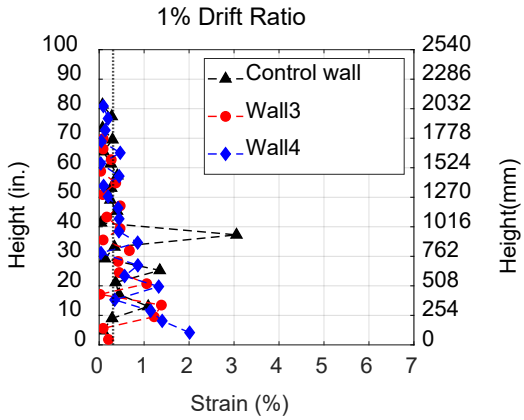

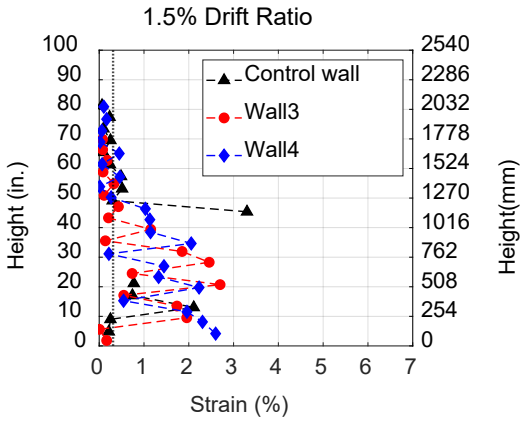

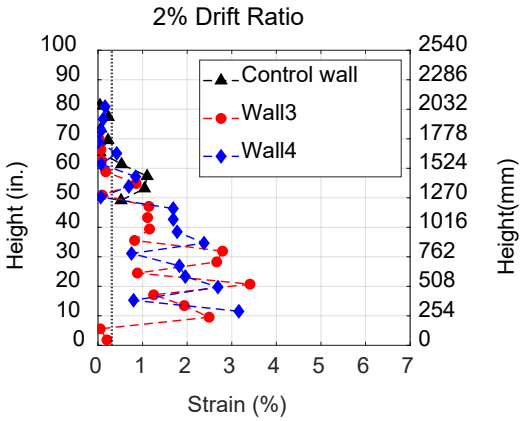

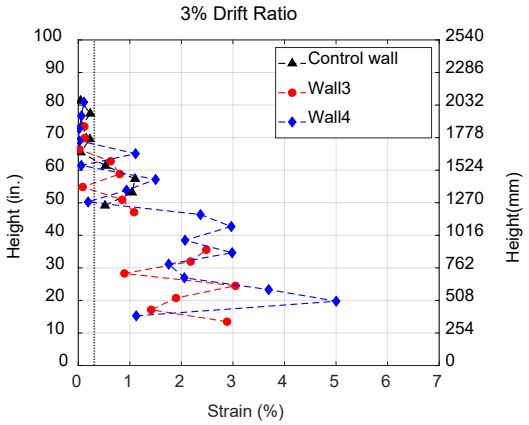

Figure 7-10:Vertical strain profiles along height for south facing MA corner reinforcing bar

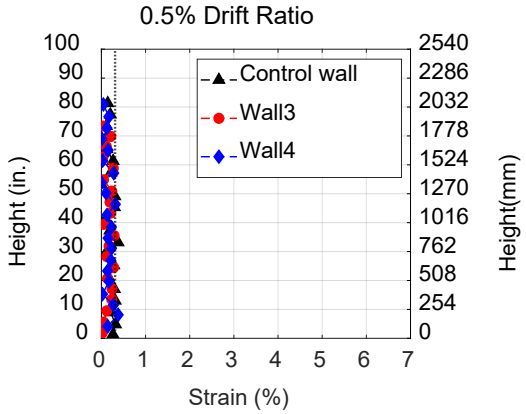

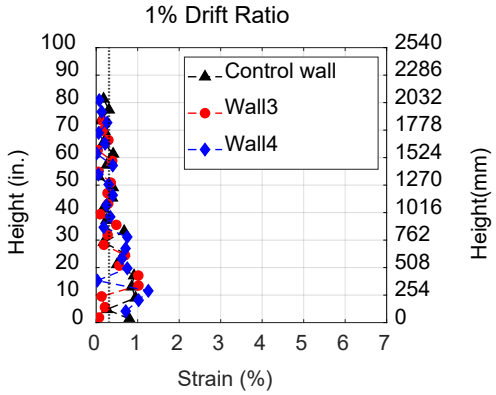

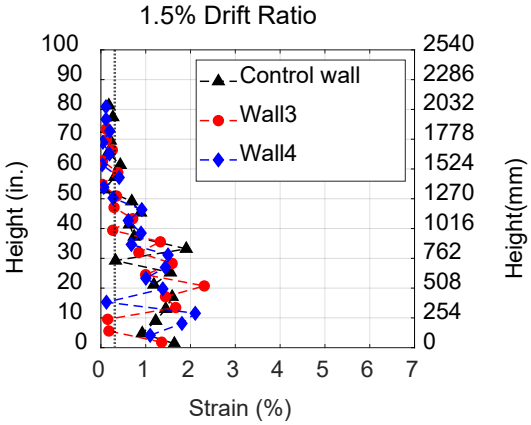

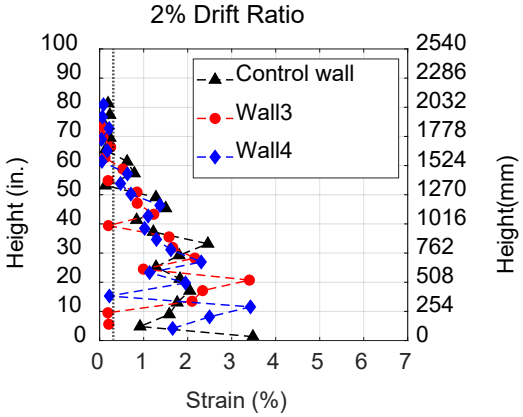

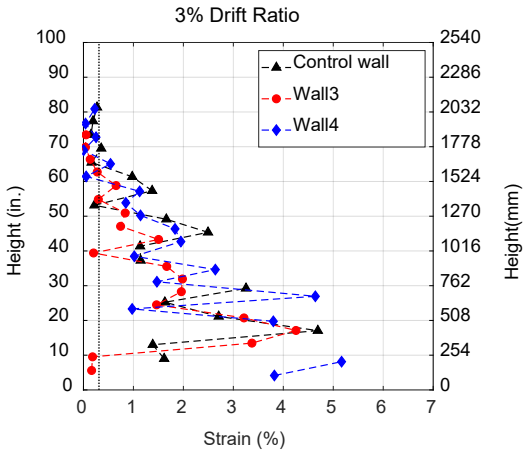

Figure 7-11: Vertical strain profiles along height for south facing MA middle reinforcing bar

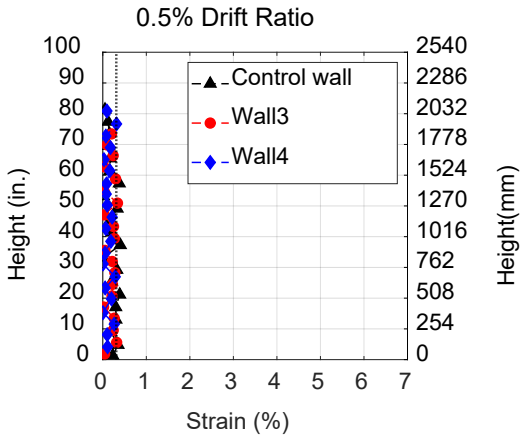

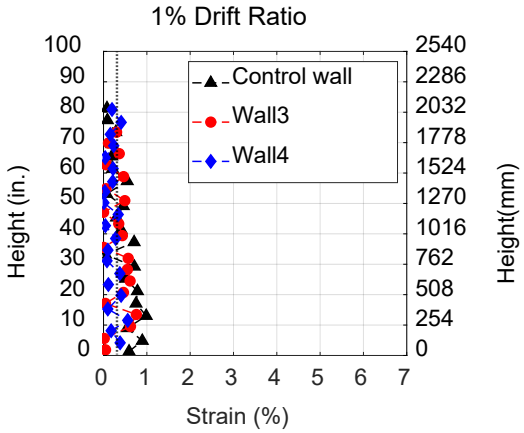

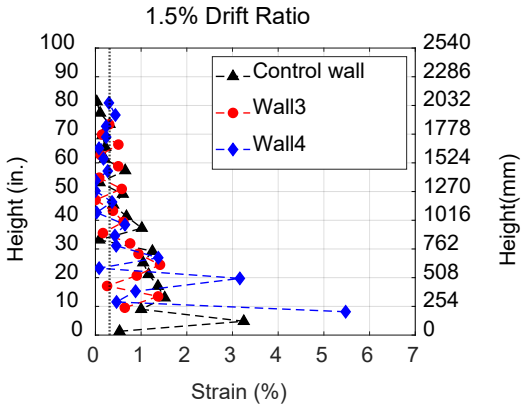

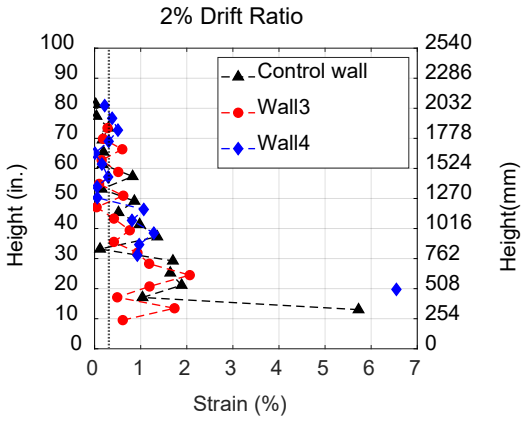

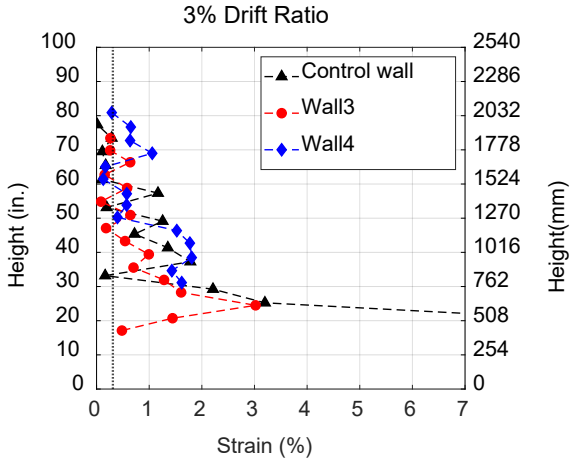

Figure 7-12: Vertical strain profiles along height for north facing corner reinforcing bar (All walls had QST bars except for Wall 4 which had MA bars)

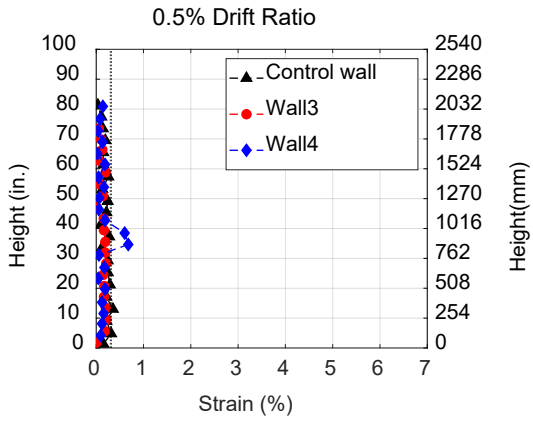

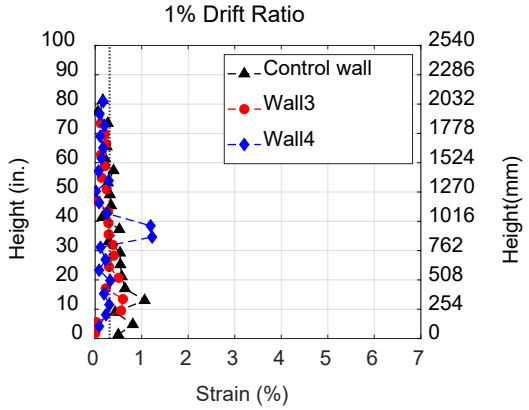

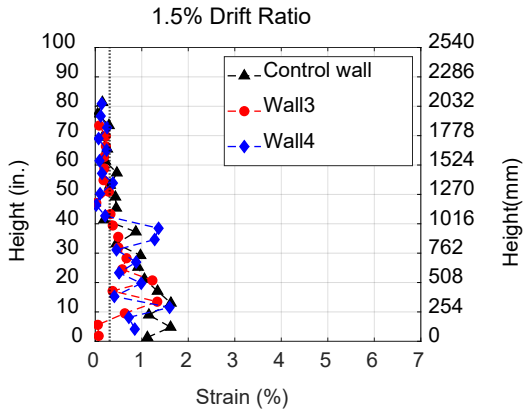

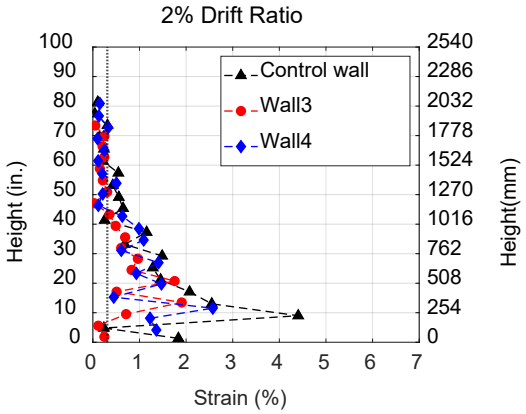

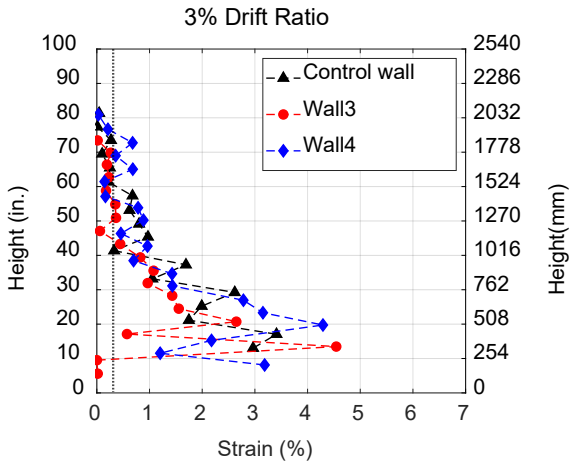

Figure 7-13: Vertical strain profiles along height for north facing middle reinforcing bar (All walls had QST bars except for Wall 4 which had MA bars)

7.4 Cumulative Strain in Longitudinal Reinforcing Bars

Cumulative strain demands on longitudinal reinforcing bars versus wall drift targets are plotted in Figure 7.14 to Figure 7.16. Cumulative strain demands were calculated as the sum of the strain excursions experienced by a bar for each half drift cycle, i.e., from the positive peak drift to the negative peak drift and then from the negative peak drift to the positive peak drift. As can be seen in Figure 7.16, QST bars spliced with friction welded couplers showed increased strain accumulation below the coupler up to 2.0% drift after which bar fractured below the coupler to the second cycle of 2.0% drift ratio. Table 7.2 and Table 7.3 shows the number of half cycles and accumulated strain just below and above the mechanical coupler from the recorded strain gauge recordings. MA bar accumulated less strain below the coupler and demonstrated better performance compared to QST bar mechanically spliced with friction welded couplers during wall test.

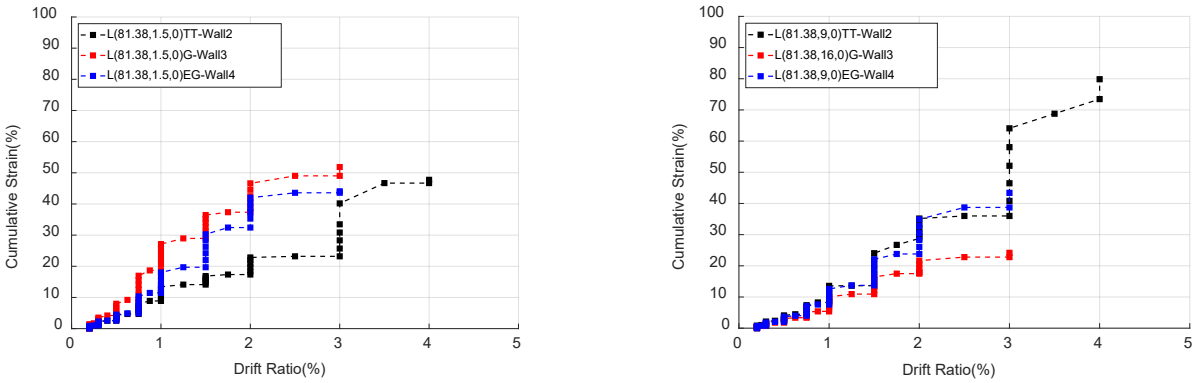

Figure 7-14: Cumulative bar strain at drift targets for MA corner reinforcing bars at the south end just below couplers at 1.5 in. (38.01mm) from base of wall, and just above couplers at 9 in. (228.6mm) or 16 in.(406.4 mm) from base of wall

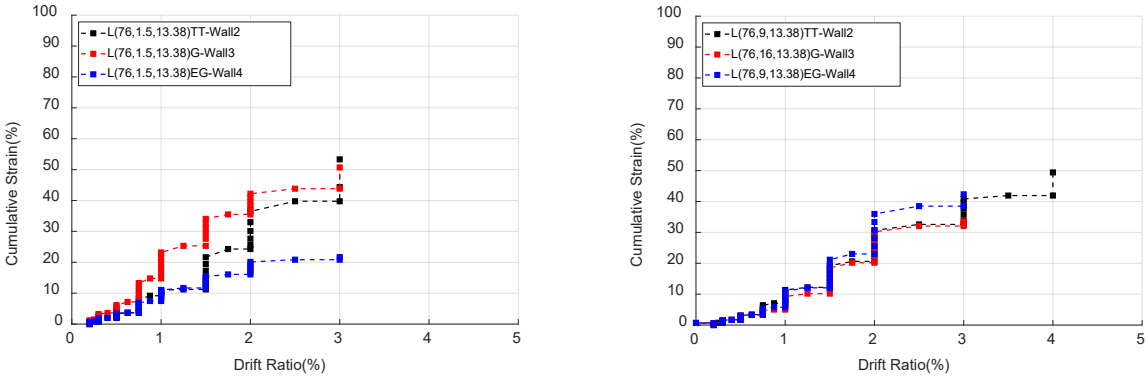

Figure 7-15: : Cumulative bar strain at drift targets for MA middle reinforcing bars at the south end just below couplers at 1.5 in. (38.01mm) from base of wall, and just above couplers at 9 in. (228.6mm) or 16 in.(406.4 mm) from base of wall

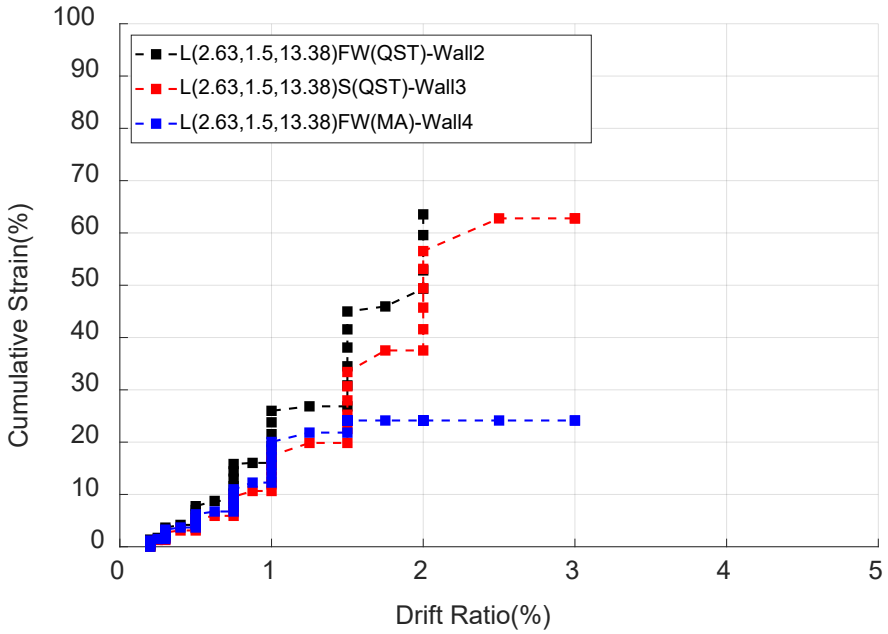

Figure 7-16: Cumulative strain versus drift targets for corner reinforcing bars at the north end just below couplers at 1.5 in. (38.01mm) from base of wall

Table 7.2: Number of half cycles and cumulative strain accumulated just below mechanical coupler

(1.5 in. ,38.01 mm from base of wall)

Bar Type	Mechanical Coupler Type	Number of half cycles (wall)	Cumulative bar strain below couplers in walls (%)	Wall Test Results
QST	Friction Welded-2	39	63.55	Bar fracture to the second cycle at 2.0% drift ratio. (below coupler) -Wall 2
MA	Friction Welded-2	45	NA	Strain gauge lost and no bar fracture was observed- Wall 4
MA	Taper threaded-2	49	47.75	No bar fracture was observed- Wall 2
MA	Grouted-2	43	51.85	Bar fracture to the first cycle at 3.0% drift ratio (below coupler)- Wall 3
MA	End Grip	45	44	Bar fracture to the first cycle at 4.0% drift ratio (below coupler)- Wall 4

Table 7.3:Number of half cycles and cumulative strain accumulated just above mechanical coupler

(9 in. (228.6 mm) in Wall 2 and Wall 4, and 16 in. (406.4 mm) in Wall3 from base of wall)

Bar Type	Mechanical Coupler Type*	Number of half cycles	Cumulative strain (%)	Wall Test Results
QST	Friction Welded-2	39	33.27	Bar fracture to the second cycle at 2.0% drift ratio. (below coupler) -Wall 2
MA	Friction Welded-2	45	52.18	No bar fracture was observed- Wall 4
MA	Taper threaded-2	49	79.85	No bar fracture was observed- Wall 2
MA	Grouted	43	24.17	Bar fracture to the first cycle at 3.0% drift ratio (below coupler)- Wall 3
MA	End Grip	45	50.02	Bar fracture to the first cycle at 4.0% drift ratio (above coupler)- Wall 4

7.5 Correlation between in-air inelastic test and wall test of Mechanical Splices

- Table 7.4 presents the number of half-cycles and cumulative strain measured below the mechanical couplers (2.5 in, 63mm from the wall-footing interface) during wall tests. The table also presents the mean half-cycles to fracture sustained by nominally identical mechanical splices during in-air inelastic cyclic testing (*Part I In-Air Testing)*. The number of half cycles sustained by mechanical splices with their corresponding strain amplitudes at drift targets were reported to be in the range of 39 to 49. QST bars spliced with friction welded couplers sustained 39 half cycles before fracture and MA bars spliced with taper threaded couplers sustained 49 half cycles until the end of test and did not fracture.
- Table 7.4 presents the strain amplitude from maximum tension to maximum compression strain measured below the couplers during each half-cycle of wall loading. The couplers that fractured prematurely, i.e., friction welded couplers spliced with QST bars, only sustained 39 half cycles in the wall.
- Considering the mean half-cycles to fracture in-air, the couplers that did not perform adequately in Wall 2 (QST Friction Welded-2) sustained the lowest number of in-air cycles coming just under 60 half-cycles on average before fracture. All other couplers performed adequately in the wall tests and had in-air performance ranging from an average of 76 half-cycles to 217 half-cycles to fracture. It is therefore recommended that an acceptance criterion exceeding 60 half-cycles to fracture be required for the pre-qualification in-air test proposed in *Part I In-Air Testing* to qualify couplers for use in hinge regions of members subjected to earthquake loading.

Table 7.4: Number of half cycles and cumulative strain accumulated just below mechanical coupler (from wall test) (1.5 in., 38.01 mm from base of wall), from Part I In-Air Testing

Bar Type	Mechanical Coupler Type	Mean-half cycles to fracture (in-air cyclic test 2.5% strain amplitude)	Cumulative bar strain below couplers in walls (%)	Wall Test Results
QST	Friction Welded-2	59.95	63.55	Bar fracture to the second cycle at 2.0% drift ratio. (below coupler) -Wall 2
MA	Friction Welded-2	76.1	NA	Strain gauge lost and no bar fracture was seen- Wall 4
MA	Taper threaded-2	76.1	47.75	No bar fracture was seen- Wall 2
MA	Grouted-2	115.5	51.85	Bar fracture to the first cycle at 3.0% drift ratio (below coupler)- Wall 3
MA	End Grip	124.9	44	Bar fracture to the first cycle at 4.0% drift ratio (below coupler)- Wall 4
QST	Swaged	216.8	62.79	Bar fracture to the second cycle at 3.0% drift (below coupler)- Wall 3

7.6 Energy Dissipation

- The amount of energy dissipated in each cycle to drift targets is plotted in Figure 7.17. The amount of energy dissipated to the first and second cycles to drift targets was comparable for the control wall, Wall 3, and Wall 4. During the first cycle to a drift ratio of 3.0% ,Wall 2 experienced multiple bar fractures in the north side boundary region and dissipated about 20% less energy than other walls, which might partly be attributed to larger hysteresis area and minimal degradation across cycles exhibited by boundary region with MA bars (Figure 6.27).

- Both boundary regions demonstrated wider and stable hysteresis loop and dissipated comparable energy up to a drift ratio of 3.0%, except where bar fractures occurred.
- Control wall, Wall 3 and Wall 4 exhibited ductile behavior demonstrating hysteretic energy dissipation and cyclic stability. Wall 2 with MA bars on the south side maintained 80% of peak lateral strength to a drift ratio of 3.0%.
- Wall 2 experienced a sharp decline in energy dissipation during the second and third cycles to a drift ratio of 3.0% as the north side boundary region experienced multiple longitudinal bar fractures.

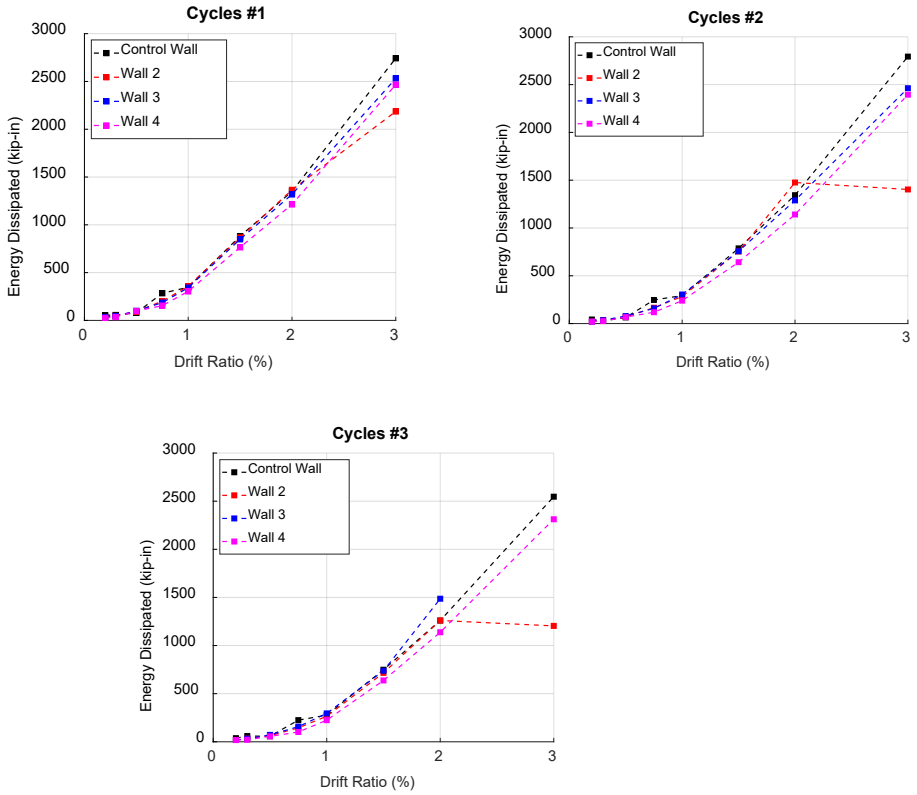

Figure 7-17: a) Energy dissipated in first cycle to each drift, b) Energy dissipated in second cycle to each drift, and c) Energy dissipated in third cycle to each drift

8 Summary and Conclusions

8.1 Background

The demand for higher grade steel reinforcement, namely Grade 80 (550) and Grade 100 (690 MPa) bars, continues to grow in the United States. Higher grade bars offer benefits of reduced congestion and improved constructability in reinforced concrete construction. Similarly, mechanical splices, which use coupling devices to connect two reinforcing bars, offer constructability benefits where lap-splicing is not practical or feasible. However, due to limited test data, uncertainty remains regarding the performance of mechanical splices combined with higher grade bars, particularly in hinge regions where bars undergo repeated inelastic strain reversals. This uncertainty has prompted ACI committee 318 to place limits on the use of mechanical splices with higher grade bars in concrete construction.

Although relatively few experiments have evaluated the performance of mechanical couplers with Grade 60 (420 MPa) bars under hinge-region demands, there has not been sufficient data to support the use of coupled Grade 80 (550 MPa) and 100 (690 MPa) reinforcing bars under harsh seismic demands. Furthermore, given the large diversity of coupler types available in the U.S. market, results from a limited set of tests cannot be generalized to all coupler types. And while testing all coupler types in concrete members subjected to realistic loading protocols is one way to qualify use of couplers in hinge regions, cost implications make such an approach impractical.

One solution is to offer cost-effective pre-qualification testing. This testing should impose realistic demands on couplers that are reflective of those occurring in hinge regions of concrete members. At the same time, the pre-qualification testing procedures should include acceptance criteria that ensure adequate seismic performance in concrete members. Unfortunately, none of the currently available specifications for qualifying mechanical splices include a loading protocol that is representative of the reversed inelastic strain demands applied to bars and couplers in seismic hinge regions. A review of current mechanical splice pre-qualification standards established that none incorporates reversed inelastic cyclic demands representative of hinge regions.

8.2 Objective and Scope

The overarching objective of this study is to provide experimental evidence supporting the safe use of mechanical couplers in hinge regions of reinforced concrete members. Of particular interest is the performance of coupler with Grade 80 (550 MPa) reinforcing bars that are seeing increasing use in critical seismic members in regions of high seismicity in the U.S. To achieve this aim, the study was divided into two core tasks: in-air low-cycle fatigue testing of mechanical splices, and full-scale wall testing with mechanical splices in hinge regions. Testing of mechanical splices in concrete walls was undertaken because walls tend to subject longitudinal reinforcement to relatively large strain demands compared with other concrete members, and because the use of mechanical splices in hinge regions of walls is commonly used for ease of construction.

In-air tests allowed the quantification of the low-cycle fatigue performance of various coupler types in production in the U.S. and provided relative performance comparisons between them and the fatigue life of the bare bars they couple. As these tests were being conducted, the protocols and test setup were adjusted to arrive at a reliable protocol that could be used for pre-qualifying devices under realistic seismic demands.

Results from wall tests served to identify correlation between the fatigue lives of mechanical splices in the walls and in the in-air tests. Wall tests therefore served to determine the minimum acceptance criteria in terms of half-cycles to fracture under the testing protocol developed in the first task, for mechanical splices to be safely used in hinge regions.

8.3 In-Air Inelastic Cyclic Testing

8.3.1 Summary

An extensive in-air experimental program was conducted to explore the low-cycle fatigue performance of commonly used mechanical couplers for connecting Grade 80 ASTM A706 supplemement-1 bars. Test variables included:

- Bar manufacturing process (micro-alloying (MA) and quenching and self-tempering (QST)).
- Coupler type (eleven representative devices from the U.S. market).

- Bar size (#8 (25 mm) and #11 (36 mm)).
- Lateral bracing condition (unbraced and braced).

Testing was conducted in two phases. In Phase 1, #8 (25mm) bars manufactured using MA and QST processes were tested unbraced. In Phase 2, #8 (25mm) and #11 (36mm) bars were tested both braced and unbraced.

A strain-controlled loading protocol was adopted in which specimens were cycled between +2 % in tension and –0.5% in compression. This protocol was selected because it represents strain demands typically sustained by longitudinal reinforcement in hinge regions of reinforced concrete members subjected to seismic events.

Through this test program, comparative performance benchmarks were established across mechanical splice types, and key insights were gained into how bar properties, coupling mechanisms, bar size, and boundary conditions influence inelastic fatigue performance. These results informed the development of a proposed qualification protocol tailored to use in seismic hinge-region applications.

8.3.2 Conclusions

- All splice systems satisfied ACI 318 Type 2 tensile strength requirements of $1.25f_y$ (specified yield strength) or f_u (specified tensile strength), but their ductility and low-cycle fatigue performance varied significantly. Some mechanical splices exhibited comparable ductility and fatigue performance to the bars they couple, while others only exhibited a fraction of the bar performance. Findings therefore suggest that a strength criterion alone cannot ensure ductility and fatigue life for mechanical splices that will be placed in hinge regions.
- For mechanical splices in locations expected to yield, a tension strain criterion is recommended. Targeting tensile strains on the order of the specified minimum uniform strain of ASTM A706 Supplement 1 is advised. Several splice types exceeded the specified minimum strain requirements in the bars they couple prior to fracture.
- Some couplers sustained only a fraction of the fatigue life of the bars they connect, while others matched or exceeded it. These findings therefore indicate that certain mechanical couplers demonstrated limited fatigue resistance and raise concerns about the reliable performance in

hinge regions of mechanical splices without appropriate pre-qualification testing. These concerns may not be confined only to Grade 80 (550 MPa) bars but may extend to other reinforcement grades as well. Since this experimental work only tested eleven coupler types, expanding the scope of testing could identify additional couplers with either superior or subpar performance across the U.S market.

- The majority of low-cycle fractures occurred in the reinforcing bars at or near the coupler interface, underscoring that this region is a critical zone of stress concentration. Limited fractures of the couplers were observed, and only in #11 (36 mm) grouted splices.
- For mechanical splice tests in Phase 1, failure occurred in the reinforcing bars rather than within the coupler assemblies, suggesting that splice capacity is governed by the strength and fatigue resistance of the bars themselves, as altered by the coupling mechanism. Because the selected bar batches in Phase 1 exhibited fatigue lives near the median performance of reinforcing bars reported in the United States, the fatigue performance of the splice specimens tested in this phase can be considered representative of the median response of Grade 80 (550 MPa) mechanical splices currently in production in the U.S.
- The influence of bar size on fatigue performance was inconsistent across splice types. While some splices showed improved performance with larger #11 (36 mm) bars, others performed better with smaller #8 (25mm) bars.
- Bracing of mechanical splice specimen was observed to improve fatigue resistance for some splices but not others. These results emphasize that while bracing can mitigate buckling and may improve fatigue performance of a splice specimen, splice type is the more critical factor governing fatigue behavior under the proposed loading protocol that limits buckling.
- A positive relationship was identified between uniform strain capacity in monotonic tension tests of splices and fatigue life in cyclic tests of splices, suggesting that bar ductility influences both tension and cyclic behaviors.
- The study recommends the following pre-qualification testing for mechanical splices that are intended for seismic hinge regions:

i. Monotonic tension tests should be conducted to verify that mechanical splices develop the minimum specified tensile strength and uniform strain of the bars being connected.

ii. Low-cycle fatigue testing should be conducted to ensure adequate fatigue performance under reversed inelastic strain demands:

- A fully reversed strain amplitude of 2.5% with clear bar gripping span of 1.5 times the bar diameter was found to be both effective in testing and representative of the demands placed on longitudinal reinforcement in special seismic members.
- The required minimum number of half-cycles to fracture for pre-qualification may be set comparable with the performance of the bars being spliced, since some splices demonstrated the ability to achieve this threshold.
- A lower minimum number of half-cycles could be acceptable when supported by satisfactory performance in concrete members. A minimum number of half-cycles to fracture of approximately 60 was justified based on wall testing results conducted in the second task of this study (see conclusions below).

8.4 Wall Testing

8.4.1 Summary

The national standard for the design of concrete buildings, ACI 318-19, restricts the use of mechanical splices with Grade 80 (550 MPa) and Grade 100 (690 MPa) bars in regions expected to yield due to concerns about the performance of mechanical couplers with higher strength bars under large inelastic strain reversals. While several studies have assessed mechanical couplers with Grade 60 (420 MPa) bars, limited data exist for couplers with higher-strength bars.

This study explored correlations between the seismic performance of concrete walls with mechanical splices and in-air testing of mechanical splices such that a minimum acceptable number of cycles to fracture can be determined for pre-qualification testing that would result in acceptable seismic performance of members.

Four full-scale rectangular walls satisfying ACI 318-19 detailing for special structural walls were tested under a constant compressive axial load of about 3.5% of gross section capacity and reversed cyclic displacements. The walls were 84 in. long (2,134 mm), 16 in. wide (406 mm) and 204 in. tall (5,182 mm) to the center of the lateral load. All walls were nominally identical in design and detailing except for the type of mechanical coupler used at the base. The concrete strengths in all walls were between 7.5 and 7.8 ksi (51.5 and 53.5 MPa). The longitudinal bars of the boundary region were sourced from the same batches used in the Phase 1 in-air tests and consisted of #8 (25mm) grade 80 A706 bars produced either using quenching and self-tempering (QST) or micro-alloying (MA) process. The test study focused on varying coupler types and bar manufacturing process of the grade 80 A706 longitudinal bars in boundary regions.

The control wall had no splices along the longitudinal bars, and all other walls had their boundary longitudinal bars spliced using mechanical couplers at 2.5 in. (63 mm) above top of footing where strain demands and effects of cyclic loading were most severe. Wall 2 had short couplers that exhibited lower in-air performance, Wall 3 had long couplers that exhibited higher in-air performance, and Wall 4 had MA bars spliced using end grip couplers and the same friction welded couplers used in Wall 2, but with MA reinforcing bars. MA bars with friction welded couplers showed better in-air inelastic performance. This selection was made to investigate if this difference in in-air performance translates into similar difference in performance in the wall tests.

8.4.2 Conclusions

8.4.2.1 General Behavior

- All specimens exhibited a flexural mode of strength degradation characterized by longitudinal bar yielding, spalling of concrete, followed by longitudinal bar buckling in most cases and longitudinal bar fracture due to low cycle fatigue
- Except for Wall2, all walls completed at least one cycle to a drift ratio of 3% with minimal lateral strength loss, which is deemed acceptable for special concrete seismic systems under an MCE level event.
- Wall 2 experienced bar fractures at the friction welded couplers during the cycles to a drift ratio of 2.0%. By the end of the cycles to a drift ratio of 2.0%, Wall 2 had lost about 50%

of its lateral strength, which is deemed to be inadequate performance for a special structural wall.

8.4.2.2 Strain Demands on Mechanical Splices

- The spread of inelastic strains in longitudinal reinforcing bars extended to similar distances from the section of peak moment. These distances were approximately equal to the full length of the wall. The plastic hinge regions were therefore on the order of the wall length (L_w) for all walls. Plasticity spread was higher in MA bars than QST bars, which can be partly attributed to the higher tensile to yield strength ratio of MA bars.
- Strain concentrations on longitudinal bars varied significantly and were influenced by the mechanical coupler type used for splicing and the properties of the bars they spliced. Generally, strain demands were higher at the critical moment section below the couplers at low drift levels and then became larger above the couplers at larger drift demands. A possible explanation is that as bars are pulled in tension from the top loading point, the couplers essentially act as head in that they resist upward movement due to their geometry, which in turn reduces strain demands on bars below them.

8.4.2.3 Mechanical Splice Performance

- Longitudinal bars fractured in some cases at the coupler-bar interface and in other cases away from the couplers, depending on the coupling device.
- Fractures typically occurred after significant bar buckling, except for Wall 2 where fractures at the friction welded couplers occurred due to low-cycle fatigue before bar buckling was observed.
- A positive correlation was observed between in-air inelastic test and in-concrete test of mechanical splices used in the study. Couplers that exhibited better low-cycle fatigue performance during in-air inelastic testing demonstrated better performance when tested in concrete walls. Particularly, the friction welded coupler with QST bar performed worse in-air than with MA bar. The same observation was seen comparing performance of the coupler in Wall 2 and Wall 4.

- Couplers with 76 mean-half cycles to fracture during in-air inelastic testing resulted in acceptable wall performance, while the coupler with only 60 mean-half cycles to fracture did not result in acceptable wall performance.
- The observed correlation between the reversed inelastic cyclic test proposed in this study and coupler performance in walls indicates that the in-air test can be used to pre-qualify mechanical splices for application in seismic hinge regions.
- Based on the number of half-cycles to fracture that each mechanical coupler type sustained prior to fracture under the pre-qualification testing protocol proposed in the first task of this study, and the coupler performance in the wall tests, a requirement of more than 60 half-cycles to fracture in the pre-qualification test is recommended to achieve acceptable seismic performance for concrete walls under an MCE level seismic event.

9 Acknowledgements

The authors would like to acknowledge the financial contributions of the Concrete Reinforcing Steel Institute (CRSI) and its members, without which this study would not have been possible. The generous financial contribution of the American Concrete Institute's Foundation Concrete Research Council is also gratefully acknowledged.

CRSI member mills NUCOR Seatle and CMC Mesa generously provided the steel bars used in the study. Coupler producers Splice Sleeve, Bar Splice, HRC, NVent, and Dayton Superior are gratefully acknowledged for providing the fully assembled mechanical splices used in this study.

Tindall in San Antonio is gratefully acknowledged for helping the research team dispose of the large wall specimens after they were tested. Whaley Steel and Spartan Reinforcing are gratefully acknowledged for their help in tying reinforcing bar cages for the walls.

10 Appendix A: Mill Certificates

CMC STEEL ARIZONA
11444 E. GERMANN RD.
MESA AZ 85212-9700

CERTIFIED MILL TEST REPORT
For additional copies call
830-372-8771

We hereby certify that the test results presented here are accurate and conform to the reported grade specification

Jacob Selzer – CMC Steel
Quality Assurance Manager

HEAT NO.:4122688 SECTION: REBAR 16MM (#5) 60'0" A615/A706-80 GRADE: ASTM A615 & A706 GR80 Dual Gr ROLL DATE: 09/24/2022 MELT DATE: 09/24/2022 Cert. No.: 85203710 / 122688F928	SOLD TO	PJs Rebar 45055 Fremont Blvd Fremont CA US 94538-6318 5107435300 5104903952	SHIP TO	PJs Rebar - Ind Dr 45060 Industrial Dr Fremont CA US 94538-6318 5107435300	Delivery#: 85203710 BOL#: 75033132 CUST PO#: 26951 CUST P/N: DLVRY LBS / HEAT: 36798.000 LB DLVRY PCS / HEAT: 588 EA

Characteristic	Value	Characteristic	Value	Characteristic	Value
C	0.26%	Elongation test 1	12%		
Mn	1.23%	Elongation Gage Lgth test 1	8IN		
P	0.015%	Tensile to Yield ratio test1	1.30		
S	0.023%	Bend Test 1	Passed		
Si	0.23%	Rebar Deformation Avg. Spaci	0.419IN		
Cu	0.36%	Rebar Deformation Avg. Heigh	0.041IN		
Cr	0.18%	Rebar Deformation Max. Gap	0.139IN		
Ni	0.12%	Bend Test Diameter	2.188IN		
Mo	0.073%	Strain at Peak Stress test 1	8.7%		
V	0.067%				
Cb	0.004%				
Sn	0.014%				
Al	0.001%				
N	0.0101%				
Carbon Eq A706	0.49%				
Yield Strength test 1	83.5ksi				
Yield Strength test 1 (metri	576MPa				
Tensile Strength test 1	108.8ksi				
Tensile Strength 1 (metric)	751MPa				

The Following is true of the material represented by this MTR:

**Material is fully killed and is Hot Rolled Steel*
**100% melted, rolled, and manufactured in the USA*
**EN10204:2004 3.1 compliant*
**Contains no weld repair*
**Contains no Mercury contamination*
**Manufactured in accordance with the latest version of the plant quality manual*
**Meets the "Buy America" requirements of 23 CFR635.410, 49 CFR 661*
**Warning: This product can expose you to chemicals which are known to the State of California to cause cancer, birth defects or other reproductive harm. For more information go to www.P65Warnings.ca.gov*

REMARKS :

Page 1 OF 1 11/09/2022 08:28:49

Figure 10-1 Mill certificate for QST #5 Grade 80 bars used in wall tests

CMC STEEL ARIZONA
11444 E. GERMANN RD.
MESA AZ 85212-9700

CERTIFIED MILL TEST REPORT
For additional copies call
830-372-8771

We hereby certify that the test results presented here are accurate and conform to the reported grade specification

Jacob Selzer – CMC Steel
Quality Assurance Manager

HEAT NO.:4120466 SECTION: REBAR 25MM (#8) 60'0" A615/A706-80 GRADE: ASTM A615 & A706 GR80 Dual Gr ROLL DATE: 07/08/2022 MELT DATE: 07/08/2022 Cert. No.: 85089919 / 120466F660	SOLD TO	PJs Rebar 45055 Fremont Blvd Fremont CA US 94538-6318 5107435300 5104903952	SHIP TO	PJs Rebar - Turlock 250 D St Turlock CA US 95380-0000 5107435271	Delivery#: 85089919 BOL#: 74861165 CUST PO#: 26757 CUST P/N: DLVRY LBS / HEAT: 48704.000 LB DLVRY PCS / HEAT: 304 EA

Characteristic	Value	Characteristic	Value	Characteristic	Value
C	0.29%	Elongation test 1	14%		
Mn	1.28%	Elongation Gage Lgth test 1	8IN		
P	0.014%	Tensile to Yield ratio test1	1.31		
S	0.025%	Bend Test 1	Passed		
Si	0.21%	Rebar Deformation Avg. Spaci	0.696IN		
Cu	0.36%	Rebar Deformation Avg. Heigh	0.064IN		
Cr	0.20%	Rebar Deformation Max. Gap	0.169IN		
Ni	0.12%	Bend Test Diameter	5.000IN		
Mo	0.069%	Strain at Peak Stress test 1	10.1%		
V	0.055%				
Cb	0.002%				
Sn	0.012%				
Al	0.002%				
N	0.0073%				
Carbon Eq A706	0.53%				
Yield Strength test 1	85.7ksi				
Yield Strength test 1 (metri	592MPa				
Tensile Strength test 1	111.9ksi				
Tensile Strength 1 (metric)	772MPa				

The Following is true of the material represented by this MTR:

**Material is fully killed and is Hot Rolled Steel*
**100% melted, rolled, and manufactured in the USA*
**EN10204:2004 3.1 compliant*
**Contains no weld repair*
**Contains no Mercury contamination*
**Manufactured in accordance with the latest version of the plant quality manual*
**Meets the "Buy America" requirements of 23 CFR635.410, 49 CFR 661*
**Warning: This product can expose you to chemicals which are known to the State of California to cause cancer, birth defects or other reproductive harm. For more information go to www.P65Warnings.ca.gov*

REMARKS :

Page 1 OF 1 11/09/2022 08:30:26

Figure 10-2 Mill certificate for #8 Grade 80 bars from batch QTB1

CMC STEEL ARIZONA
11444 E. GERMANN RD.
MESA AZ 85212-9700

CERTIFIED MILL TEST REPORT
For additional copies call
830-372-8771

We hereby certify that the test results presented here are accurate and conform to the reported grade specification

Jacob Selzer – CMC Steel
Quality Assurance Manager

HEAT NO.:4133755 SECTION: REBAR 36MM (#11) 60'0" A615/A706-80 GRADE: ASTM A615&A706a-22 GR80 DualGr ROLL DATE: 10/18/2023 MELT DATE: 10/18/2023 Cert. No.: 10/18/2023 / 133755F182	SOLD TO		SHIP TO		Delivery#: BOL#: CUST PO#: CUST P/N: DLVRY LBS / HEAT: 0.000 LB DLVRY PCS / HEAT:

Characteristic	Value	Characteristic	Value	Characteristic	Value
C	0.28%	Elongation Gage Lgth test 1	8IN		
Mn	1.27%	Tensile to Yield ratio test1	1.31		
P	0.011%	Bend Test 1	Passed		
S	0.032%	Rebar Deformation Avg. Spaci	0.950IN		
Si	0.26%	Rebar Deformation Avg. Heigh	0.080IN		
Cu	0.39%	Rebar Deformation Max. Gap	0.145IN		
Cr	0.23%	Bend Test Diameter	9.870IN		
Ni	0.11%	Uniform Elongation test 1	11.8%		
Mo	0.056%	Deform radius/height ratio 1	1.97		
V	0.081%				
Cb	0.002%				
Sn	0.011%				
Al	0.002%				
N	0.0113%				
Carbon Eq A706	0.52%				
Yield Strength test 1	87.4ksi				
Yield Strength test 1 (metri	603MPa				
Tensile Strength test 1	114.8ksi				
Tensile Strength 1 (metric)	792MPa				
Elongation test 1	14%				

The Following is true of the material represented by this MTR:

**Material is fully killed and is Hot Rolled Steel*
**100% melted, rolled, and manufactured in the USA*
**EN10204:2004 3.1 compliant*
**Contains no weld repair*
**Contains no Mercury contamination*
**Manufactured in accordance with the latest version of the plant quality manual*
**Meets the "Buy America" requirements of 23 CFR635.410, 49 CFR 661*
**Warning: This product can expose you to chemicals which are known to the State of California to cause cancer, birth defects or other reproductive harm. For more information go to www.P65Warnings.ca.gov*

REMARKS : MEETS THE SUPPLEMENTARY REQUIREMENTS OF A706-22A FOR EARTHQUAKE-RESISTANT STRUCTURES. ALSO MEETS AASHTO M31
PLEASE EMAIL CMC_AZ_QUALITY@CMC.COM WITH ANY FEEDBACK, QUESTIONS, OR CONCERNS

Page 1 OF 1 07/11/2024 15:19:05

Figure 10-3 Mill certificate for #11 Grade 80 bars from batch QTB2

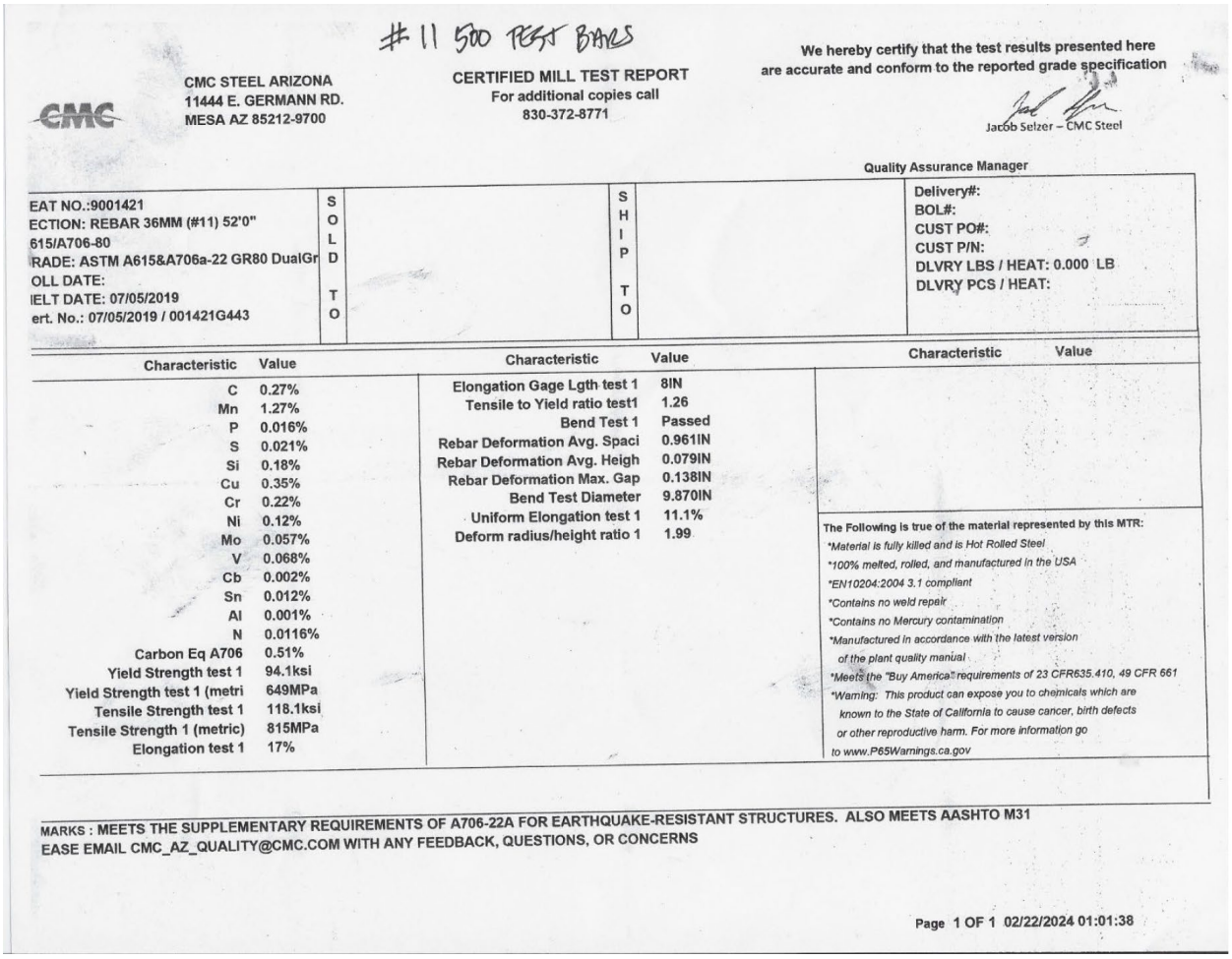

#11 500 TEST BARS

CMC STEEL ARIZONA
11444 E. GERMANN RD.
MESA AZ 85212-9700

CERTIFIED MILL TEST REPORT
For additional copies call
830-372-8771

We hereby certify that the test results presented here are accurate and conform to the reported grade specification

Jacob Selzer – CMC Steel
Quality Assurance Manager

EAT NO.:9001421
ECTION: REBAR 36MM (#11) 52'0"
615/A706-80
RADE: ASTM A615&A706a-22 GR80 DualGr
OLL DATE:
IELT DATE: 07/05/2019
ert. No.: 07/05/2019 / 001421G443

SOLD TO

SHIP TO

Delivery#:
BOL#:
CUST PO#:
CUST P/N:
DLVRY LBS / HEAT: 0.000 LB
DLVRY PCS / HEAT:

Characteristic	Value
C	0.27%
Mn	1.27%
P	0.016%
S	0.021%
Si	0.18%
Cu	0.35%
Cr	0.22%
Ni	0.12%
Mo	0.057%
V	0.068%
Cb	0.002%
Sn	0.012%
Al	0.001%
N	0.0116%
Carbon Eq A706	0.51%
Yield Strength test 1	94.1ksi
Yield Strength test 1 (metri	649MPa
Tensile Strength test 1	118.1ksi
Tensile Strength 1 (metric)	815MPa
Elongation test 1	17%

Characteristic	Value
Elongation Gage Lgth test 1	8IN
Tensile to Yield ratio test1	1.26
Bend Test 1	Passed
Rebar Deformation Avg. Spaci	0.961IN
Rebar Deformation Avg. Heigh	0.079IN
Rebar Deformation Max. Gap	0.138IN
Bend Test Diameter	9.870IN
Uniform Elongation test 1	11.1%
Deform radius/height ratio 1	1.99

Characteristic	Value

The Following is true of the material represented by this MTR:
*Material is fully killed and is Hot Rolled Steel
*100% melted, rolled, and manufactured in the USA
*EN10204:2004 3.1 compliant
*Contains no weld repair
*Contains no Mercury contamination
*Manufactured in accordance with the latest version of the plant quality manual
*Meets the "Buy America" requirements of 23 CFR635.410, 49 CFR 661
*Warning: This product can expose you to chemicals which are known to the State of California to cause cancer, birth defects or other reproductive harm. For more information go to www.P65Warnings.ca.gov

MARKS : MEETS THE SUPPLEMENTARY REQUIREMENTS OF A706-22A FOR EARTHQUAKE-RESISTANT STRUCTURES. ALSO MEETS AASHTO M31
EASE EMAIL CMC_AZ_QUALITY@CMC.COM WITH ANY FEEDBACK, QUESTIONS, OR CONCERNS

Page 1 OF 1 02/22/2024 01:01:38

Figure 10-4 Mill certificate for #11 Grade 80 bars from batch QTB3

NUCOR®

Mill Certification

11/18/2022

MTR#:
Lot #:350002567720
2424 SW ANDOVER ST
SEATTLE, WA 98106 US
206 933-2222
Fax: 206 933-2207

Sold To:

Ship To:

Customer P.O		Sales Order #	
Product Group	Rebar	Product #	3020149
Grade	A706 Gr 80	Lot #	350002567720
Size	#8	Heat #	3500025677
BOL #		Load #	
Description	REBAR #8 A706 Gr 80 60' 0" 6001-10000 lbs	Customer Part #	
Production Date	05/28/2022	Qty Shipped LBS	0
Product Country Of Origin	United States	Qty Shipped EA	
Original Item Description		Original Item Number	

I hereby certify that the material described herein has been manufactured in accordance with the specifications and standards listed above and that it satisfies those requirements.

Melt Country of Origin : United States Melting Date: 05/22/2022

C (%)	Mn (%)	P (%)	S (%)	Si (%)	Ni (%)	Cr (%)	Mo (%)	Cu (%)	V (%)	Nb (%)
0.28	1.11	0.012	0.027	0.14	0.10	0.11	0.03	0.27	0.132	0.002

ASTM A706 6.4 CE & ASTM F1554 CE (%) : 0.47

Tensile testing

	Yield (PSI)	Tensile (PSI)	Elongation in 8" (%)
(1)	83187	109605	15.6

Mechanical

	Average Deformation Height (IN)	Bend Test	Total Elongation at Maximum Force (%)
(1)	0.065	Pass	16.0

Other Test Results

Tensile / Yield Ratio : 1.32 Weight Percent Variance (%) : -4.64

Comments:

inc. = incomplete

ASTM A706-16 Gr 80, AASHTO M 31-21 Type W Gr 80
Nucor-Seattle is ISO 9001-2015, 14001, 45001 and ABS certified. All manufacturing processes of the steel materials in this product, including melting, have occurred within the United States. Mercury, in any form has not been intentionally added at any point during the the production and testing of this material. This material is free of HG contamination and is ROHS compliant. No weld repair was performed. Parts meet the requirements of the purchase order and have been produced under the Nucor Steel Seattle quality manual.

The melting, casting and rolling processes for manufacturing the this material are in full compliance with the American Iron and Steel requirement as mandated in EPA's State Revolving Fund Programs. This material was manufactured in the US and complies with the Buy American Act, and (FTA) Buy America Requirements (49 C.F.R. part 661)

Erik Nissen, Plant Metallurgist

Page **1** of **1**

Figure 10-5 Mill certificate for #8 Grade 80 bars from batch MAB1

NUCOR

Mill Certification

05/21/2024

MTR#:1674166-7
Lot #:350003607020
2424 SW ANDOVER ST
SEATTLE, WA 98106 US
206 933-2222
Fax: 206 933-2207

Sold To: NUCOR STEEL SEATLLE INC DONATION CUSTOME
2424 SW ANDOVER ST
SEATTLE, WA 98106 US

Ship To: NUCOR STEEL SEATLLE INC DONATION CUSTOME
NUCOR REBAR FABRICATION
4421 192ND ST E
TACOMA, WA 98446 US

Customer PO	BUNDLES FOR RESEARCH	Sales Order #	35035142 - 8.1
Product Group	Rebar	Product #	3057463
Grade	A706 Gr 80	Lot #	350003607020
Size	#11	Heat #	3500036070
BOL #	BOL-1720698	Load #	1674166
Description	Rebar #11/36mm A706 Gr 80 60' 0" [720"] 4001-8000 lbs	Customer Part #	
Production Date	02/02/2024	Qty Shipped LBS	12752
Product Country Of Origin	United States	Qty Shipped EA	40
Original Item Description		Original Item Number	

I hereby certify that the material described herein has been manufactured in accordance with the specifications and standards listed above and that it satisfies those requirements.

Melt Country of Origin : United States — Melting Date: 01/29/2024

C (%)	Mn (%)	P (%)	S (%)	Si (%)	Ni (%)	Cr (%)	Mo (%)	Cu (%)	V (%)	Nb (%)
0.29	1.18	0.012	0.030	0.20	0.09	0.16	0.03	0.32	0.138	0.003

Mechanical

	Average Deformation Height (IN)	Bend Test	Total Elongation at Maximum Force (%)
(1)	0.074	Pass	09.8

ASTM A706 6.4 CE & ASTM F1554 CE (%) : 0.50

Tensile testing

	Yield (PSI)	Tensile (PSI)	Elongation in 8" (%)
(1)	84606	111738	17.2

Other Test Results

Tensile / Yield Ratio : 1.32 — Weight Percent Variance (%) : -5.77

Comments:

ASTM A706-22a Gr 80, AASHTO M 31-21 Type W Gr 80
Nucor-Seattle is ISO 9001, 14001, 45001 and ABS certified. All manufacturing processes of the steel materials in this product, including melting, casting and rolling have occurred within the United States. Mercury, in any form has not been intentionally added at any point during the production and testing of this material. This material is free of HG contamination and is ROHS compliant. No weld repair was performed.

This material was manufactured in the US and complies with the requirements of 49 USC 5323(J)(8),d Federal Transit Administration's (FTA) Buy America Requirements (49 CFR part 661), as well as Buy American Requirements – Surface Transportation Assistance Act of 1982, as amended Title 49 Section 661.5 (d)(1)(2) and 23 CFR 635.410 Buy America requirements (FHWA). The melting, casting and rolling processes for manufacturing are in full compliance with the American Iron and Steel requirement as mandated in EPA's State Revolving Fund Programs.

Parts meet the requirements of the purchase order and have been produced under the Nucor Steel Seattle quality manual.

Erik Nissen, Plant Metallurgist

Page 1 of 1

Figure 10-6 Mill certificate for #11 Grade 80 bars from batch MAB2

11 Appendix B: Fracture Pictures

11.1 Coupler types

Figure B1 Threaded-1

Figure B2 Swaged

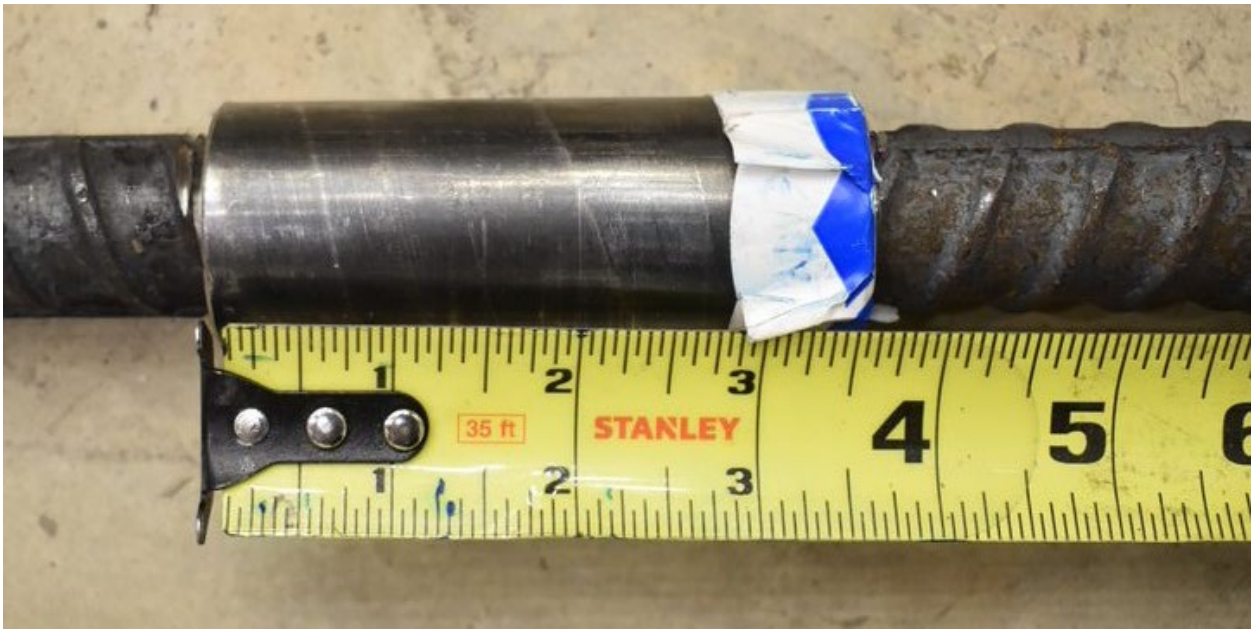

Figure B3 Taper Threaded-1

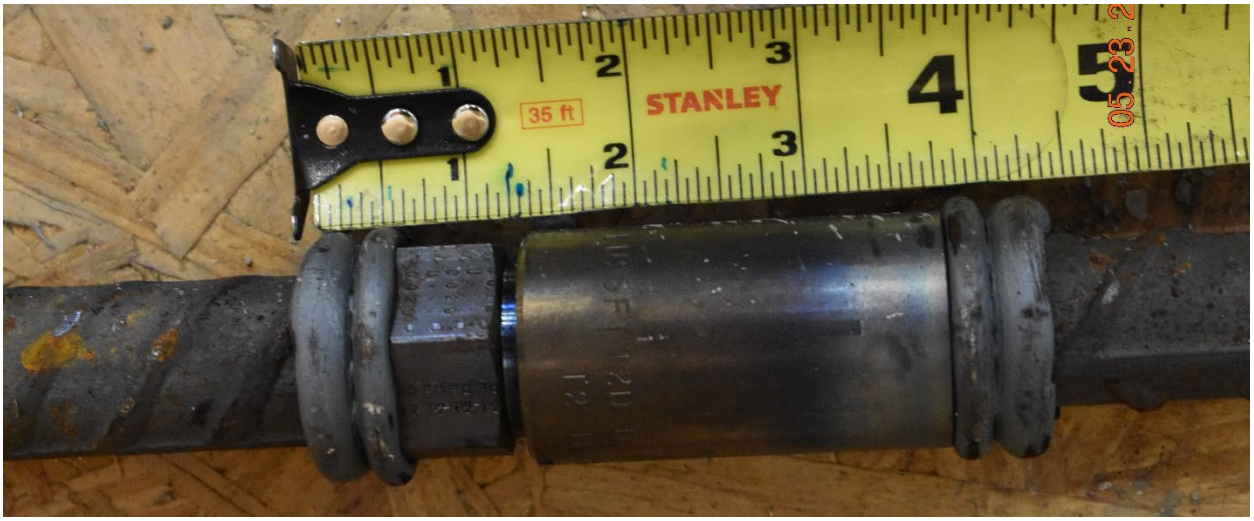

Figure B4 Friction Welded-1

Figure B5 Taper Threaded-2

Figure B6 Grouted/Threaded-1

Figure B7 End Grip

Figure B8 Friction Welded-2

Figure B9 Threaded-2

Figure B10 Grouted-1

Figure B11 Grouted-2

11.2 Bare Bar Batch (MAB1)

Figure B12 IC-M8-80-MA(-0.5_2)1.5db_1

Figure B13 IC-M8-80-MA(-0.5_2)1.5db_2

Figure B14 IC-M8-80-MA(-0.5_2)1.5db_3

11.3 Bare Bar Batch (QTB1)

Figure B15 IC-Q8-80-QST(-0.5_2)1.5db_1

Figure B16 IC-Q8-80-QST(-0.5_2)1.5db_2

Figure B17 IC-Q8-80-QST(-0.5_2)1.5db_3

11.4 Threaded-1 (MAB1)

Figure B18 IC-M8-80-Threaded-1(-0.5_2)1.5db_1

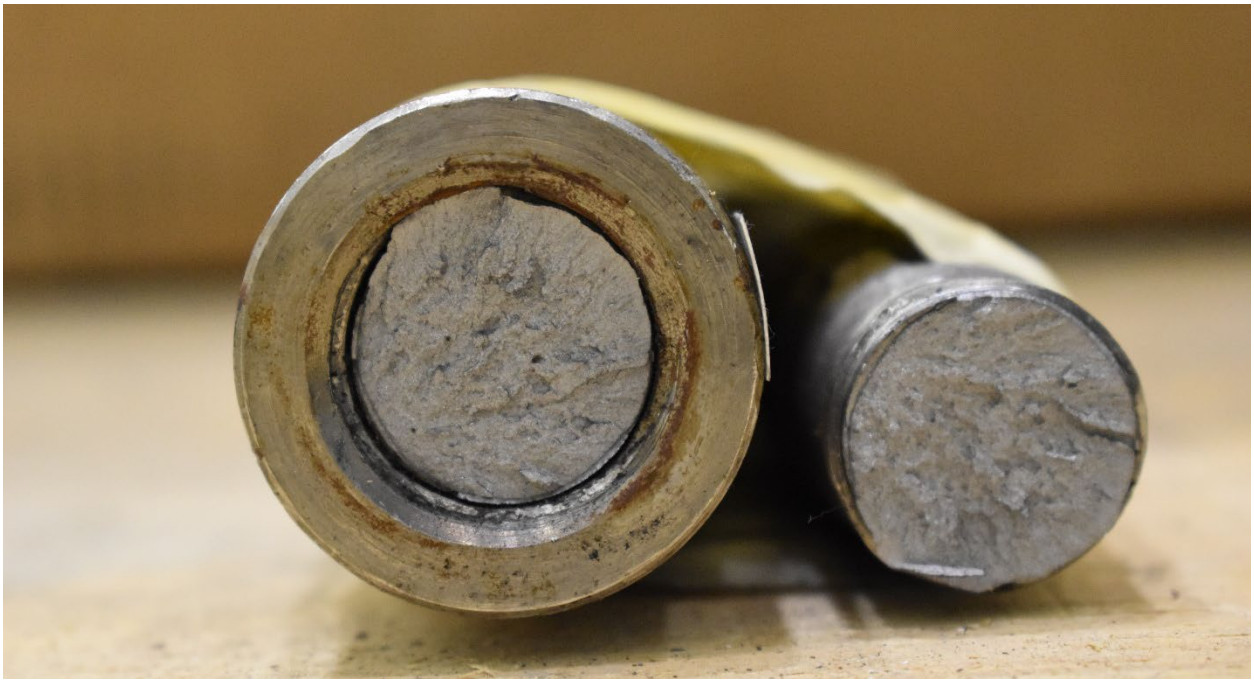

Figure B19 IC-M8-80-Threaded-1(-0.5_2)1.5db_2

Figure B20 IC-M8-80-Threaded-1(-0.5_2)1.5db_3

11.5 Threaded-1 (QTB1)

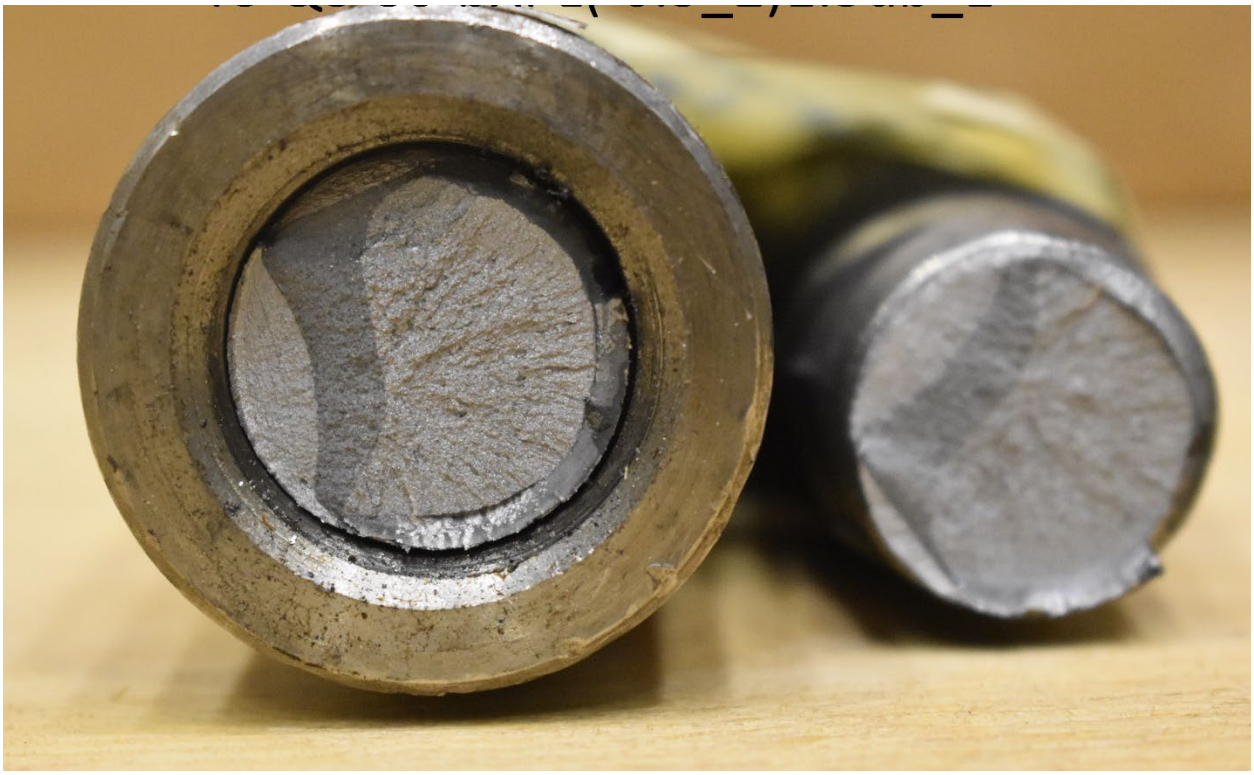

Figure B21 IC-Q8-80-Threaded-1(-0.5_2)1.5db_1

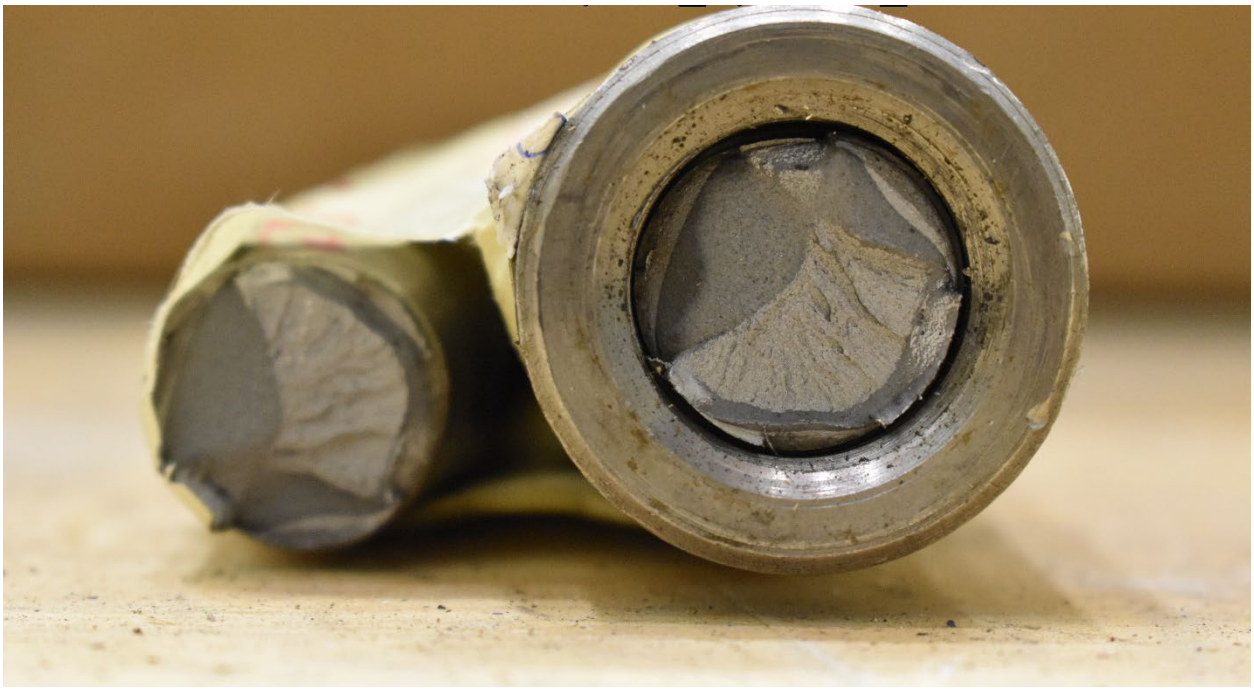

Figure B22 IC-Q8-80-Threaded-1(-0.5_2)1.5db_2

Figure B23 IC-Q8-80-Threaded-1(-0.5_2)1.5db_3

11.6 Swaged (MAB1)

Figure B24 IC-M8-80-Swaged(-0.5_2)1.5db_1

Figure B25 IC-M8-80-Swaged(-0.5_2)1.5db_2

Figure B26 IC-M8-80-Swaged(-0.5_2)1.5db_3

11.7 Swaged (QTB1)

Figure B27 IC-Q8-80-Swaged(-0.5_2)1.5db_1

Figure B28 IC-Q8-80-Swaged(-0.5_2)1.5db_2

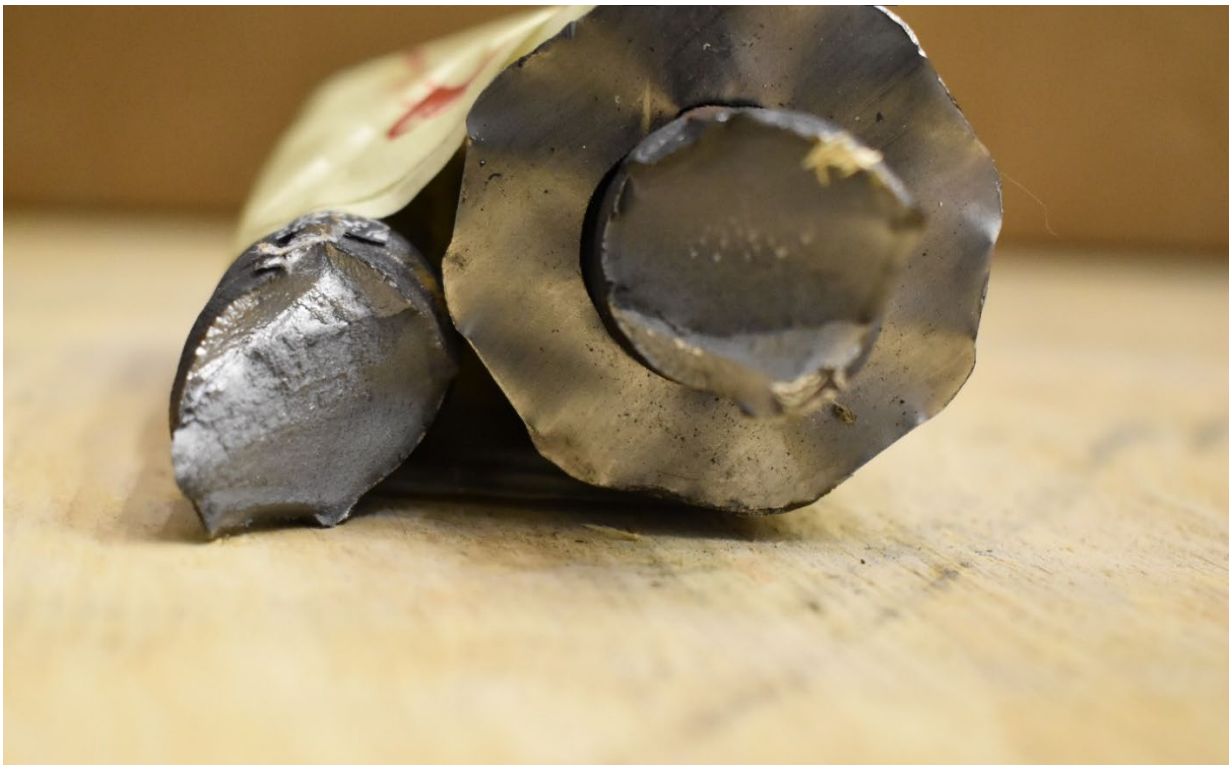

Figure B29 IC-Q8-80-Swaged(-0.5_2)1.5db_3

11.8 Threaded-1 (MAB1)

Figure B30 IC-M8-80-Taper Threaded-1(-0.5_2)1.5db_1

Figure B31 IC-M8-80-Taper Threaded-1(-0.5_2)1.5db_2

Figure B32 IC-M8-80-Taper Threaded-1(-0.5_2)1.5db_3

Figure B33 IC-M8-80-Taper Threaded-1(-0.5_2)1.5db_4

11.9 Threaded-1 (QTB1)

Figure B34 IC-Q8-80-Taper Threaded-1(-0.5_2)1.5db_1

Figure B35 IC-Q8-80-Taper Threaded-1(-0.5_2)1.5db_2

Figure B36 IC-Q8-80-Taper Threaded-1(-0.5_2)1.5db_3

11.10 Threaded-2 (MAB1)

Figure B37 IC-M8-80-Threaded-2(-0.5_2)1.5db_1

Figure B38 IC-M8-80-Threaded-2(-0.5_2)1.5db_2

Figure B39 IC-M8-80-Threaded-2(-0.5_2)1.5db_3

11.11 Threaded-2 (QTB1)

Figure B40 IC-Q8-80-Threaded-2(-0.5_2)1.5db_1

Figure B41 IC-Q8-80-Threaded-2(-0.5_2)1.5db_2

Figure B42 IC-Q8-80-Threaded-2(-0.5_2)1.5db_3

11.12 Friction Welded-2 (MAB1)

Figure B43 IC-M8-80-Friction Welded-2(-0.5_2)1.5db_1

Figure B44 IC-M8-80-Friction Welded-2(-0.5_2)1.5db_2

Figure B45 IC-M8-80-Friction Welded-2(-0.5_2)1.5db_3

11.13 Friction Welded-2 (QTB1)

Figure B46 IC-Q8-80-Friction Welded-2(-0.5_2)1.5db_1

Figure B47 IC-Q8-80-Friction Welded-2(-0.5_2)1.5db_2

Figure B48 IC-Q8-80-Friction Welded-2(-0.5_2)1.5db_3

Figure B49 IC-Q8-80-Friction Welded-2(-0.5_2)1.5db_4

11.14 End Grip (MAB1)

Figure B50 IC-M8-80-End Grip(-0.5_2)1.5db_1

Figure B51 IC-M8-80-End Grip(-0.5_2)1.5db_3

Figure B52 IC-M8-80-End Grip(-0.5_2)1.5db_4

Figure B53 IC-M8-80-End Grip(-0.5_2)1.5db_5

Figure B54 IC-M8-80-End Grip(-0.5_2)1.5db_6

11.15 End Grip (QTB1)

Figure B55 IC-Q8-80-End Grip(-0.5_2)1.5db_1

Figure B56 IC-Q8-80-End Grip(-0.5_2)1.5db_4

Figure B57 IC-Q8-80-End Grip(-0.5_2)1.5db_5

Figure B58 IC-Q8-80-End Grip(-0.5_2)1.5db_6

11.16 Taper Threaded-2 (MAB1)

Figure B59 IC-M8-80-Taper Threaded-2(-0.5_2)1.5db_1

Figure B60 IC-M8-80-Taper Threaded-2(-0.5_2)1.5db_2

Figure B61 IC-M8-80-Taper Threaded-2(-0.5_2)1.5db_3

Figure B62 IC-M8-80-Taper Threaded-2(-0.5_2)1.5db_4

Figure B63 IC-M8-80-Taper Threaded-2(-0.5_2)1.5db_5

11.17 Taper Threaded-2 (QTB1)

Figure B64 IC-Q8-80-Taper Threaded-2(-0.5_2)1.5db_1

Figure B65 IC-Q8-80-Taper Threaded-2(-0.5_2)1.5db_2

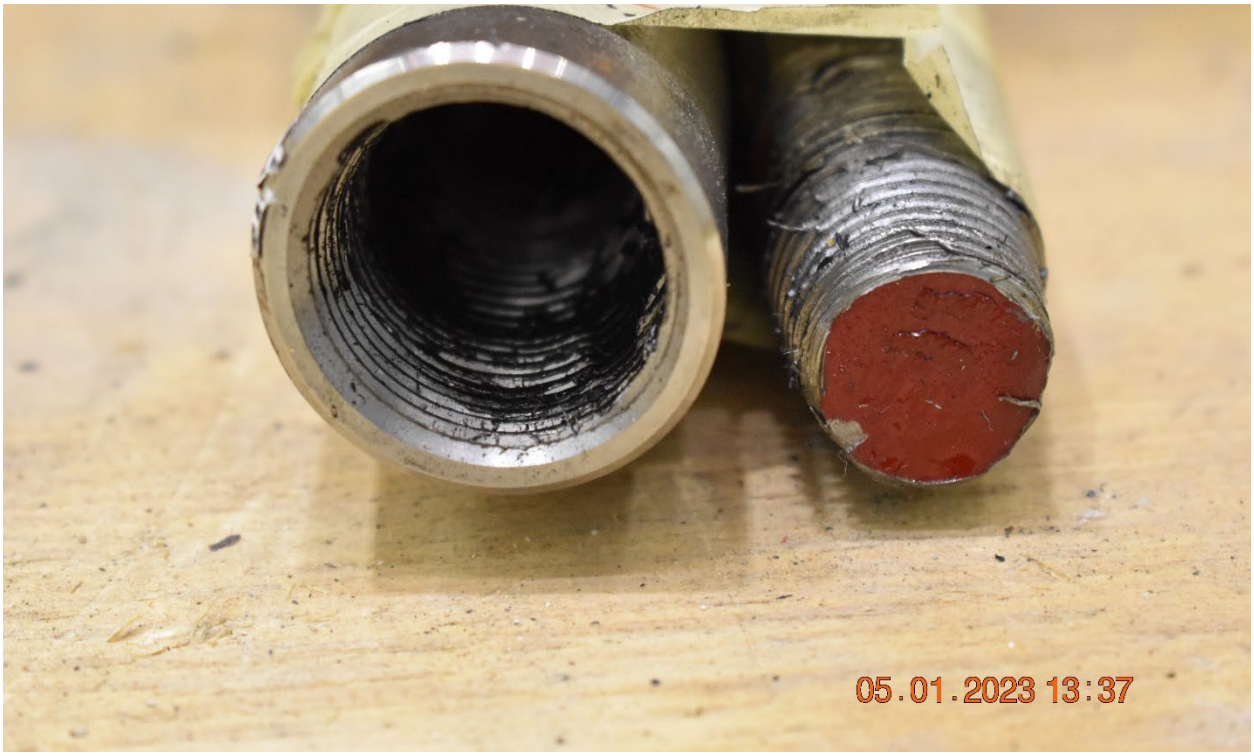

Figure B66 IC-Q8-80-Taper Threaded-2(-0.5_2)1.5db_3

Figure B67 IC-Q8-80-Taper Threaded-2(-0.5_2)1.5db_4

11.18 Grouted/Threaded-1 (MAB1)

Pull out failure between targets 3 and 5

Figure B68 Pull- out

Figure B69 IC-M8-80-Grouted/Threaded-1(-0.5_2)1.5db_3

Figure B70 IC-M8-80-Grouted/Threaded-1(-0.5_2)1.5db_5

Figure B71 IC-M8-80-Grouted/Threaded-1(-0.5_2)1.5db_5

Figure B72 IC-M8-80-Grouted/Threaded-1(-0.5_2)1.5db_6

11.19 Grouted/Threaded-1 (QTB1)

Figure B73 IC-Q8-80-Grouted/Threaded-1(-0.5_2)1.5db_2

Figure B74 IC-Q8-80-Grouted/Threaded-1(-0.5_2)1.5db_6

Figure B75 IC-Q8-80-Grouted/Threaded-1(-0.5_2)1.5db_7

11.20 Friction Welded-1 (MAB1)

Figure B76 IC-M8-80-Friction Welded-1(-0.5_2)1.5db_1

Figure B77 IC-M8-80-Friction Welded-1(-0.5_2)1.5db_2

Figure B78 IC-M8-80-Friction Welded-1(-0.5_2)1.5db_3

11.21 Friction Welded-1 (QTB1)

Figure B79 IC-Q8-80-Friction Welded-1(-0.5_2)1.5db_1

Figure B80 IC-Q8-80-Friction Welded-1(-0.5_2)1.5db_2

Figure B81 IC-Q8-80-Friction Welded-1(-0.5_2)1.5db_3

Figure B82 IC-Q8-80-Friction Welded-1(-0.5_2)1.5db_4

11.22 Grouted-2 (MAB1)

Figure B83 IC-M8-80-Grouted-2(-0.5_2)1.5db_2

Figure B84 IC-M8-80-Grouted-2(-0.5_2)1.5db_3

11.23 Grouted-2 (QTB1)

Figure B85 IC-Q8-80-Grouted-2(-0.5_2)1.5db_1

Figure B86 IC-Q8-80-Grouted-2(-0.5_2)1.5db_2

Figure B87 IC-Q8-80-Grouted-2(-0.5_2)1.5db_3

11.24 Grouted-1 (QTB1)

Figure B88 IC-Q8-80-Grouted-1(-0.5_2)1.5db_1

11.25 Bare Bar (MAB2)

Figure B89 BIC-M11-80-MA(-0.5_2)1.5db_1

Figure B90 BIC-M11-80-MA(-0.5_2)1.5db_2

Figure B91 BIC-M11-80-MA(-0.5_2)1.5db_3

Figure B92 BIC-M11-80-MA(-0.5_2)1.5db_4

11.26 Bare Bar (QTB2)

Figure B93 BIC-Q11-80-QST(-0.5_2)1.5db_1

Figure B94 BIC-Q11-80-QST(-0.5_2)1.5db_2

Figure B95 BIC-Q11-80-QST(-0.5_2)1.5db_3

11.27 Bare Bar (QTB3)

Figure B96 BIC-Q11-80-Barebar(-0.5_2)1.5db_1

Figure B97 BIC-Q11-80-Barebar(-0.5_2)1.5db_2

Figure B98 BIC-Q11-80-Barebar(-0.5_2)1.5db_3

11.28 End Grip (QTB3)

Figure B99 BIC-Q11-80-End Grip(-0.5_2)1.5db_1

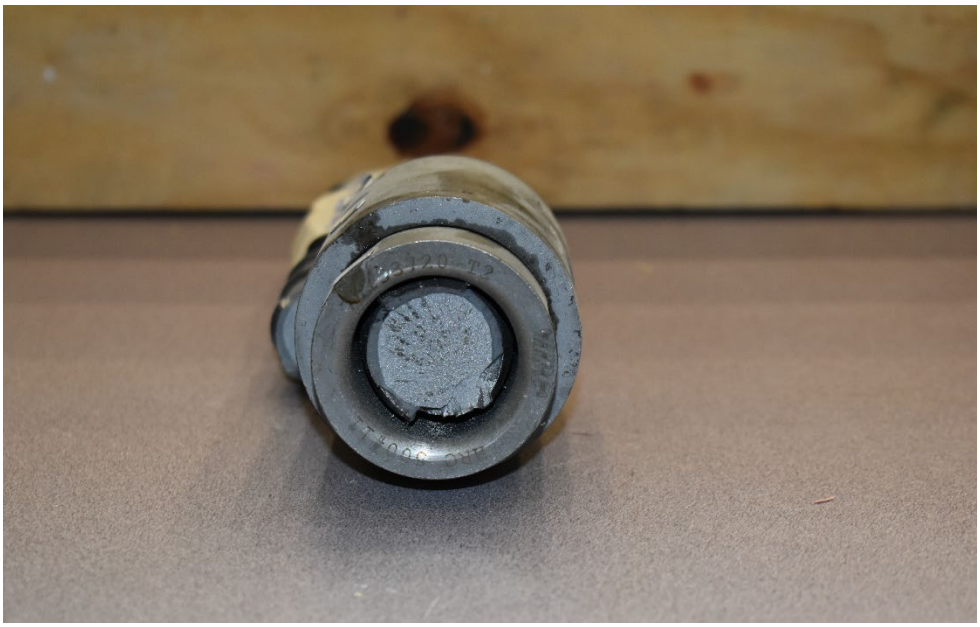

Figure B100 BIC-Q11-80-End Grip(-0.5_2)1.5db_2

Figure B101 BIC-Q11-80-End Grip(-0.5_2)1.5db_3

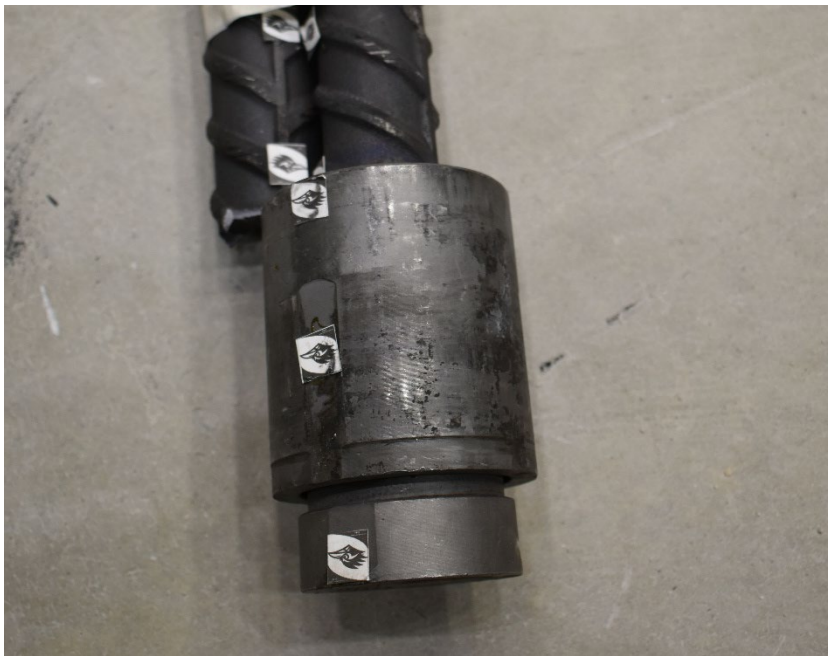

Figure B102 BIC-Q11-80-End Grip(-0.5_2)1.5db_4

Figure B103 BIC-Q11-80-End Grip(-0.5_2)1.5db_5

Grouted-1(QTB2)-Braced

Figure B104 BIC-Q11-80-Grouted-1(-0.5_2)1.5db_1

11.29 Grouted-2(QTB1)-Braced

Figure B105 BIC-Q8-80-Grouted-2(-0.5_2)1.5db_2

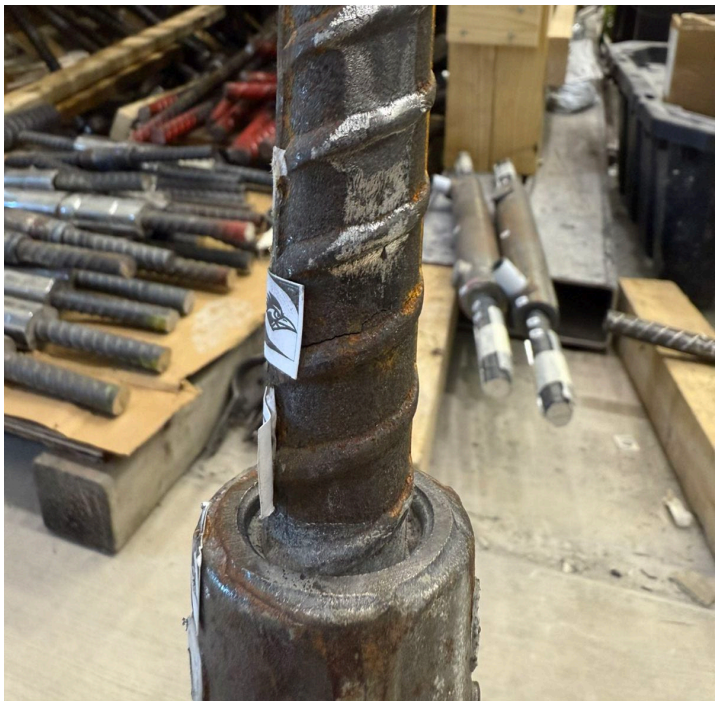

Figure B106 BIC-Q8-80-Grouted-2(-0.5_2)1.5db_3

Figure B107 BIC-Q8-80-Grouted-2(-0.5_2)1.5db_4

11.30 Grouted-2(MAB1)-Braced

Figure B108 BIC-M8-80-Grouted-2(-0.5_2)1.5db_1

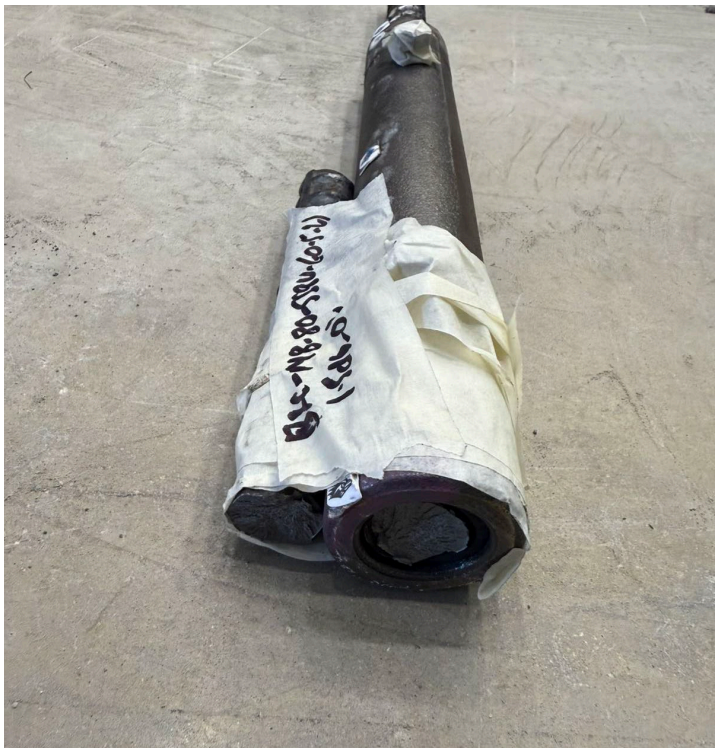

Figure B109 BIC-M8-80-Grouted-2(-0.5_2)1.5db_2

Figure B110 BIC-M8-80-Grouted-2(-0.5_2)1.5db_3

12 Appendix C: Vertical Strain Profiles (Compressive)-DIC System

Vertical surface strains along the height of the wall specimen at the boundary regions were calculated from the recorded target displacements as described in section 6.1.5 .

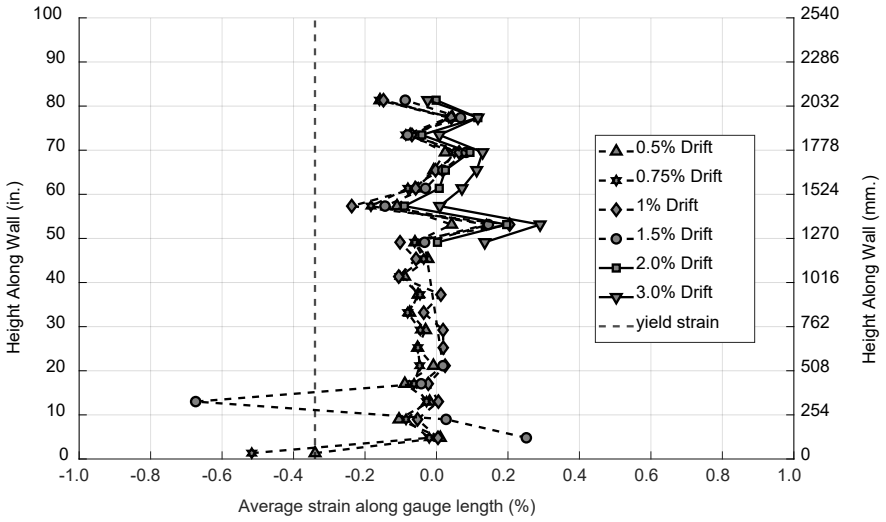

Figure 9-1:Vertical strain profiles from surface targets facing the south MA corner reinforcing bar

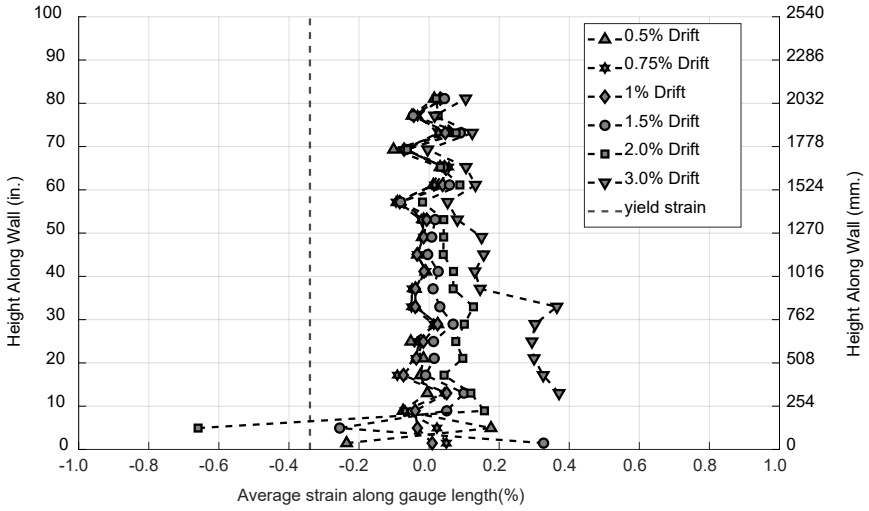

Figure 12-1: Vertical strain profiles from surface targets facing the south MA middle reinforcing bar

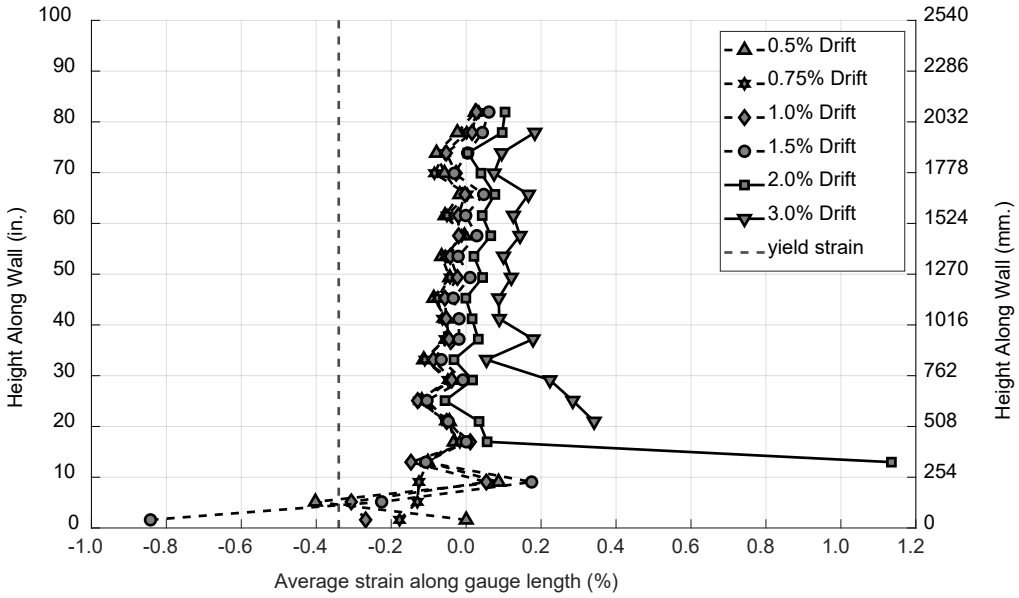

Figure 12-2: Vertical strain profiles from surface targets facing the north QST corner reinforcing bar

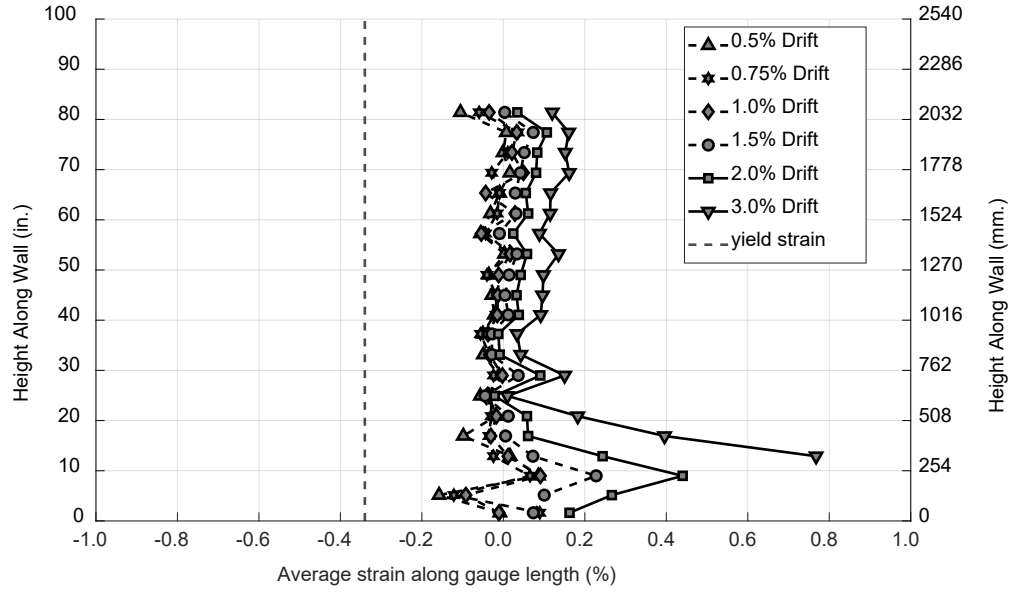

Figure 12-3: Vertical strain profiles from surface targets facing the north QST middle reinforcing bar

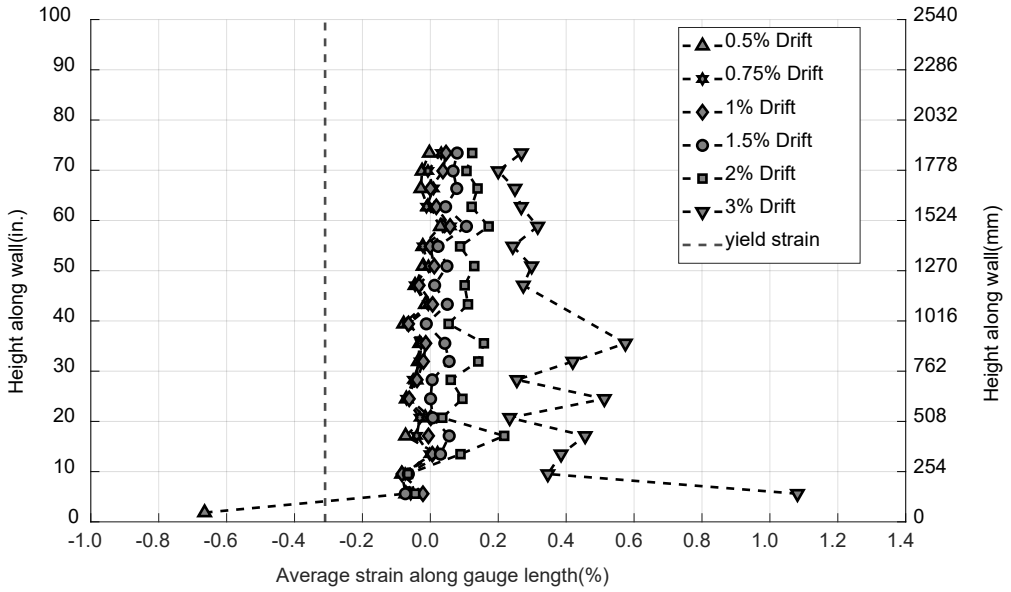

Figure 12-4: Vertical strain profiles from surface targets facing the south MA corner reinforcing bar with a grouted coupler

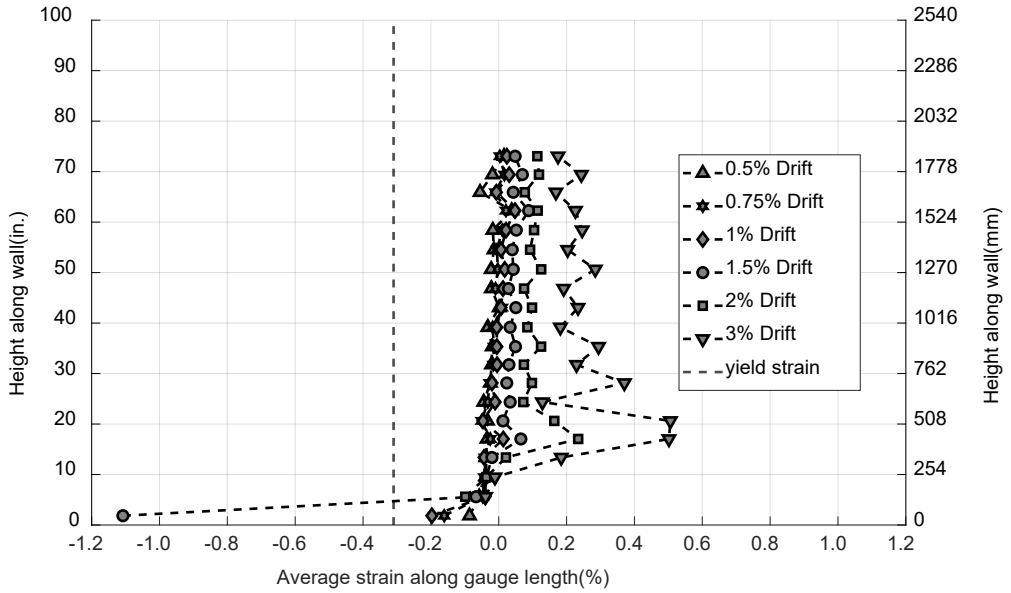

Figure 12-5 : Vertical strain profiles from surface targets facing the south MA middle reinforcing bar with a grouted coupler

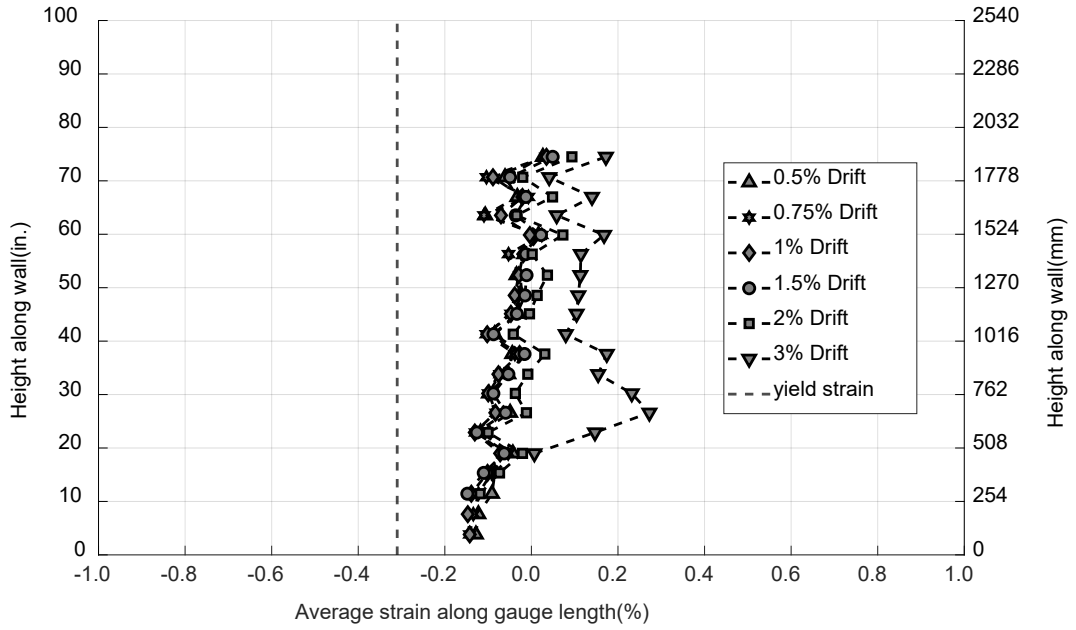

Figure 12-6: Vertical strain profiles from surface targets facing the north QST corner reinforcing bar with a swaged coupler

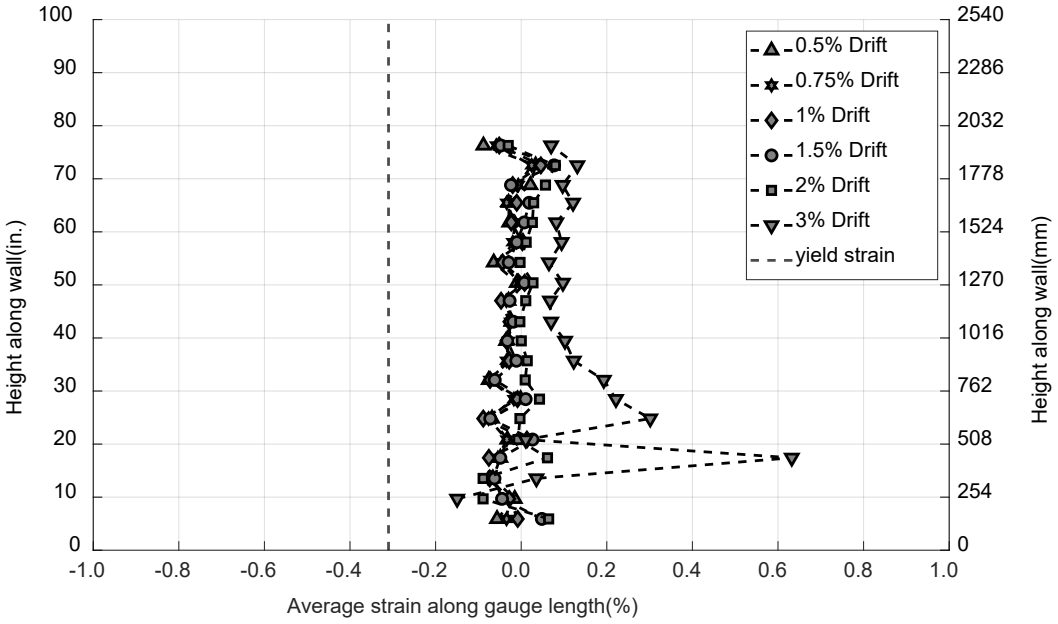

Figure 12-7: Vertical strain profiles from surface targets facing the north QST middle reinforcing bar with a swaged coupler

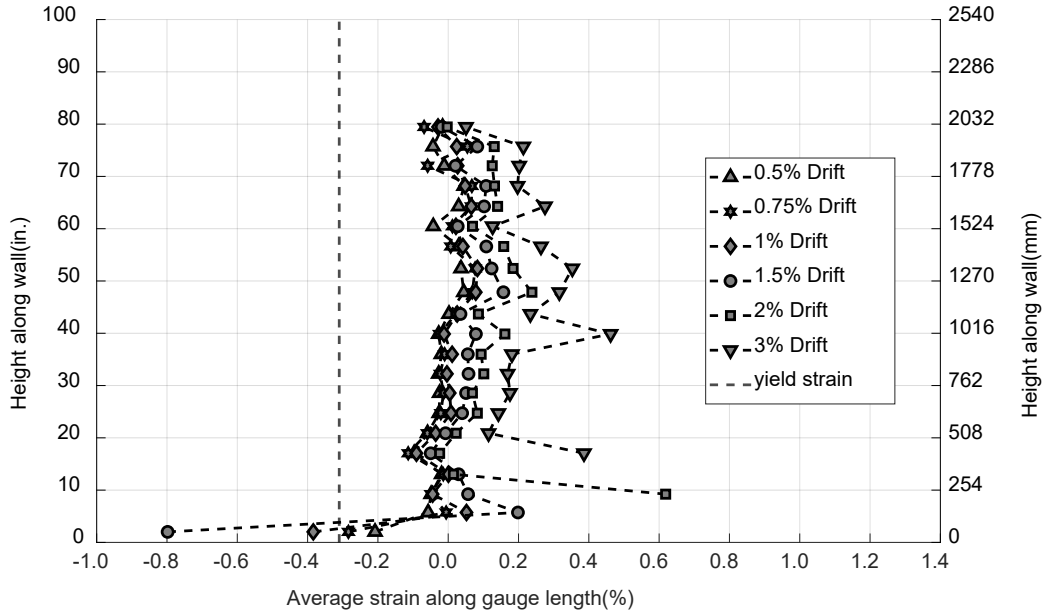

Figure 12-8: Vertical strain profiles from surface targets facing the south MA corner reinforcing bar with an end grip coupler

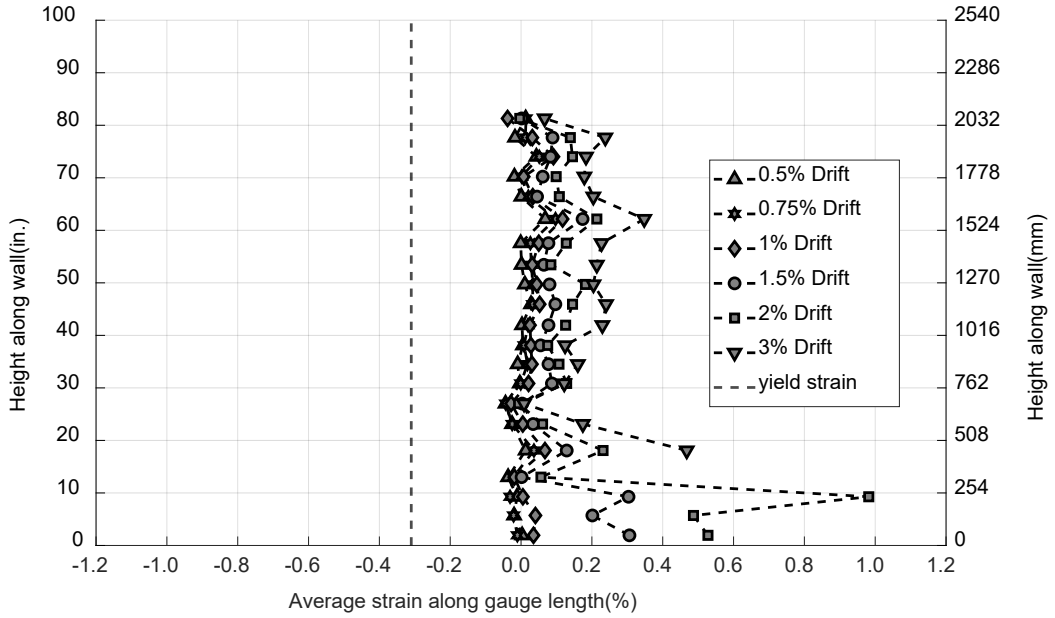

Figure 12-9: Vertical strain profiles from surface targets facing the south MA middle reinforcing bar with an end grip coupler

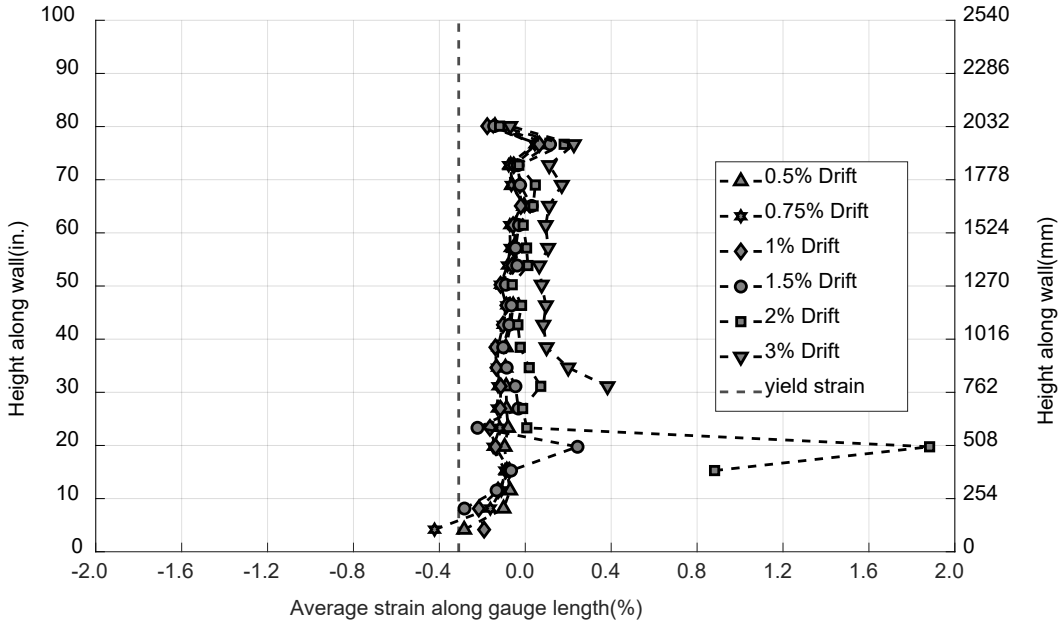

Figure 12-10- Vertical strain profiles from surface targets facing the south MA corner reinforcing bar with a friction welded coupler

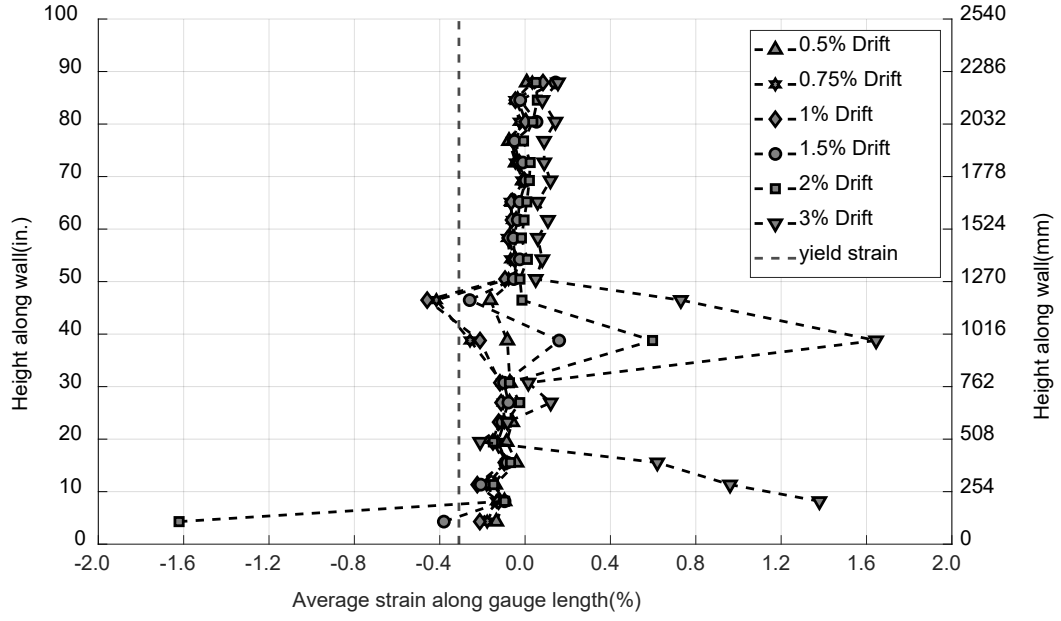

Figure 12-11: Vertical strain profiles from surface targets facing the south MA middle reinforcing bar with a friction welded coupler

13 Appendix D: Free Body Diagrams and Static Equilibrium Equations

Applied lateral load and axial load were computed by large-deformation equilibrium on test-setup using recorded actuator loads and axial pressure from hydraulic rams. Lateral forces applied to the wall were taken as point loads from actuators. The location of actuators was measured initially for the calculation of initial angles. Two wire-pots measured the horizontal displacement of wall for calculation of angle differences and resulting forces. A free-body diagram of applied forces is shown in the figure below.

$$\Theta_A = \tan^{-1}\left(\frac{D_A}{L_A+\Delta HE}\right), \qquad \Theta_B = \tan^{-1}\left(\frac{D_B}{L_B+\Delta HW}\right)$$

$$\Theta_E = \sin^{-1}\left(\frac{\Delta HE}{\Delta HR}\right), \qquad \Theta_W = \sin^{-1}\left(\frac{\Delta HW}{\Delta HR}\right)$$

$V = V_A.\cos\theta_A + V_B.\cos\theta_B - P_A.\sin\theta_E - P_B.\sin\theta_W$

$P = P_A + P_B$

Δ_{HE} = Horizontal displacement east-wire pot

Δ_{HW} = Horizontal displacement west-wire pot

Δ_H = Average horizontal displacement of wire-pots

Δ_{HAact} = Movement of Actuator-A

Δ_{HBact} = Movement of Actuator-B

H_R = Assumed distance between pivot points for P-delta effect (assumed to be constant)

V_A = Lateral load from Actuator-A

V_B = Lateral load from Actuator-B

i) Lateral Load from North to South

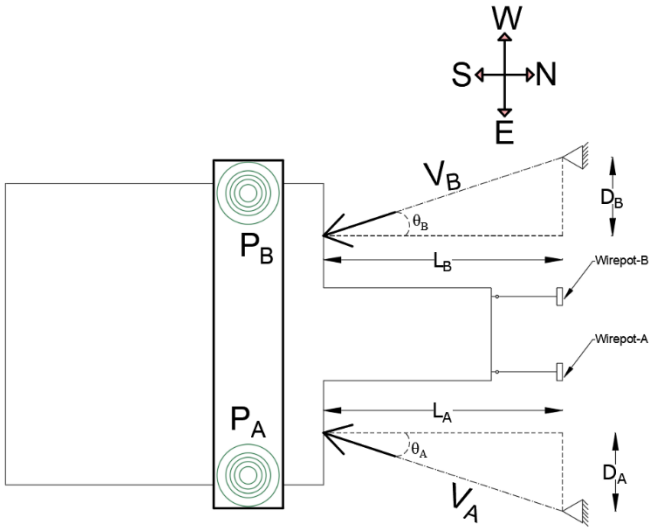

Figure 13-1: Test setup shown in plan (Lateral load from North to South)

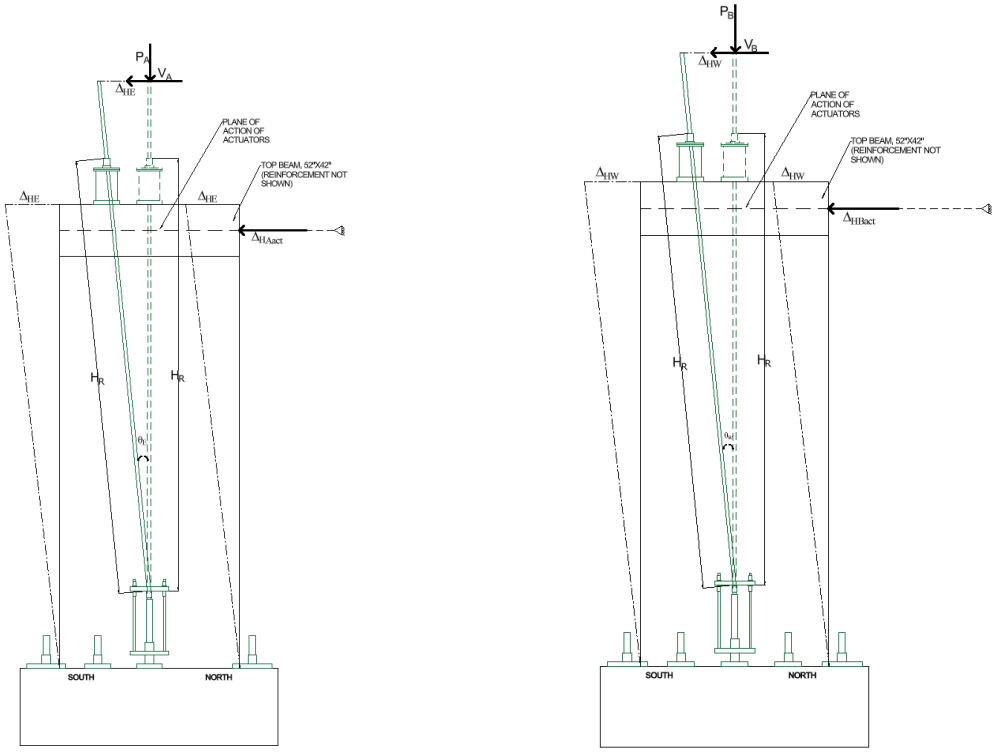

Figure 13-2: Free body diagram of test setup (Lateral load from North to South)

ii) Lateral Load from South to North

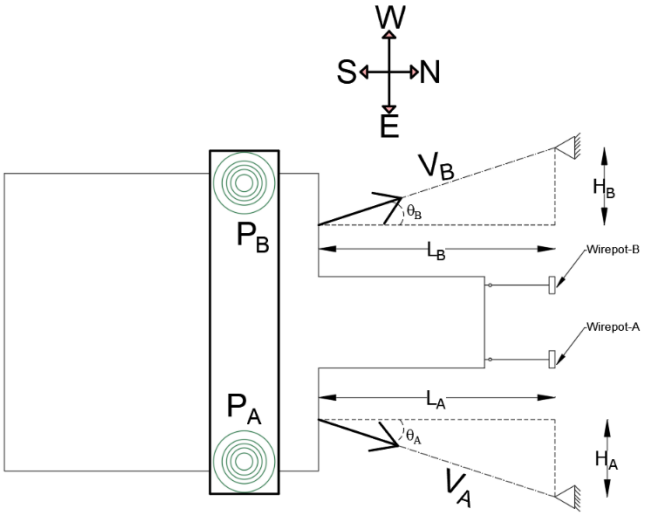

Figure 13-3: Test setup shown in plan (Lateral load from South to North)

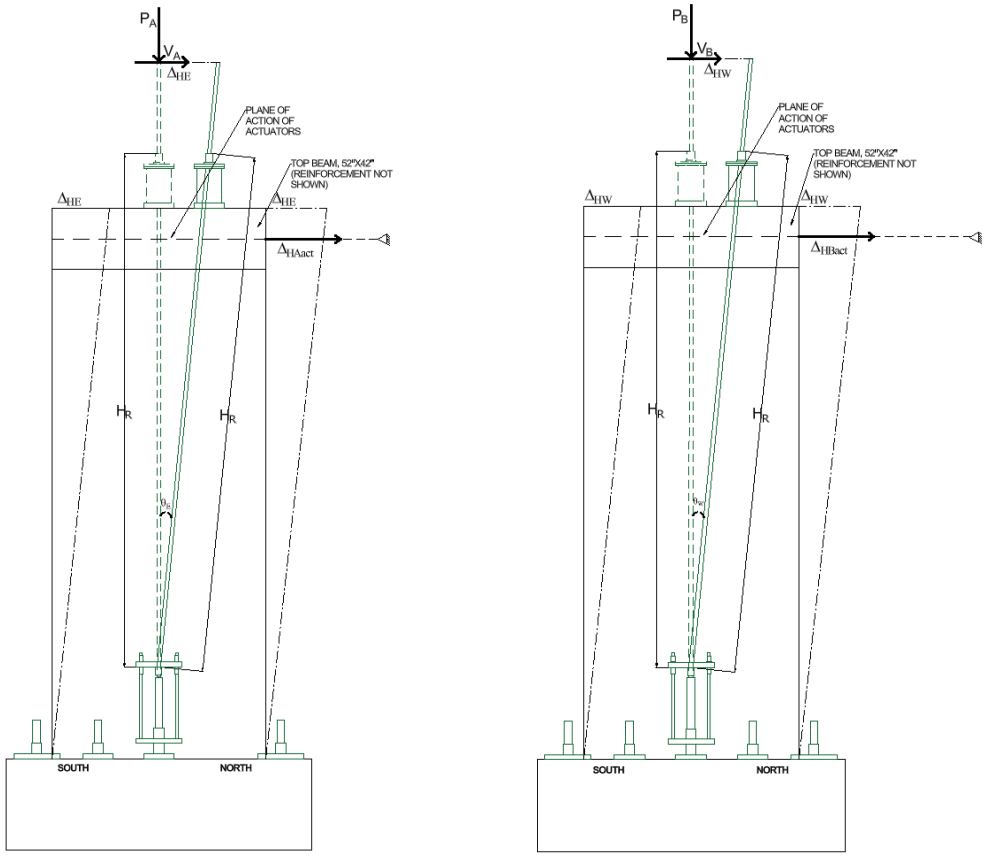

Figure 13-4: Free body diagram of test setup (Lateral load from South to North)

Appendix A. Detailed Drawing and Reinforcement Layouts

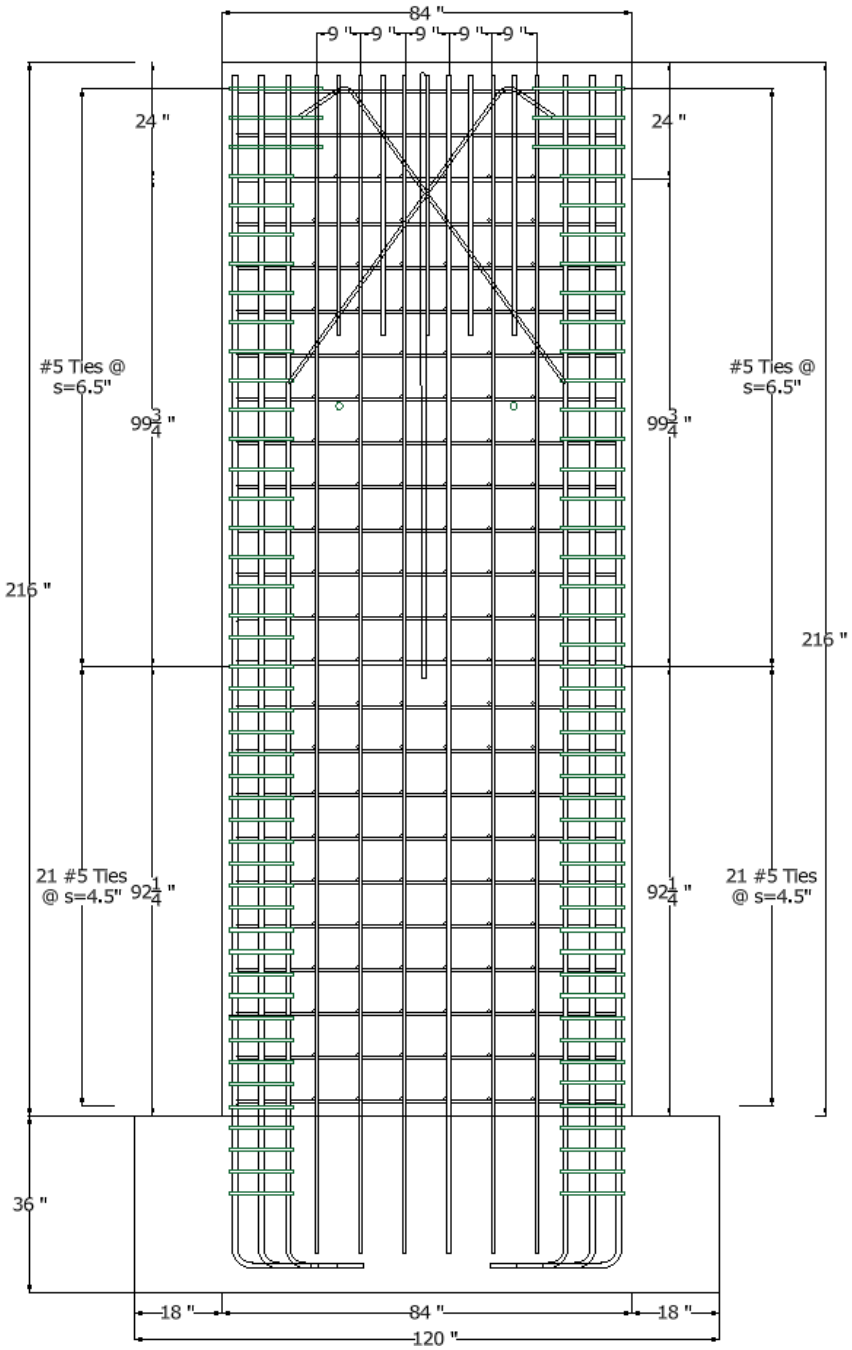

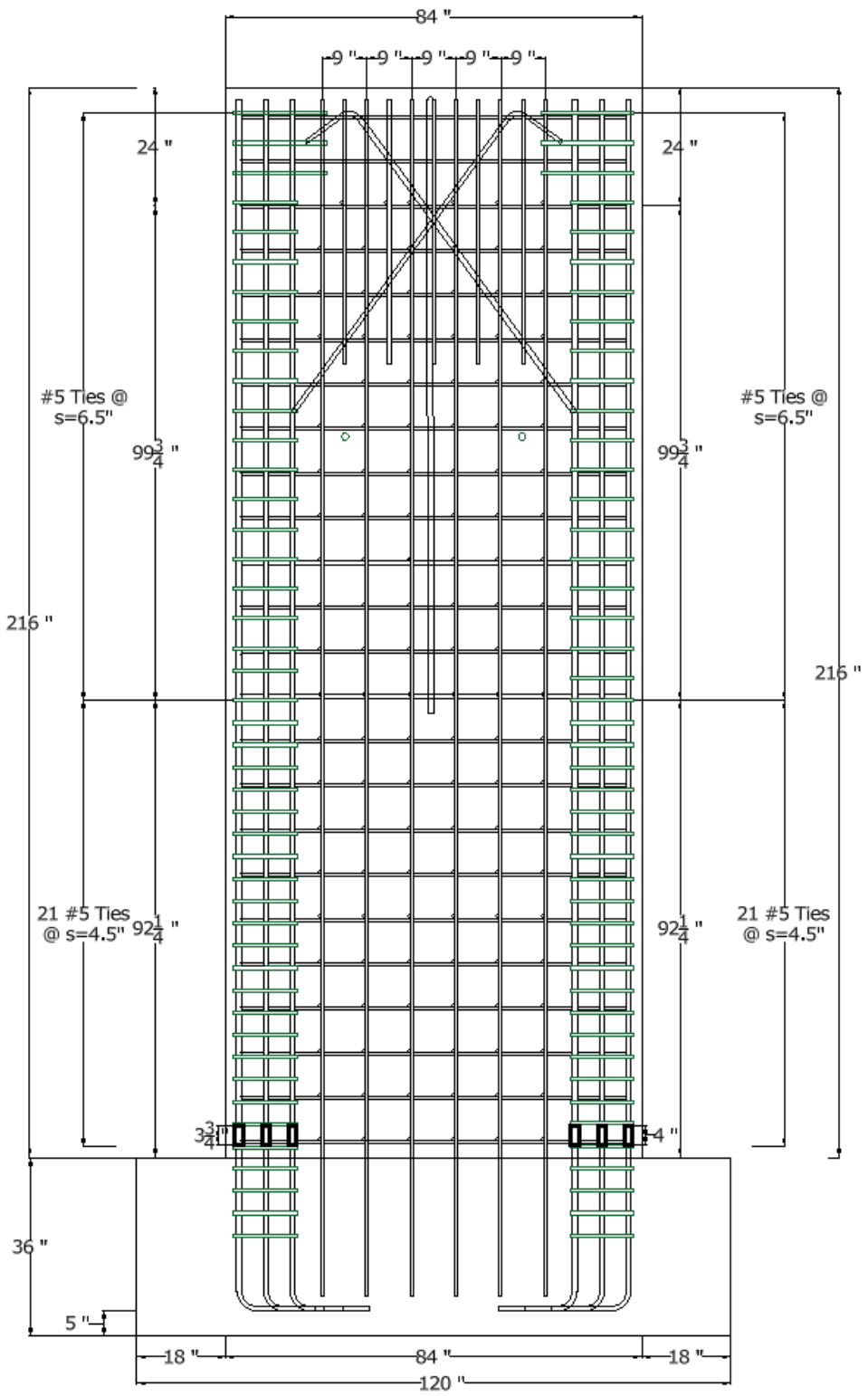
84 "
9 "
9 "
9 "
9 "
9 "
24 "
24 "
#5 Ties @
s=6.5"
#5 Ties @
s=6.5"
99 3/4 "
99 3/4 "
216 "
216 "
21 #5 Ties
@ s=4.5"
92 1/4 "
92 1/4 "
21 #5 Ties
@ s=4.5"
3 3/4 "
4 "
36 "
5 "
18 "
84 "
18 "
120 "

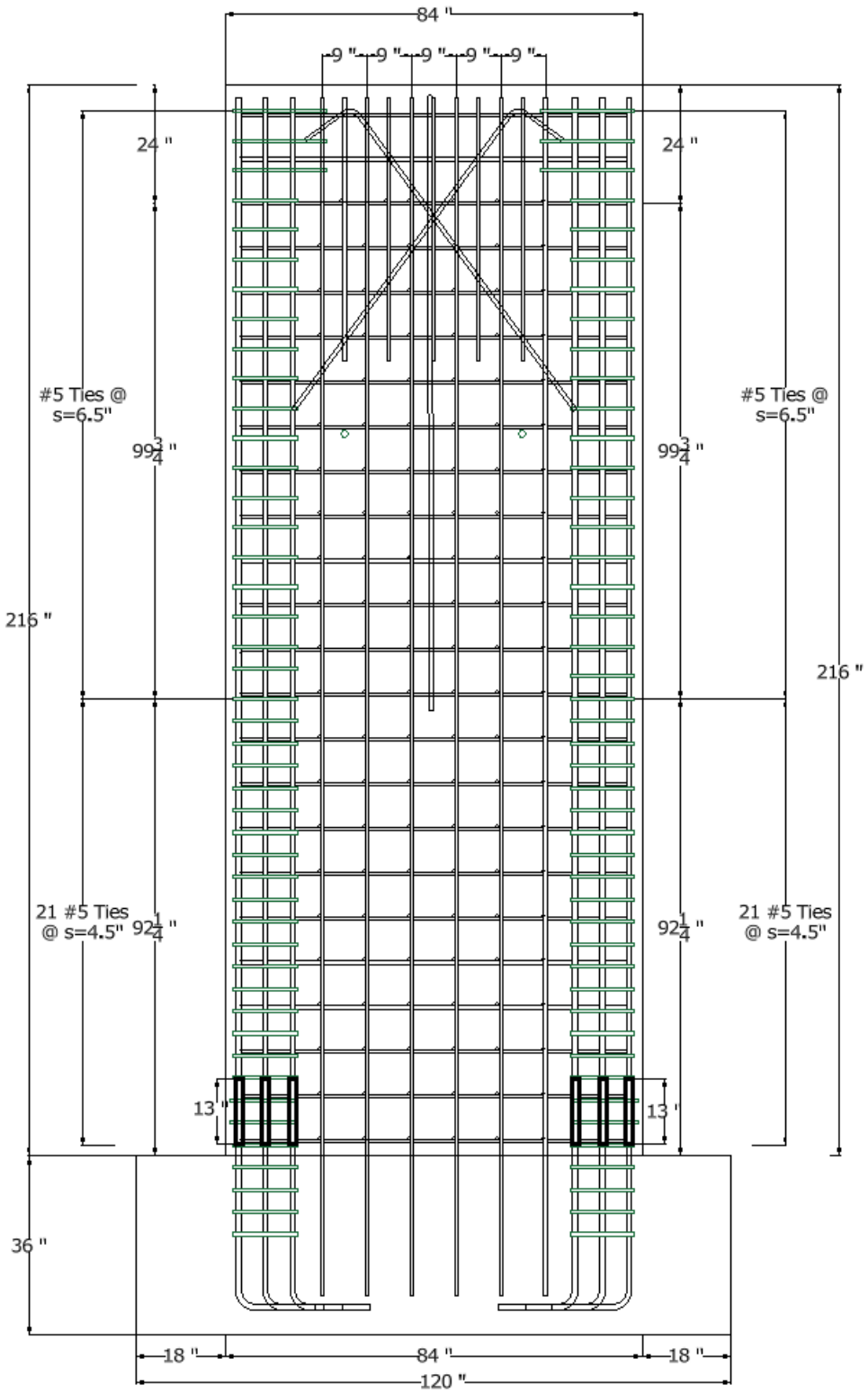
84 "
9 "
9 "
9 "
9 "
9 "
24 "
24 "
#5 Ties @
s=6.5"
#5 Ties @
s=6.5"
99 3/4 "
99 3/4 "
216 "
216 "
21 #5 Ties
@ s=4.5"
92 1/4 "
92 1/4 "
21 #5 Ties
@ s=4.5"
13 "
13 "
36 "
18 "
84 "
18 "
120 "

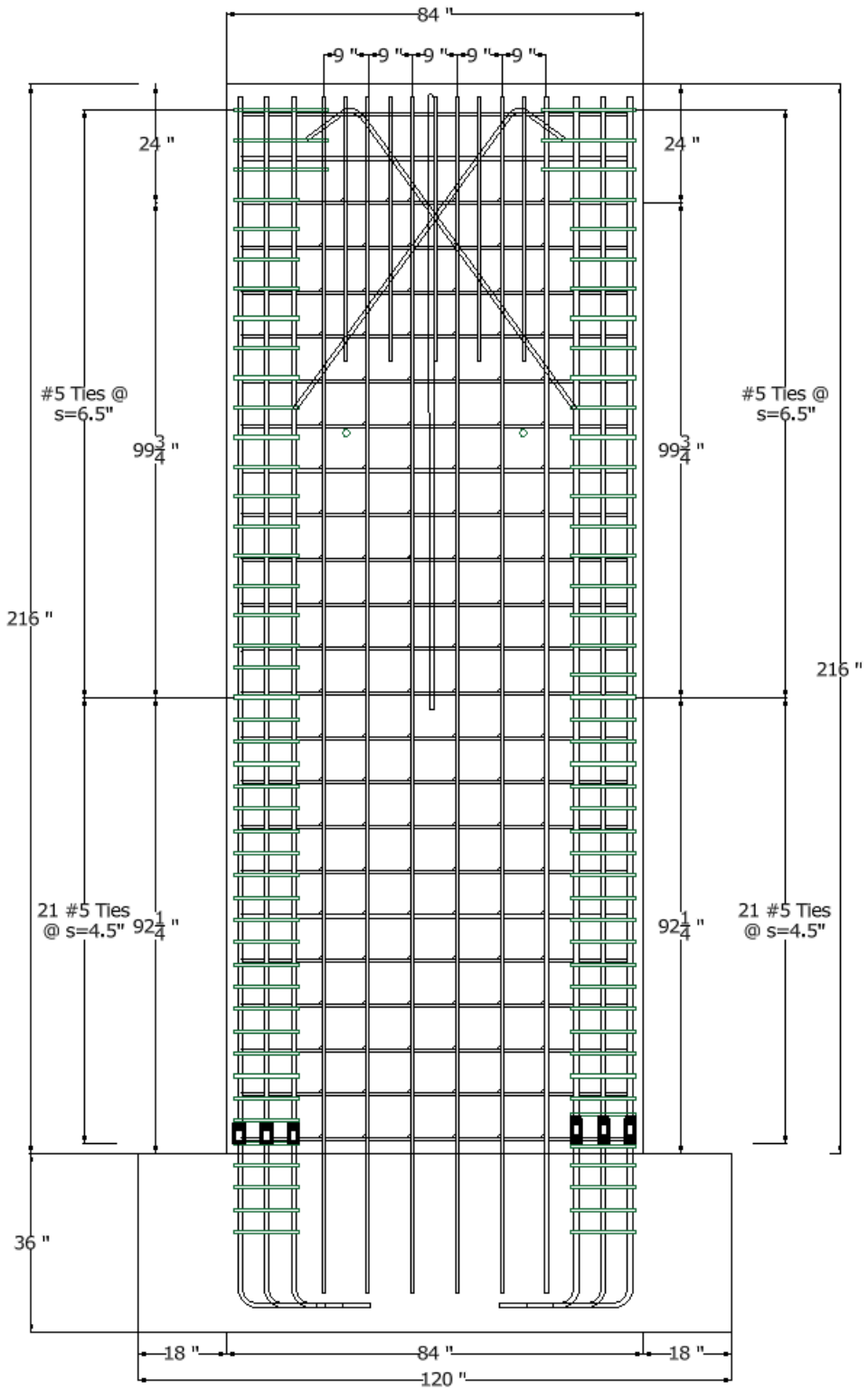
84 "
9 "
9 "
9 "
9 "
9 "
24 "
24 "
#5 Ties @
s=6.5"
#5 Ties @
s=6.5"
99 3/4 "
99 3/4 "
216 "
216 "
21 #5 Ties
@ s=4.5"
92 1/4 "
92 1/4 "
21 #5 Ties
@ s=4.5"
36 "
18 "
84 "
18 "
120 "

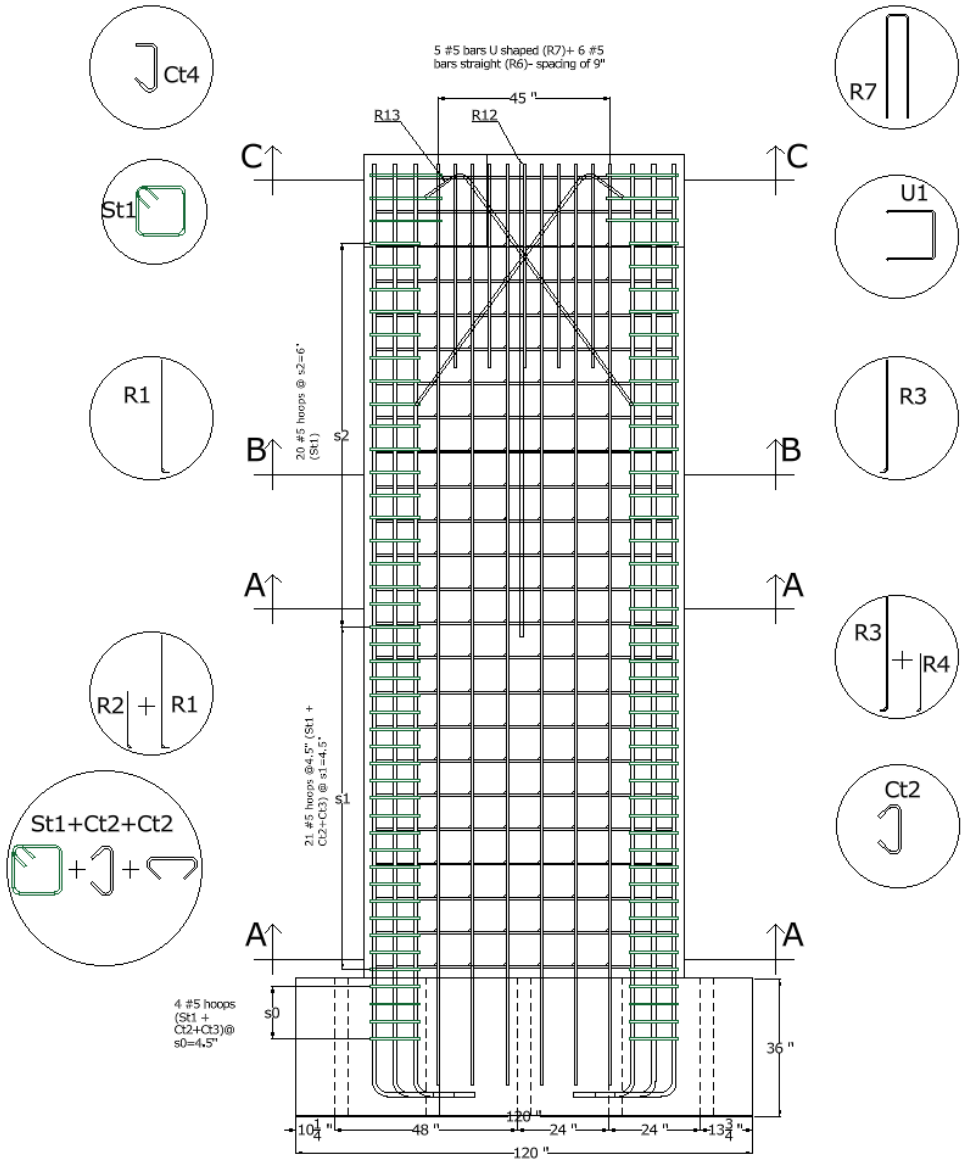
Ct4
St1
R1
R2
R1
St1+Ct2+Ct2
5 #5 bars U shaped (R7)+ 6 #5 bars straight (R6)- spacing of 9"
45 "
R13
R12
C
C
B
B
A
A
20 #5 hoops @ s2=6" (St1)
s2
21 #5 hoops @4.5" (St1 + Ct2+Ct3) @ s1=4.5"
s1
4 #5 hoops (St1 + Ct2+Ct3)@ s0=4.5"
s0
36 "
120 "
10 1/4 "
48 "
24 "
24 "
13 3/4 "
120 "
R7
U1
R3
R3
R4
Ct2

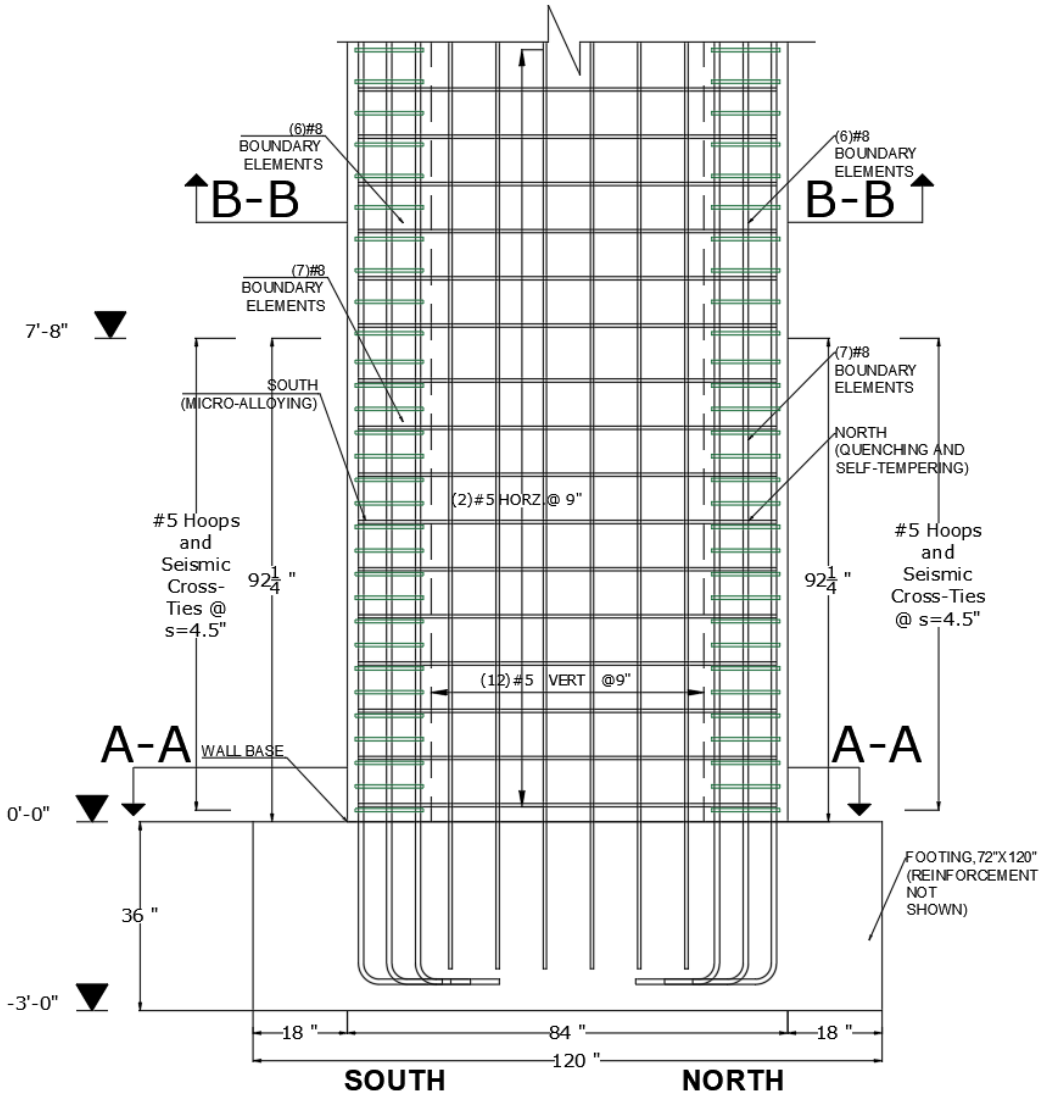
(6)#8 BOUNDARY ELEMENTS
B-B
(6)#8 BOUNDARY ELEMENTS
B-B
(7)#8 BOUNDARY ELEMENTS
7'-8"
SOUTH (MICRO-ALLOYING)
(7)#8 BOUNDARY ELEMENTS
NORTH (QUENCHING AND SELF-TEMPERING)
(2)#5 HORZ @ 9"
#5 Hoops and Seismic Cross-Ties @ s=4.5"
92 1/4 "
92 1/4 "
#5 Hoops and Seismic Cross-Ties @ s=4.5"
(12)#5 VERT @9"
A-A
WALL BASE
A-A
0'-0"
FOOTING,72"X120" (REINFORCEMENT NOT SHOWN)
36 "
-3'-0"
18 "
84 "
18 "
120 "
SOUTH
NORTH

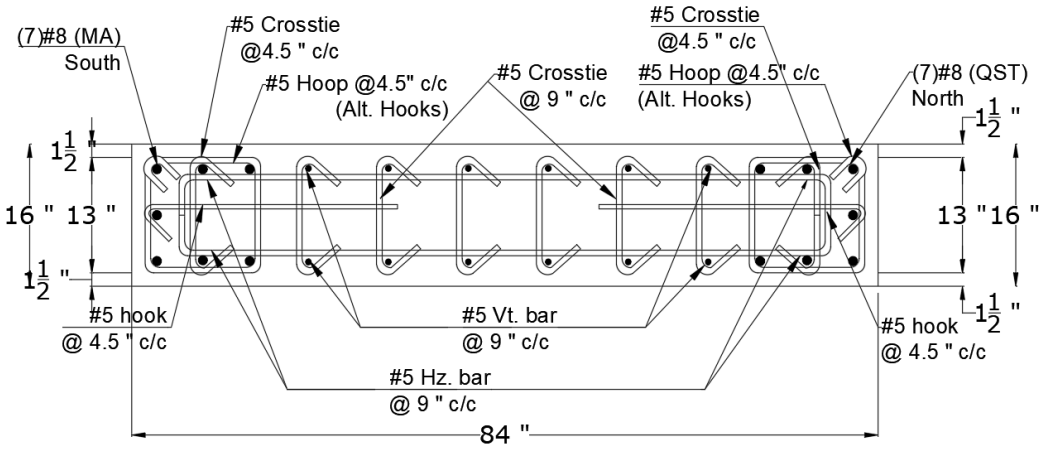
(7)#8 (MA) South
#5 Crosstie @4.5 " c/c
#5 Hoop @4.5" c/c (Alt. Hooks)
#5 Crosstie @ 9 " c/c
#5 Crosstie @4.5 " c/c
#5 Hoop @4.5" c/c (Alt. Hooks)
(7)#8 (QST) North
1 1/2 "
16 " 13 "
13 "16 "
1 1/2 "
#5 hook @ 4.5 " c/c
#5 Vt. bar @ 9 " c/c
#5 hook @ 4.5 " c/c
#5 Hz. bar @ 9 " c/c
84 "

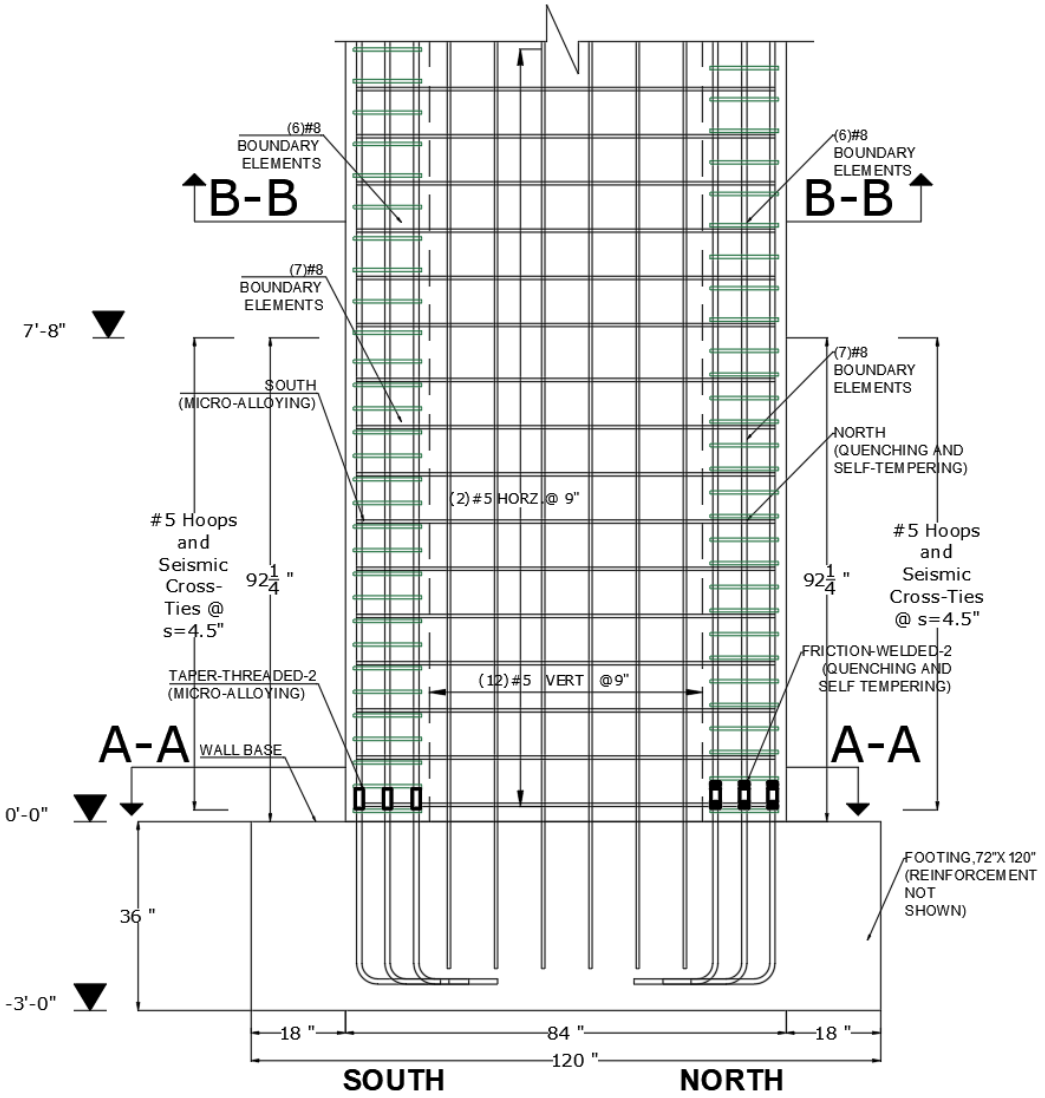
(6)#8 BOUNDARY ELEMENTS
B-B
(6)#8 BOUNDARY ELEMENTS
B-B
(7)#8 BOUNDARY ELEMENTS
7'-8"
SOUTH (MICRO-ALLOYING)
(7)#8 BOUNDARY ELEMENTS
NORTH (QUENCHING AND SELF-TEMPERING)
(2)#5 HORZ @ 9"
#5 Hoops and Seismic Cross-Ties @ s=4.5"
92 1/4 "
92 1/4 "
#5 Hoops and Seismic Cross-Ties @ s=4.5"
FRICTION-WELDED-2 (QUENCHING AND SELF TEMPERING)
TAPER-THREADED-2 (MICRO-ALLOYING)
(12)#5 VERT @9"
A-A
WALL BASE
A-A
0'-0"
FOOTING,72"X 120" (REINFORCEMENT NOT SHOWN)
36 "
-3'-0"
18 "
84 "
18 "
120 "
SOUTH
NORTH

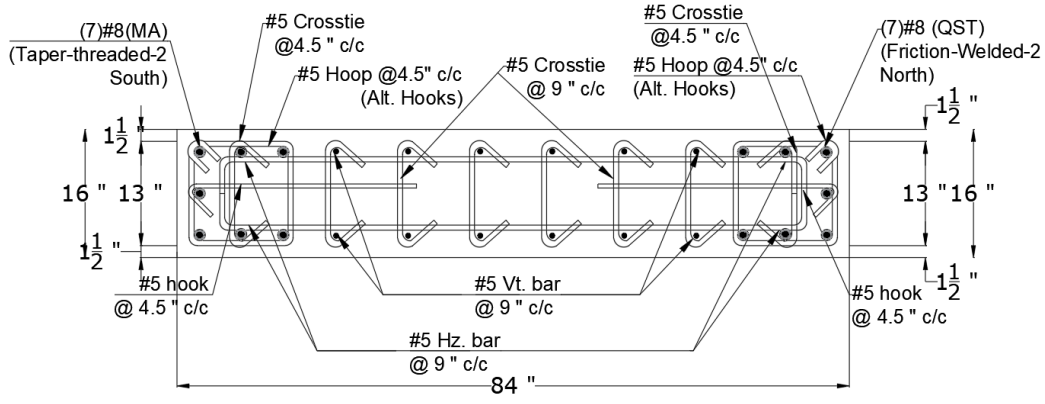
(7)#8(MA) (Taper-threaded-2 South)
#5 Crosstie @4.5 " c/c
#5 Hoop @4.5" c/c (Alt. Hooks)
#5 Crosstie @ 9 " c/c
#5 Crosstie @4.5 " c/c
#5 Hoop @4.5" c/c (Alt. Hooks)
(7)#8 (QST) (Friction-Welded-2 North)
1 1/2 "
16 "
13 "
13 "
16 "
1 1/2 "
1 1/2 "
#5 hook @ 4.5 " c/c
#5 Vt. bar @ 9 " c/c
#5 hook @ 4.5 " c/c
#5 Hz. bar @ 9 " c/c
84 "

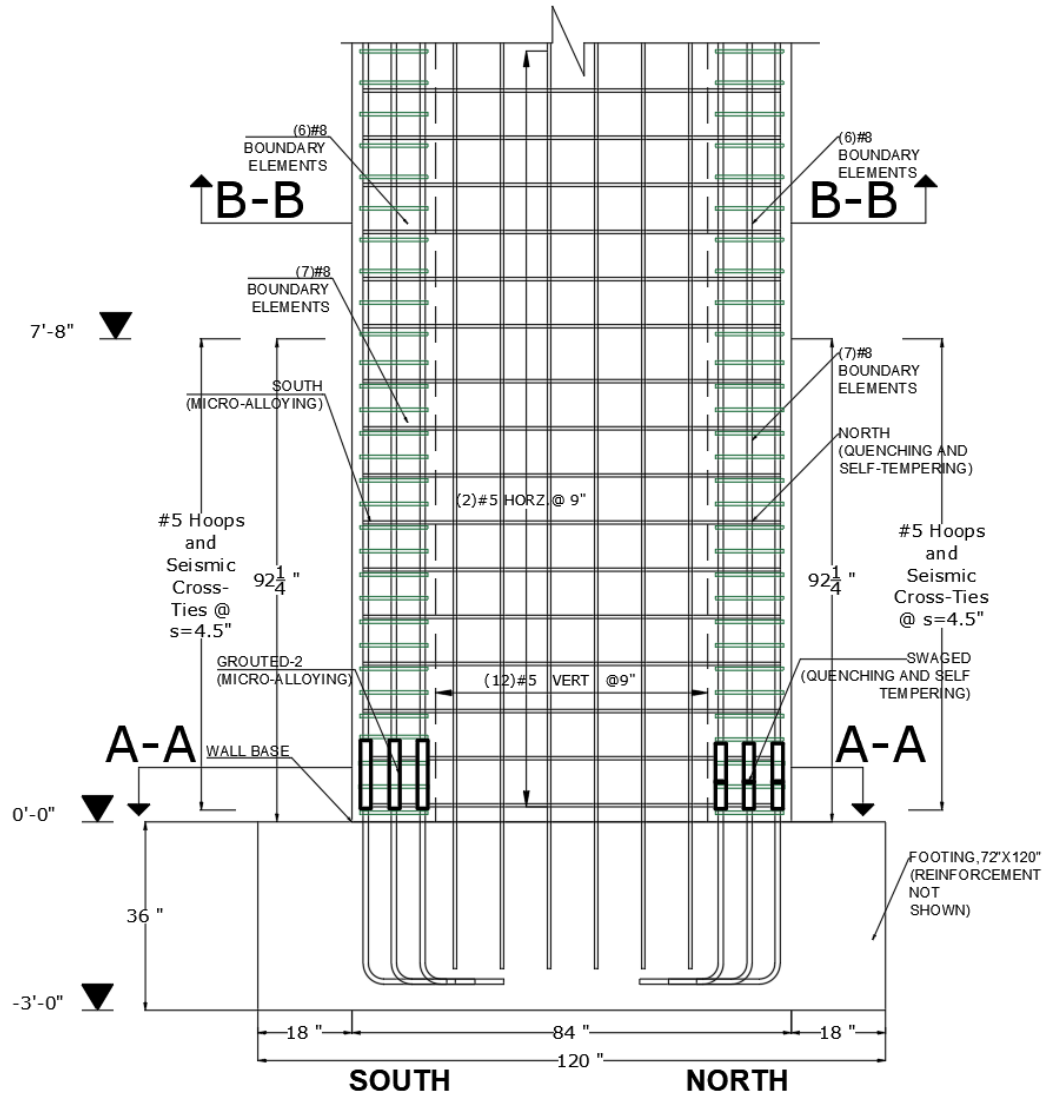
(6)#8 BOUNDARY ELEMENTS
B-B
(6)#8 BOUNDARY ELEMENTS
B-B
(7)#8 BOUNDARY ELEMENTS
7'-8"
SOUTH (MICRO-ALLOYING)
(7)#8 BOUNDARY ELEMENTS
NORTH (QUENCHING AND SELF-TEMPERING)
(2)#5 HORZ. @ 9"
#5 Hoops and Seismic Cross-Ties @ s=4.5"
92¼ "
92¼ "
#5 Hoops and Seismic Cross-Ties @ s=4.5"
GROUTED-2 (MICRO-ALLOYING)
(12)#5 VERT @9"
SWAGED (QUENCHING AND SELF TEMPERING)
A-A
WALL BASE
A-A
0'-0"
FOOTING,72"X120" (REINFORCEMENT NOT SHOWN)
36 "
-3'-0"
18 "
84 "
18 "
120 "
SOUTH
NORTH

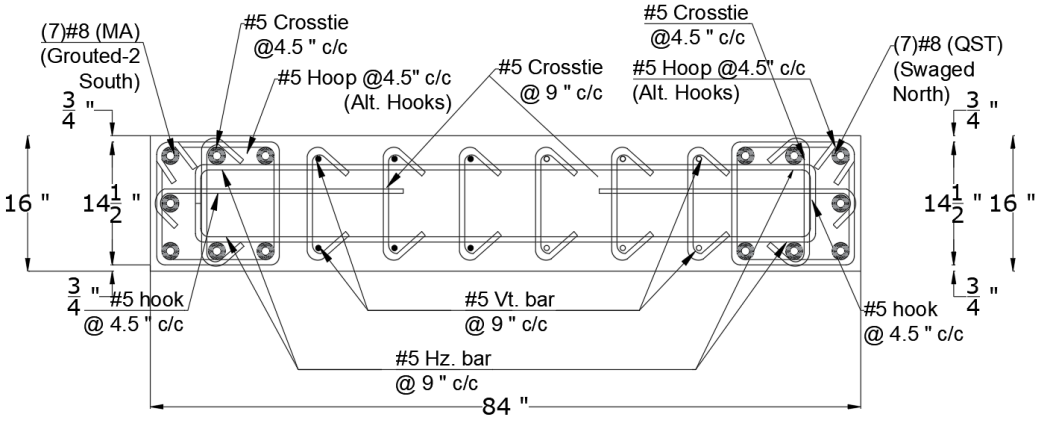
(7)#8 (MA) (Grouted-2 South)
#5 Crosstie @4.5 " c/c
#5 Hoop @4.5" c/c (Alt. Hooks)
#5 Crosstie @ 9 " c/c
#5 Crosstie @4.5 " c/c
#5 Hoop @4.5" c/c (Alt. Hooks)
(7)#8 (QST) (Swaged North)
¾ "
¾ "
16 "
14½ "
14½ " 16 "
¾ "
¾ "
#5 hook @ 4.5 " c/c
#5 Vt. bar @ 9 " c/c
#5 hook @ 4.5 " c/c
#5 Hz. bar @ 9 " c/c
84 "

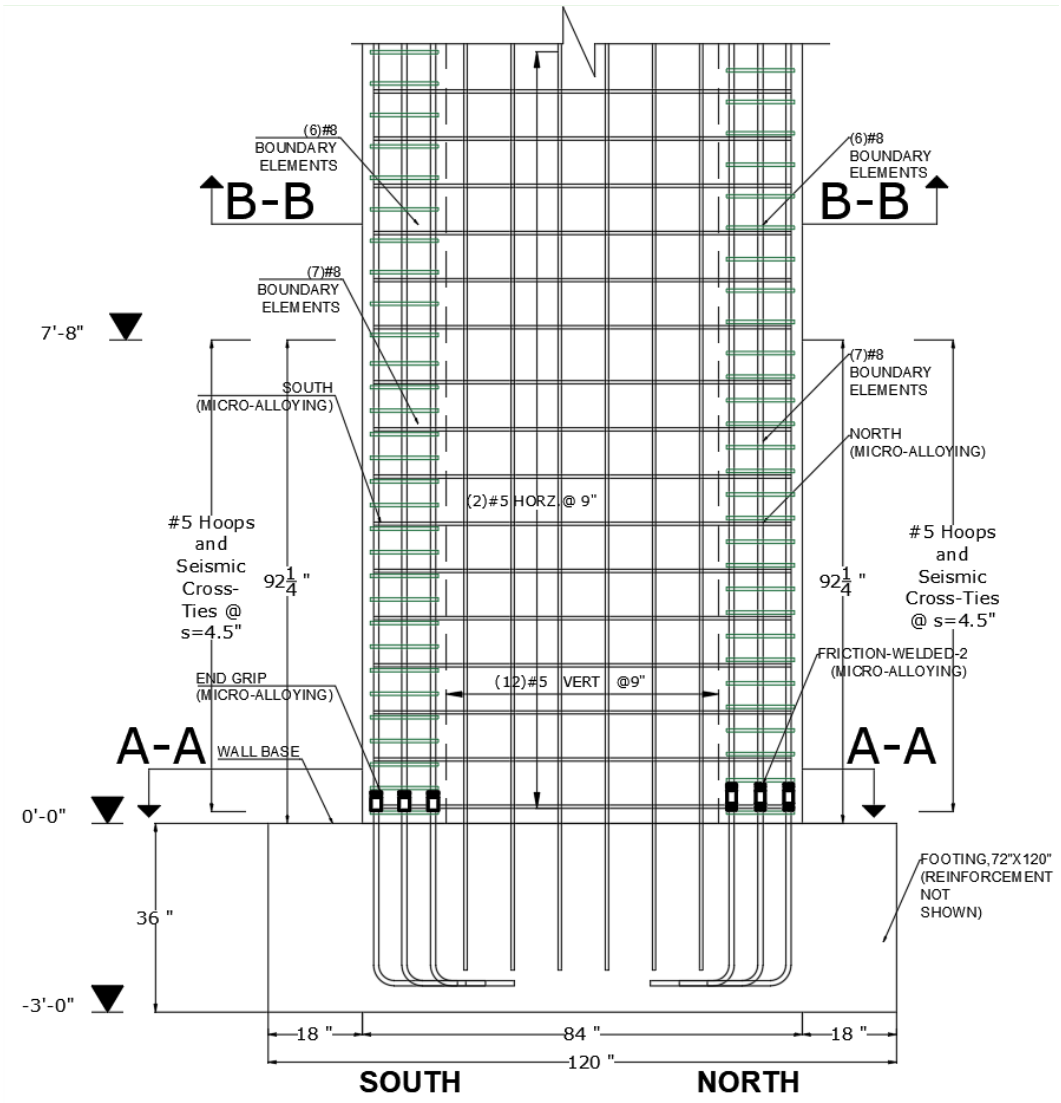
(6)#8 BOUNDARY ELEMENTS
(6)#8 BOUNDARY ELEMENTS
B-B
B-B
(7)#8 BOUNDARY ELEMENTS
(7)#8 BOUNDARY ELEMENTS
7'-8"
SOUTH (MICRO-ALLOYING)
NORTH (MICRO-ALLOYING)
(2)#5 HORZ @ 9"
#5 Hoops and Seismic Cross-Ties @ s=4.5"
92 1/4 "
92 1/4 "
#5 Hoops and Seismic Cross-Ties @ s=4.5"
FRICTION-WELDED-2 (MICRO-ALLOYING)
END GRIP (MICRO-ALLOYING)
(12)#5 VERT @9"
A-A
WALL BASE
A-A
0'-0"
FOOTING,72"X120" (REINFORCEMENT NOT SHOWN)
36 "
-3'-0"
18 "
84 "
18 "
120 "
SOUTH
NORTH

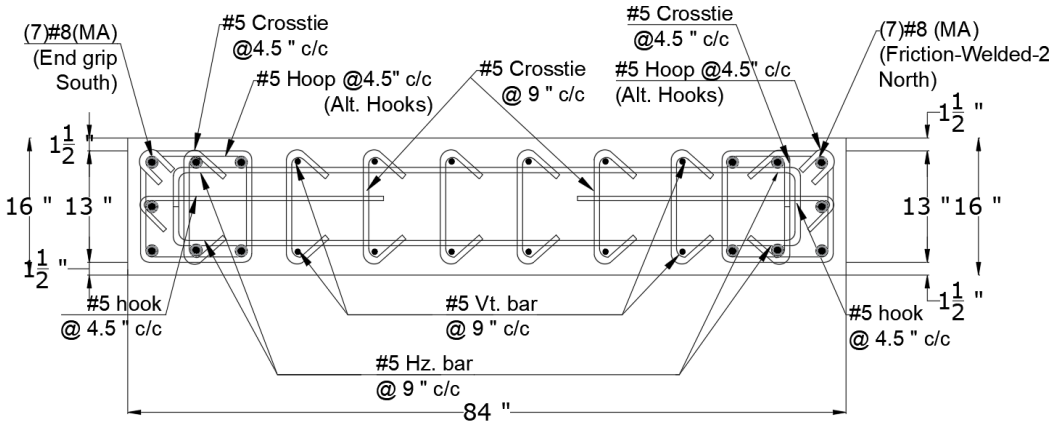
(7)#8(MA) (End grip South)
#5 Crosstie @4.5 " c/c
#5 Hoop @4.5" c/c (Alt. Hooks)
#5 Crosstie @ 9 " c/c
#5 Crosstie @4.5 " c/c
#5 Hoop @4.5" c/c (Alt. Hooks)
(7)#8 (MA) (Friction-Welded-2 North)
1 1/2 "
1 1/2 "
16 " 13 "
13 " 16 "
1 1/2 "
1 1/2 "
#5 hook @ 4.5 " c/c
#5 Vt. bar @ 9 " c/c
#5 hook @ 4.5 " c/c
#5 Hz. bar @ 9 " c/c
84 "

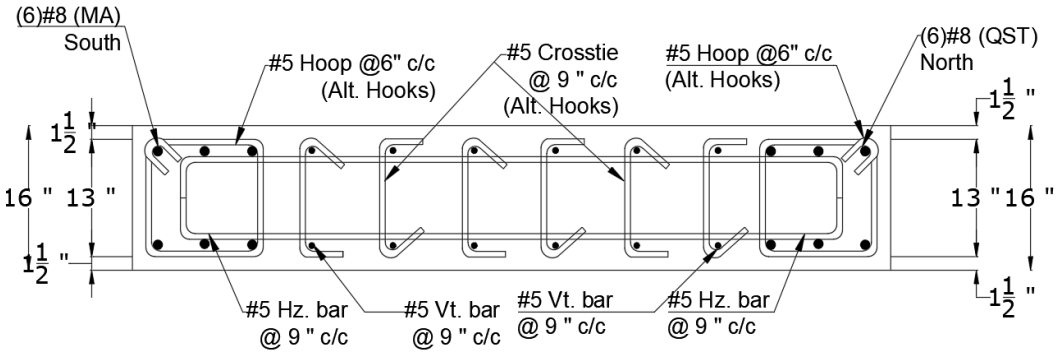

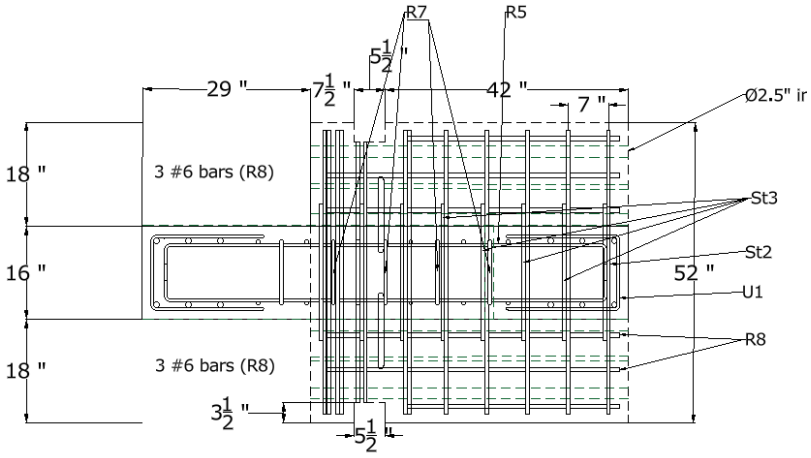

12 Stirrups (St2+ St3) @7"

SECTION C-C

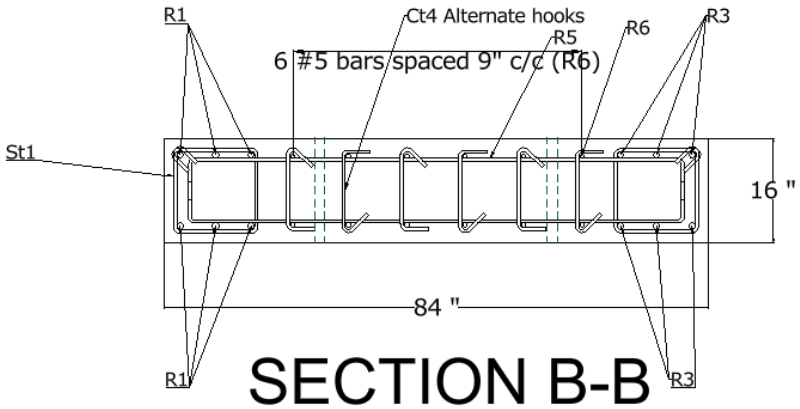

SECTION B-B

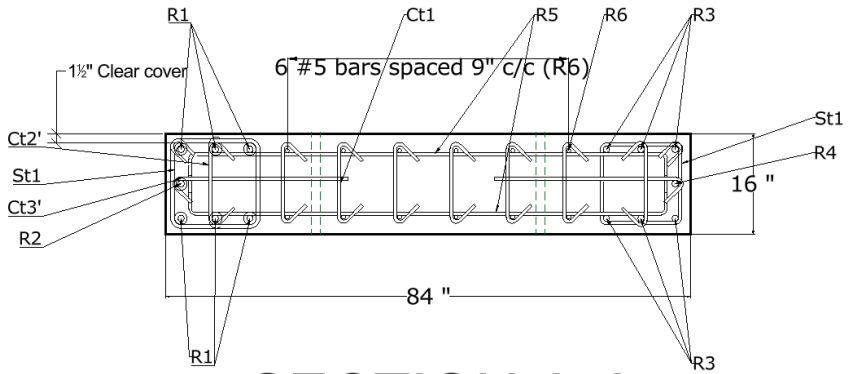

SECTION A-A

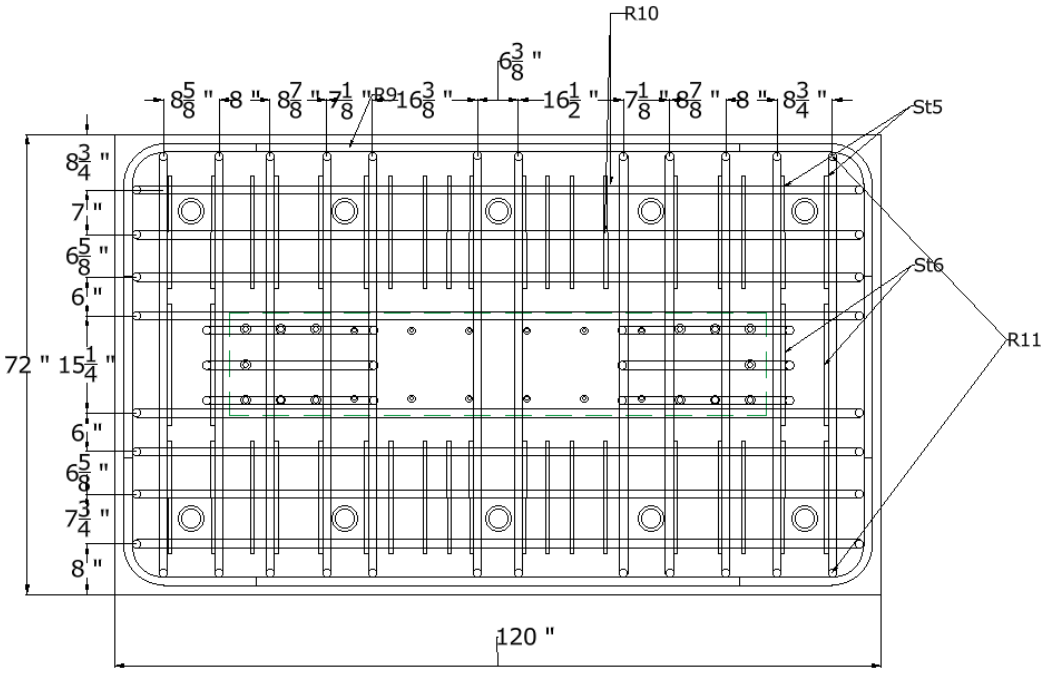

FOOTING BOTTOM BARS

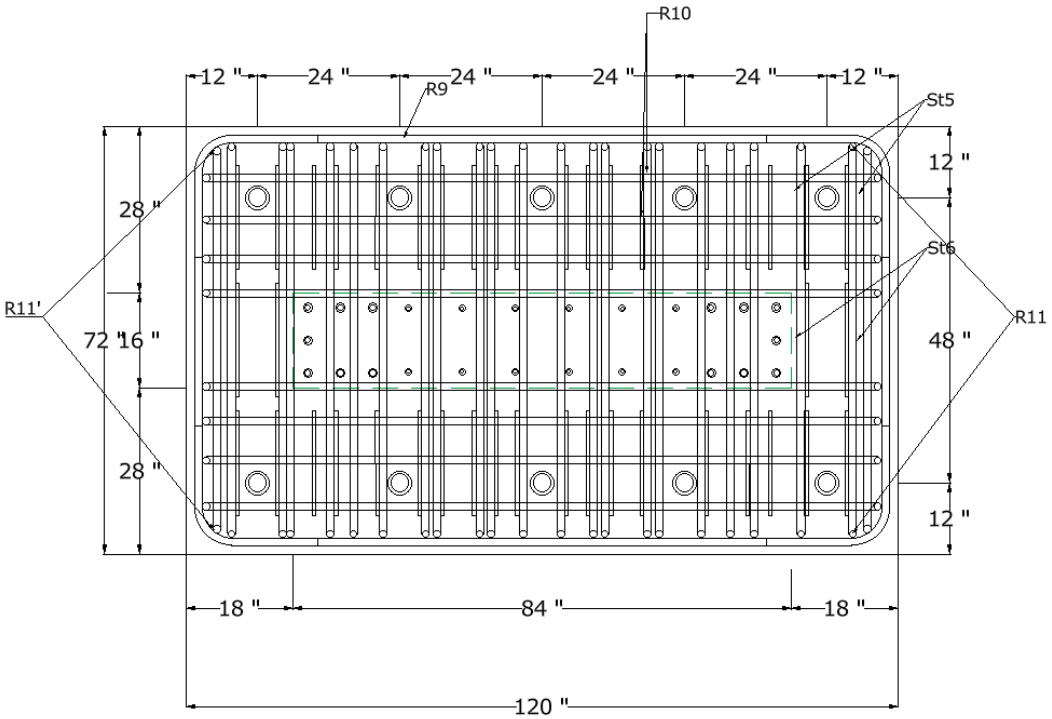

FOOTING TOP BARS

LABEL:	R1
CATEGORY:	TENS AND COMPRESSION STEEL
BAR SIZE:	No. 8
QUANTITY:	6
STEEL:	A706 GRADE 80 FROM CMC

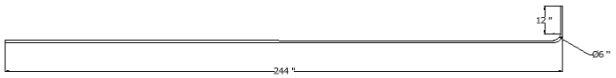

NOTE:
THESE BARS ARE FROM CMC AND SHOULD BE PAINTED RED

LABEL:	R2
CATEGORY:	TENS AND COMPRESSION STEEL
BAR SIZE:	No. 8
QUANTITY:	2
STEEL:	A706 GRADE 80 FROM CMC

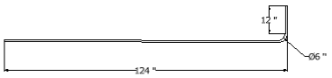

NOTE:
THESE BARS ARE FROM CMC AND SHOULD BE PAINTED RED

LABEL:	R5
CATEGORY:	TENS AND COMPRESSION STEEL
BAR SIZE:	No. 5
QUANTITY:	58
STEEL:	A706 GRADE 80

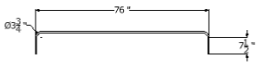

LABEL:	R6
CATEGORY:	TENS AND COMPRESSION STEEL
BAR SIZE:	No. 5
QUANTITY:	15
STEEL:	A706 GRADE 80

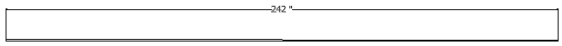

LABEL:	R7
CATEGORY:	TENS AND COMPRESSION STEEL
BAR SIZE:	No. 5
QUANTITY:	6
STEEL:	A706 GRADE 80

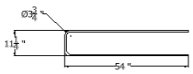

PROJECT:
GRADE 80 BARS WITH COUPLERS

CONTENT:
A706 GRADE 80 FROM CMC

FACILITY:
UNIVERSITY OF TEXAS AT SAN ANTONIO

DRAWN BY:	APPROVED	DRAWING NO.
	SCALE	W-04

REV	DATE	DESCRIPTION

LABEL:	U1
CATEGORY:	CONFINEMENT
BAR SIZE:	No. 5
QUANTITY:	8
STEEL:	A706 GRADE 80

NOTE:
ONLY IN SECTION C-C

LABEL:	Ct1
CATEGORY:	CONFINEMENT
BAR SIZE:	No. 5
QUANTITY:	80
STEEL:	A706 GRADE 80

NOTE:
ONLY IN SECTION A-A

LABEL:	Ct2
CATEGORY:	CONFINEMENT
BAR SIZE:	No. 5
QUANTITY:	60
STEEL:	A706 GRADE 80

NOTE:
ONLY IN THE FOUNDATION AND SECTION A-A IN THE BOUNDARY ELEMENTS

LABEL:	Ct3
CATEGORY:	CONFINEMENT
BAR SIZE:	No. 5
QUANTITY:	60
STEEL:	A706 GRADE 80

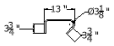

NOTE:
ONLY IN THE FOUNDATION AND SECTION A-A IN THE BOUNDARY ELEMENTS

LABEL:	Ct4
CATEGORY:	CONFINEMENT
BAR SIZE:	No. 5
QUANTITY:	80
STEEL:	A706 GRADE 80

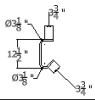

NOTE:
ONLY IN SECTION B-B

LABEL:	St1
CATEGORY:	CONFINEMENT
BAR SIZE:	No. 5
QUANTITY:	108
STEEL:	A706 GRADE 80

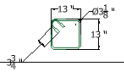

NOTE:
ONLY IN THE BOUNDARY ELEMENTS FROM THE FOUNDATION TO THE TOP OF THE WALL

PROJECT: GRADE 80 BARS WITH COUPLERS	DRAWN BY:	APPROVED	DRAWING NO.
CONTENT: A706 GRADE 80 FROM CMC		SCALE	W-05
FACILITY: UNIVERSITY OF TEXAS AT SAN ANTONIO	REV.	DATE	DESCRIPTION

LABEL:	R8
CATEGORY:	TENS AND COMPRESSION STEEL
BAR SIZE:	No. 6
QUANTITY:	15
STEEL:	A615 GRADE 60

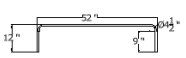

LABEL:	St2
CATEGORY:	CONFINEMENT
BAR SIZE:	No. 5
QUANTITY:	20
STEEL:	A615 GRADE 60

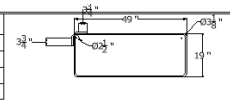

LABEL:	St3
CATEGORY:	CONFINEMENT
BAR SIZE:	No. 5
QUANTITY:	10
STEEL:	A615 GRADE 60

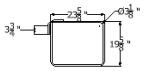

LABEL:	R9
CATEGORY:	CONFINEMENT
BAR SIZE:	No. 10
QUANTITY:	6
STEEL:	A615 GRADE 60

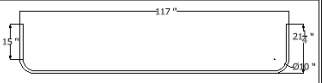

LABEL:	R9'
CATEGORY:	CONFINEMENT
BAR SIZE:	No. 10
QUANTITY:	6
STEEL:	A615 GRADE 60

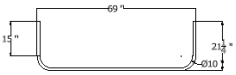

LABEL:	R10
CATEGORY:	TENS AND COMPRESSION STEEL
BAR SIZE:	No. 8
QUANTITY:	40
STEEL:	A615 GRADE 60

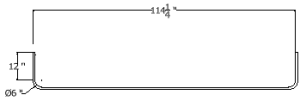

LABEL:	R11
CATEGORY:	TENS AND COMPRESSION STEEL
BAR SIZE:	No. 8
QUANTITY:	106
STEEL:	A615 GRADE 60

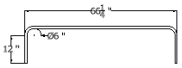

LABEL:	St6
CATEGORY:	CONFINEMENT
BAR SIZE:	No. 5
QUANTITY:	14
STEEL:	A615 GRADE 60

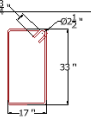

LABEL:	St5
CATEGORY:	CONFINEMENT
BAR SIZE:	No. 5
QUANTITY:	38
STEEL:	A615 GRADE 60

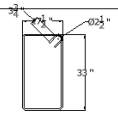

LABEL:	R12
CATEGORY:	TENS AND COMPRESSION STEEL
BAR SIZE:	No. 8
QUANTITY:	3
STEEL:	A615 GRADE 60

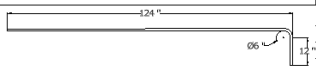

LABEL:	R13
CATEGORY:	TENS AND COMPRESSION STEEL
BAR SIZE:	No. 5
QUANTITY:	6
STEEL:	A615 GRADE 60

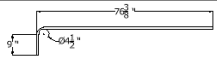

PROJECT:
SHEAR WALL WITH GRADE 80 COUPLERS

CONTENT:
A615 GRADE 60 FROM CMC

FACILITY:
UNIVERSITY OF TEXAS AT SAN ANTONIO

DRAWN BY:	APPROVED	DRAWING NO.
	SCALE	W-06

REV	DATE	DESCRIPTION

LABEL:	St4
CATEGORY:	CONFINEMENT
BAR SIZE:	No. 5
QUANTITY:	20
STEEL:	A706 GRADE 80

LABEL:	Cl2'
CATEGORY:	CONFINEMENT
BAR SIZE:	No. 5
QUANTITY:	8
STEEL:	

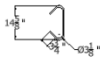

NOTE:
ONLY IN SECTION A-A

LABEL:	Cl3'
CATEGORY:	CONFINEMENT
BAR SIZE:	No. 5
QUANTITY:	8

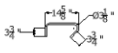

NOTE:
ONLY IN THE FOUNDATION AND SECTION A-A IN THE BOUNDARY ELEMENTS

PROJECT: GRADE 80 BARS WITH COUPLERS	DRAWN BY:	APPROVED	DRAWING NO.
CONTENT: A706 GRADE 80 FROM CMC		SCALE	W-07
FACILITY: UNIVERSITY OF TEXAS AT SAN ANTONIO	REV	DATE	DESCRIPTION

	R3
CATEGORY:	TENS AND COMPRESSION STEEL
BAR SIZE:	No. 8
QUANTITY:	6
STEEL:	A706 GRADE 80

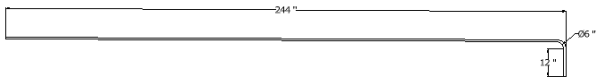

NOTE:
THESE BARS ARE FROM NUCOR AND SHOULD BE PAINTED BLUE

	R4
CATEGORY:	TENS AND COMPRESSION STEEL
BAR SIZE:	No. 8
QUANTITY:	2
STEEL:	A706 GRADE 80

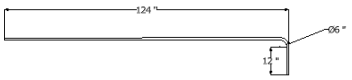

NOTE:
THESE BARS ARE FROM NUCOR SHOULD BE PAINTED BLUE

PROJECT:
SHEAR WALL WITH GRADE 80 COUPLERS

CONTENT:
A706 GRADE 80 FROM NUCOR

FACILITY:
UNIVERSITY OF TEXAS AT SAN ANTONIO

DRAWN BY:	APPROVED	DRAWING NO.
	SCALE	W-08

REV	DATE	DESCRIPTION

14 REFERENCES

318-19, A. (2019). Building code requirements for structural concrete (ACI 318-19).

Aaleti, S., Brueggen, B. L., Johnson, B., French, C. E., & Sritharan, S. (2013). Cyclic Response of Reinforced Concrete Walls with Different Anchorage Details: Experimental Investigation. *Journal of Structural Engineering*, *139*(7), 1181-1191. https://doi.org/10.1061/(asce)st.1943-541x.0000732

AASHTO, S. G. S. (2011). *AASHTO guide specifications for seismic bridge design*. American Association of State Highway and Transportation Officials.

AASHTO. (2011). *AASHTO guide specifications for LRFD seismic bridge design*. AASHTO.

AC133, I. C. C.-E. S. (2020). Acceptance Criteria for Mechanical Connector Systems for Steel Reinforcing Bars. In.

ACI Committee 318. (2002a). Building Code Requirements for Structural Concrete. In. Farmington Hills, MI: American Concrete Institute.

ACI Committee 318. (2002b). Building code requirements for structural concrete (ACI 318-02) and commentary. In. Farmington Hills, : American Concrete Institute.

ACI Committee 318. (2014). Building code requirements for structural concrete (ACI 318-14) and commentary. In: American Concrete Institute.

ACI Committee 318. (2019). Building code requirements for structural concrete (ACI 318-19) and commentary. In (pp. 624): ACI Farmington Hills, MI, USA.

ACI Innovation Task Group 5 (ACI ITG-5). (2009). Requirements for design of special unbonded post-tensioned precast shear wall satisfying ACI ITG-5.1 (ACI ITG-5.2-09) and commentary. *Reported by ACI Innovation Task Group*, *5*.

Almeida, J. P., Prodan, O., Tarquini, D., & Beyer, K. (2017). Influence of Lap Splices on the Deformation Capacity of RC Walls. I: Database Assembly, Recent Experimental Data, and Findings for Model Development. *Journal of Structural Engineering*, *143*(12), 04017156. https://doi.org/doi:10.1061/(ASCE)ST.1943-541X.0001853

Ameli, M. J., & Pantelides, C. P. (2017). Seismic Analysis of Precast Concrete Bridge Columns Connected with Grouted Splice Sleeve Connectors. *Journal of Structural Engineering*, *143*(2). https://doi.org/10.1061/(asce)st.1943-541x.0001678

American Society of Civil Engineers (ASCE). (2022). *Minimum Design Loads and Associated Criteria for Buildings and Other Structures*. ASCE. https://doi.org/doi:10.1061/9780784415788

Aragon, T. C., Kurama, Y. C., & Meinheit, D. F. (2017). A Type III Grouted Seismic Connector for Precast Concrete Structures. *PCI Journal*, *62*(5), 76-95. https://www.pci.org/PCI_Docs/Publications/PCI%20Journal/2017/September-

October/A%20Type%20III%20grouted%20seismic%20connector%20%20for%20precast%20concrete%20structures%20.pdf

ASTM A370-22. (2022). Standard Test Methods and Definitions for Mechanical Testing of Steel Products. In: ASTM International.

ASTM A1034/A1034M-23 (2023). Standard Test Methods for Testing Mechanical Splices for Steel Reinforcing Bars. *ASTM International*, 5.

ASTM E8/E8M-22. (2022). Standard Test Methods for Tension Testing of Metallic Materials. In. West Conshohocken, PA: ASTM International.

ASTM Standard A706/A706M-22a. (2022). Standard Specification for Low-Alloy Steel Deformed and Plain Bars for Concrete Reinforcement. In (pp. 9). West Conshohocken, PA: ASTM International.

ASTM Standard A706/A706M-24. (2024). Standard Specification for Low-Alloy Steel Deformed and Plain Bars for Concrete Reinforcement. In (pp. 9). West Conshohocken, PA: ASTM International.

Barcley, L., & Kowalsky, M. (2019). Critical Bending Strain of Reinforcing Steel and the Buckled Bar Tension Test. *ACI Materials Journal*, *116*(3).

Bompa, D. V., & Elghazouli, A. Y. (2018). Monotonic and cyclic performance of threaded reinforcement splices. *Structures*, *16*, 358-372. https://doi.org/10.1016/j.istruc.2018.11.009

Bompa, D. V., & Elghazouli, A. Y. (2019). Inelastic behaviour of RC members incorporating threaded reinforcement coupler. *Eng Struct*, *180*, 468–483.

Brown, J., & Kunnath, S. K. (2004). Low-cycle fatigue failure of reinforcing steel bars. *ACI Materials Journal*, *101*(6).

Brueggen, B., Waugh, J., Aaleti, S., Johnson, B., French, C., Sritharan, S., & Nakaki, S. D. (2007). Tests of structural walls to determine deformation contributions of interest for performance-based design. In *Structural Engineering Research Frontiers* (pp. 1-16).

Caltrans CT670. (2022). Method of Tests for Mechanical and Welded Reinforcing Steel Splices. In.

DMS 4510. (2023). *Departmental Materials Specification DMS-4510: Mechanical Couplers for Reinforcing Steel*.

Ghannoum, W. M., Diaz, M., Rajae, S., Banjade, S., Chapagain, B., & Hogsett, G. (2021). *CIV - Civil Infrastructure Vision© v1.0: Bridge Calibration User Manual and Validation Manual* (FHWA/TX-21/0-6950-1).

Ghannoum, W. M., & Slavin, C. M. (2016). Low-Cycle Fatigue Performance of High-Strength Steel Reinforcing Bars. *ACI Materials Journal*, *113*(6), 803-814.

Gonzalez, J. (2022). *Improving Fatigue Life Properties of Steel Reinforcing Bars* (Publication Number 29169460) [M.S., The University of Texas at San Antonio]. Dissertations & Theses @ University of Texas - San Antonio; ProQuest One Academic. United States -- Texas.

Gonzalez, J., Sasan Khedmatgozar Dolati, S., Suselo, A., Stalheim, D., Araujo, A., & Ghannoum, W. M. (2025). Improving Fatigue Properties of Reinforcing Steel Bars. *ACI Materials Journal*, *122*(1), 3-18.

Haber, Z. B., Saiidi, M., & Sanders, D. H. (2014). Seismic Performance of Precast Columns with Mechanically Spliced Column-Footing Connection. *ACI Structural Journal*, *111*(3), 639–650.

Institute, A. C. (2019). *ACI 318-19 Building Code Requirements for Structural Concrete and Commentary* American Concrete Institute.

Institution, B. (2004). Eurocode 2: Design of concrete structures: Part 1-1: General rules and rules for buildings. In: British Standards Institution London, UK.

ISO 15835. (2018). Steels for the reinforcement of concrete–Reinforcement couplers for mechanical splices of bars–Part 1: Requirements. *International Organization for Standardization*.

Kheyroddin, A., Mohammadkhah, A., Dabiri, H., & Kaviani, A. (2020). Experimental investigation of using mechanical splices on the cyclic performance of RC columns. *Structures*, *24*, 717-727. https://doi.org/10.1016/j.istruc.2020.01.043

Mander, J., Panthaki, F., & Kasalanati, A. (1994). Low-cycle fatigue behavior of reinforcing steel. *Journal of Materials in Civil Engineering*, *6*(4), 453-468.

Mander, J. B., Panthaki, F. D., & Kasalanati, A. (1994). Low-Cycle Fatigue Behavior of Reinforcing Steel. *Journal of Materials in Civil Engineering, ASCE*, *6*(4), 453–468.

Matamoros, A. (1999). *Study of Drift Limits for High-Strength Concrete Columns* [PhD Thesis, University of Illinois at Urbana-Champaign]. Urbana, IL. Department of Civil Engineering

MathWorks. (2024). butter (Butterworth filter design). https://www.mathworks.com/help/signal/ref/butter.html

Moehle, J. P. (2014). *Seismic Design of Reinforced Concrete Buildings*. McGraw-Hill Education.

Mohamed, N., Laurent, M., Emmanuel, F., Aron, G., Rémi, G., Richard, B., Philippe, H., Poissonnet, C., & jean-marie, D. (2025). Impact of incorporating parallel-threaded mechanical coupler splices on the seismic behaviour of reinforced concrete columns. *Engineering Structures*, *323*. https://doi.org/10.1016/j.engstruct.2024.119289

N.Z.S. (2006). *Concrete Structures Standard - The Design of Concrete Structures*. Standards, New Zealand.

Neupane, U., Lequesne, R. D., Lepage, A., & Darwin, D. (2025). Behavior of Earthquake-Resistant Rectangular Walls with Mechanically-Spliced Grade 100 Steel Bars. *ACI Structural Journal*.

Normalisation, A. F. d. (2017). Steel products - Mechanical splices and mechanical anchorages for ribbed or indented reinforcing steel - Part 1: requirements. In. La Plaine Saint-Denis, France: Association Française de Normalisation (AFNOR).

Rajae, S., Hoggsett, G., Chapagain, B., Banjade, S., & Ghannoum, W. M. (2023). Vision-Based Large-Field Measurements of Bridge Deformations. *Journal of Bridge Engineering*, *28*(11), 04023075.

Rautenberg, J. M., Pujol, S., Tavallali, H., & Lepage, A. (2012). Reconsidering the use of high-strength reinforcement in concrete columns. *Engineering Structures*, *37*, 135-142.

Reetz, R. J., von Ramin, M., & Matamoros, A. B. (2004). *Performance of Mechanical Splices Within the Plastic Hinge Region of Beams Subjected to Cyclic Loading* 13th World Conference on Earthquake Engineering, Vancouver, Canada. https://www.iitk.ac.in/nicee/wcee/article/13_1073.pdf

Sajedul Huq, M., Weber-Kamin, A. S., Ameen, S., Lequesne, R. D., & Lepage, A. (2017). *High-Strength Steel Bars in Reinforced Concrete Walls: Influence of Steel Mechanical Properties on Deformation Capacity* ((06-14)).

Sharma, L., Abdullah, W., Niroula, S., Budhathoki, N., & Ghannoum, W. M. (2025). Inelastic Cyclic Performance of Mechanical Couplers with Grade 80 Bars. *ACI Structural Journal*, *122*(1), 225-240. https://doi.org/10.14359/51743341

Slavin, C. M., & Ghannoum, W. M. (2015). *Defining Structurally Acceptable Properties of High-Strength Steel Bars through Material and Column Testing, PART I: MATERIAL TESTING REPORT* ((05-14)_1).

Smith, B. J., & Kurama, Y. C. (2014). Seismic design guidelines for solid and perforated hybrid precast concrete shear walls. *PCI Journal*, *59*(3), 43-59.

Sokoli, D., & Ghannoum, W. M. (2016). High-Strength Reinforcement in Columns under High Shear Stresses. *ACI Structural Journal*, *113*(3), 605-614.

Sokoli, D., & Ghannoum, W. M. (2016). High-strength reinforcement in columns under high shear stresses. *ACI Structural Journal*, *113*(3), 605.

Sokoli, D., Hogsett, G., Limantono, A., Suselo, A., Al-Tarafany, D., Rodgers, S., & Ghannoum, W. M. (2019). *Acceptable Elongations and Low-Cycle Fatigue Performance for High-Strength Reinforcing Bars* ((03-16)).

Sokoli, D., Limantono, A., Duy, V. T., Moehle, J. P., & Ghannoum, W. M. (2025). From Global to Local Deformations of Concrete Frame Members Accounting for Steel Properties. *ACI Structural Journal*, *122*(3).

Sokoli, D., Limantono, A., & Ghannoum, W. M. (2020). Special Moment Frames with High-Strength Reinforcement--Part 2: Columns. *ACI Structural Journal*, *117*(2).

Sokoli, D., Limantono, A., & Ghannoum, W. M. (2020). Special Moment Frames with High-strength Reinforcement – Part 2- Columns. *ACI Structural Journal*, *117*(2), 253-267.

Sokoli, D., Limantono, A., To, D., Moehle, J. P., & Ghannoum, W. M. (2025). From Global to Local Deformations of Concrete Frame Members Accounting for Steel Properties. *ACI Structural Journal*, *122*(3), 133-145.

Sokoli, D., Shekarchi, W., Buenrostro, E., & Ghannoum, W. M. (2014). Advancing behavioral understanding and damage evaluation of concrete members using high-resolution digital

image correlation data. *Earthquakes and Structures*, *7*(5), 609-626. https://doi.org/http://dx.doi.org/10.12989/eas.2014.7.5.609

Sokoli et., a. (2014). Sokoli, D., Shekarchi, W., Buenrostro, E. and Ghannoum, W. M., "Advancing Behavioral Understanding and Damage Evaluation of Concrete Members Using High-

179

Resolution Digital Image Correlation Data," Earthquakes and Structures, V. 7, No. 5, 2014, pp. 609-626. doi: 10.12989/eas.2014.7.5.609.

Standardization, E. C. f. (2004). *Eurocode 8: Design of structures for earthquake resistance – Part 1: General rules, seismic actions and rules for buildings* (Vol. EN 1998-1:2004). CEN.

Tex-744-I. (2019). Testing Mechanical Couplers for Reinforcing Steel. In (pp. 1-5). Texas, USA: Texas Department of Transportation, Materials and Tests Division.

To, D., Sokoli, D., Ghannoum, W. M., & Moehle, J. P. (2021). Seismic Performance of Tall Moment Frames with High-Strength Reinforcement. *ACI Structural Journal*, *118*(1), 113-124.

Transportation, C. D. (2013). Seismic Design Criteria (SDC) Version 1.7. In.

Venture, N. C. J., & Venture, N. C. J. (2017). *Use of high-strength reinforcement in earthquake-resistant concrete structures*. US Department of Commerce, National Institute of Standards and Technology.

Villalobos, E., Escolano-Margarit, D., Ramírez-Márquez, A. L., & Pujol, S. (2017). Seismic response of reinforced concrete walls with lap splices. *Bulletin of Earthquake Engineering*, *15*(5), 2079-2100.

Zhong, K., Ghannoum, W. M., & Deierlein, G. G. (2021). Influence of High Strength Reinforcing Bars on Seismic Safety of Concrete Frames. *ACI Structural Journal*, *118*(5), 299-311.